Multidisciplinary design and optimization of innovative electrical power systems for aerospace applications

POLITECNICO DI TORINO

SCUOLA DI DOTTORATO

Dottorato di Ricerca in Ingegneria Aerospaziale

XXVI ciclo

Tesi di Dottorato

Multidisciplinary design and optimization of innovative electrical power systems for aerospace applications

Enrico Testa

SSD: ING-IND/05

Tutor

Prof. Paolo Maggiore

Coordinatore del corso di dottorato

Prof.ssa Fulvia Quagliotti

2014

SUMMARY

One of the main engineering research areas focuses on the development of new power sources technologies. Proton Exchange Membrane Fuel Cells (PEMFCs) promise low emissions, but also high power densities (W kg^{-1}) if compared to conventional electrical batteries, in the meanwhile having the possibility to continuously operate if supplied with hydrogen, instead of needing to be charged as it is for batteries themselves. In the last few years, the electric energy demand has increased dramatically worldwide: this is mainly due to the Industrialized Countries tending to absorb a constantly raising amount of energy, but also because of the rapid expansion of the developing countries. So far, about 85% of the energy need is satisfied by fossil fuels combustion releasing dangerous pollutants in the atmosphere, such as NOx, CO, HC. Moreover, the whole international scientific community considers the reduction of the gas emissions as necessary in order to preserve the current earth's climate. A sustainable development based on hydrogen as a clean energetic vector seems to be the best solution to date.

All of these aspects make fuel cells attractive also for aerospace applications as candidate substitutes for both primary and secondary power generation systems. The use of fuel cells for aircraft is an ever-growing concept in today's environmentally conscious world. NASA studies have indicated that PEM fuels cells are becoming reasonably practical for propulsion in small aircrafts and Unmanned Aerial Vehicles (UAVs), and could be promising in future large-scale commercial aircraft. Dealing with space applications, the current efforts are devoted instead towards the so-called regenerative fuel cell system, consisting of a fuel cell stack coupled with an electrolyser stack used alternatively to generate and store electric power, in substitution of conventional secondary batteries. Primary batteries could also be easily substituted by fuel cells with the promise of lower weight. For these applications, it is important to understand the fuel cell-based power system from a system integration and power management perspective. Optimizing the integration of each component into the system and understanding the overall power system compatibility is essential for a successful design. Nevertheless, this foreseeing objective cannot be reached without a basic, robust, adaptable and multidisciplinary model of the entire power plant, as well as of the core of the system, the *fuel cell stack* and the *electrolyser stack*.

The aim of this thesis is the development of a confident and robust fuel cell system lumped model, developed mainly in Matlab and Simulink environments, in order to create a powerful predictive virtual test bench to be used with confidence for robust fuel cell systems design, development, analysis and optimization. The two main cores of the presented model are the fuel cell stack, based on the PEM technology, and an electrolyser stack, based both on alkaline and PEM technologies. All of the possible ancillary equipment is also developed and created in Simulink

environment to create a collection of “model blocks” capable to integrate together to build any possible system configuration. The models merge together all of the main and most relevant aspects involved in fuel cells operations, with a particular attention to the modelling of the transient phenomena.

The first part of chapter 1 focuses at getting an introduction to fuel cells and electrolysers technologies, providing an introduction and history of them, and giving the reader a brief description of the potential and current applications available in the engineering world. The second part of chapter 1, instead, shows an identification and classification of the different types of fuel cells and electrolysers, and briefly introduces the basic functioning principles from an electrochemical point of view.

Chapter 2 contains the development of the alkaline and PEM electrolysers models. In particular, the alkaline one is considered in depth, since the equations for the PEM one are almost coincident. The electrolyser model was developed as a lumped one. The main element of the electrolyser consisted in the stack itself, the cooling flow circuit and the hydrogen/oxygen storage tanks. The stack model here presented collects most of the already available models in the literature, with a particular attention in modelling most of the phenomena involved.

Chapter 3 can be considered the core of the thesis, since it contains the fuel cell stack and system model. All of the physical aspects involved in the fuel cell operation are considered. The first part of Chapter 3 deals with the models already available in literature, considering pros and cons of the most relevant ones. The importance of modelling the transient phenomena involved in this particular kind of technology is underlined and analysed. The second portion of this chapter contains mainly the development of the fuel cell stack. Validation, calibration and simulation of this main component will be considered in Chapter 4. The third portion of Chapter 3 contains the models of all to other elements of the fuel cell system, in particular the model for the air compressor, motor, intercooler, air and water membrane humidifiers and flow mixers. For these secondary elements the calibration and validation of the models with the experimental data are provided. Further simulations will be contained in Chapter 4.

Chapter 4 is the main results chapter. The first part of this chapter is dedicated to the stack model calibration and validation process with experimental data. Given the model validation, several system simulation results are presented in the second part of the chapter. The calibration and validation of the electrolyser plant is instead given in the third part of Chapter 4. The final part of this chapter contains the simulation data for the electrolyser plant.

Chapter 5 presents an activity done in parallel with the lumped models development. In this chapter, optimization studies for fuel cells is addressed from a CFD model viewpoint. It presents the setup of a complete multidisciplinary design optimization model, automatically performed; sensitivity analyses, multi-objective optimization techniques and robust design optimization techniques are explored. The model used in this chapter is based on a validated proprietary CFD model of a PEM fuel cell described in Chapter 5.

Chapter 6 contains the conclusions and possible further improvements of the thesis.

SOMMARIO

Una delle principali aree di ricerca ingegneristica consiste nello sviluppo di nuove tecnologie per la generazione di potenza elettrica. Le celle a combustibile PEM (Proton Exchange Membrane) permettono di contenere molto le emissioni inquinanti e, allo stesso tempo, di avere alte densità di potenza (W kg^{-1}) rispetto alle batterie elettriche convenzionali e avendo la possibilità di operare in continuo se alimentate continuamente con idrogeno. Negli ultimi anni, la domanda di energia elettrica è aumentata notevolmente in tutto il mondo. Questo è dovuto principalmente ai paesi industrializzati che tendono ad assorbire una quantità di energia in costante aumento, ma anche a causa della rapida espansione dei paesi in via di sviluppo. Finora, circa il 85% del fabbisogno energetico è soddisfatto da combustibili fossili, con conseguente rilascio di notevoli quantità di sostanze inquinanti pericolose in atmosfera, come NO_x, CO, HC. Inoltre, tutta la comunità scientifica internazionale ritiene che la riduzione delle emissioni di gas sia necessaria al fine di preservare il clima terrestre. Uno sviluppo sostenibile basato sull'idrogeno come vettore energetico pulito sembra essere la soluzione migliore per diversi aspetti. Tutti questi aspetti rendono le celle a combustibile attraenti anche per applicazioni aerospaziali, come sostitute per entrambi i sistemi primari e secondari di generazione di energia. L'utilizzo di celle a combustibile per velivoli è un concetto in continua crescita nel mondo. Gli studi della NASA hanno indicato che le celle a combustibile PEM possano essere ragionevolmente impiegate allo stato attuale per la propulsione di piccoli velivoli e Unmanned Aerial Vehicles (UAV). Nell'ambito delle applicazioni spaziali, gli attuali sforzi sono dedicati invece verso il cosiddetto sistema di cella a combustibile rigenerativa, costituito da uno stack di celle a combustibile accoppiato con uno stack di elettrolizzatore utilizzato alternativamente per generare ed immagazzinare l'energia elettrica, in sostituzione di batterie ricaricabili convenzionali. Batterie non ricaricabili potrebbero anche essere facilmente sostituite da celle a combustibile grazie al minor peso imbarcato al lancio. Per queste applicazioni, è importante conoscere il comportamento del sistema di alimentazione basato a cella a combustibile dal punto di vista dell'integrazione e gestione della potenza sviluppata. L'ottimizzazione e l'integrazione di ciascun componente nel sistema sono essenziali per il successo dell'intero progetto. Tuttavia, tale obiettivo non può essere raggiunto senza un modello di base, robusto, adattabile e multidisciplinare dell'intero impianto di alimentazione, nonché del nucleo del sistema, lo stack di celle a combustibile e l'elettrolizzatore.

Lo scopo di questa tesi è lo sviluppo di un modello a parametri concentrati di cella a combustibile robusto, sviluppato prevalentemente in ambiente Matlab e Simulink, al fine di creare un potente banco di prova virtuale predittivo da utilizzare come aiuto nella progettazione. I due nuclei principali del modello presentato sono lo stack di celle a combustibile, basato sulla tecnologia PEM, e uno stack di elettrolisi, basato sia su tecnologia alcalina che PEM. Sono inoltre stati sviluppati tutti gli elementi ausiliari del sistema, sempre in ambiente Simulink, per creare una

collezione di "blocchi" da poter utilizzare e assemblare insieme per ottenere qualsiasi configurazione di sistema possibile. I modelli considerano tutti gli aspetti principali e più rilevanti coinvolti nel funzionamento delle celle a combustibile, con una particolare attenzione alla modellazione dei fenomeni transitori.

La prima parte del capitolo 1 fornisce un'introduzione alle celle a combustibile e agli elettrolizzatori, fornendo un breve elenco di applicazioni nel passato, e dando al lettore una breve descrizione delle potenziali ed attuali applicazioni disponibili nel mondo dell'ingegneria aerospaziale. La seconda parte del capitolo 1, invece, presenta la classificazione dei diversi tipi di celle a combustibile ed elettrolizzatori, e introduce brevemente i principi di funzionamento di base da un punto di vista elettrochimico.

Il capitolo 2 contiene lo sviluppo dei modelli di elettrolizzatori alcalini e PEM. In particolare, quello alcalino è considerato nel dettaglio, in quanto le equazioni per la tecnologia PEM sono quasi coincidenti. Il modello di elettrolizzatore è stato sviluppato a parametri concentrati. L'elemento principale del elettrolizzatore consiste nello stack stesso, il circuito di raffreddamento e i serbatoi di stoccaggio di idrogeno/ossigeno. Il modello di stack qui presentato raccoglie la maggior parte dei modelli già disponibili in letteratura, con particolare attenzione nel modellare la maggior parte dei fenomeni coinvolti.

Il capitolo 3 può essere considerato il cuore della tesi, contenendo il modello dello stack di celle a combustibile e il suo sistema completo. Tutti gli aspetti fisici coinvolti nel funzionamento delle celle a combustibile sono considerati. La prima parte del capitolo 3 tratta i modelli già disponibili in letteratura, considerando pro e contro di quelli più rilevanti. L'importanza di modellare i fenomeni transitori coinvolti in questo particolare tipo di tecnologia è sottolineata e analizzata. La seconda parte di questo capitolo contiene principalmente lo sviluppo del modello di cella a combustibile. La validazione, calibrazione e simulazione di questo componente principale verranno prese in considerazione nel capitolo 4. La terza parte del capitolo 3 contiene i modelli di tutti gli altri elementi del sistema di cella a combustibile, in particolare il modello per gli umidificatori, il compressore d'aria, il motore, l’intercooler, gli umidificatori ad aria e acqua a membrana e i miscelatori di flusso. Per questi elementi secondari la calibrazione e validazione dei modelli con i dati sperimentali o dei costruttori vengono dati in questo capitolo. Ulteriori simulazioni saranno contenute nel capitolo 4.

Il capitolo 4 è il capitolo contenente i risultati principali. La prima parte di questo capitolo è dedicato alla calibrazione e validazione del modello di stack. Diversi risultati di simulazione del sistema sono presentati nella seconda parte del capitolo. La calibrazione e validazione dell’elettrolizzatore sono invece riportati nella terza parte del capitolo 4. La parte finale di questo capitolo contiene i dati di simulazione per il sistema di elettrolizzatore completo.

Il capitolo 5 presenta un’attività svolta in parallelo con lo sviluppo modelli a parametri concentrati. In questo capitolo viene considerata l’ottimizzazione di celle a combustibile usando un modello di cella in CFD (Computational Fluid Dynamics). Vengono presentate analisi di sensitivity e ottimizzazione con tecniche multi-obiettivo. Il modello utilizzato in questo capitolo si basa su un modello CFD validato di una cella a combustibile PEM.

Il capitolo 6 infine contiene le conclusioni e i possibili ulteriori miglioramenti della tesi.

INDEX

LIST OF SYMBOLS AND ACRONYMS

Symbols

a	Water activity (-)
$acty$	Water activity (-)
A	Cell area (m^2)
A_{exc}	Exchange current density constant (V)
A_{humid}	Humidifier Nafion channels total area (m^2)
A_{ic}	Intercooler exchange area (m^2)
A_{real}	Real surface area of the electrode (m^2)
C_{dl}	Double layer capacitance (F)
C_{ez}	Electrolyser thermal capacity ($J\ K^{-1}$)
C_{mem}	Membrane water concentration ($mol\ m^{-3}$)
c_p	Specific heat ($J\ mol^{-1}\ K^{-1}$)
$c_{p_{stack}}$	Stack thermal capacity ($J\ kg^{-1}\ K^{-1}$)
c_v	Specific heat at constant volume ($J\ kg^{-1}\ K^{-1}$)
d	Capacitor plates distance (m)
D_{GDL}	GDL diffusivity (m^2)
D_{mem}	Membrane water diffusivity inside the membrane
E	Reversible cell voltage (V)
E^0	Reversible cell voltage at standard conditions (V)
E_{act}	Activation energy ($J\ mol^{-1}$)
f	Gas bubbles resistance coefficient (-)
$\hat{f}$	Generic function
h	Molar enthalpy ($J\ mol^{-1}$)
hA_a	Anode heat exchange constant ($J\ kg^{-1}$)
hA_c	Cathode heat exchange constant ($J\ kg^{-1}$)
hA_{cool}	cooling flow heat exchange constant ($J\ kg^{-1}$)
$h_{C_{ic}}$	Intercooler cold-wall interface convective heat coefficient ($W\ m^{-2}\ K^{-1}$)
h_{cond}	Conductive heat transfer coefficient ($W\ K^{-1}$)
h_{conv}	Convective heat transfer coefficient ($W\ K^{-1}\ A^{-1}$)
$h_{H_{ic}}$	Intercooler hot-wall interface convective heat coefficient ($W\ m^{-2}\ K^{-1}$)
$H_{2_{a,in}}$	Hydrogen anode side inlet mass flow ($kg\ s^{-1}$)
$H_{2_{flow_{min}}}$	Minimum hydrogen inlet flow ($kg\ s^{-1}$)
$H_2O_{a,evap}$	Anode water evaporation mass flow ($kg\ s^{-1}$)

List of symbols and acronyms

$H_2O_{c,evap}$	Cathode water evaporation mass flow (kg s^{-1})
$H_2O_{l_{a,in}}$	Liquid water mass flow at anode inlet (kg s^{-1})
$H_2O_{l_{c,in}}$	Liquid water mass flow at cathode inlet (kg s^{-1})
$H_2O_{v_{a,in}}$	Water vapour mass flow at anode inlet (kg s^{-1})
$H_2O_{v_{a,in,max}}$	Maximum water vapour mass flow at anode inlet (kg s^{-1})
$H_2O_{v_{c,in}}$	Water vapour mass flow at cathode inlet (kg s^{-1})
$H_2O_{v_{c,in,max}}$	Maximum water vapour mass flow at cathode inlet (kg s^{-1})
$H_{2_{react}}$	Hydrogen mass flow consumption (kg s^{-1})
H_2O_{react}	Water mass flow production (kg s^{-1})
i	Current density (A m^{-2})
I	Net current (A)
i_0	Exchange current density (A m^{-2})
$i_{0_{ref}}$	Reference exchange current density (A m^{-2})
I_{in}	Input current entering the stack (A)
i_n	Cross-over current density (A m^{-2})
i_{max}	Maximum current density (A m^{-2})
J_{cm}	Motor + compressor inertia (kg m^2)
k_{D_w}	PEM membrane water diffusivity calibration constant (-)
k_{f1}	Faraday efficiency first constant (A^2 m^{-4})
k_{f2}	Faraday efficiency second constant (-)
k_{mem}	Membrane diffusion constant (-)
KOH_{conc}	Potassium hydroxide mass concentration (kg l^{-1})
k_T	Torque gain (N m A^{-1})
k_V	EMF gain [V(rad s^{-1})$^{-1}$]
$K_{1C_{ic}}$	Intercooler cold side first thermal constant (kg^{-1})
$K_{2C_{ic}}$	Intercooler cold side second thermal constant (s^{-1})
$K_{1H_{ic}}$	Intercooler hot side first thermal constant (kg^{-1})
$K_{2H_{ic}}$	Intercooler hot side second thermal constant (s^{-1})
$K_{1W_{ic}}$	Intercooler wall side first thermal constant (s^{-1})
$K_{2W_{ic}}$	Intercooler wall side second thermal constant (s^{-1})
$\dot{m}_C$	Intercooler cold side mass flow (kg s^{-1})
$\dot{m}_H$	Intercooler hot side mass flow (kg s^{-1})
$m_{H_2O_v}$	Mass of water vapour (kg)
M_{KOH}	KOH solution molarity (mol l^{-1})
$\mathcal{M}_{mem}$	Membrane equivalent weight (kg mol^{-1})
$m_{N_2O_2}$	Mass of nitrogen plus oxygen (kg)
m_{stack}	Stack mass (kg)
$\dot{n}$	Molar flow (mol s^{-1})
n_{bd}	Back-diffusion flow (kg s^{-1})
n_c	Number of cells (-)
n_d	Electro-osmotic drag flow (kg s^{-1})
n_e	Number of electrons transferred (-)
Nm^3	Normal cubic meter conditions (m^3)
$N_{2_{a,in}}$	Nitrogen anode side inlet mass flow (kg s^{-1})
$N_{2_{mem}}$	Nitrogen membrane crossover mass flow (kg s^{-1})
$N_{2_{mole_{ratio}}}$	Molar ratio of nitrogen in the oxygen side mixture (-)

Ohm_{coeff}	Ohmic coefficient tuning parameter (-)
$O_{2_{flow_{min}}}$	Minimum oxygen inlet flow (kg s^{-1})
$O_{2_{react}}$	Oxygen mass flow consumption (kg s^{-1})
p	Pressure (Pa or bar)
P_{el}	Electrical output power (W)
p_{sat}	Saturation pressure (Pa)
$p_{set_{H_2}}$	Hydrogen side maximum pressure (Pa)
$p_{set_{O_2}}$	Oxygen side maximum pressure (Pa)
P_{tot}	Total power (W)
p_{vap}	Vapour pressure (Pa)
$\dot{Q}_{cool}$	Cooling power (W)
$\dot{Q}_{gen}$	Heat generation (W)
$\dot{Q}_{latent}$	Latent heat (W)
$\dot{Q}_{loss}$	Heat lost by radiation (W)
$\dot{Q}_{mass}$	Mass heat transport (W)
$\dot{Q}_{net}$	Net power generated (W)
$\dot{Q}_{sens}$	Sensible heat (W)
R^2	Linear correlation coefficient (-)
R_{act}	Activation voltage resistance (Ω)
R_{conc}	Concentration voltage resistance (Ω)
r_f	Electrolyte resistance (Ω m)
R_m	Motor electric resistance (Ω)
R_{ohm}	Ohmic cell resistance (Ω)
R_{sep}	Separator electrical resistance (Ω m^2)
R_{therm}	Thermal resistance (K W^{-1})
R_{tot}	Total electric resistance (Ω m^2)
s	Molar entropy (J mol^{-1} K^{-1})
t	Electrolyte film thickness (m)
T	Temperature (K)
T_{amb}	Ambient temperature (K)
T_C	Intercooler cold side temperature (K)
t_{GDL}	GDL thickness
t_{humid}	Humidifier Nafion channel thickness (m)
$T_{cool_{in}}$	Cooling inlet temperature (K)
$T_{cool_{out}}$	Cooling outlet temperature (K)
T_H	Intercooler hot side temperature (K)
t_{mem}	Membrane thickness (m)
T_{room}	Ambient temperature (K)
T_{stack}	Stack temperature (K)
T_W	Wall temperature (K)
UA_{humid}	Humidifier heat exchange coefficient (W K^{-1})
V	Voltage (V)
V_{act}	Activation voltage (V)
V_c	Cell voltage (V)
$V_{GDL_{step}}$	GDL transient step constant (-)
$V_{GDL_{time}}$	GDL transient time constant (-)
V_{H_2}	Hydrogen side volume – vessel volume (m^3)

List of symbols and acronyms

V_{in}	Electrolyte inlet velocity (m s^{-1})
V_{ohm}	Ohmic voltage loss (V)
Vol	Fluid channels volume (m^3)
V_{O_2}	Oxygen side volume – vessel volume (m^3)
V_m	Motor voltage (V)
V_{stack}	Stack voltage (V)
V_{TN}	Thermo-neutral voltage (V)
W	electrolysis cell width (m)
$wt\%$	Percentage in weight (-)
y_{H_2}	Hydrogen inlet mass fraction (-)
y_{N_2}	Nitrogen mass fraction (-)
y_{O_2}	Oxygen inlet mass fraction (-)
Z	Compressibility factor (-)
α_1	Butler-Volmer reduction transfer coefficient (-)
α_2	Butler-Volmer oxidation transfer coefficient (-)
α_b	Bubble volume fraction in the electrolyte (-)
α_{ctc}	Charge transfer coefficient (-)
β	Symmetry factor (-)
ΔG	Change in molar Gibbs free energy (J mol^{-1})
Δh	Change in molar enthalpy (J mol^{-1})
ΔH_{vap}	Heat of vaporization (J kg^{-1})
Δp	Pressure loss (Pa)
Δs	Change in molar entropy (J mol^{-1} K^{-1})
ε	Electrical permittivity (F m^{-1})
η_{com}	Compressor efficiency (-)
η_F	Faraday efficiency (-)
η_m	Motor efficiency (-)
η_{th}	Thermal efficiency (-)
λ_{mem}	Membrane humidification (-)
ρ	Mass density (kg m^{-3})
ρ_{mem}	Membrane dry density (kg m^{-3})
ρ_{mol}	Molar density (kmol m^{-3})
σ	Electric conductivity (S m^{-1})
σ_b	Electrolyte bubbles slip ratio (-)
τ_{com}	Compressor torque (N m)
$\tau_{GDL,mem}$	Gas diffusion layer / membrane time constants (s)
τ_m	Motor torque (N m)
ϕ	Relative humidity (-)
ω_m	Motor speed (rad s^{-1})

Pedices

a	Anode side
ave	Average
c	Cathode side
cool	Cooling flow
des	Desired
dry	Humidifier dry air duct side
GDL	Gas Diffusion Layer

H_2	Hydrogen
H_2O_g	Gaseous water
H_2O_l	Liquid water
hum	Humidifier humid air duct side
humid	Humidifier
ic	Intercooler
in	Inlet station
KOH	Potassium hydroxide
l	Liquid
mem	Membrane
mix	Hydrogen flow mixer
out	Outlet station
O_2	Oxygen
v	Gaseous
wat	Humidifier water duct side
x	x-species

Constants

γ	Gas constant (1.4)
ε_0	Electric permittivity in vacuum (8.854188 x 10^{-12} F m^{-1})
ρ_{mem}	Membrane dry density (1000 kg m^{-3})
$c_{p_{H_2}}$	Hydrogen specific heat (0.058758 J kg^{-1} K^{-1})
$c_{p_{H_2O_l}}$	Liquid water specific heat (4186.0 J kg^{-1} K^{-1})
$c_{p_{H_2O_v}}$	Water vapour specific heat (1.359 J kg^{-1} K^{-1})
$c_{p_{N_2}}$	Nitrogen specific heat (0.815360 J kg^{-1} K^{-1})
$c_{p_{O_2}}$	Oxygen specific heat (0.942080 J kg^{-1} K^{-1})
$c_{v_{N_2}}$	Nitrogen specific heat at constant volume (740.8220 J kg^{-1} K^{-1})
$c_{v_{O_2}}$	Oxygen specific heat at constant volume (660.2721 J kg^{-1} K^{-1})
c_r	Condensation rate constant (100 s^{-1})
F	Faraday's constant (96485.309 C mol^{-1})
$\mathcal{M}_{H_2}$	Hydrogen molar mass (2.02 x 10^{-3} kg mol^{-1})
$\mathcal{M}_{H_2O}$	Water molar mass (18.02 x 10^{-3} kg mol^{-1})
$\mathcal{M}_{mem}$	Membrane equivalent weight (1.1 kg mol^{-1})
$\mathcal{M}_{N_2}$	Nitrogen molar mass (28.01 x 10^{-3} kg mol^{-1})
$\mathcal{M}_{O_2}$	Oxygen molar mass (32.0 x 10^{-3} kg mol^{-1})
R	Universal gas constant (8.31451 J mol^{-1} K^{-1})
T_0	Reference temperature (298.15 K)

Acronyms

BWR	Bennedict-Webb-Rubin
EZ	ElectrolyZer
FC	Fuel Cell
FEM	Finite Element Method
GDL	Gas Diffusion Layer
GE	General Electric

List of symbols and acronyms

HHV	Higher Heating Value
LHV	Lower Heating Value
NASA	National Aeronautics and Space Administration
PEM	Proton Exchange Membrane
PEMFC	Proton Exchange Membrane Fuel Cell
RFC	Regenerative Fuel Cell
SLPM	Standard Litres Per Minute
SPE	Solid Polymer Electrolyte
SOFC	Solid Oxide Fuel Cell
UAV	Unmanned Aerial Vehicle
URFC	Unitized Regenerative Fuel Cell

1. INTRODUCTION

1.1 History

In this introductory paragraph, past and present use of hydrogen technologies are briefly discussed. This paragraph focuses mainly on aerospace applications of fuel cell and water electrolysis.

1.1.1 Fuel cells

The Fuel Cell (FC) was developed as an intermediate-term power source for space applications. The fuel cell resembles a battery since it converts the chemical energy of a fuel directly into DC electricity. However, unlike a battery, it does not run down in energy and has to be recharged. It produces electricity as long as the fuel is supplied. The fuel cell is "a gas battery". A typical fuel gas is hydrogen or a hydrogen-rich mixture and an oxidant.

The basic operation of the hydrogen fuel cell is extremely simple. The first demonstration of a fuel cell was by the lawyer and scientist William Grove in 1839, using an experiment along the lines of that shown in Figure 1.1 (left), while in Figure 1.1 (right) water is being electrolyzed into hydrogen and oxygen by passing an electric current through it. In Figure 1.1 (right), the power supply has been replaced with an ammeter, and a small current is flowing.

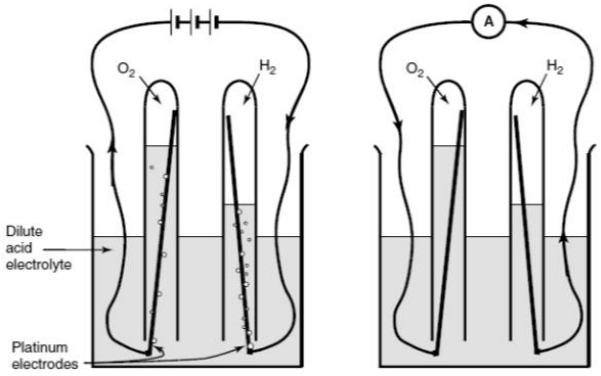

Figure 1.1 (a) water electrolysis process; (b) fuel cell basic function principle

The basic principle of a fuel cell is thus the reverse of the electrolysis of water. In the electrolysis, electricity is passed between two electrodes in water to produce hydrogen and oxygen. In the fuel cell, hydrogen and oxygen are combined to produce electricity and water. The energy conversion is direct from chemical to electrical. Since the process is isothermal, the conversion efficiency is not limited by the Carnot efficiency. This is unlike many chemical-to-thermal-to-mechanical-to-electrical energy converters using steam or internal combustion engines (as in the Joule-Brayton cycle). It skips the usual combustion step of conventional power systems and converts a high percentage of the fuel chemical energy directly into electricity. The fuel cell efficiency, therefore, can be about twice than that of the thermodynamic converters. It is as high as 65% in some designs and 75 to 80% in Solid Oxide Fuel Cells (SOFC) developed for ground base power plants. Its superior reliability with no moving parts is an additional benefit over thermodynamic power generators.

The first use of a fuel cell system in space was in the Gemini program on August 21, 1962. At that time, the first of seven Gemini manned spacecraft was launched with a Proton Exchange Membrane (PEM) electrolyte fuel cell known at that time as the solid polymer electrolyte ion exchange membrane fuel cell. Six more Gemini spacecraft were successfully flown with this fuel cell through 1966. The Biosatellite 2, launched September 7, 1967, utilized a PEM fuel cell system with an important change involving the use of an improved membrane material known as Nafion® (a sulfonated tetrafluorethylene copolymer), a registered trademark of the DuPont Company. Since then, Nafion® has been the membrane of choice for all PEM fuel cells. While the PEM fuel cell served well in this initial application, it did not have the power density capabilities of the alkaline type of fuel cell that was concurrently under development. Subsequent Apollo manned flights (1968-72) utilized the alkaline electrolyte fuel cell containing potassium hydroxide electrolyte held in an asbestos separator. The shuttle orbiter fuel cell power plant contained three H_2/O_2 alkaline fuel cell power plants supplying 12 kW at peak and 6 kW of average power. The operating temperature was 83-105°C. The current density was 66-450 $mAcm^{-2}$. The system was capable of 2,000 hours of operation. The shuttle orbiter fuel cell power plant was 23 kg lighter and delivered eight times the power of the Apollo fuel cell system (Table 1.1).

Table 1.1 Comparison of FCs used in manned space missions (Halpert et al. 1999)

Characteristics	**Mission**		
	Gemini	Apollo	Space shuttle
Stack type / units	PEM / 3	AFC / 2	AFC / 3
Energy (kWh/unit)	65	115	2600
Current density ($mAcm^{-2}$)	36	68	172
Average power (W/unit)	1000	1420	7000
Stack specific power W kg^{-1})	33.33	12.99	60.87
Stack mass (kg)	30	110	115
Lifetime (h)	1000	400	2000

In the aeronautics, fuel cells own two main areas of applicability:

- Propulsion power for small airplanes (e.g. general aviation class), Unmanned Aerial Vehicles (UAVs) or gliders; in this case, the fuel cell provides electric energy to an electric motor in substitution of a conventional internal combustion engine driving the propeller. The same fuel cell provides also all of the electric energy required by onboard equipment (avionics and electronics), making the vehicle "all electric". PEM fuel cells are currently adopted for this purpose.
- Auxiliary electric power generation, both onboard airplanes in the form of Auxiliary Power Units (APUs) or at the airport as Ground Power Units (GPUs). In this second application

field, a fuel cell converts chemical energy to electric energy driving pneumatic pumps or gears, in substitution of a conventional oil powered turbine. The SOFC and the PEM technologies are usually adopted.

The year 2008 has been an important year for the hydrogen technology development applied to aeronautics engineering. Two of the main events regarding fuel cells was the first flight of the Boeing Dimona fuel cell powered airplane, and the fuel cell testing onboard an Airbus A320.

The Dimona airplane (Figure 1.2) was developed by Diamond aircraft industries of Austria and it is a clear example of how the hydrogen technology is going ahead in the aeronautics engineering. The main foreseeing objectives of this research project consisted in the reduction of weights, fuel usage and pollutants emissions. Such vehicle was equipped with a PEM fuel cell and a lithium-ion battery powering a traditional electrical engine. During the flight, the airplane raised at 1000 meters using the power coming directly from the hydrogen and the battery; then the cruise was conducted for 20 minutes at an average speed of 100 km h^{-1}. The electrical power output was about 20 kW.

The second event was completely different from the first one. The main purpose of this test was to verify the capabilities of the fuel cell technology during flight conditions. An Airbus A320 was equipped with a fuel cell system delivering up to 20 kW. The success of this test consisted in the robustness and fidelity of the fuel cell during high gravitational loads and null gravity conditions.

Fuel cells have a strong applicability in the aeronautics industry. It must be remarked that fuel cells using direct hydrogen will not have any practical application for high capacity civil transport, standing the main difficulty in hydrogen storage in gaseous form, unless new storage technologies are revealed. Hence, fuel cells could have a practical and immediate application for general aviation airplanes, gliders or other small sized-aircrafts.

Figure 1.2 The Boeing Dimona demonstrator

Lots of studies have been carried out from universities and centers to evaluate concepts for fuel cell-based propulsion systems for all-electric high altitude, long endurance (Unmanned Aerial Vehicles - UAVs) applications. Fuel cells exhibit a higher efficiency if compared to internal combustion engines, and therefore may enhance or enable long endurance UAV missions. When operated on hydrogen, the by-products of the fuel cell reaction are heat and water. Although large quantities of heat can be generated during operation, in many instances the heat can be recaptured and supplied to other processes, such as heating of reactants or fuel processing, or the hot exit streams can be expanded in a turbine to produce power. As part of this effort, system studies were conducted to identify concepts with high payoff potential and associated technology areas for further

development. Areas under consideration included several system engineering aspects: proton exchange membrane versus solid oxide fuel cells; primary, regenerative, and hybrid systems; hydrogen, methanol, methane, and jet fuels; gaseous, cryogenic, and liquid fuel storage. The two main fuel cell types under consideration for aircraft applications are, as just mentioned, the PEM and the SOFC technologies. Each of these systems offers distinct advantages as well as issues associated with their use in aircraft propulsion applications. PEM fuel cell technology is at a relatively high state of development due to major investments in recent years by the automotive industry. PEM fuel cells operate at relatively low temperatures (20 to 90°C) and use a proton-conducting polymer membrane as electrolyte. For the most part, PEM fuel cells use hydrogen as the fuel, although some small direct methanol systems have been developed.

1.1.2 Electrolysers

Given the similarity between fuel cells and electrolysers, being the electrolysis process the inverse of the fuel cell one, electrolysers developed before and in parallel with fuel cell technologies. In the area of space missions, few electrolysers were developed for some particular usage, as in the case of the water electrolysers used onboard the International Space Station to produce breathing oxygen for the crewmembers. Electrolysis, however, never met the same broad use and importance of the fuel cells for space applications. The two main electrolysers technologies developed until now are the alkaline and PEM electrolysers. Alkaline electrolysers were commercially available and affordable well before the PEM ones. At present, the alkaline technology is the most widely used, but the PEM one is growing, despite the higher cost of PEM systems requiring noble metal catalysts. In the aeronautics field, the use of electrolysers is not currently considered.

1.2 Fuel cell technologies

The fuel cell is an electrochemical generator which converts the energy released by a chemical reaction between a fuel (typically hydrogen) and an oxidizer (oxygen) directly into electric energy and heat. A fuel cell system includes several parallel *stacks;* each stack is composed by a number (n_c) of individual fuel cells connected in series.

It is similar to a chemical battery, so it is made up of two electrodes, cathode and anode where takes place the reduction and oxidation reaction respectively, and an electrolyte (both liquid and solid) that, allowing the migration of ions, closes the electrical circuit into the cell. In spite of classical batteries, where the fuel is the built-in expendable electrode, the reactants are continuously renewed, so the cell can give a permanent and constant power output.

The hydrogen and the oxidant gas (oxygen or air) arrive respectively to the anode and cathode (on the opposite side of the one in contact with the electrolyte). Thanks to the porosity of the electrode, the chemical reactions are continuously fed. The chemical process is similar to the opposite of electrolysis.

As an example, the functioning of a pure H_2/O_2 solid electrolyte FC is analyzed below:

- At the anode (negative), hydrogen atoms release electrons (oxidation reaction) and the H^+ ions migrate into the electrolyte; contemporary, the lost electrons move along the anode and enter the external electric circuit.
- At the cathode (positive), oxygen gains the electrons coming from the external circuit (reduction reaction) and becomes an O^{2-} ion. Then the hydrogen ions move towards the cathode where they recombine with O^{2-} to form water.

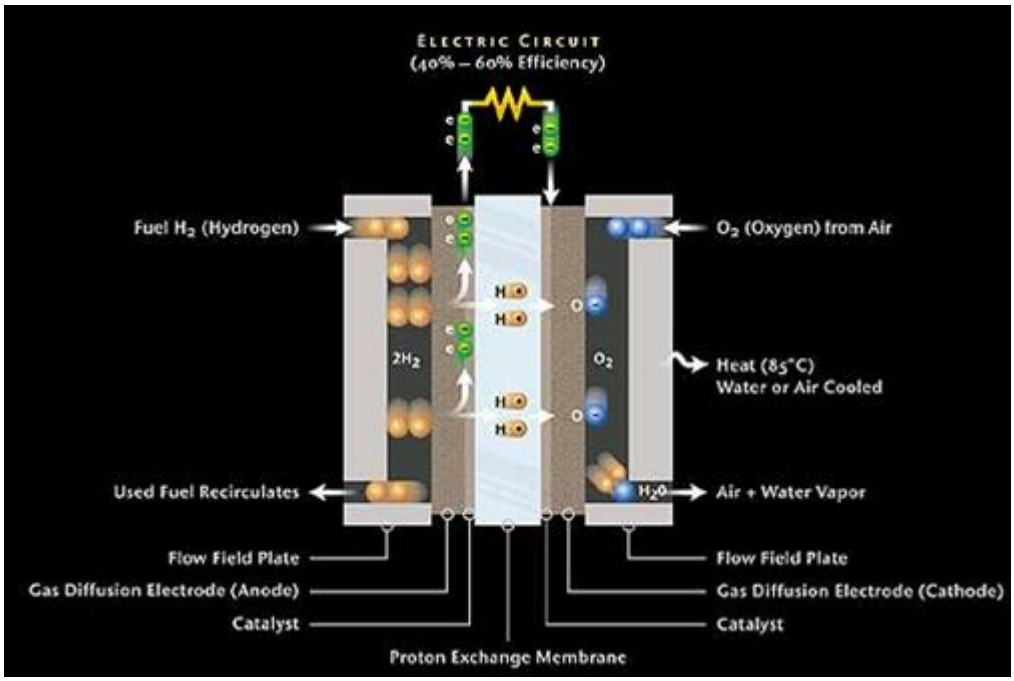

Figure 1.3 A typical PEM fuel cell operation

According to the fuels and oxidizers used and the technology implemented, also a gaseous exhaust could be present (i.e. CO or CO_2).

The fuel cell also releases heat at the operating temperature. For an optimum reaction velocity, the operating temperature must be kept in a proper range of values. So a dedicated temperature control system needs to be added to the cell to maintain a constant temperature.

For low temperature fuel cells, the reaction needs a catalyst to take place due to the low operating temperature (~80°C) and the electrode is made of a porous material to augment the surface exposed to the hydrogen or oxygen. For this reason, the electrodes are covered by a layer of platinum and ruthenium (typical ≤0.60 mg Pt/cm^2 cathode and 0.25 mg Pt/cm^2, 0.12 mg Ru/cm^2 anode, EG&G 2004).

The reduction and oxidation reactions change with the technology considered. Table 1.2 shows the chemical reactions of the fuel cell technologies analyzed further in this document.

Table 1.2 Anode, cathode and cell chemical reactions

Fuel cell technology	**Anode reaction**	**Cathode reaction**	**Cell reaction**
Low temperature fuel cells			
Solid polymer	$H_2 \rightarrow 2H^+ + 2e^-$	$½\ O_2 + 2H^+ + 2e^- \rightarrow H_2O$	$H_2 + ½O_2 \rightarrow H_2O$
Phosphoric acid	$H_2 \rightarrow 2H^+ + 2e^-$	$½\ O_2 + 2H^+ + 2e^- \rightarrow H_2O$	$H_2 + ½O_2 \rightarrow H_2O$
Alkaline	$H_2 + 2(OH)^- \rightarrow 2H_2O + 2e^-$	$½O_2 + H_2O + 2e^- \rightarrow 2(OH)^-$	$H_2 + ½O_2 \rightarrow H_2O$
Peroxide	$NaBH_4 + 8Na^+ + 8(OH)^- \rightarrow NaBO_2 + 6H_2O + 8Na^+ + 8e^-$	$8Na^+ + 8e^- + 4H_2O_2 \rightarrow 8Na^+ + 8(OH)^-$	$NaBH_4 + 4H_2O_2 \rightarrow NaBO_2 + 6H_2O$
High temperature fuel cells			
Solid oxide	$H_2 + O^= \rightarrow H_2O + 2e^-$	$½\ O_2 + 2e^- \rightarrow O^=$	$H_2 + ½O_2 \rightarrow H_2O$
Molten carbonate	$H_2 + CO_3^= \rightarrow H_2O + CO_2 + 2e^-$	$½\ O_2 + CO_2 + 2e^- \rightarrow CO_3^=$	$H_2 + ½O_2 \rightarrow H_2O$

1.2.1 Technologies

Different fuel cell classifications are available. One of the most generic and at high level one is the subdivision of fuel cells in low-temperature and high-temperature fuel cells. The difference between these two classes of technologies consists usually in having not only different operating temperatures but also different fuels used.

1.2.1.1 Low temperature fuel cells

The low temperature fuel cells usually makes use of pure hydrogen and air or oxygen as fuel and oxidant. Most of them operate at temperatures between ambient temperature and 100-150°C.

Alkaline FC (AFC)

Alkaline fuel cells were one of the first fuel cell technologies developed, and they were the first type widely used in the U.S. space program to produce electrical energy and water onboard spacecraft. At present, an AFC power system can give a 5-80 kW class of power output. These fuel cells use a solution of potassium hydroxide (KOH) in water as the electrolyte and can use a variety of precious or non-precious metals as a catalyst at the anode and cathode (Pt/Ni). High-temperature AFCs operate at temperatures between 100°C and 250°C. However, more-recent AFC designs operate at lower temperatures of roughly 23°C to 70°C. AFCs are high-performance fuel cells due to the rate at which chemical reactions take place in the cell. They are also very efficient, reaching efficiencies of 60 percent in space applications. The disadvantage of this fuel cell type is that it is easily poisoned by carbon dioxide (CO_2). In fact, even a small amount of CO_2 (~0.01%) in the fuel or oxidizer can affect the cell operation, making it necessary to purify both the hydrogen and oxygen used in the cell. Susceptibility to poisoning also affects the cell lifetime. Moreover, the electrolyte has to circulate through the cell, so the cell needs a KOH circulation circuit. AFC stacks have been shown to maintain sufficiently stable operation for more than 8000 operating hours. Low operating temperatures allow the use of lightweight and inexpensive materials such as graphite and polymers; also, the start-up time is really low, in the order of some minutes.

Proton Exchange Membrane FC (PEM, PEFC, SPFC)

Proton Exchange Membrane fuel cells — also called Polymer Electrolyte Fuel Cells or Solid Polymer Fuel Cells— deliver high power density and offer the advantages of low weight and volume, compared to other fuel cells. They are already used for transportation applications and some stationary applications. Due to their fast startup time, low sensitivity to orientation, and favorable power-to-weight ratio, PEM fuel cells are particularly suitable for use in passenger vehicles, such as cars and buses. This cell is the best candidate chosen to substitute the old AFCs in space applications, and NASA is conducting experiments to develop both PEM based RFCs and URFCs. PEM fuel cells use a solid polymer (Nafion®) - as thin as a paper sheet - as electrolyte and porous carbon electrodes containing a platinum catalyst. In addition to oxygen and hydrogen, they require water to operate because the Nafion® membrane must be taken wet (100% humidity) for a correct cell functioning, and do not require corrosive fluids like some fuel cells. The membrane must be kept humid even when the FC is inactive. The humidification system could be an issue as it must be perfect. Polymer electrolyte membrane fuel cells operate at relatively low temperatures, around 80°C. Low temperature operation allows them to start quickly (only few minutes) and results in less wear on system components, resulting in better durability. The efficiency of these cells is quite lower than the AFC one, between 50 and 60%. As well as in the case of the AFCs,

platinum catalyst is extremely sensitive to CO poisoning. Developers are currently exploring platinum/ruthenium catalysts that are more resistant to CO.
The power output could be raised up to 250 kW with the available technology.

Phosphoric Acid FC (PAFC)

Phosphoric acid fuel cells are commercially available today. Hundreds of fuel cell systems have been installed in several nations; even if it is a mature technology for terrestrial applications, they have never been used in space. PAFCs generate electricity at more than 40% efficiency and nearly 85% if the steam this fuel cell produces is used for cogeneration. Phosphoric acid fuel cells use liquid phosphoric acid as the electrolyte and operate at about 200°C. One of the main advantages to this type of fuel cell, besides the nearly 85% cogeneration efficiency, is that it can use impure hydrogen as fuel. PAFCs can tolerate a CO concentration of about 1.5%, which broadens the choice of fuels they can use. Nevertheless, it uses noble metals as catalyzer. The medium temperature increases start-up times up to few hours.

H_2O_2 based FC

H_2O_2 fuel cells are standard PEM cells, but the typical gaseous pure oxygen that feeds the reaction is substituted by liquid hydrogen peroxide (H_2O_2), thus giving an H_2/H_2O_2 FC. Even the fuel can be replaced by $NaBH_4$ (sodium tetrahydroborate), a powder which can be dissolved in water or in alkaline solution to be used as fuel, thus creating a $NaBH_4/H_2O_2$ FC. This powder is flammable, due to the high concentration of hydrogen, and slightly toxic. With 2 mg of $NaBH_4$ there will be enough fuel to operate a single cell at 100 mA for about 1 hour. It is very important to underline that in both cases, the chemical reactions are invertible, and so it is possible to develop a regenerative fuel cell. In the case of $NaBH_4/H_2O_2$ cells the chemical reactions at the anode, cathode and total are:

$$NaBH_4 + 2H_2O \rightarrow NaBO_2 + 8H^+ + 8e^- \tag{1.1}$$

$$4H_2O_2 + 8H^+ + 8e^- \rightarrow 8H_2O \tag{1.2}$$

$$NaBH_4 + 4H_2O \rightarrow NaBO_2 + 6H_2O \tag{1.3}$$

One of the major advantage consists in the phase of the reactants, that are liquid at room temperature so they do not need cryogenic and/or high pressure tanks; moreover there is not the problem of the "boiling off" resulting from long-time storage periods. Even the efficiency and cell voltage are greater than a usual H_2/O_2 based system. The higher efficiency reached until now is 80%. The following graph compares four types of FCs (AFC, PEM, H_2/H_2O_2 and $NaBH_4/H_2O_2$). It results that the better solution is the last one, giving higher current densities and output voltage (Figure 1.4).

1.2.1.1 High temperature fuel cells

High temperature FCs have the advantage of very high power output – in the class of MWs – and high efficiency when coupled with co-generation which uses the large amount of waste heat to produce electrical energy (80-85% of overall efficiency). Therefore, they can be used for terrestrial stationary applications, but are impractical for a space environment. The chemical

reactions occur spontaneously due to the high temperature, so the electrodes do not require the use of Pt as catalyst, or the catalyst itself, in some cases. On the other hand, the warm-up periods to activate these FCs are long, in the order of some hours.

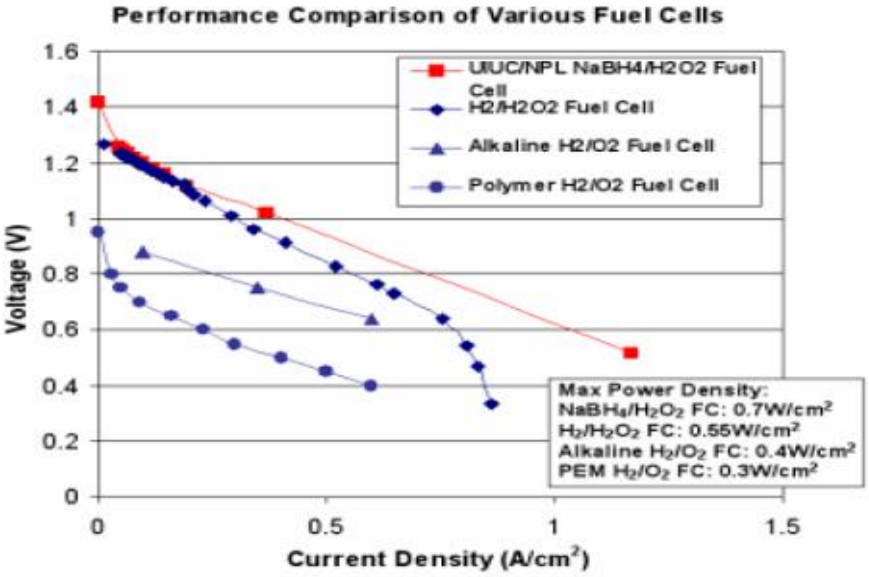

Figure 1.4 H_2O_2 fuel cell performance (Luo et al. 2008)

Solid Oxide FC (SOFC)

Solid oxide fuel cells use a hard, non-porous ceramic compound as the electrolyte (zirconium oxide). SOFCs are expected to be around 50-60 percent efficient at converting fuel to electricity. In applications designed to capture and utilize the system's waste heat (co-generation), overall fuel use efficiencies could top 80-85 percent. Solid oxide fuel cells operate at very high temperatures - around 1000°C. It also allows SOFCs to reform fuels internally, which enables the use of a variety of fuels and reduces the cost associated with adding a reformer to the system. SOFCs are also the most sulfur-resistant fuel cell type. In addition, they are not poisoned by carbon monoxide (CO), which can even be used as fuel. This allows SOFCs to use gases made from coal. High-temperature operation has disadvantages: significant thermal shielding to retain heat and protect persons, which may be acceptable for utility applications but not for transportation and small portable applications. The high operating temperatures also place stringent durability requirements on materials. The development of low-cost materials with high durability at cell operating temperatures is the key technical challenge facing this technology.

Molten Carbonate FC (MCFC)

Molten carbonate fuel cells are currently being developed for natural gas and coal-based power plants for electrical utility, industrial, and military applications. MCFCs use an electrolyte composed of a molten carbonate salt mixture suspended in a porous, chemically inert ceramic lithium aluminum oxide ($LiAlO_2$) matrix. Improved efficiency is another reason MCFCs offer significant cost reductions over phosphoric acid fuel cells (PAFCs). Molten carbonate fuel cells can reach efficiencies approaching 60 percent, considerably higher than the 37-42 percent efficiencies of a phosphoric acid fuel cell plant. When the waste heat is captured and used, overall fuel efficiencies can be as high as 85 percent. Molten carbonate fuel cells are not prone to carbon

monoxide or carbon dioxide poisoning —they can even use carbon oxides as fuel—making them more attractive for fueling with gases made from coal. Because they are more resistant to impurities than other fuel cell types, scientists believe that they could even be capable of internal reforming of coal, assuming they can be made resistant to impurities such as sulfur and particulates that result from converting coal, a dirtier fossil fuel source than many others, into hydrogen. The primary disadvantage of current MCFC technology is durability. The high temperatures at which these cells operate and the corrosive electrolyte used accelerate component breakdown and corrosion, decreasing cell life. Scientists are currently exploring corrosion-resistant materials for components as well as fuel cell designs that increase cell life without decreasing performance.

Protonic Ceramic FC (PCFC)

This new type of fuel cell is based on a ceramic electrolyte material that exhibits high protonic conductivity at elevated temperatures. PCFCs share the thermal and kinetic advantages of high temperature operation at 700 degree Celsius with MCFCs and SOFCs, while exhibiting all of the intrinsic benefits of proton conduction in PEM and PAFC cells. The high operating temperature is necessary to achieve very high electrical fuel efficiency with hydrocarbon fuels. PCFCs can operate at high temperatures and electrochemically oxidize fossil fuels directly to the anode, with carbon dioxide as the primary reaction product.

Table 1.3 Comparison between different fuel cell technologies

Characteristics	**Fuel cell technology**				
	AFC	PEM	PAFC	MCFC	SOFC
Electrolyte	KOH	Polymer	Phosphoric acid	Li/Al carbonate	Solid oxide
Temperature (°C)	90 - 100	50 - 100	150 - 200	600 - 700	650 – 1000
Catalyzer	Pt/Pd, Ni	Pt	Pt	Ni	Not needed
Materials	Polymers, graphite, Inconel	Graphite, metals, asbestos	Graphite	Nickel, stainless steel	Ceramics, metals
Efficiency (%)	60 – 70 (electric)	50 – 60 (electric)	80 – 85 (CHP) 36 – 42 (elec)	85 (CHP) 60 (elec)	85 (CHP) 30– 60 (elec)
Pow. ($mWcm^{-2}$)	300 - 500	300 - 900	150 - 300	150	150 – 270
Power (kW)	5 - 80	<1 - 250	50 - 1000	<1 - 1000	5 - 3000
Start-up time	Minutes	Minutes	1 – 4 hrs	5 – 10 hrs	5 – 10 hrs

Table 1.4 shows the present range of power outputs with the different FC technologies available today:

Table 1.4 Power ranges of different fuel cell technologies

Fuel cell technology	Power (kW)							
	$1x10^{-3}$	$1x10^{-2}$	$1x10^{-1}$	1	10	100	1,000	10,000
AFC	NO	NO	NO	YES	YES	YES	NO	NO
PEM	YES	YES	YES	YES	YES	YES	NO	NO
PAFC	NO	NO	NO	NO	NO	YES	YES	YES
SOFC	NO	YES	YES	YES	YES	YES	YES	YES
MCFC	NO	NO	NO	NO	NO	YES	YES	NO

1.2.1.2 Regenerative fuel cells

The fuel cells presented above convert energy one way: from fuel to electricity. They are not designed for the reverse recharging operation. Recharging the fuel cell requires an electrolyser (EZ) to decompose the water back into hydrogen and oxygen. The electrolyser is generally a separate unit from the fuel stack and the two cannot operate simultaneously. The coupling of a FC stack and an EZ stack is conventionally known as Regenerative Fuel Cell (RFC). The hydrogen-oxygen regenerative fuel cell has been developed for energy storage in short-term space missions, but not used in space yet. The RFC was considered for the ISS but dropped in favor of the NiH_2 battery due to its poor round trip energy efficiency. However, a high-power long-term manned mission to the Moon or Mars may find the RFC practical. It would use an external power source (such as solar arrays or a nuclear plant) and electrolysis units for hydrogen and oxygen production. This is advantageous not only for the energy storage, but also for life support and for auxiliary thrusters as well. The RFC is based on a H_2/O_2 fuel cell and electrolyser technology. The fuel stacks consists of multiple cells, each with certain active area operated at 60 psi, 80°C and nominal 50 A m^{-2} current density. Cells are series-parallel connected and include bypass diodes. The electrolyser stack consists of multiple cells with certain active areas, operated at 315 psi and a nominal current density of 20 A m^{-2}. The hydrogen and oxygen reactants are stored in gaseous form at 3000 psi, while water is stored at 14.7 psi. The fuel cell operating temperature is maintained by a radiator using water as the working fluid. The electrical energy efficiency for the electrolyser is 90% and that of the fuel cell is 60%, thus the overall round trip efficiency of the systems is about 54%. The life is estimated to be 10000 hrs. The RFC has a good peak power capability, about 10 times the base power. This may be useful for providing power pulses. The primary disadvantage of RFC is the peripheral pumps and plumbing that can handle fluids reliably over a long mission life in GEO or Moon/Mars surface. Providing redundancy in such a system may incur significant mass penalty. Other than the reliability issue, the fuel cell is a well-developed technology. Because of the lower efficiency compared to the battery, both the solar array charging power and the thermal cooling requirement would be greater. In high power applications, mass optimized RFC units may provide up to 1000 Wh/kg. The specific energy, however, is sensitive to various thermal and electrical design requirements.

A RFC could provide much higher specific energies -300 to 1000 Wh kg^{-1}, than any advanced battery system, and potentially the highest storage capacity and lowest weight of any non-nuclear device. Due to irreversible heat generation the Round Trip Efficiency (RTE), that is, the fraction of energy put into the system that actually gets back to the user, is limited to about 75% ideal. Round trip efficiency is one of the most important attributes for the user since it dictates, along with the energy density, how much storage installation size will be required in order to accommodate user energy demands and how much power from the primary source will be required to replenish that storage. For many mechanical, and some magnetic and electrochemical storage devices, the round trip efficiencies can be as high as 80%. However, they do not compete with the RFC on energy content per unit weight. Performance estimates made for recent hydrogen oxygen PEM RFCs conceptual designs have predicted round trip efficiencies of roughly 50 to 60% depending on stack polarization performance and current densities applied.

1.2.1.1 Unitized regenerative fuel cells

NASA has for some time recognized the potential for a RFC to store large amounts of energy for space applications where energy production is cyclic, as is the case for solar energy power generation. NASA familiarity with fuel cell primary power led to NASA recognition of the viability of coupling the fuel cell with an electrolyser and a means of storing oxygen and hydrogen

to form a secondary "battery" energy storage system. The Unitized Regenerative Fuel Cell (URFC), also known as reversible PEM fuel cell, or reversible regenerative fuel cells, refines this concept by using the same cell electrodes to perform both the electrolyser function (equivalent to battery charging) and the fuel cell function (equivalent to battery discharging). A Unitized Regenerative Fuel Cell System (URFCS) incorporates the URFC into an overall energy storage system.

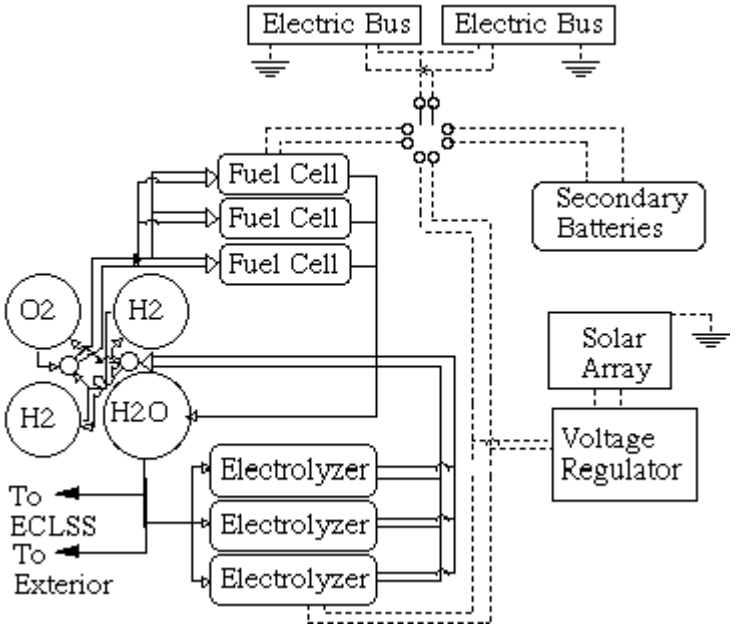

Figure 1.5 Hypothetical electric power system based on RFCs

The system is based on PEM cells, and uses bi-functional electrodes (oxidation and reduction electrodes reverse roles when switching from charge to discharge, as with a rechargeable battery) for cathode feed electrolysis (water is fed from the hydrogen side of the cell) or anode feed electrolysis (water is fed from the oxygen side of the cell). No system performance or efficiency is lost compared to either fuel cells or electrolysers constructed in this reversible geometry. During electrolysis, water vapor is fed to the electrodes from a third and separate water compartment. Water is evaporated from the water compartment within the URFC stack and diffuses to the electrolysis reaction sites. As water vapor is electrolyzed at the electrode surface, a vapor diffusion gradient is created which provides the driving force for continued evaporation from the water compartment. During fuel cell operation, the oxygen and hydrogen reactants are not circulated throughout the URFCS but are fed passively to the cell stack. The product water is removed passively because of a pressure differential between the cell stack gas compartments and the cell stack water compartment. The pressure of the gases is always greater than the pressure of the water, so liquid water is not free inside the gas compartments but is retained inside the water compartment. This cell is an air-cooled cell, but if desired could be made liquid-cooled.

An alternative version to the traditional hydrogen-oxygen cell is the peroxide one. The development of a URFC based on this technology is feasible; a first prototype of such a cell developed an energy density of 65 Wh kg^{-1} (Luo et al. 2008) with encouraging results and possible future enhancement. At present NPL Associates (Nuclear Plasma Laboratory), the University of Illinois at Urbana-Champaign (UIUC) and NASA JPL and GRC are the major centers of development of this technology.

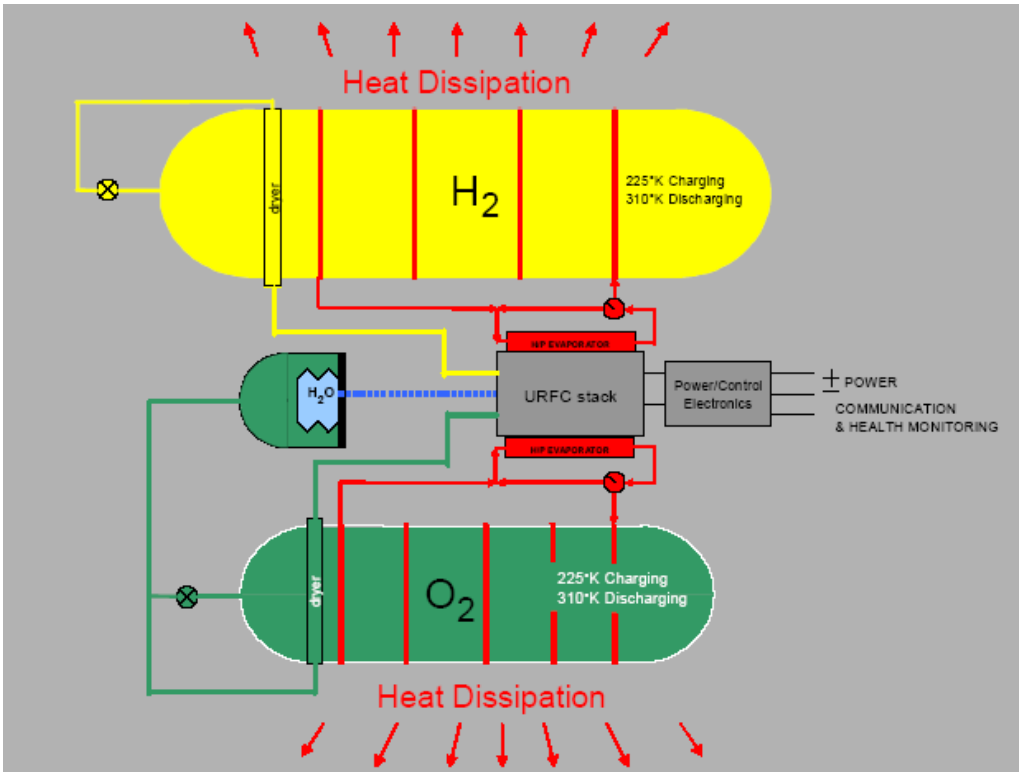

Figure 1.6 URFC system concept

1.3 Fuel cells principles

The experiment shown in Figure 1.1 makes a reasonable demonstration of the basic principle of the fuel cell, but the currents produced are very small. The main reasons for the small current are the low contact area between the gas, the electrode, and the electrolyte – basically just a small ring where the electrode emerges from the electrolyte and the large distance between the electrodes – and the electrolyte resisting the flow of electric current. To overcome these problems, the electrodes are usually made flat, with a thin layer of electrolyte, as in Figure 1.7. The structure of the electrode is porous so that both the electrolyte from one side and the gas from the other can penetrate it. This is to give the maximum possible contact between the electrode, the electrolyte, and the gas. However, to understand how the reaction between hydrogen and oxygen produces an electric current, and where the electrons come from, it is mandatory to consider the separate reactions taking place at each electrode. These important details vary for different types of fuel cells, but starting with a cell based around an acid electrolyte (as in a PEM fuel cell), as used by Grove, it is a good way to start with the simplest and still the most common type. At the anode of an acid electrolyte fuel cell, the hydrogen gas ionizes, releasing electrons and creating H^+ ions (or protons):

$$2H_2 \rightarrow 4H^+ + 4e^-$$

This reaction releases energy. At the cathode, oxygen reacts with electrons taken from the electrode, and H^+ ions from the electrolyte, to form water:

$$O_2 + 4e^- + 4H^+ \rightarrow 2H_2O$$

Clearly, for both these reactions to proceed continuously, electrons produced at the anode must pass through an electrical circuit to the cathode. Also, H^+ ions must pass through the electrolyte. An acid is a fluid with free H^+ ions, and so serves this purpose very well. Certain polymers can also be made

to contain mobile H^+ ions. These materials are called *proton exchange membranes*, being an H^+ ion a proton.

It should be noted that the electrolyte must only allow H^+ ions to pass through it, and not electrons. Otherwise, the electrons would go through the electrolyte, and not round the external circuit, losing all of the electric current produced.

The voltage of a fuel cell is quite small, about 0.7 V when drawing a useful current. This means that to produce a useful voltage many cells have to be connected in series. Such a collection of fuel cells in series is known as a "stack". The most obvious way to do this is by simply connecting the edge of each anode to the cathode of the next cell, as in Figure 1.7.

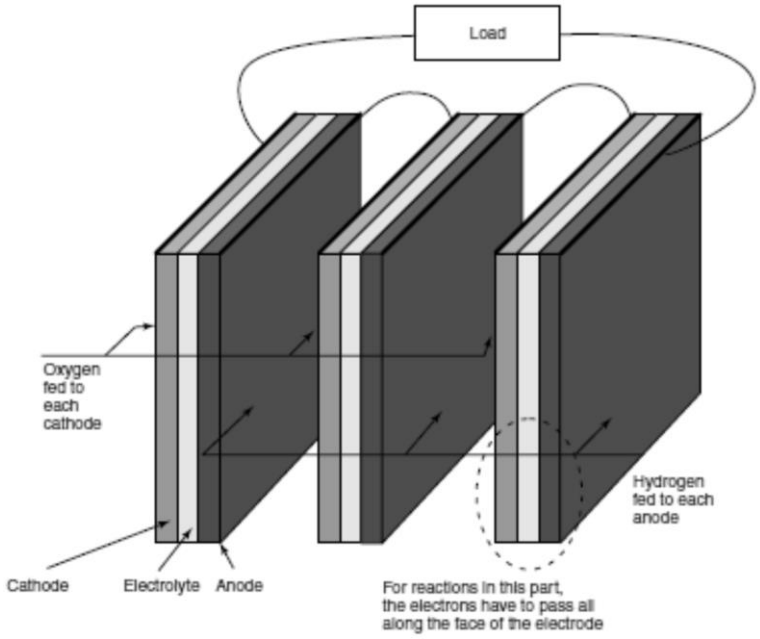

Figure 1.7 Edge connection of cells in series

The problem with this method is that the electrons have to flow across the face of the electrode to the current collection point at the edge. The electrodes might be quite good conductors, but if each cell is only operating at about 0.7 V, even a small voltage drop is important. Unless the current flows are very low, and the electrode is a particularly good conductor, or very small, this method is not used. A much better method of cell interconnection is to use a "bipolar plate". This makes connections all over the surface of one cathode and the anode of the next cell (hence bipolar); at the same time, the bipolar plate serves as a means of feeding oxygen to the cathode and fuel gas to the anode. Although a good electrical connection must be made between the two electrodes, the two gas supplies must be strictly separated.

The method of connecting to a single cell, all over the electrode surfaces, while at the same time feeding hydrogen to the anode and oxygen to the cathode, is shown in Figure 1.8. The plates are made of a good conductor such as graphite, or stainless steel and have channels cut in them so that the gases can flow over the face of the electrodes. At the same time, they are made in such a way that they make a good electrical contact with the surface of each alternate electrode.

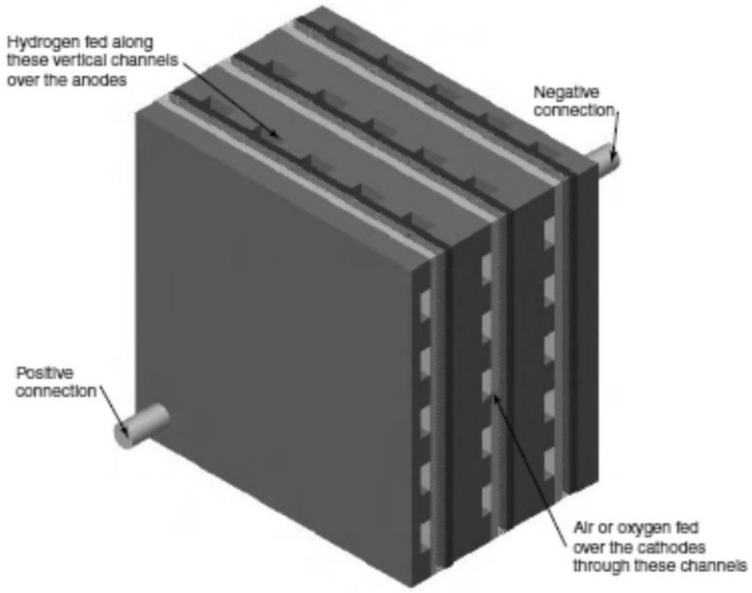

Figure 1.8 Fuel cell stack layout visualizing bipolar plates interposition

Paying a little more attention to PEM fuel cells, their most important feature consists in having a solid electrolyte (polymer). Typical cell components within a PEFC stack include (Figure 1.9):

- The ion exchange membrane.
- An electrically conductive porous backing layer (usually called GDL - Gas Diffusion Layer).
- An electro-catalyst (the electrodes) at the interface between the backing layer and the membrane (called with the acronym of CL - Catalyst Layer).
- Cell interconnects and flow plates that deliver the fuel and oxidant to reactive sites via flow channels and electrically connect the cells.

PEFC stacks are almost universally of the planar bipolar type. Typically, the electrodes are cast as thin films that are either transferred to the membrane or applied directly to the membrane.

Alternatively, the catalyst-electrode layer may be deposited onto the backing layer, then bonded to the membrane.

Different companies produce several optimized polymer electrolytes; however, a common theme is the use of sulphonated fluoropolymers, usually fluoroethylene. The most well known and well established of these is Nafion®, which has been developed through several variants since the 1960s.

The starting point is the basic polyethylene. Its molecular structure is modified by substituting fluorine for the hydrogen. This process is applied to many other compounds and is called *perfluorination*. The modified polymer, shown in Figure 1.10, is polytetrafluoroethylene, or PTFE. It is also sold as Teflon. This remarkable material has been very important in the development of fuel cells. The strong bonds between the fluorine and the carbon make it durable and resistant to chemical attack. Another important property is that it is strongly hydrophobic, and so it is used in fuel cell electrodes to drive the product water out of the electrode, preventing flooding. However, to make an electrolyte, a further stage is needed. The basic PTFE polymer is "sulphonated" – a side chain is added, ending with sulphonic acid HSO_3. One possible side chain structure is shown in Figure 1.10. The HSO_3 group added is ionically bonded, and so the end of the side chain is actually

an SO_3^- ion. For this reason, the resulting structure is called an *ionomer*. The result of the presence of these SO_3^- and H^+ ions is that there is a strong mutual attraction between the + and − ions from each molecule. A key property of sulphonic acid is that it is highly hydrophyllic – it attracts water.

In Nafion, this means creating hydrophyllic regions within a generally hydrophobic substance, which is bound to create interesting results. The hydrophyllic regions around the clusters of sulphonated side chains can lead to the absorption of large quantities of water, increasing the dry weight of the material by up to 50%. Within these hydrated regions, the H^+ ions are relatively weakly attracted to the SO_3^- group and are able to move. This creates what is essentially a dilute acid. The resulting material has different phases – dilute acid regions within a tough and strong hydrophobic structure. Although the hydrated regions are somewhat separate, it is still possible for the H^+ ions to move through the supporting long molecule structure. In a well hydrated electrolyte, there will be about 20 water molecules for each SO_3^- side chain. This will typically give a conductivity of about 0.1 S cm^{-1}. As the water content falls, the conductivity falls in a more or less linear trend.

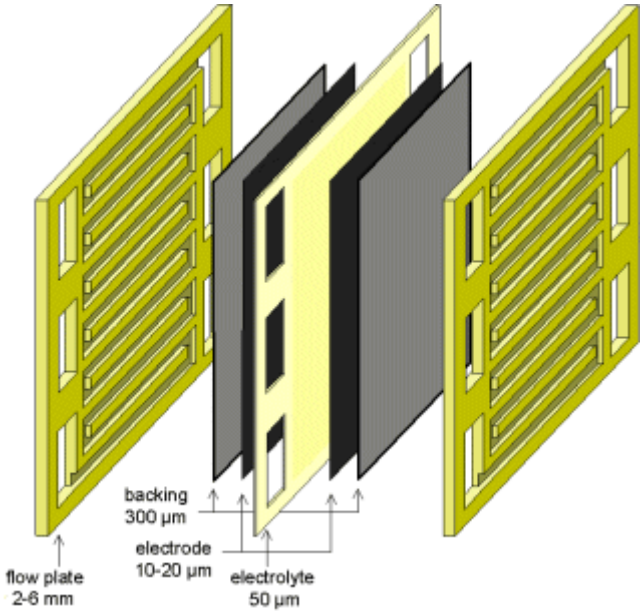

Figure 1.9 A practical single PEM cell construction with width dimensions

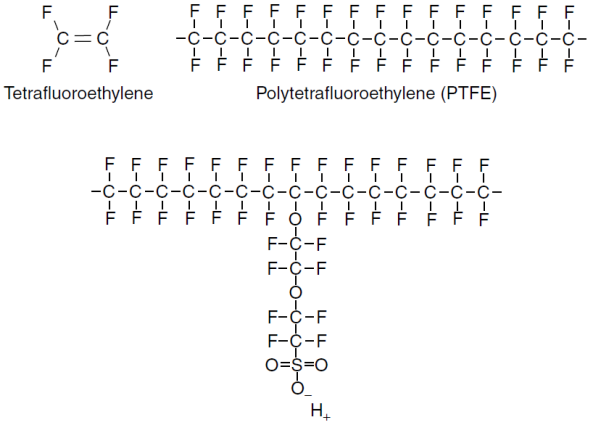

Figure 1.10 Example chemical structure of tetrafluoroethylene (upper left side), PTFE (upper right side) and sulphonated fluoroethylene (lower central side)

1.3.1 PEM fuel cells electrochemical basics

In fuel cells, electrolysers and in any electrochemical cell, several energy losses in form of voltage losses occur, due to several electrical and electrochemical phenomena. The four main losses are: activation losses, exchange current losses, ohmic losses and concentration losses. The following discussion applies for both alkaline and PEM devices. Figure 1.11 shows a typical low temperature hydrogen-oxygen fuel cell polarization curve (in black color). Four main detrimental effects on the cell voltage are described, and will be explained later in the text.

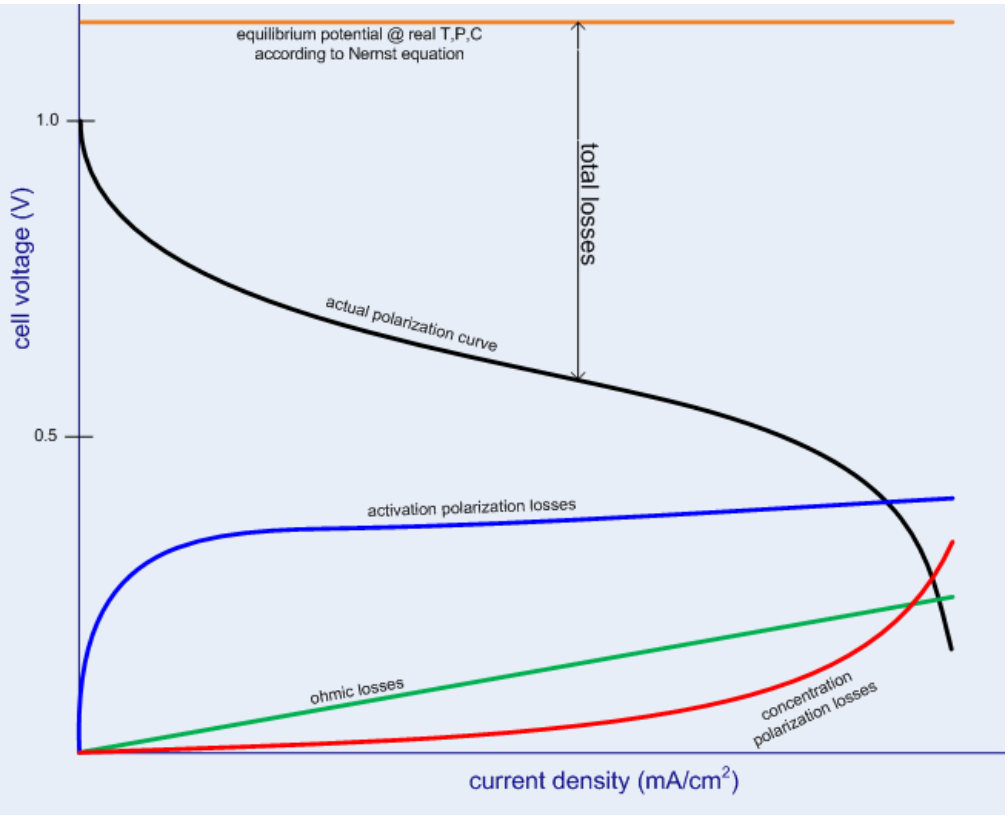

Figure 1.11 Low temperature fuel cell polarization curve (Larminie and Dicks 2003)

1.3.1.1 Activation losses

As a result of experiments, rather than theoretical considerations, Tafel observed and reported in 1905 that the overvoltage at the surface of an electrode followed a similar pattern in a great variety of electrochemical reactions (Bagotsky 2006). Such pattern is the same reported in Figure 1.12. It shows that if a graph of the overvoltage (i.e. voltage loss, *V*) against the logarithm of current density (A m^{-2}) is plotted, for most values of overvoltage the graph approximates to a straight line. Such plots of overvoltage against the logarithm of current density are known as *Tafel plots*. The diagram shows two typical plots.

For most values of overvoltage range, its value is given by the Eq.(1.4).

$$\Delta V_{act} = A_{exc} \ln\left(\frac{i}{i_0}\right) \tag{1.4}$$

Eq.(1.4) is known as the Tafel equation. *i* (expressed in A m^{-2}) is the current density represented at the x-axis of Figure 1.12. The constant A_{exc} (V) increases with decreasing speed of reaction. The

constant i_0 (A m^{-2}) is the well-known *exchange current density* and it is higher if the reaction is faster. The exchange current density can be considered as the current density at which the overvoltage begins to move from zero. It is important to remember that the Tafel equation only holds true when $i > i_0$.

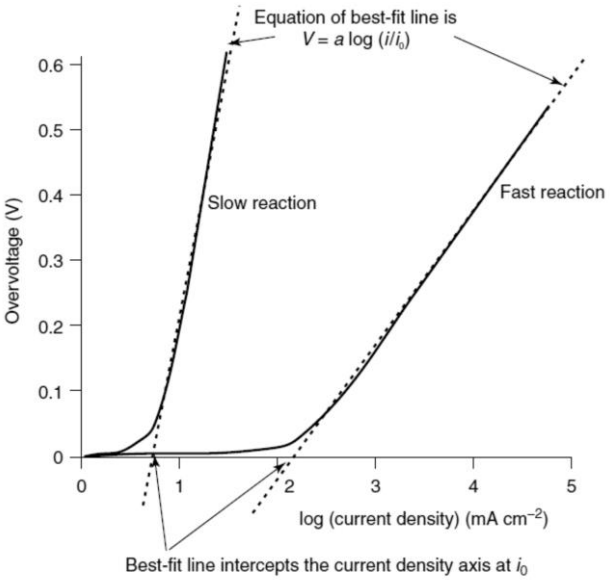

Figure 1.12 Tafel plots for a slow and a fast reaction

Although the Tafel equation was originally deduced from experimental results, it also has a theoretical basis. It can be shown that for a hydrogen cell with two electrons transferred per hydrogen molecule, the constant A in the last equation above is given by:

$$A_{exc} = \frac{RT}{n_e \alpha_{ctc} F} \tag{1.5}$$

The constant α_{ctc} is the so-called charge transfer coefficient (dimensionless) and is the proportion of the electrical energy applied that is harnessed in changing the rate of an electrochemical reaction. Its value depends on the reaction involved and the material the electrode is made from, but it must be in the range of 0 to 1. For the hydrogen electrode, its value is about 0.5 for a great variety of electrode materials and used in all of the CFD models in Table 1.5. At the oxygen electrode, the charge transfer coefficient shows more variation, but it is between about 0.1 and 0.5 in most circumstances. The term n_e is the number of electrons transferred during the reaction, and it is equal to 2 for the hydrogen side and by-product water, and 4 for the oxygen side.

The appearance of temperature in the equation might give the impression that raising the temperature increases the overvoltage. However, temperature affects also the exchange current density, rising it with temperature rising in a way that overcomes completely the rising of A. Indeed, the key to making the activation overvoltage as low as possible is this i_0, which can vary by several orders of magnitude. Furthermore, it is affected by several parameters other than the material used for the electrode.

The exchange current density can be thought as follows. The reaction at the oxygen electrode of a proton exchange membrane fuel cell is:

$$O_2 + 4e^- + 4H^+ \rightarrow 2H_2O \tag{1.6}$$

Table 1.5 Reference CFD fuel cell models available in literature

Model author	Computational domain	Electrochemical model	N° Phases, thermal model	Diffusivity, permeability and porosity model
Meng (2007)	2D	3D	2, non-isotherm	Distributed
Dawes et al. (2009)	3D	1D	Pseudo-2, isotherm	Lumped
Sivertsen et al. (2004)	3D	3D	1, non-isotherm	Distributed
Dutta et al. (1999; 2000)	3D	1D	1, isotherm	Distributed (diffusivity)
Su et al. (2010)	3D	3D	2, non-isotherm	Distributed (diffusivity)
Nitta et al. (2007)	3D	3D	1, non-isotherm	Distributed (diffusivity)
Lum et al. (2005)	3D	1D	1, isotherm	Distributed (diffusivity)
Yuan et al. (2010)	3D	3D	2, non-isotherm	Distributed (diffusivity)

At zero current density, i.e. when any electrons moving is revealed in the electric circuit, it is possible to suppose that there was no activity at the electrode and that this reaction does not take place. In fact this is not so. The reaction is taking place all the time, but the reverse reaction is also taking place at the same rate. There is an equilibrium, expressed as:

$$O_2 + 4e^- + 4H^+ \leftrightarrow 2H_2O \tag{1.7}$$

Therefore, there is a continual backwards and forwards flow of electrons from and to the electrolyte, never exiting the cell. This current density is i_0, the "exchange" current density. It is reasonable to think that if this current density is high, then the surface of the electrode is more "active" or "ready" and a current in one particular direction is more likely to flow. The current flowing through the electric circuit is a simple shifting in one particular direction of a reaction already going on, rather than starting from zero.

The exchange current density is crucial in controlling the performance of a fuel cell electrode. It is vital to make its value as high as possible.

The rearrangement from the logarithmic to the exponential form gives:

$$i = i_0 \, exp\left(\frac{2\alpha F \Delta V}{RT}\right) \tag{1.8}$$

This equation is similar to the *Butler–Volmer* equation and is quite often used as an equivalent alternative to the Tafel equation.
Considering the superposition principle, it is possible to imagine a fuel cell affected only by the activation losses; considering the activation voltage loss only for a single electrode, its real voltage will be:

$$\mathrm{V} = V_{id} - A_{exc} \, ln\left(\frac{i}{i_0}\right) \tag{1.9}$$

Figure 1.13 shows several plots of Eq.(1.9) using the values of 0.01, 1.0, and 100 mA cm^{-2} for the exchange current density, and a typical value for A_{exc} of 0.06 V (taken from Larminie and Dicks 2002). The importance of i_0 can be clearly seen. The effect, for most values of current density, is to reduce the cell voltage by a fixed amount, as we could predict from the Tafel equation. The smaller the i_0, the greater is this voltage drop. It is also important to note that when i_0 is 100 mA cm^{-2}, there

is no voltage drop until the current density i is greater than 100 mA cm^{-2}, since the Tafel approximation looses validity, as explained before. This brought to the use of a different formulation for the activation losses in the models (Par. 3.3.1.3).

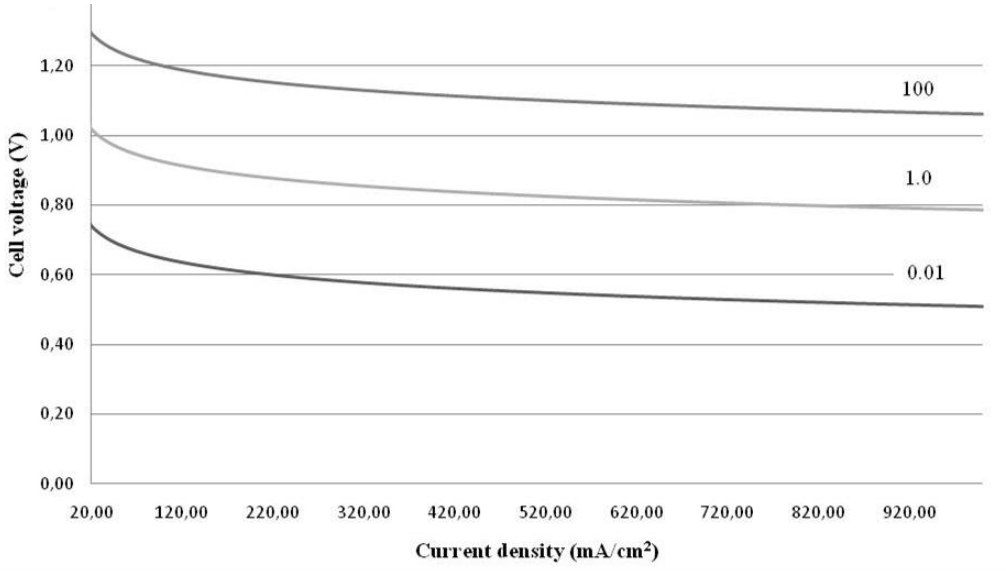

Figure 1.13 Effects of the activation losses on the polarization curve

It is possible to measure this overvoltage at each electrode, either using reference electrodes within a complete cell or using half-cells. Table 1.6 gives the values of i_0 for the hydrogen electrode at 25°C, and for various metals used. The measurements are for flat smooth electrodes. The most striking thing about these figures is their great variation, indicating a strong catalytic effect for some of them. The measured exchange current densities for the oxygen electrode vary greatly but are generally higher by a factor of about 10^5, that is, they are much greater than those expressed in Table 1.6. This would give a figure that is about 10^{-8} A cm^{-2}, even using Pt catalyst, far worse than even the lowest curve on Figure 1.13. The values of i_0 for a real electrode are much higher than the ones in table, because of the roughness of the electrode. This makes the real surface area many times bigger, typically at least 10^3 times larger than the nominal length × width.

The i_0 value at the oxygen electrode (the cathode) is much smaller than that at the hydrogen anode, sometimes 10^5 times smaller. Indeed, it is generally reckoned that the overvoltage at the anode is negligible compared to that of the cathode, at least in the case of hydrogen cells. For a low temperature, hydrogen-fed fuel cell running on air at ambient pressure, a typical value for i_0 would be about 0.1 mA cm^{-2} at the cathode and about 200 mA cm^{-2} at the anode.

1.3.1.1 Crossover currents

An important aspect to be underlined is the fact is that it is possible to recognize that the ideal fuel cell voltage of about 1.23 V at standard conditions, stated theoretically, is never reached at zero current density, as can be seen in Figure 1.11. Although the electrolyte of a fuel cell must be chosen for its proton selective conducting properties, it will always be able to support very small amounts of electron conduction (known as internal currents). However, probably more important in a practical fuel cell is that some hydrogen will diffuse from the anode through the electrolyte to the cathode. Here, because of the catalyst, it will react directly with the oxygen, producing no current

from the cell. This small amount of wasted fuel migrating through the electrolyte is known as *fuel crossover*.

Table 1.6 i_0 for the hydrogen electrode for various metals for acid electrolyte (Larminie and Dicks 2003)

Metal	i_0 (A cm^{-2})
Pb	2.5×10^{-13}
Zn	3×10^{-11}
Ag	4×10^{-7}
Ni	6×10^{-6}
Pt	5×10^{-4}
Pd	4×10^{-3}

These effects – fuel crossover and internal currents – are essentially equivalent. The crossing over of one hydrogen molecule from anode to cathode wastes two electrons, the same as two electrons crossing from anode to cathode internally. Furthermore, if the major loss in the cell is the transfer of electrons at the cathode interface, which is the case in hydrogen fuel cells, then the effect of both these phenomena on the cell voltage is the same. Although internal currents and fuel crossover are essentially equivalent, and the fuel crossover is probably more important, the effect of these two phenomena on the cell voltage is easier to understand if we just consider the internal current. Fuel crossover is the equivalent to an internal current. A quantitative and qualitative explanation of this mechanism is given in Larminie and Dicks (2003): the flow of fuel and electrons will be small, typically the equivalent of only a few mA cm^{-2}. In terms of energy loss this irreversibility is not very important. However, in low-temperature cells it does cause a very noticeable voltage drop at open circuit. Users of fuel cells can readily accept that the working voltage of a cell will be less than the theoretical "no loss" reversible voltage. However, at open circuit, when no work is being done, it should be the same. With low-temperature cells, such as PEM cells, if operating on air at ambient pressure, the voltage will usually be at least 0.2 V less than the 1.2 V reversible voltage that might be expected. Supposing to have a fuel cell that only has losses caused by the activation ones on the cathode, then the voltage will be as in Eq.(1.9). Using reference values of E = 1.2 V, A_{exc} = 0.06 V and i_0 = 0.4 A m^{-2} it is possible to obtain the following table at low current density using Eq.(1.9):

Table 1.7 Cell voltages at low current density

Current density (mA cm^{-2})	Voltage (V)
0	1.2
0.25	1.05
0.5	1.01
1.0	0.97
2.0	0.92
3.0	0.90
4.0	0.88
5.0	0.87
6.0	0.86
7.0	0.85
8.0	0.84
9.0	0.83

Because of the internal current density, the cell current density is *not* zero, even if the cell is at open circuit. Therefore, for example, if the internal current density is 1 mA cm^{-2}, then the open circuit would be 0.97 V, more than 0.2 V less than the theoretical open circuit voltage. This large deviation from the reversible voltage is caused by the very steep initial fall in voltage, recognizable in the polarization curve. The steepness of the curve also explains another observation about low-temperature fuel cells, which is that the open circuit voltage is highly variable. Table 1.7 indicates that a small change in fuel crossover and/or internal current caused, for example, by a change in humidity of the electrolyte, can cause a large change in the open circuit voltage. The equivalence of the fuel crossover and the internal currents on the open circuits is an approximation, but is quite a fair one in the case of hydrogen fuel cells where the cathode activation overvoltage dominates.
The fuel crossover and internal currents are obviously not easy to measure. One way of measuring it is to measure the consumption of reactant gases at open circuit. For single cells and small stacks, the very low gas usage rates cannot be measured using normal gas flow meters, and it will normally have to be done using bubble counting, gas syringes, or similar techniques. For example, a small PEM cell of area equal to 10 cm^2 might have an open circuit hydrogen consumption of 0.0034 cm^3 s^{-1}, equivalent to 1.40 x 10^{-7} mol s^{-1}, indicating a current density of 2.7 mA cm^{-2} (27 A m^{-2}). Other works with experimental setup procedures tried to measure both the internal currents and the fuel crossover directly, trying to obtain a measurement of the gas diffusivities inside the membrane and correlating these data with the corresponding internal current, as in Vilekar and Datta (2010). The crossover current can be modelled with the following equation, integrating this loss with the activation one, where i_n indicates the crossover current:

$$\Delta V_{act} = A_{exc} \ln\left(\frac{i + i_n}{i_0}\right) \tag{1.10}$$

Plotting the above equation with E = 1.23 V (Figure 1.14), it is possible to recognize how the crossover currents, instead of penalizing the whole cell performance, affects only the activation voltage loss zone, keeping unaffected the remaining of the performance, starting from about 0.06 A cm^{-2}, very far from the usual range of the fuel cell usage. In Figure 1.14 three curves are plotted. One without considering the crossover currents, and the other two with two values of i_n, equal to 20 and 40 mA cm^{-2}.
Combining the activation losses of the anode and cathode electrode, with the Tafel law it would result the following equation:

$$\Delta V_{act} = \Delta V_{anode} + \Delta V_{cathode} = A_{exc_a}\, ln\left(\frac{i + i_n}{i_{0a}}\right) + A_{exc_c}\, ln\left(\frac{i + i_n}{i_{0c}}\right) \tag{1.11}$$

Since the crossover currents must be the same on the two sides of the cell, the i_n value is the same at the two sides.

1.3.1.1 Ohmic losses

The losses due to the electrical resistance of the electrodes, and the resistance to the flow of ions in the electrolyte, are the simplest to understand and to model. The size of the voltage drop is simply proportional to the current, that is:

$$\Delta V_{ohm} = RI \tag{1.12}$$

In most cells the resistance is mainly caused by the electrolyte (membrane in case of PEM or similar cells), since the cell plates and gas diffusion layers and current collectors are highly conductive media.

To be consistent with the other equations for voltage loss, the equation should be expressed in terms of current density. Using the electric conductivity σ ($\Omega^{-1}m^{-1}$ or S m^{-1}) and the current density expressed in A m^{-2}, the corresponding voltage loss can be formulated as:

$$\Delta V_{ohm} = \frac{t_m}{\sigma} i \tag{1.13}$$

where i is, as usual, the current density (A m^{-2}) and t_m is the membrane (or electrolyte) thickness (measured in m).

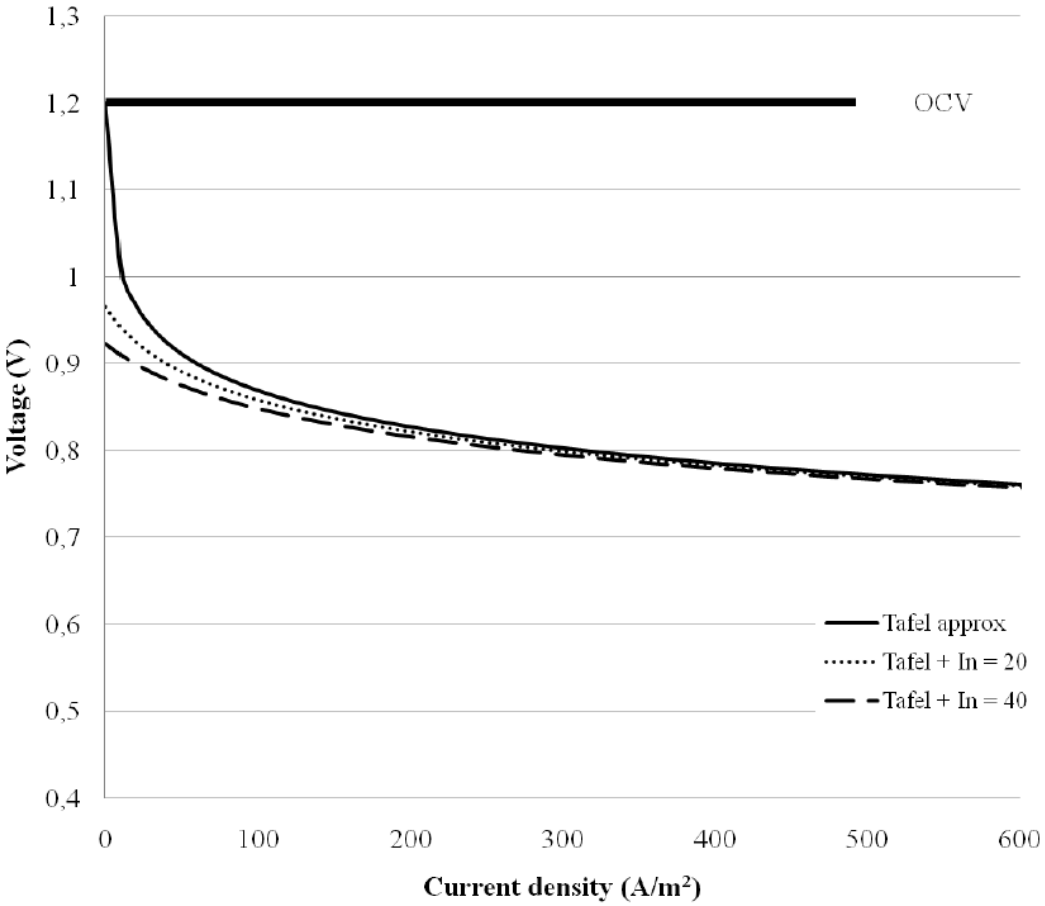

Figure 1.14 Effect of crossover current on the polarization curve

Using the same approach shown before, it is possible to distinguish this particular irreversibility from the others. This voltage loss is important in all types of cells, and its direct influence on the polarization curve is to "bend" the horizontal portion of the lines shown in Figure 1.13. A mitigation can be achieved with the use of electrodes with the highest possible conductivity and making the electrolyte as thin as possible. However, this last option is often difficult, as the electrolyte sometimes needs to be fairly thick as it is the support onto which the electrodes are built, or it needs to be wide enough to be structurally resistant. In any case, it must certainly be thick enough to prevent any shorting of one electrode to another through the electrolyte, which requires a certain level of physical robustness.

Figure 1.15 plots the voltage losses contributing to a decrease in the open-circuit voltage. As can be seen, cathode activation losses (cathode loss, fed with air or pure oxygen) are the main form of

voltage drop, followed by ohmic losses (indicated as Electrolyte IR Loss); the anode activation loss (Anode Loss) is quite negligible.

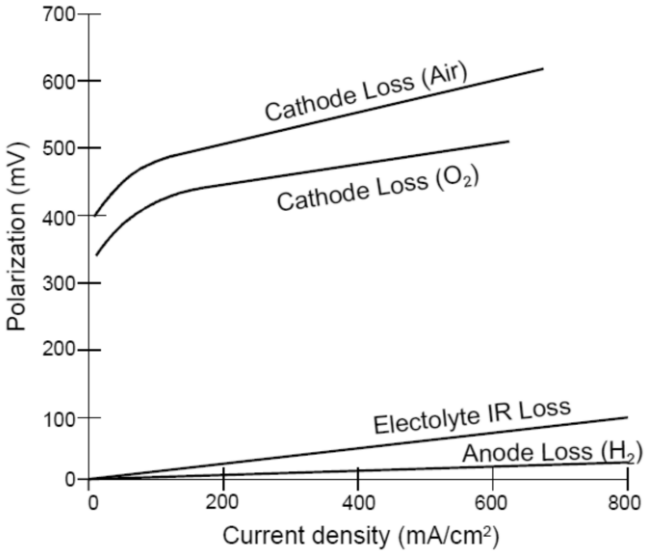

Figure 1.15 – Contribution to polarization voltage losses of anode and cathode (EG&G 2004)

1.3.1.2 Concentration losses

As a reactant is consumed at the electrode by electrochemical reactions, it is often diluted by the products, since finite mass transport rates limit the supply of fresh reactant and the evacuation of products. Consequently, a concentration gradient is formed between the reactive surface and the fluid flow inside the channel, driving the mass transport process. In a cell with purely gas phase reactants and products, gas diffusion processes control mass transfer. In other cells, multi-phase flow in the porous electrodes can have a significant impact. In fuel cells, the evacuation of product is often more limiting than the supply of fuel, given the difference between the diffusivities of hydrogen and water (vapor). For electrolysers using submerged electrodes, concentration losses are not a particular issue, since it would be sufficient to remove the produced gases from the electrode surface to allow water to reach the reaction sites.

1.4 Electrolyser technologies

1.4.1 Alkaline electrolysers

The electrolyte used in conventional alkaline water electrolysers has traditionally been aqueous potassium hydroxide (KOH), mostly with solutions of 20-30 wt% because of the optimal conductivity and remarkable corrosion resistance of stainless steel in this concentration range (Ulleberg 2003). The typical operating temperatures and pressures of these electrolysers are 70-100°C and 1-30 bar, respectively.

Physically an electrolyser stack consists of several cells linked in series. Two distinct cell designs are used: monopolar and bipolar. In the monopolar design the electrodes are either negative or positive with parallel electrical connection of the individual cells (Figure 1.16, left), while in the bipolar design the individual cells are linked in series electrically and geometrically (Figure 1.16, right). One advantage of the bipolar electrolyser stack is that it is more compact than monopolar

systems. The advantage of the compactness of the bipolar cell design is that it gives shorter current paths in the electrical wires and electrodes. This reduces the losses due to internal ohmic resistance of the electrolyte, and therefore increases the electrolyser efficiency. However, there are also some disadvantages with bipolar cells.

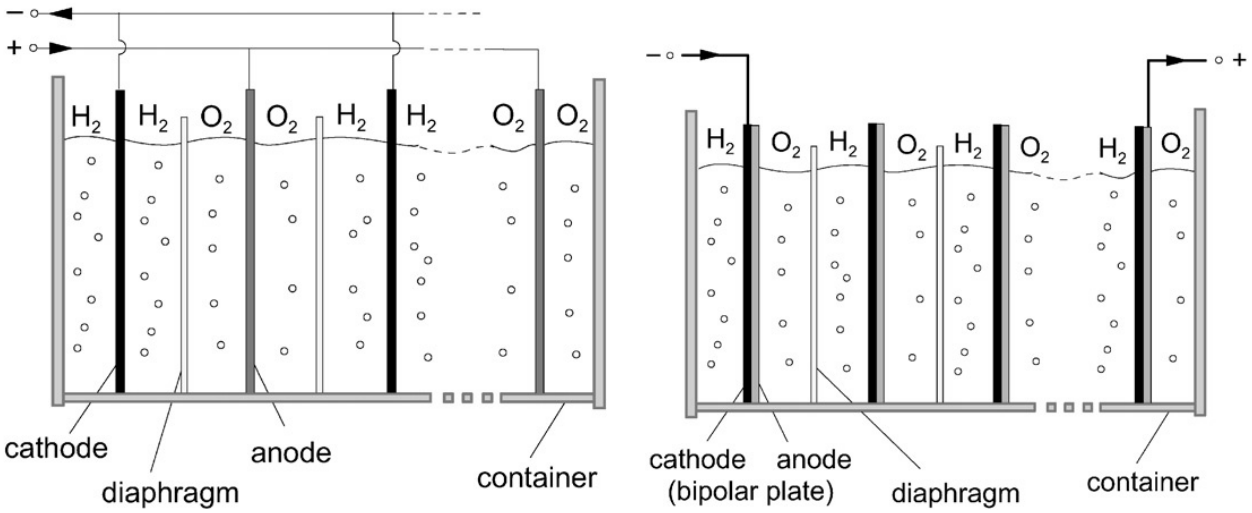

Figure 1.16 Monopolar (left) and bipolar (right) electrolyser stack configuration for alkaline water electrolysis

One example are the parasitic currents that can cause corrosion problems. Furthermore, the compactness and high pressures of the bipolar electrolysers require relatively sophisticated and complex system designs, and consequently increases the manufacturing costs. The relatively simple monopolar systems are in comparison less costly to manufacture. Nevertheless, most commercial alkaline electrolysers manufactured today are bipolar.

In new advanced alkaline electrolysers, the operational cell voltage reduced and the current density increased if compared to the more conventional electrolysers. Reducing the cell voltage reduces the unit cost of electrical power and thereby the operation costs, while increasing the current density reduces the investment costs (Ulleberg 2003). However, there is a conflict of interest here because the ohmic resistance in the electrolyte increases with increasing current due to increasing gas bubbling. Increased current densities also lead to increased overpotentials (losses) at the anodes and cathodes. Three basic improvements can be implemented in the design of advanced alkaline electrolysers:

- New cell configurations to reduce the surface-specific cell resistance despite increased current densities (e.g., zero-gap cells and low-resistance diaphragms).
- Higher process temperatures (up to 160°C) to reduce the electric cell resistance in order to increase the electric conductivity of the electrolyte.
- New catalysts to reduce anodic and cathodic overpotentials (e.g., mixed-metal coating containing cobalt oxide at anode and Raney-nickel coatings at cathode).

1.4.2 PEM electrolysers

The development of PEM electrolysers is coupled to the invention of proton exchange membrane (PEM) fuel cells. In the mid-1950s researchers at the General Electric Corporation (GE) developed fuel cells using a sulfonated polystyrene. In 1973 GE developed SPE water electrolysers

using proton exchange membrane technology that were initially used for oxygen generation in nuclear submarines (Grimes et al. 2008). SPE (or PEM) water electrolysers have now become an industrially viable, well-accepted technology. These electrolysers are compact and ecologically clean; in comparison to alkaline electrolysers, SPE electrolysers are able to operate at lower cell voltages, higher current densities, as well as higher pressures and temperatures (Grimes et al. 2008). An additional major advantage of PEM technology is that it can generate very high purity (>99.999%) hydrogen. PEM electrolysers (Figure 1.17), have a device configuration similar to that of zero-gap bipolar alkaline electrolysers, but a proton conducting perfluorinated polymer membrane like Nafion (also known as perfluorosulfonic acid) having side chains terminated in sulphonate ion exchange groups, serves simultaneously as electrolyte and the separator. Highly pure water circulated through the cell is split into hydrogen and oxygen with the help of electrocatalysts on the membrane surface. The membrane is normally a 150 – 300 μm thick sheet that is impermeable to water and product gases. It possesses poor electronic conductivity but high proton conductivity when saturated with water. The sulfonic acid groups (-SO3H) incorporated in the membrane become hydrated when exposed to water and then dissociate facilitating proton conduction as in the case of PEM fuel cells. The structure of a PEM cell is shown in Figure 1.17. The basic unit of a PEM electrolyser is an electrode-membrane-electrode structure that consists of the polymer membrane coated on either side with layers (typically several microns thick) of suitable catalyst materials acting as electrodes, with an electrolyser module consisting of several such cells connected in series. The polymer membrane is highly acidic and hence acid resistant materials must be used in the structure fabrication. Noble metals like Pt, Ir, Rh, Ru or their oxides or alloys are generally used as electrode materials. Generally Pt and other noble metal alloys are used as cathodes, and Ir, IrO2, Rh, Pt, Rh-Pt, Pt-Ru etc. are used as anodes. The single cell configuration is identical to the fuel cell one. Graphite is generally used for making the bipolar plates. In comparison to alkaline electrolysers, PEM electrolysers could be more efficient, reliable, and safer. Since PEM electrolysers use solid electrolyte, there is no risk of corrosive chemical leaks nor issues of unwanted gas crossover. As the cells in PEM electrolysers are connected in series high voltage dc supplies can be used which are less expensive compared to the low voltage high current dc supplies. Currently these cells generally operate at temperatures of 80-150°C and pressures below 30 bar, anyway high pressure (≈ 135 bar) PEM electrolysers being developed. Cell voltages range from 1.4 V to 2.0 V, with current densities up to about 2.0 A cm^{-2}. These cells can intrinsically adjust to variations in electrical power hence are well suited for operation using power from inherently intermittent solar cells or wind mills. However, PEM electrolysers are comparatively expensive due to the high cost of the polymer membranes and noble metal electrodes, as well as requiring very high purity water. Other design nuances are that precise control of the differential pressure across the anodic and cathodic compartments is necessary for membrane stability. In thin membranes, hydrogen diffusion to the anode can adversely affect device efficiency.

1.5 Electrolysis cells principles

In this paragraph, the basic thermodynamics considerations and principles of the electrolysis process are discussed. The equations given here partially coincides with the same equations used for a fuel cell operation.

1.5.1 Electrolysers electrochemical basics

The oxidation-reduction reaction for a generic electrolyser differentiate if an alkaline or acid electrolyte is considered. For an alkaline electrolyte (this is the case of alkaline electrolysers), the half-cell reactions are:

$$4H_2O + 4e^- \rightarrow 2H_2 + 4OH^- \quad \text{(cathode)} \quad (1.14)$$

$$4OH^- \rightarrow O_2 + 2H_2O + 4e^- \quad \text{(anode)} \quad (1.15)$$

In the case of acid electrolyte (as in the case of a Nafion® based or a H_2SO_4 electrolyser) the half-cell reactions are quite different:

$$4H^+ + 4e^- \rightarrow 2H_2 \quad \text{(cathode)} \quad (1.16)$$

$$2H_2O \rightarrow O_2 + 4H^+ + 4e^- \quad \text{(anode)} \quad (1.17)$$

The complete cell reaction, in both cases is the same of the fuel cell operation and it is:

$$2H_2O \rightarrow 2H_2 + O_2 \quad (1.18)$$

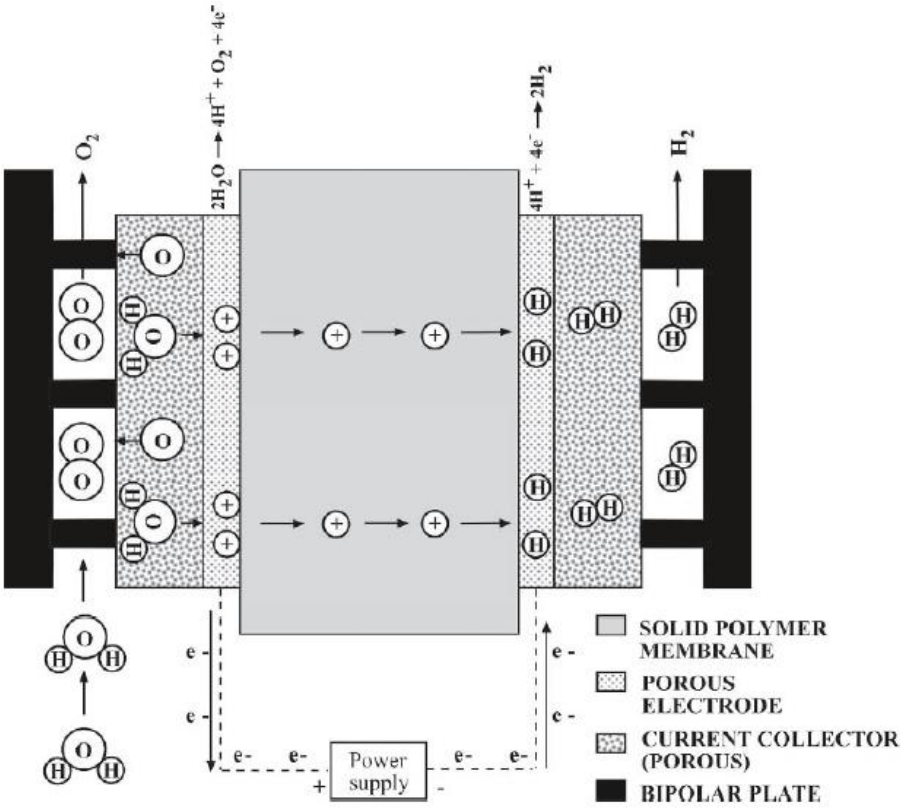

Figure 1.17 A solid polymer electrolyser cell configuration

The energy associated with the reaction in Eq.(1.18), given by the variation of the Gibbs energy (Δg) between products (H_2 and O_2) and reactants (H_2O) is the same associated with the fuel cell operation, and equal to -237.15 kJ mol^{-1} at 298.15K, 0.1 MPa and for water in liquid form. The Gibbs free energy depends basically on temperature. Its determination is given in the appendix (Par.A.1).

The ideal (reversible) cell voltage (E^0) at standard conditions (298.15 K, 0.1 MPa) - required to obtain the split of a mole of water molecules into hydrogen and oxygen, is given by:

$$E^0 = -\frac{\Delta G}{2F} \cong 1.229\ V \tag{1.19}$$

Where F is the Faraday's constant (given in C mol^{-1}) and E^0 is expressed in volts. The reversible voltage at standard conditions is then equal to 1.229 V. The dependence of the Gibbs free energy on pressure can be written in the so-called Nernst equation form (Larminie and Dicks 2004):

$$E = -\frac{\Delta G}{2F} + \frac{RT}{2F}\ln\left(p_{H_2}\frac{p_{O_2}^{0.5}}{p_{H_2O}}\right) = E^0 + \frac{RT}{2F}\ln\left(p_{H_2}\frac{p_{O_2}^{0.5}}{p_{H_2O}}\right) \tag{1.20}$$

Where R is the universal gas constant and T is the operating temperature (in K). p_{H_2}, p_{H_2O}, and p_{O_2} are the partial pressures of hydrogen, water vapour and oxygen, and must be expressed in bars if used in this form. As can be seen, the reversible voltage rises with pressure. In practical cases, however, it is sometimes preferable to work at high pressure to limit the evaporation of liquid electrolytes, if present (Cemmi and Pozio 2008). Since the reaction in Eq.(1.18) is endothermic (Grimes et al. 2008), its proceeding requires external heat. In addition, the temperature influences the reversible voltage. The presence of temperature in the second right-hand side term of Eq.(1.20) is balanced by the dependence of E^0 with temperature (inversely proportional), with the result of a global reduction of E with increasing temperature.

Under real operations, together with the electrochemical reactions described in Eqs. (1.14) - (1.18), there is a change in the molar enthalpy, described by the first law of the thermodynamics:

$$\Delta H = \Delta G + T\Delta s \tag{1.21}$$

Where ΔH and Δs are the change in the molar enthalpy and entropy associated with the reaction of Eq.(1.18), given in J mol^{-1} and J mol^{-1} K^{-1}, respectively. Under real operations, the voltage supplied to the cell is higher than the reversible voltage (E) - due to irreversibility, and heat is produced (the $T\Delta s$ term). The derivation of $\Delta H(T)$ and $\Delta s(T)$ values are given in Par.A.1. If the energy supplied (in terms of voltage) equals the value of ΔH, then the reaction will be isotherm, and the heat produced by the irreversibility will be fully absorbed by the reaction. At standard conditions (298.15 K, 0.1 MPa), the voltage required to obtain this condition is the so-called *thermo-neutral voltage*, and is simply equal to:

$$V_{TN} = -\frac{\Delta H}{2F} = \frac{285838}{2 \cdot 96485.309} \cong 1.481\ V \tag{1.22}$$

Above $V_{TN,}$ the reaction becomes exothermic and the heat generated must be removed from the cell. Table 1.8 summarizes the different voltage ranges involved in the electrolysis process. In actual operations, however, the irreversibility losses are sufficiently high to force the electrolysis cell to operate always above the V_{TN} value.

Table 1.8 Dependence of electrolysis reactions upon voltage

Cell voltage at standard conditions (V)	Condition
$V_c < 1.229$	No reaction occurs.
$V_c = 1.229 = E^0$	Minimum voltage required in ideal conditions.
$1.229 < V_c < 1.481$	Endothermic reaction.
$V_c = 1.481 = V_{TN}$	Isotherm reaction.
$V_c > 1.481$	Exothermic reaction.

Figure 1.18 shows the dependence of *ΔG* (line 'b') and *ΔH* (line 'a') with temperature. The region between line 'a' and 'b' represents the endothermic operation, while the exothermic operation is above line 'a'.

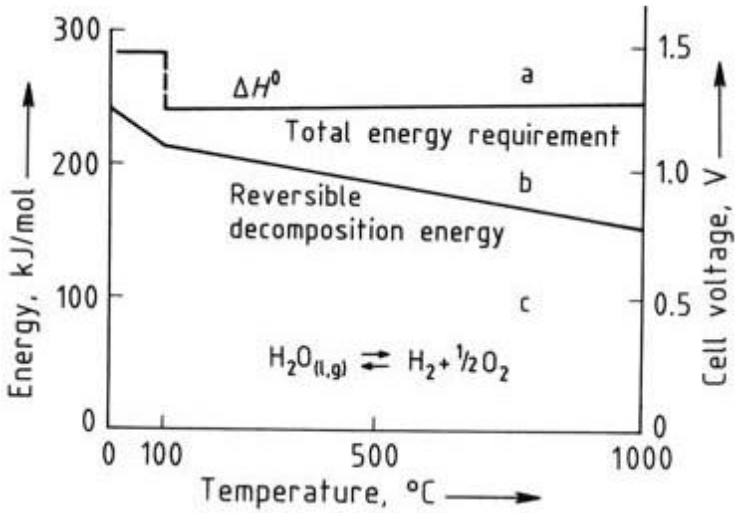

Figure 1.18 Energy requirement for electrolysis as function of temperature (Häussinger et al., 2012)

1.5.1.1 Efficiency

The efficiency of water electrolysis is usually defined as the ratio of the energy content of hydrogen (the energy that can be obtained by the oxidation of hydrogen and reduction of oxygen into water) to the electrical energy supplied to the electrolyser (as in Ivy 2004). In terms of voltage, the efficiency can be expressed as:

$$\eta_{th} = \frac{V_{TN}}{V_c} \tag{1.23}$$

Ideally, a cell operating at V_{TN} can produce hydrogen at 100% thermal efficiency. Moreover, the energy in excess of *ΔG* does not need to be supplied in the form of electrical energy, hence a voltage as low as *E* can also be used to split water if the system is allowed to absorb heat from its surroundings (this is the so-called *allothermal operation*). The cell is about 120% voltage efficient when the operating voltage is *E*. This means that the fuel value of the hydrogen produced will be 120% of the heating value of the electrical energy input at this operating condition (Grimes et al. 2008). When a cell is operated above V_{TN}, heat generated inside the cell due to losses supply the extra energy needed for driving the water splitting reaction (*autothermal operation*). The cells should be operated at low voltages and high current densities (the opposite of a fuel cell) to achieve high efficiencies and high hydrogen production rates. Practical efficiencies lie in the range 50 to 90% (Grimes et al. 2008; Cemmi and Pozio 2008).

The cell voltage (V_c) is largely decided by the operating temperature and pressure. The ideal voltage for water splitting (*E*) reduces with an increase in operating temperature, as already mentioned (*E*=1.18 V at 80 °C; 0.1 MPa). The irreversibility is lowered considerably at elevated temperatures due to the increased conductivity of the electrolyte and higher electrode activities. The reduction in thermodynamic voltage as well as over-voltages at elevated temperatures lower the operating voltage of the electrolytic cell, thereby increasing the water splitting efficiency with resultant energy savings.

A second way to indicate the efficiency of an electrolyser, usually adopted by electrolyser manufacturers, is the input energy required to the system (expressed in kWh) to obtain 1.0 Nm^3 of hydrogen. Typical values ranges usually from 3.9 to 6.0 kWh Nm^{-3} (Ivy 2004, Cemmi and Pozio 2008; Häussinger at al. 2012). A more detailed discussion about efficiencies estimation can be found in Zhang et al. (2010).

2. ELECTROLYSER SYSTEM MODEL

In this chapter, the electrolyser system model is presented. The model presented here is similar to most of the few available electrolyser models, and collects most of the main important aspects investigated in them. In the following paragraphs, a typical electrolyser system layout and a brief description of the models available in literature is provided. Then, it follows the detailed description of the model implementation in Matlab-Simulink environment. The calibration, validation and simulation of the model are part of Chapter 4.

2.1 Bibliography and available models

Given the simplicity of operations and layout (Par.2.2) of electrolyser systems, the models result in being quite simple if compared to fuel cells. On the other hand, the limited application and market of electrolysers reduce the interest in this technology. Few model of electrolysers can be found. All of them are lumped parameters models. CFD models of the entire system are not present in literature. As an example, one of the two main important models are the Evangelista et al. (1975) and Ulleberg (2003). The model presented in this work collects the most relevant aspects found in these two models adding some new features.

Also for the case of electrolysers, different kinds of models can be found, and are similar to the same kinds of models for fuel cells. One important and new model implementing semi-empirical relations for the electrolyser stack only can be found in Henao et al. (2014). Other models implement classic model equations as in Ulleberg (2003) and Garcìa-Valverde (2012).

2.2 Typical system layout

The typical system layout, valid for both the alkaline and PEM electrolysers, is shown in Figure 2.1. The DC current or voltage input given to the stack splits water into hydrogen and oxygen. The fluxes at the exit of the stack can contain a large amount of water, given the fact that the gas bubbles are generated inside a water film covering the electrodes of the electrolyser. Moreover, the high temperature of operation of electrolysers, typically above 50°C make the flow at the stack exit saturated with water. In case of alkaline electrolysers, moreover, the flow might also contain small traces of KOH in form of suspended aerosol. For this reason, the system usually makes use of two “water separators” and condensers, to separate the gases from the stack and to force the condensation of water. This process, in the case of a regenerative system might be considered superfluous. Nevertheless, in the case of hydrogen and/or oxygen storage, a high purity

of gas is usually required. The recuperated water and electrolyte are always re-introduced inside the stack. The electrolyte circulation (or simply the water circulation in case of PEM electrolysers) acts both to supply the reactant to the cell (i.e. water) and to be used as a cooling fluid for the stack.

Depending on the system technology and architecture, some filters or impurity separators or watered-ionizers might also be present together with valves and ancillary equipment.

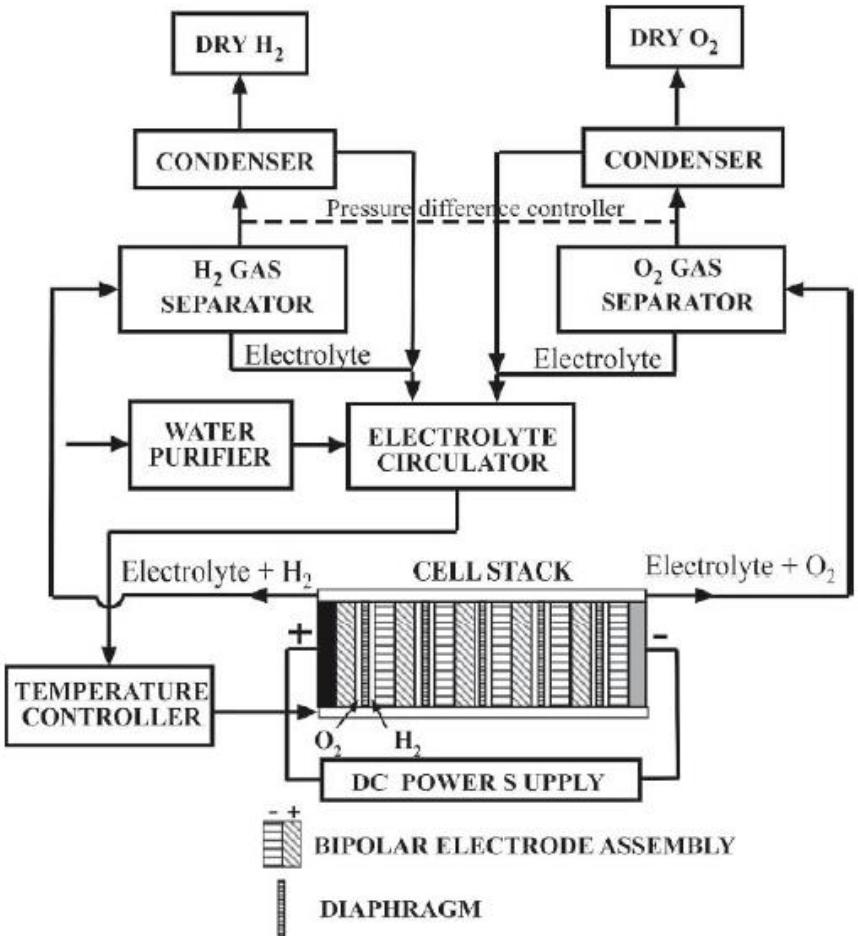

Figure 2.1 Typical alkaline or PEM electrolyser system layout

2.3 Model description

In the following paragraphs, the Matlab-Simulink model is developed. The subdivision into sub-paragraphs is coincident with the Matlab-Simulink model sub-division.

2.3.1 Electrolyser block

This block contains some important sub-blocks, described below.

Inlet data block

Given the current value, the net current directly converted to hydrogen and oxygen is calculated taking into account the faradaic efficiency. Faraday efficiency describes the efficiency with which electrons are transferred in a system facilitating an electrochemical reaction. Faradaic losses are experienced by both electrolytic and galvanic cells. These losses are usually in the form of misdirected electrons which participate in unproductive reactions, product recombination, short

circuit the system, and other diversions for electrons. These losses are physically expressed in the system as heat and sometimes as chemical by-products.

An example of side reaction can be found in the oxidation of water to oxygen. During this process, electrons are commonly diverted to the production of hydrogen peroxide. The fraction of electrons so diverted would represent a faradaic loss and vary between different apparatus. If the proper electrolysis products are produced, there can still be losses if the products are permitted to recombine. During water electrolysis, the desired products, hydrogen and oxygen, are produced but could be allowed to recombine to form water. Not all the electrons separated from hydrogen at the anode are directed through the electrical load and back to the cathode. Some of the electrons bleed through the electrolyte membrane reaching the cathode directly without performing work. Ideally, the electrolyte membrane would be a perfect insulator. This bring to the so-called crossover currents (Par.1.3.1.1).

In this model, faradaic losses are calculated in the form (Ulleberg 2003):

$$\eta_F = \frac{k_{f2}\left(\frac{I_{in}}{A}\right)^2}{k_{f1} + \left(\frac{I_{in}}{A}\right)^2} \tag{2.1}$$

Where I_{in} indicates the current entering the stack and A represent the cell area. The constants k_{f1} and k_{f2} can be derived experimentally. The net current participating in the production of hydrogen and oxygen inside the electrolyser is given by $I = \eta_F I_{in}$.
It is assumed that no accumulation of gases occur within the cells for simplicity. This means that a step variation in the current value gives a step response in hydrogen and oxygen production. Hydrogen and oxygen production are given by the Faraday's law in the form:

$$\dot{n}_{H_2} = \frac{n_c I}{2F}; \quad \dot{n}_{O_2} = \frac{n_c I}{4F} \tag{2.2}$$

Where n_c is the number of cells comprised in the stack, and $\dot{n}$ are expressed in mol s^{-1}. The water (both in gas and in liquid form) exiting the stack is calculated as the difference of the molar flow entering the stack minus the water consumption (expressed as $\dot{n}_{H_2O} = n_c I/2F$). Water exit from the subsystem is given both in l min^{-1} and in kg min^{-1}.

The "water density" block implements the variation of liquid water density with temperature (outlet side) interpolating empirical data (Haynes et al. 2012) in the form:

$$\rho_{H_2O_l} = 2 \times 10^{-5}(T - 273)^3 - 0.006(T - 273)^2 + 0.0248(T - 273) + 999.95 \tag{2.3}$$

Stack voltage and efficiency block

The calculation of the reversible voltage allows for the determination of the amount of heat generated by losses, in terms of difference in voltage between the reversible and the actual voltage. The reversible voltage is calculated in the form given by Eq.(1.20). The term E^0 is calculated using a power-law formula for the temperature (Cemmi and Pozio 2008):

$$E^0 = 1.5184 - 1.5421 \times 10^{-3} T_{stack} + 9.523 \times 10^{-5} T_{stack} \ln(T_{stack}) + 9.84 \times 10^{-8} T_{stack}^2 \tag{2.4}$$

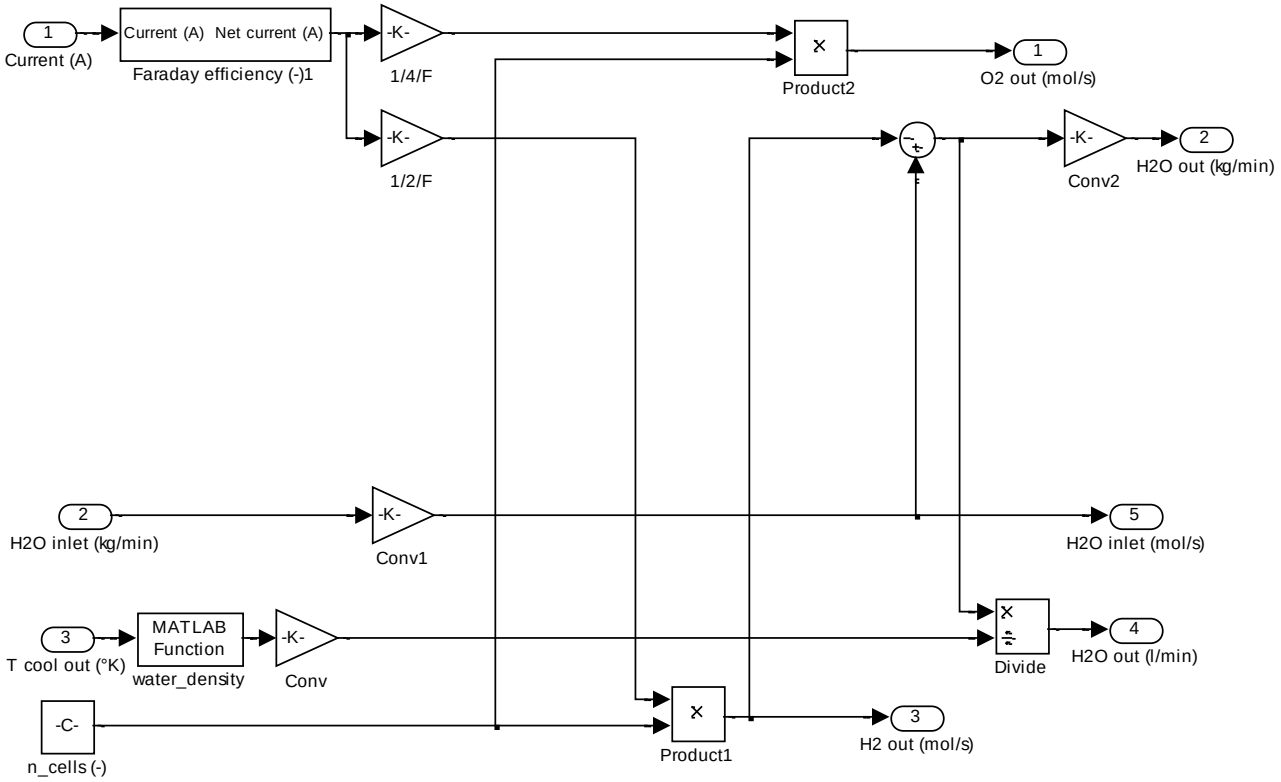

Figure 2.2 Inlet data block in Simulink

It is assumed to use the stack temperature. The partial pressure of water (p_{H_2O}), given in Eq.(1.20) is here substituted with the formula given in Evangelista et al. (1975), since the assumption of equivalence of water activity with partial pressure is meaningless in case of liquid water. The formula given by Evangelista et al. (1975) is in the form:

$$a_{H_2O} = \exp\left(\frac{2.7}{0.431} KOH_{conc}\right) \tag{2.5}$$

The energy generated by losses can be then computed as:

$$\dot{Q}_{gen} = (V_c - E) In_c \tag{2.6}$$

Where $\dot{Q}_{gen}$ is expressed in W. It is important to underline that part of this heat might be absorbed by the electrochemical reaction. The thermo-neutral voltage (V_{TN}) and entropy change (Δs) are calculated using Eqs. (A.1.1)-(A.1.8), thanks to Matlab scripting. The net heat power generated, given by the sum of entropy increase and heat generated is calculated as:

$$\dot{Q}_{net} = T_{stack} \Delta s \cdot \dot{n}_{H_2} + \dot{Q}_{gen} \tag{2.7}$$

Efficiency is calculated as in Eq.(1.23).

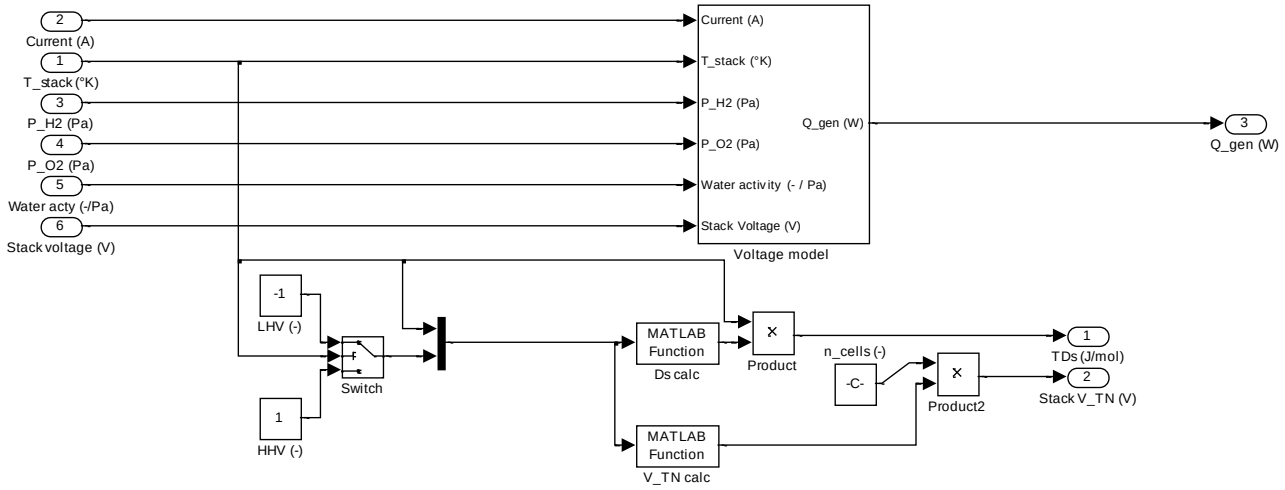

Figure 2.3 Stack voltage / efficiency model block in Simulink

Thermal model block

The sensible heat transported by the exiting gases is given by:

$$\dot{Q}_{sens} = c_{p_{H_2}} \dot{n}_{H_{2_{out}}} (T_{stack} - T_0) + c_{p_{O_2}} \dot{n}_{O_{2_{out}}} (T_{stack} - T_0) + \frac{1.5849 \cdot I}{F} c_{p_{H_2O}} (T_{stack} - T_0) \quad (2.8)$$

Where T_0 is a reference temperature (298.15 K).

The stack outlet temperature is computed as (Ulleberg 2003):

$$T_{cool_{out}} = T_{cool_{in}} + \left(T_{stack} - T_{cool_{in}}\right) \left[1 - \exp\left(\frac{h_{cond} - I h_{conv}}{c_{p_{H_2O}} \dot{n}_{H_2O}}\right)\right] \quad (2.9)$$

Where $T_{cool_{in}}$ and $T_{cool_{out}}$ are the inlet and outlet temperature of the cooling fluid. $\dot{n}_{H_2O}$ is the flow (in mol s^{-1}) of liquid water entering the stack (used both as reactant and cooling fluid). h_{cond} and h_{conv} are two coefficients for the conductive and convective heat flow transfer, respectively.

The heat removed from the stack ($\dot{Q}_{cool}$) can be obtained from Eq.(2.9) as:

$$\dot{Q}_{cool} = \left(T_{stack} - T_{cool_{in}}\right) \left[1 - \exp\left(\frac{h_{cond} - I h_{conv}}{c_{p_{H_2O}} \dot{n}_{H_2O}}\right)\right] \left(c_{p_{H_2O}} \dot{n}_{H_2O}\right) \quad (2.10)$$

The thermal loss associated with the irradiation is given by the difference between the ambient and stack temperature as:

$$\dot{Q}_{loss} = \frac{T_{stack} - T_{amb}}{R_{therm}} \quad (2.11)$$

Where R_{therm} is given as a constant. T_{amb} is the ambient, surrounding temperature.

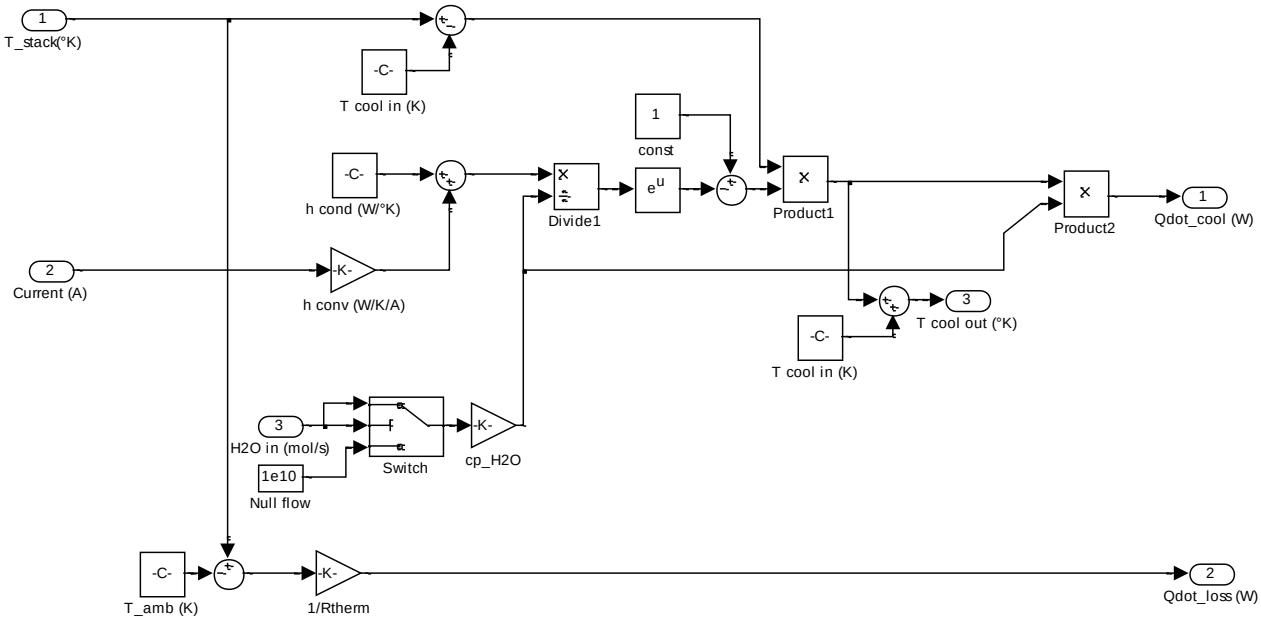

Figure 2.4 Thermal cooling model block in Simulink

The stack temperature is obtained as a first order evolution as:

$$T_{stack} = \int \frac{\dot{Q}_{net} - \dot{Q}_{sens} - \dot{Q}_{cool} - \dot{Q}_{loss}}{C_{ez}} dt \tag{2.12}$$

Where C_{ez} is the thermal capacity of the electrolyser (expressed in J K^{-1}).

Current evaluation block

This model simply contains a list of input parameters which are used for the calculation of the current entering the electrolyser stack. Since the electrolyser is usually controlled varying the input voltage to obtain a determined current value, proportional to the hydrogen and oxygen generation rates, this block simply traduces the input voltage to an input current. This block operates inverting the equations contained in Par.2.3.3 and using the Matlab *fzero* routine, which finds the zero of non-linear single variable equations.

Coolant flow block

The coolant flow block simply consists of a PID controller to keep the temperature of the electrolyser stack at the desired operating temperature. The controller compares the actual stack temperature with the desired temperature of the stack. Given this discrepancy, the controller modifies the mass flow of the water circulating inside the stack itself. A saturation controls the maximum output for the water flow and the output given by the integrator of the PID controller. The commanded mass flow of the PID controller can be then written simply as:

$$\dot{m}_{H_2O} = K_{prop}\left(T_{stack} - T_{stack_{des}}\right) + K_{der}\frac{d\left(T_{stack} - T_{stack_{des}}\right)}{dt} + K_{int}\int\left(T_{stack} - T_{stack_{des}}\right)dt \tag{2.13}$$

Where K_{prop}, K_{der} and K_{int} are the controller constants.

2.3.2 Pressure subsystem block

The gas storage subsystem, comprising pressure vessels for both the hydrogen and oxygen gases, is modelled in Simulink with a feedback signal to the electrolyser. It is assumed that the pipes connecting the stack to the pressure vessels are considered as part of the vessels and the temperature inside the vessels is kept constant and equal to the electrolyser stack. Possible modification of this assumption can be achieved simply taking into account a heat transfer between the gases and the ambient.

In the model, two conditional operators (switches) are used to compare the actual pressure with the maximum pressure allowed within the tanks. When the maximum pressure is reached, accumulation of the gas is inhibited, simulating a sort of pressure relief valve. The pressure level directly influences the operation of the stack, since higher pressure of the gases implies more voltage required to the cells (Nernst equation, Eq.(1.20)).

For pressure values lower than the maximum pressure ($P_{set_{O_2}}$ and $P_{set_{H_2}}$ for the oxygen and hydrogen side, respectively), gas accumulation is allowed, and its partial pressure is calculated with the ideal gas law:

$$p_{O_2} = \frac{n_{O_2}RT}{V_{O_2}}$$
$$p_{H_2} = \frac{n_{H_2}RT}{V_{H_2}} \tag{2.14}$$

The volumes in Eq.(2.14) are the volume of the pressure vessels of oxygen and hydrogen, respectively. The moles of hydrogen and oxygen in Eq.(2.14) are obtained integrating the molar flow of oxygen and hydrogen produced and calculated with Eq.(2.2). In this model, the gas is considered comprised only of oxygen/hydrogen and water vapor. Reactants crossover and impurities are not considered, given the very low traces. It is assumed a saturation condition, with relative humidity (φ) equal to one. The vapor pressure is calculated using Eq.(2.15) by Sivertsen and Djilali (2005).

$$p_{H_2O} \equiv p_{sat} = 1000 \cdot 10^{1.69\times10^{-10}T^4 + 3.85\times10^{-7}T^3 - 3.39\times10^{-4}T^2 + 0.143T - 20.92} \tag{2.15}$$

Where p_{sat} is the saturation pressure of water vapor (given in Pa).

The pressure inside the vessels is given by the sum of the partial pressure of vapor and hydrogen/oxygen. In case of the reaching of the maximum pressure (saturation block in Simulink) the integrator block stops integrating other moles of H_2 and O_2. The pressure model subsystem is shown in Figure 2.5.

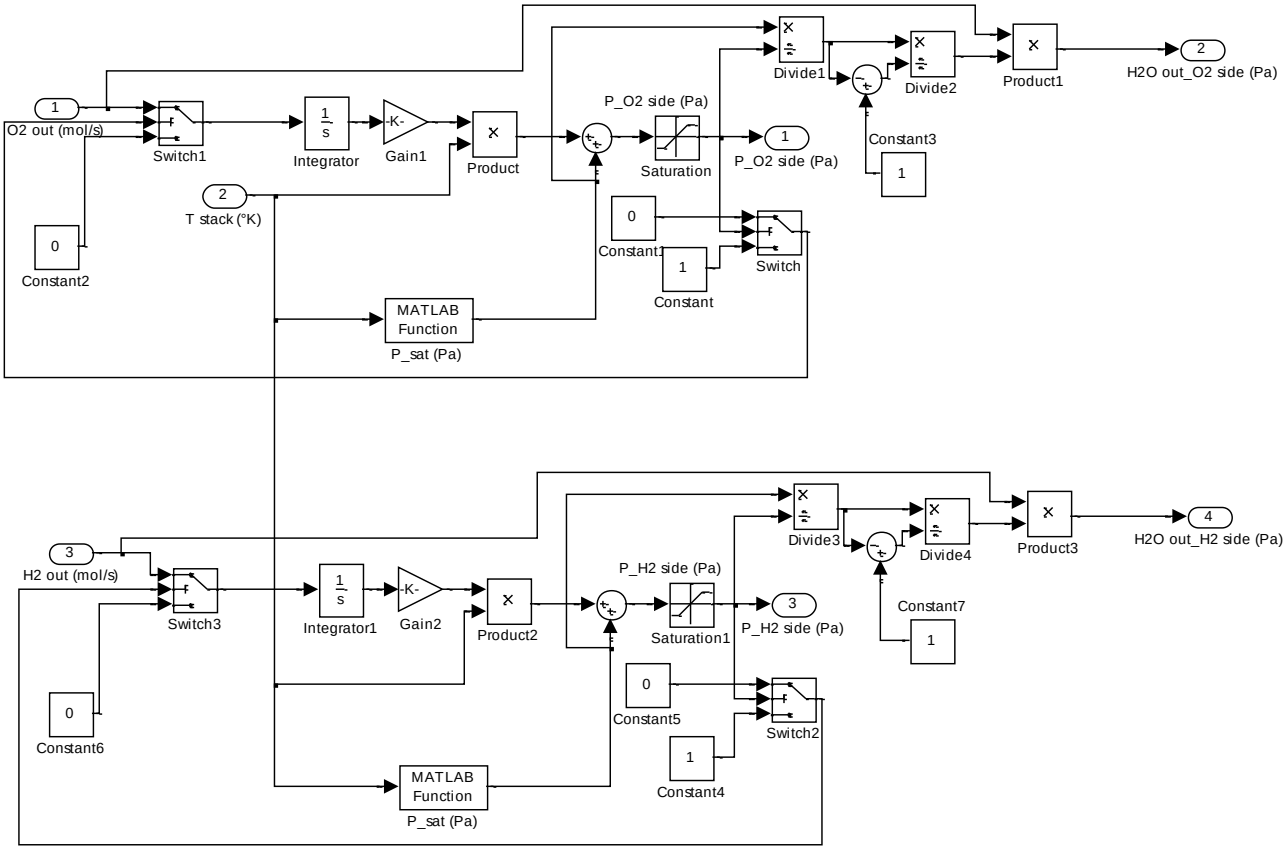

Figure 2.5 Pressure model block in Simulink

2.3.3 Electrochemical model block

The electrochemical model belongs to a 1D formulation. The formulation given in the following can be considered as reference for both the electrolysers and fuel cells. The electrochemical model is divided into its main elements, namely the theoretical voltage and the voltage losses associated with the irreversibility and fluid flow behavior.

Activation losses model equations

The activation losses terms expressed with the Tafel approximation, V_{act}, could reach negative values whenever the logarithm argument is minor than one.

The standard Tafel approximation in Eq.(1.4) derives directly from the complete Butler-Volmer equation, given usually in the form (Bagotsky 2006):

$$i = i_0 \left(e^{\alpha_1 \left(\frac{F}{RT}\right) V_{act}} - e^{-\alpha_2 \left(\frac{F}{RT}\right) V_{act}} \right) \tag{2.16}$$

Where *i* indicates the electric current density (A m^{-2}). This equation applies separately for the anode and cathode electrodes; the exchange current density, i_0, is typically calculated using an Arrhenius-type relation in the form:

$$i_0 = A_{exc} e^{-\frac{E_{act}}{RT}} \tag{2.17}$$

Where the constant A_{exc} is a function of cell temperature and partial pressures.

The coefficients α_1 and α_2 are the so-called *reduction* and *oxidation transfer coefficients* and are dimensionless parameters related to the electron transfer processes occurring across the electrode-electrolyte interface. These two variables are quite difficult to find, since their values involve a perfect knowledge of all of the intermediate chemical reactions steps at the two electrodes.

The general approximation made for PEM and Solid Oxide Fuel Cells (SOFCs) models is to assume each reaction occurrence to be a one-step, single-electron transfer process. This results in the following form of the Butler-Volmer (B-V) equation which can be recognized in all of the CFD models available in literature and making use of a 3D electrical field (as in Min et al. 2006):

$$i = i_0 \left(e^{(1-\beta)\left(\frac{F}{RT}\right)\Delta V_{act}} - e^{-\beta\left(\frac{F}{RT}\right)\Delta V_{act}} \right) \tag{2.18}$$

Where the parameter β is the so-called *symmetry factor*, defined as the fraction of the activation voltage loss that affects the activation energy barrier.

Since the full B–V equation must be solved implicitly for the activation voltage loss, several explicit approximations have been proposed and used in the literature. It is crucial to understand the range of applicability of each of these equations not only to prevent higher order errors such as negative activation losses, but also to minimize minor modeling inaccuracies. When the activation loss is large (at about $V_{act} > 200\ mV$), the first exponential term in the B–V equation is much larger in magnitude than the second one. If the second exponential is neglected, the resulting equation is the Tafel equation. Moreover this equation is better valid only when $i/i_0 > 4$, as discussed extensively in Noren and Hoffman (2005):

$$\Delta V_{act} \cong \frac{RT}{\alpha_1 F} ln\left(\frac{i}{i_0}\right) \tag{2.19}$$

Moreover, if the exponential terms in the B-V equation are expanded in a power series and the higher-order, non-linear terms are neglected, the resulting equation becomes a linear equation of current vs. potential, valid when $i/i_0 < 1$, as discussed in Noren and Hoffman (2005):

$$\Delta V_{act} \cong \frac{RT}{F}\left(\frac{i}{i_0}\right) \tag{2.20}$$

The shape of these two approximations are given in Figure 2.6 and Figure 2.7. A reference value of 20000 Pa (similar to the atmospheric O_2 partial pressure) was used for the oxygen partial pressure and i_{0c} = 0.01 A m^{-2} (as in Dawes et al. (2009); Lum and McGuirck (2005)). At the anode side, a reference value of i_{0a} = 0.1 A m^{-2} and a partial pressure of 80000 Pa was used. The considerations just reported are clearly matched with the plot. Finally yet importantly, the approximation of the linear current equation is much more inexact.

Considering the models available and making use of a 1D electrochemical field, the general trend follows three strategies:

- The Tafel approximation is used at the cathode side; the activation losses at the anode are neglected. This is the case of Dutta et al. (1999; 2000; 2001); Lum and McGuirck (2005). These assumptions lead not only to a partial loss of activation losses brought by the anodic reaction, but also to an inaccurate and underestimated value for the cathode losses in the very high voltage range; moreover these losses could invert their sign when $i < i_0$. For instance, using the case study of the precedent two plots, it is obvious that the activation losses are negative up to a value of i = 80 mA m^{-2}.

- The Tafel approximation is used at the cathode side. At the anode side a linear approximation is adopted. This model brings to the same considerations just done for the cathode side. At the anode side, it is obvious how a linear simplification will certainly lead to over-estimated voltage losses, but at the same time, anode losses cannot became negative.
- The Tafel approximation is used at both the anode and cathode side, as in Dutta et al. (1999); Dawes at al. (2009). With this last option, the combination of Figure 2.6 and Figure 2.7 gives the plot reported in Figure 2.8.

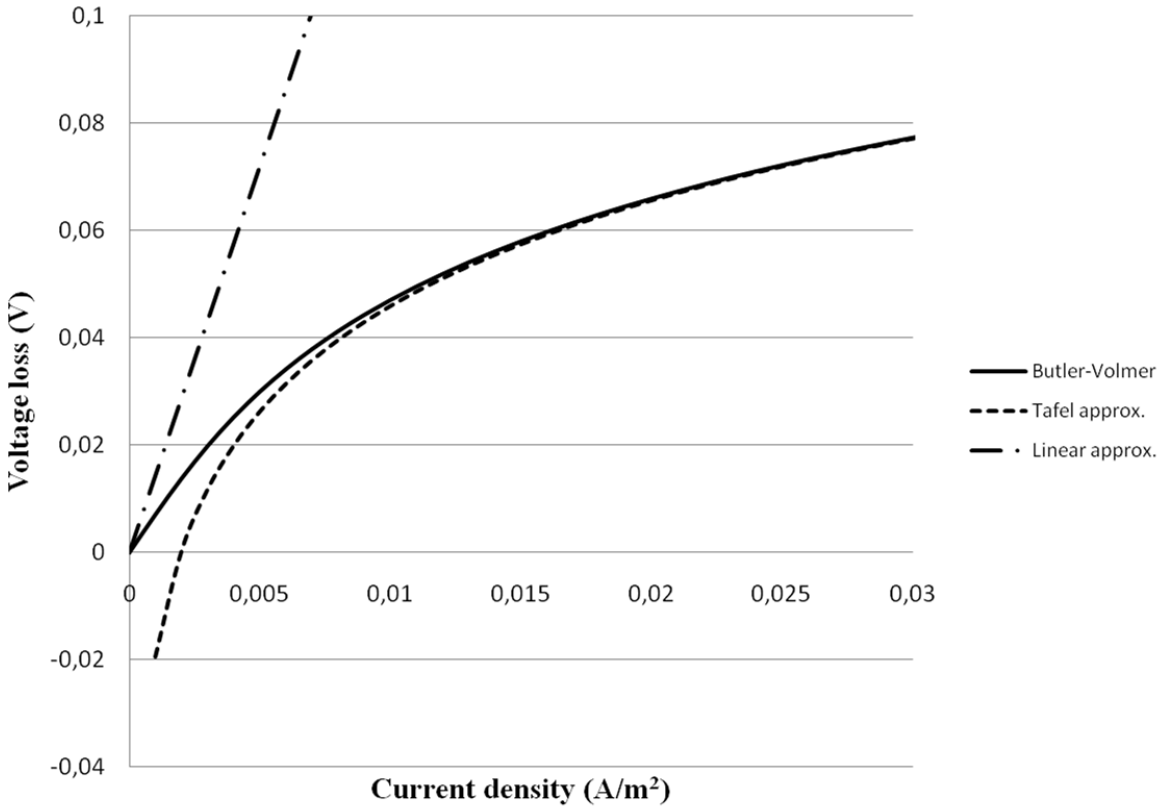

Figure 2.6 Butler-Volmer equation and approximation comparisons for the cathode side

It is clearly recognizable an initial error in considering the Tafel approximation, up to 0.2 A m^{-2}, where the difference falls slightly above the 2% of error.

In this thesis, a different approximation was implemented, and never used before. This approximation is the *hyperbolic arcsine approximation*. It derives from the fact that when α_1 *and* α_2 are assumed equal (i.e. $\beta = 0.5$), the Butler-Volmer equation assumes the hyperbolic sine formula, and it is possible to obtain the following explicit approximation:

$$\Delta V_{act} = \frac{RT}{\alpha_1 F} \sinh^{-1}\left(\frac{i}{2i_0}\right) \tag{2.21}$$

The only assumption done here consists in assuming a perfect reaction symmetry, with the choice of $\beta = 0.5$. Anyway, in many works this parameter was sufficiently studied, being its correct determination quite difficult to obtain. In Noren and Hoffman (2005), it is assured that this value could range from 0.3 to 0.6, often used as a calibration parameter to fit analytical and experimental data. In Sivertsen and Djilali (2004), CFD studies about this parameter were performed, and it is

reported an empirically determined value between 0.4 and 0.6. This study confirms this estimation. Moreover, all of the works found in literature are calibrated with this kind of value ranges.

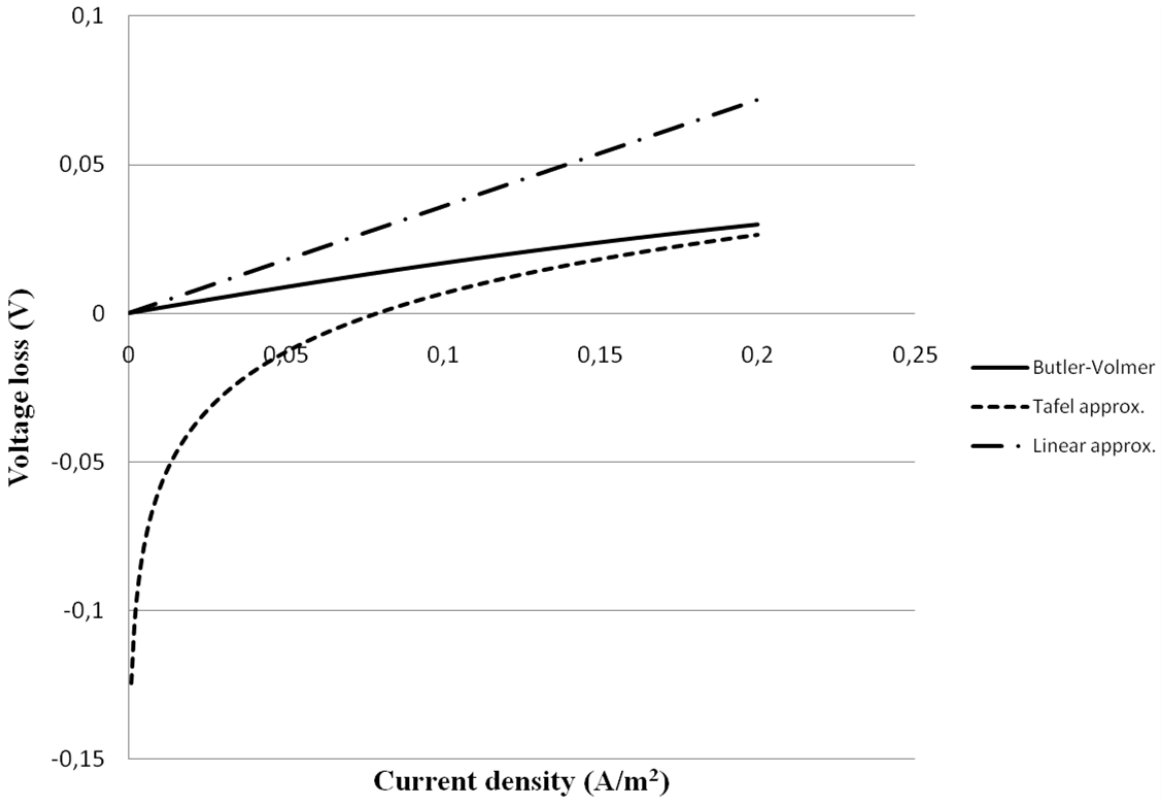

Figure 2.7 Butler-Volmer equation and approximation comparisons for the anode side

Anyway, an analysis about the impact of the β variation on the correct estimate of the exchange current density is now shown in Figure 2.9, where it is possible to note maximum differences in the order of 20 mV for values ranging from 0.1 to 0.3, and about 30 mV disagreement for the value of 0.7 at i/i_0 ~1.1. As can be clearly seen, the hyperbolic sine approximation given in Eq.(2.21) perfectly matches with the B-V equation for a value of $\beta = 0.5$.

Since the exchange current density values can have a strong impact on the performance of the polarization curve, determining the length of the initial steep curve, a characterization of these two parameters dependent upon temperature is adopted (Eq.(2.22), (2.23)). The influence of exchange current density variation for fuel cells can be seen in Figure 2.10, where a hyperbolic sine approximation has been used to draw the curve, and where the ohmic and concentration losses are not considered.

$$i_{0_a} = i_{0_{a_{ref}}} \exp\left(-\frac{E_{act,a}}{RT_{stack}}\right) \tag{2.22}$$

$$i_{0_c} = i_{0_{c_{ref}}} \exp\left(-\frac{E_{act,c}}{RT_{stack}}\right) \tag{2.23}$$

The variables $i_{0_{a_{ref}}}$ and $i_{0_{c_{ref}}}$ in Eq.(2.22) and Eq.(2.23) are the reference exchange current density values, and can be considered as a sort of standard temperature values (298.15 K) of the exchange current densities.

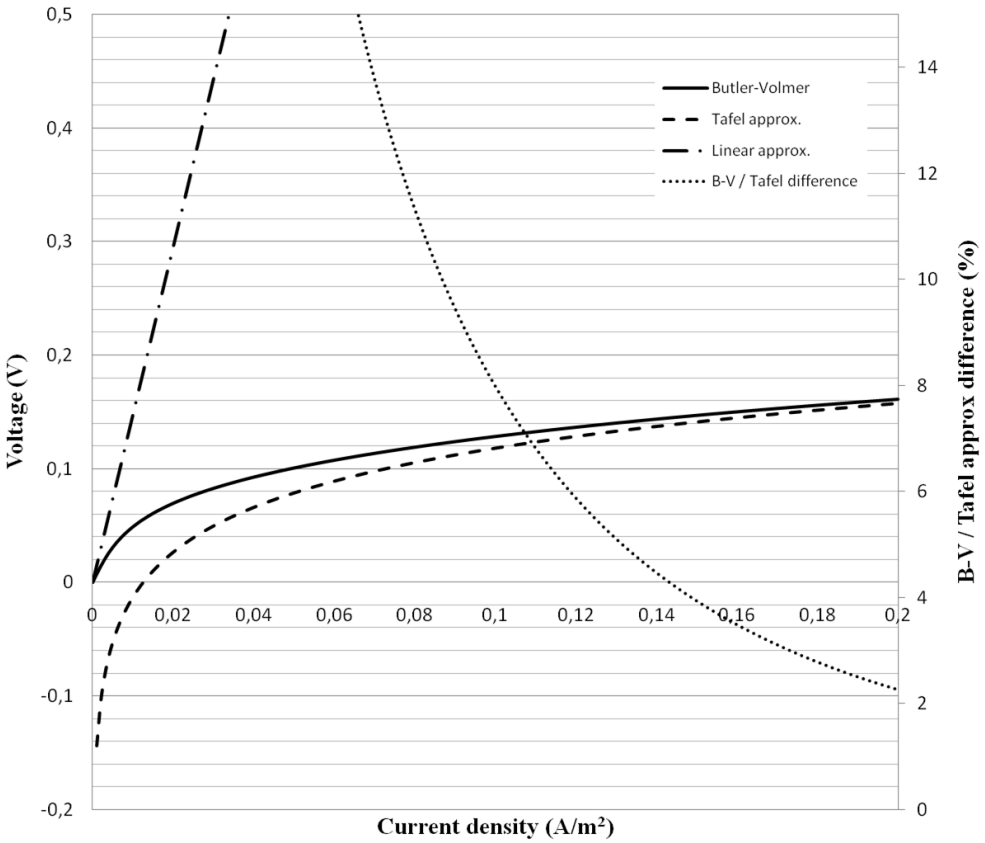

Figure 2.8 Butler-Volmer equation and complete activation losses

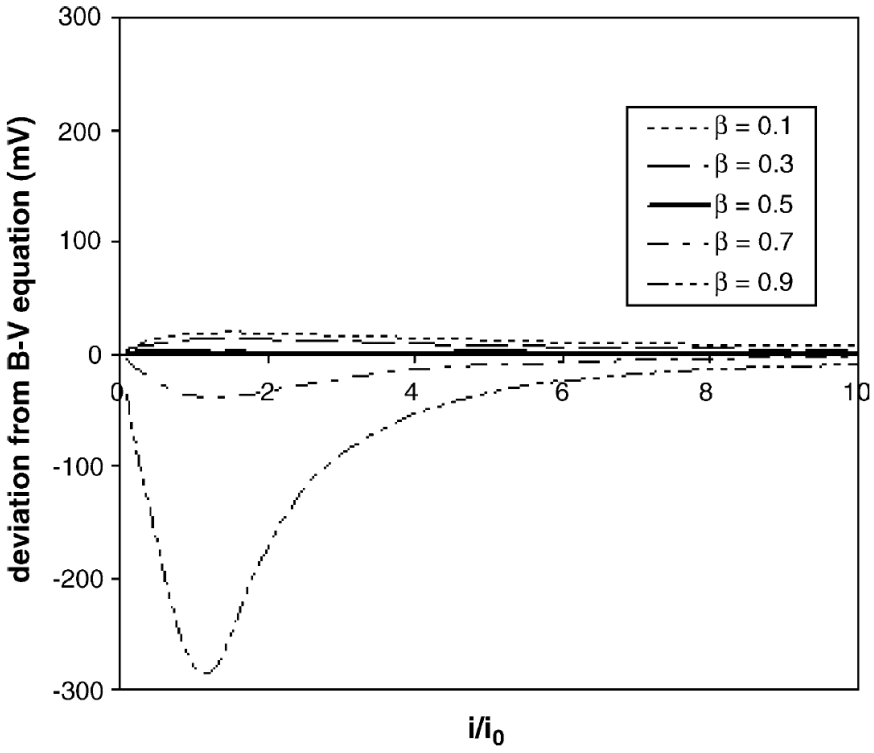

Figure 2.9 Deviation of the hyperbolic sine approximation respect to the B-V equation

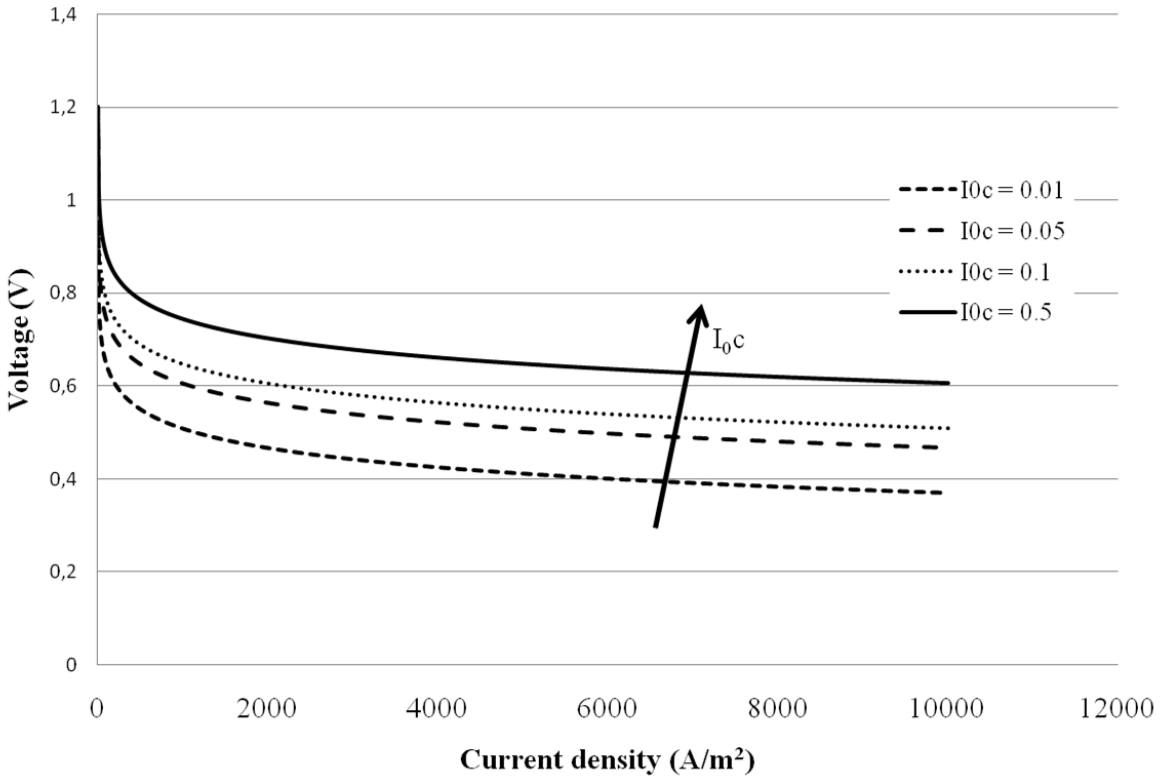

Figure 2.10 Dependence of the exchange current density on the polarization curve

These values (given in A m^{-2}) will be used as tuning parameters in the whole of this thesis. The activation energies ($E_{act,a}$ and $E_{act,c}$), instead, are fixed values dependent upon the chemical reaction involved, and are assumed equal to 76,000 J mol^{-1} and 18,000 J mol^{-1} for the anode and cathode side, respectively (Ni et al. 2008).

The use of a tuning factor comes from the fact that this parameter shows high uncertainties, and many different values for the reference conditions are usually found.

Theoretical voltage model equations

In this model, the Nernst equation has been implemented, to take into account the pressure influence on the electrochemical performance:

$$V_{id} = E^0(T) + \frac{RT_{stack}}{2F} ln\left(\frac{P_{H_2} P_{O_2}^{0.5}}{acty}\right) \tag{2.24}$$

Where the $E^0(T)$ term coincides with Eq.(2.4). The partial pressures in Eq.(2.24) are expressed in bar. In the case of liquid electrolytes the term *acty* is substituted by the KOH concentration given as mass concentration, i.e. kilograms of KOH per liter of water (kg l^{-1}). The activity, in this second case, is given by Eq.(2.5).

Ohmic losses for the alkaline electrolyser

The Ohmic losses in an electrolysis cell are the sum of the terms due to the anode, separator and cathode resistances. The conductivity of KOH and NaOH solutions exhibit maxima when plotted versus concentration at constant temperature and consequently, the electrolyte concentration

is often chosen to be at this value so as to minimize the ohmic loss. For KOH solutions at 28°C, the maximum conductivity occurs at 20% KOH, increasing to 35% KOH at 80°C. The gases produced bubbling up through the electrolyte, contribute to the ohmic loss. In addition, vapor bubbles could also be produced further increasing the ohmic resistance. The volume rate of bubbles produced will depend upon pressure, temperature, electrolyte concentration and current density. These factors, together with electrolyte conductivity determine the ohmic loss in the electrolysis cell. In this model, the electric resistance given by plates and current collectors are not considered, given their high conductivity.

The total ohmic resistance, R_{tot}, defined in Ω m^2, can be expressed as (Evangelista et al. 1975):

$$R_{tot} = R_{sep} + r_{f_a} t_a f_A + r_{f_c} t_c f_c \tag{2.25}$$

Where R_{sep} is the separator (or membrane) resistance, measured in Ω m^2 and it is considered constant for simplicity in this model. r_{f_a} and r_{f_c} are the anode and cathode side electrolyte resistivity, given by the liquid film thickness between the electrode and the bipolar plates. They are measured in Ω m. t_a and t_c are the electrolyte film thicknesses (in m), while f_a and f_c are two dimensionless values used to take into account the additional gas bubbles resistances, and are defined as (Tobias 1959):

$$f = \frac{1}{(1-\alpha_b)^{1.5}} \tag{2.26}$$

Where α_b is the gas bubble volume fraction (dimensionless).

The value of f and α will obviously vary in the direction of electrolyte flow, being zero at the cell inlet and increasing until the cell exit is reached. The value of α at the cell exit can be calculated using the assumption that no accumulation takes place, and consequently the rate at which the gas leaves the cell is equal to the rate with which it is generated. Moreover, assuming that the gas is saturated with vapor, the volume fraction of bubbles at the exit of the cell becomes:

$$f = \frac{1}{(1-\alpha_b)^{1.5}} \tag{2.27}$$

$$\alpha_{b_a} = \frac{iART_{stack}}{iART_{stack} + 2F\left(p_a - p_{vap}(T_{stack})\right)\sigma_{b_a} V_{in_a} W t_a} \tag{2.28}$$

$$\alpha_{b_c} = \frac{iART_{stack}}{iART_{stack} + 4F\left(p_c - p_{vap}(T_{stack})\right)\sigma_{b_c} V_{in_c} W t_c} \tag{2.29}$$

It is assumed the temperature of the bubbles coincide with the stack temperature (T_{stack}). σ_b is the slip ratio of the bubbles, defined as the ratio between the gas bubbles and the surrounding liquid. A indicates the cell area, as usual (in m^2). p_a and p_c are the anode and cathode pressures, while p_{vap} is the vapor pressure (in Pa). V_{in_a} and V_{in_c} are the inlet velocities of the electrolyte inside the cell (measured in m s^{-1}). W is the width of the cell. In this model, it is assumed the cell is rectangular, with height h, width W and thickness t. In the case of a circular cell, these values cannot be used. Anyway, these value are geometrical constants, and the use of a tuning factor (introduced in the following) can take into account also this aspect. Since the α value at the inlet is equal to zero, it is possible to use an average value of the bubble fractions between its minimum (zero at inlet) and its maximum (Eq.(2.28), (2.29)). In this model, a simple average ($\alpha_a/2$ and $\alpha_c/2$) is used.

The electrolyte resistance (r_f) is modeled as in Gilliam et al. (2007) as:

$$r_f = \frac{100}{-2.041M_{koh} - 0.0028M_{KOH}^2 + 0.005332M_{KOH}T_{stack} + \frac{207.2M_{KOH}}{T_{stack}} + 0.001043M_{KOH}^3 - 0.0000003M_{KOH}^2T_{stack}^2} \quad (2.30)$$

Where M_{KOH} is the molarity of the solution, expressed in mol l^{-1}. The conversion between M_{KOH} and KOH_{conc} can be simply done with the following relation:

$$M_{KOH} = \frac{KOH_{conc}}{\mathcal{M}_{KOH}} \quad (2.31)$$

Where $\mathcal{M}_{KOH}$ is the molar mass of potassium hydroxide (0.0561 kg mol^{-1}). The empirical equation for r_f given in Eq.(2.30) is better valid for temperatures in the range 273 – 373 K and for KOH mass concentrations between 0 and 70 %.

The ohmic voltage loss is then given by:

$$V_{ohm} = k_{ohm}iR_{tot} = (R_{sep} + r_{f_a}t_af_A + r_{f_c}t_cf_c)ik_{ohmic} \quad (2.32)$$

Ohmic losses for the PEM electrolyser

For the PEM electrolyser, the only difference with the alkaline electrolyser is given by the calculation of the ohmic losses, which in the case of the PEM electrolyser are related to the PEM solid electrolyte instead of the liquid alkaline electrolyte. All of the other equations, given the model developed, are the same. The V_{ohm} value is calculated in the PEM model as in Eq.(3.66) and Eq.(3.67). In this case, the membrane is considered always covered by water. In this case, the membrane humidification will be complete, and the value of λ is equal and constant to 14.4.

3. FUEL CELL SYSTEM MODEL

3.1 Bibliography and available models

Many models about fuel cells can be found in literature. Most of these models are given only for the stack without considering the entire system and its importance on the stack performance. Dealing with the sole stack system modeling, three main kinds of models can be found:

- Lumped models considering the stack as a unique control volume divided into three parts consisting in the anode, cathode and membrane. Most of these models divide each of these three regions into inlet, stack and outlet regions, usually. This is the case of the model here developed.
- Lumped models dividing the fluidic path of anode and cathode into several segments. These are usually called "segmented models".
- Semi-empirical or abstract models using empirical or semi-empirical data to obtain look-up tables and curves through functions and polynomial combinations.

The models belonging to the first kind are the most diffused in literature. As an example, the work by Adzapka and Agbossou (2008), Chu et al. (2007), Huisseune et al. (2008), Yu et al. (2005), Pathapati et al. (2004) and Sharifi et al. (2010) can be cited. All of these models share some aspect with the model here developed and all pay attention to the transient response of the stack under different inputs.

The models belonging to the second kind, instead, are more rare to find in literature. These models usually divide both the anodic and cathode flow channel into several segments, as in Chen and Peng (2008). A typical method of fuel cell division is shown in Figure 3.1. This kind of model might introduce some additional benefit in considering the single cell in a more discretized way. The localization of possible flooding area using this model becomes practical, for instance, and the higher the number of control volumes the higher the prediction of flooded regions identification. However, this kind of model introduces additional numerical problems and efforts to address for the solution. Moreover, the process of subdivision of the domain into sub-volumes must be done for each bipolar plate geometry and cannot be adapted from cell to cell.

The last class of models, using empirical data to obtain functions describing the behaviour of fuel cells is the last class of available lumped parameters model. The use of these models allows a rapid simulation, since the model solution consists in simply solving explicit or implicit single-variable mathematical functions. On the other hand, these models are limited in capturing only some

particular aspects of the stack behaviour. Examples of these models are the Pisani et al. (2002) and the Hou et al. (2010) works.

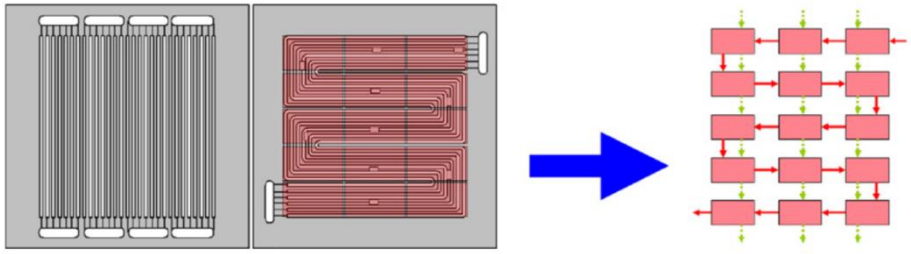

Figure 3.1 Segmented model fuel cell subdivision in 15 control volumes

Few system models can be found instead in literature. Most of them are available in books, as in Pukrushpan (2004), Nehrir and Wang (2009), Xue et al. (2004) and Bao et al. (2009). Some of them model all of the main components of the system at different levels of precision and investigation. The stack is usually modeled in a way similar to the first kind of models.

3.1.1 Importance of modeling transient phenomena

One of the most important aspects to take into account when modeling fuel cell systems is its transient response. If compared to classic dynamic systems, where a first or a second order behaviors are usually seen, PEM fuel cells shows usually a sort of first order behavior, but with the presence of overshoot and undershoot.

Typical first order behavior can be seen in the thermal-related aspects in fuel cells. In fact, a fuel cell usually have a slow thermal response, and the rapid variation in the electrochemical or operating parameters modify the fuel cell stack temperature quite slowly. A typical thermal response of a SOFC (Solid Oxide Fuel Cell), usually operating at high temperatures (Par.1.2.1.1) can be seen in Figure 3.2, taken from Menon et al. (2012). In this figure, the temperature taken at different positions and under two different boundary conditions is shown. The response here plotted is the typical temperature response given by a step current change at about 4800 seconds.

In fuel cells, second order dynamics occurs rarely, since the transient phenomena involved in fuel cells prevent the system response from showing second order dynamics in the conventional way.

One of the main transient phenomena occurring in fuel cells are overshoots and undershoots always clearly visible in the voltage vs. current plots, as can be seen in Figure 3.3. In this figure, the cathode activation losses (Par.1.3.1.1) versus time are plotted using two different boundary conditions for a SFOC model.

As can be seen in Figure 3.3, in response to an increase in current density, the activation voltage changes abruptly, and behaves similarly to a first order dynamics, but showing also an undershoot. The shape of the curve after the step current variation is similar to a first order dynamics, in fact, but it is reversed.

This kind of response is typical of fuel cells. Several factors affect their transient response. In particular, dealing with PEM fuel cells, the three main phenomena involved in this particular behavior are:

- Transient phenomena related to the fluid flow and its properties inside the stack.

- Transient phenomena related to the low Gas Diffusion Layer (GDL) permeability.
- Transient phenomena related to the PEM membrane hydration.
- Transient phenomena related to the electro-chemistry and electrostatic properties.

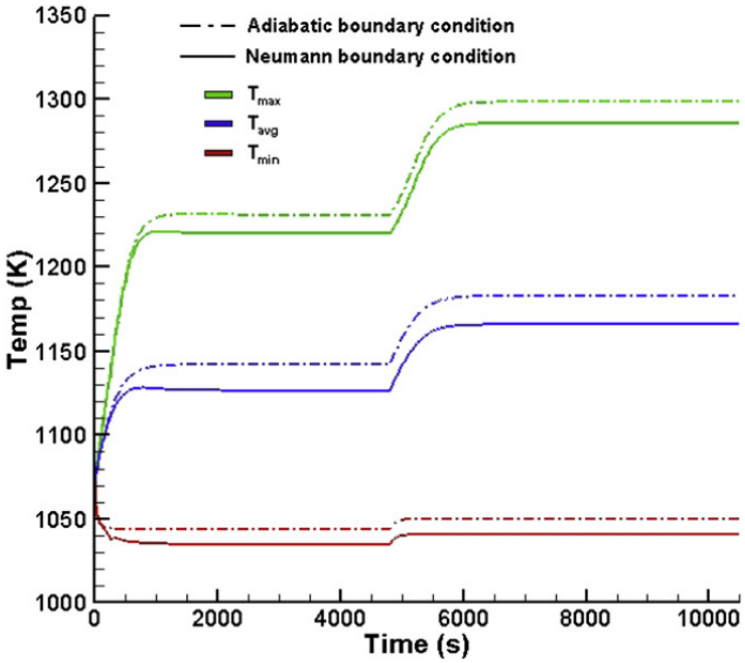

Figure 3.2 SOFC thermal response under a step current density variation. Different boundary conditions and temperatures are shown.

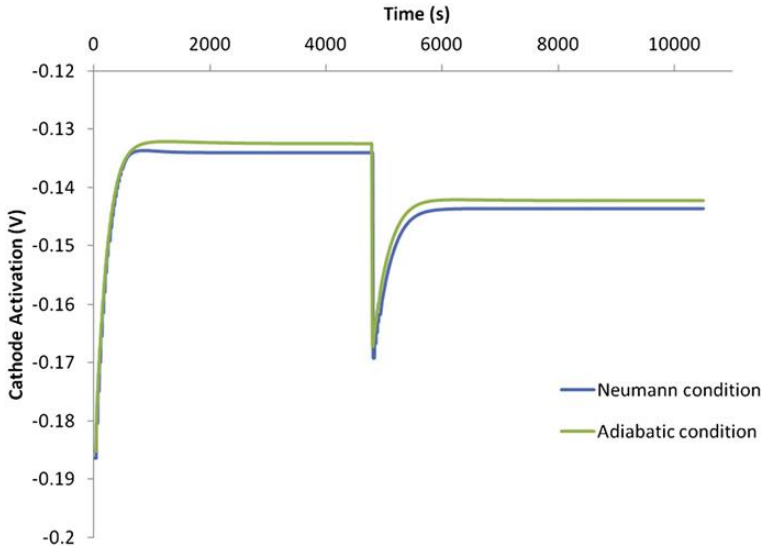

Figure 3.3 Fuel cell stack activation voltage vs. time in response of a step current change

The transient phenomena just listed have different characteristic times. In particular, the transient phenomena related to the electrochemistry are in the order of some milliseconds (Par. 3.3.1.3, double-layer effects), while the other three aspects show a transient curve lasting for some seconds.

Transient phenomena could be of importance and must be taken into account for the logic controlling the system performance and operation, especially in case of applications where rapid changes in the operating point might occur frequently (as in the case of the automotive industry).

The time constant related to the first point, namely the fluid flow transient, depends strongly on the channel length and geometry, as well as in the ancillary equipment responsible for the fuel cell stack feeding (e.g. air pumps, humidifiers, filters etc.). The time constant related to the GDL permeability depends on its thickness and permeability to gases and liquid water, in the form:

$$\tau_{GDL} \propto \frac{t_{GDL}}{D_{GDL}} \tag{3.1}$$

Where τ_{GDL} is the GDL time constant (s), t_{GDL} is its thickness (m) and D_{GDL} is its diffusivity (m^2). In the literature, the GDL permeability, diffusivity, porosity and effects on the fuel cells behavior is widely documented and can be considered one of the main areas of interest. GDL studies are complicated by the inhomogeneous microstructure and properties of this important element contained inside the stack. Typical GDL time constants can be considered in the range 0.1 – 1.0 seconds (Wang 2004).

Transient phenomena related to the PEM membrane hydration are the most important ones in modeling fuel cells, since their value is quite high, in the order of some seconds or tenths of seconds. The average time constant of this aspect can be roughly estimated using the formula:

$$\tau_{mem} \sim \frac{\frac{\rho_{mem}}{\mathcal{M}_{mem}} t_{mem} \Delta\lambda_{mem}}{i/2F} \tag{3.2}$$

Where ρ_{mem} is the membrane dry density (1000 kg m^{-3}), $\mathcal{M}_{mem}$ is the membrane equivalent weight (1.1 kg mol^{-1}) and $\Delta\lambda_{mem}$ is the variation in the membrane humidification (Par.3.3.1.4, dimensionless). Using a value of about 100 μm, a variation of 10 in the membrane humidification and about 1 A cm^{-2} of current density, the resulting time constant is of about 18 seconds.

All the aspects just introduced show the importance of a correct modeling of transient phenomena, which will be used as an indication of the goodness of results of fuel cells models.

Notes on the modelling of GDL gaseous species transport

One of the most difficult elements to be modelled in fuel cells is the gas diffusion layer. This layer has some peculiar characteristics. First, its structure is porous. This determines the necessity to take into account this aspect when considering the diffusion of species inside its pores. The non-homogeneous microstructure of the pores, moreover, might complicate a correct modeling. The other main problem arising with GDL modeling is the presence of both gaseous and liquid species. Gaseous species, on the other hand, are never present separately inside the GDL, but at least two gaseous species can be identified, namely hydrogen and vapor on the anode side and oxygen, nitrogen and vapor on the cathode side. The presence of liquid water combined with the porous structures of the GDL further complicates everything.

One of the main issues in modeling the GDL diffusion comes from the fact that the diffusivity of species varies with not only temperature, but it is also influenced by all of the other species. This brings to the so-called binary diffusion coefficients relating the diffusivity of two species.

Several studies, anyway, can be found about the GDL modeling. In particular, Ceraolo et al. (2003), Adzakpa et al. (2008) and Verhaert et al. (2011) can be considered the main reference works about

this topic. In all of these works, three gas species are considered and their related differential equations expressing the molar concentration of them along the GDL depth were obtained and implemented numerically, consisting in a system of three interdependent differential equations. Given the nature of these equations, the method adopted for the numerical solution was based on a traditional Finite Element Method (FEM) or a Galerkin method, given the presence of both diffusion and convection phenomena. The use of finite element methods forced the use of very small time-steps in order to prevent numerical problems or instabilities. These time-steps must satisfy the CFL condition, imposing to have time-steps inversely proportional to the square of the discretized segment considered, and could be estimated in the order of $10^{-5} – 10^{-9}$ seconds. These values prohibit the use of a detailed and multi-species model for the GDL in the case of a complete fuel cell system. All of the works just cited, in fact, devoted their attention to the GDL only. For this reason, the GDL transient response was not directly modeled in this work. In the appendix (Par.A.2), a method for obtaining a detailed solution of the GDL is given. The simulation times required to have convergence were in the order of 10^{-7} seconds for a standard GDL thickness divided into 30 segments.

3.1.2 Notes on models implementing the cathode and anode outlet orifice

One of the most diffused models used for the description of a PEM fuel cell stack is the one given by Pukrushpan et al. (2004). This model was widely adopted in the following years for many works (e.g. Bao et al. 2006, Sharifi 2010 and Pathapati 2004). The peculiarity of this model is its implementation of the stack outlet flow making use of an orifice model for calculating the outlet flow parameters (mass flow and temperature). The system modeled was the following:

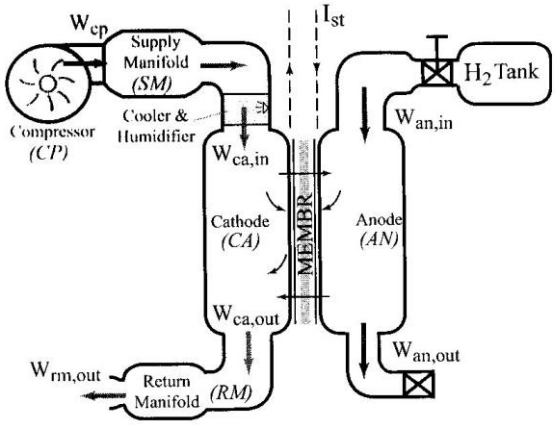

Figure 3.4 System layout modeled in Pukrushpan et al. (2004)

Using this model, it was possible to obtain directly the outlet conditions. The main problem consists in using the nozzle equations to obtain the mass flow at the anode and cathode sides. Using these equations, in fact, the mass flow is not related to the mass flow entering or present inside the stack, but it is only related to the pressure difference between the stack and the ambient conditions in the following form:

$$\dot{m}_{rm} = \begin{cases} \frac{C_{d,rm} A_{rm} p_{rm}}{\sqrt{R T_{rm}}} \left(\frac{p_{amb}}{p_{rm}}\right)^{\frac{1}{\gamma}} \left\{ \frac{2\gamma}{\gamma - 1} \left[1 - \left(\frac{p_{amb}}{p_{rm}}\right)^{\frac{\gamma-1}{\gamma}} \right] \right\}^{\frac{1}{2}}, & \frac{p_{amb}}{p_{rm}} > \left(\frac{2}{\gamma+1}\right)^{\frac{\gamma}{\gamma-1}} \\ \frac{C_{d,rm} A_{rm} p_{rm}}{\sqrt{R T_{rm}}} \sqrt{\gamma} \left(\frac{2}{\gamma+1}\right)^{\frac{\gamma+1}{2(\gamma-1)}}, & \frac{p_{amb}}{p_{rm}} \leq \left(\frac{2}{\gamma+1}\right)^{\frac{\gamma}{\gamma-1}} \end{cases} \quad (3.3)$$

Where the subscript *rm* refers to the return manifold and γ is equal to 1.4 for bi-atomic gases or mixtures. $C_{d,rm}$ is the nozzle discharge coefficient, and was considered constant over time. The variation in the stack gases content is also calculated, as if the gases inside the stack could accumulate arbitrarily. In the real case, however, the velocities and pressures inside the stack are not sufficiently high to generate gas compression at an appreciable level. In this way, the outlet mass flow decouples from the inlet mass flow. Using the just mentioned approach, it is even possible to have, in some circumstances and apart from the temporary accumulation of gas inside the stack, an outlet flow higher than the inlet one. This is, obviously, a non-physical behavior.

Another non-physical behavior of this model consists in the calculation of the outlet pressure of the stack in the following way, where the perfect gas law is used:

$$\frac{dp}{dt} = \frac{RT}{V} (\dot{m}_{in} - \dot{m}_{out}) \quad (3.4)$$

In this way, the accumulation of gases causes an increment in the pressure of the reactants. Also in this case, for some particular conditions, the pressure inside the stack was higher than the supply manifold pressure, since the pressure inside the stack was decoupled by the supply manifold. In presence of a mass flow, the ideal gas law alone cannot be used to determine the pressure of a closed volume, since the volume is no longer closed. Moreover, an important aspect not taken into account by this model is the pressure drop given by friction and viscous forces. This latter aspect is more relevant than the pressure variations induced by mass accumulation. Moreover, it is the pressure drop only which acts on the compressor operation, since the compressor is used to pressurize the gas flow to win the viscous drops inside the stack, mainly.

This model was verified implementing the Pukrushpan model in Simulink. Both the entire system model and the stack model were tested. The system was tested imposing a constant current value (0.6 A cm^{-2}). The desired compressor anode and cathode inlet pressures were set to 2.0 bar. The cathode mass flow was set at 0.005 kg s^{-1}. As can be seen from Figure 3.5, where the anode and cathode pressures are given, their values inside the stack are higher than the inlet conditions, given by the fact of having a total mass flow (gases and liquid water) higher at the inlet if compared to the outlet during the transient phase.

Using this approach, the pressure and inside the stack and the mass flows made this model not reliable for a complete system model.

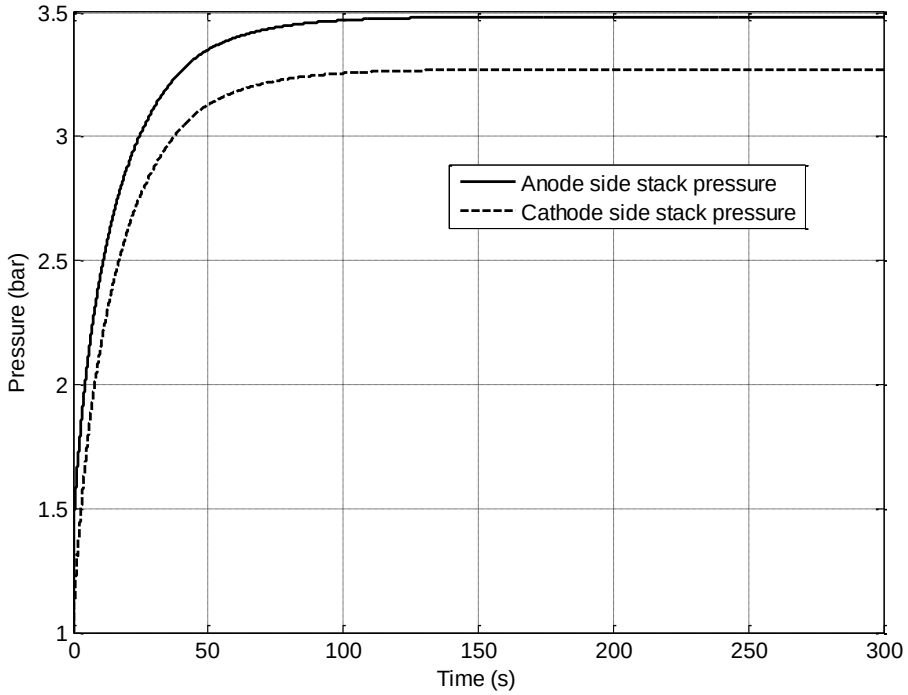

Figure 3.5 Anode and cathode side stack pressure used in the orifice model

3.2 Typical system layout

Given the wide power output ranges offered by the PEM technology, ranging from few watts to several tents of kilowatts, the typical system layout of a PEM fuel cell stack can vary widely. For few hundreds of watt and up to some kilowatts of output power, it should be sufficient to use air as a cooling medium, and in some cases the air flow used to supply oxygen to the cathode side might also be used as a cooling medium. Also the water and humidification management can differ widely. For small-sized fuel cells, it is possible to use only the water coming from the chemical reaction at the cathode side without any external humidification requirement. This last consideration can be valid for both the anode and cathode sides. When the power output rises, on the other hand, the system starts in growing its complexity. In the worst scenario, a liquid water loop for cooling of the stack, two humidifiers and intercoolers, as well as compressors, might be required. The model layout used as reference in this work will be more similar to this last one system layout (Figure 4.23). A typical system layout for a medium or high power fuel cell stack is shown in Figure 3.6.

3.3 Model description

This and the following paragraphs are devoted to the main core of the thesis, consisting in the development of the fuel cell stack and fuel cell stack system. The sub-division into paragraphs reflects the sub-division of the implemented model as it is in Simulink environment.

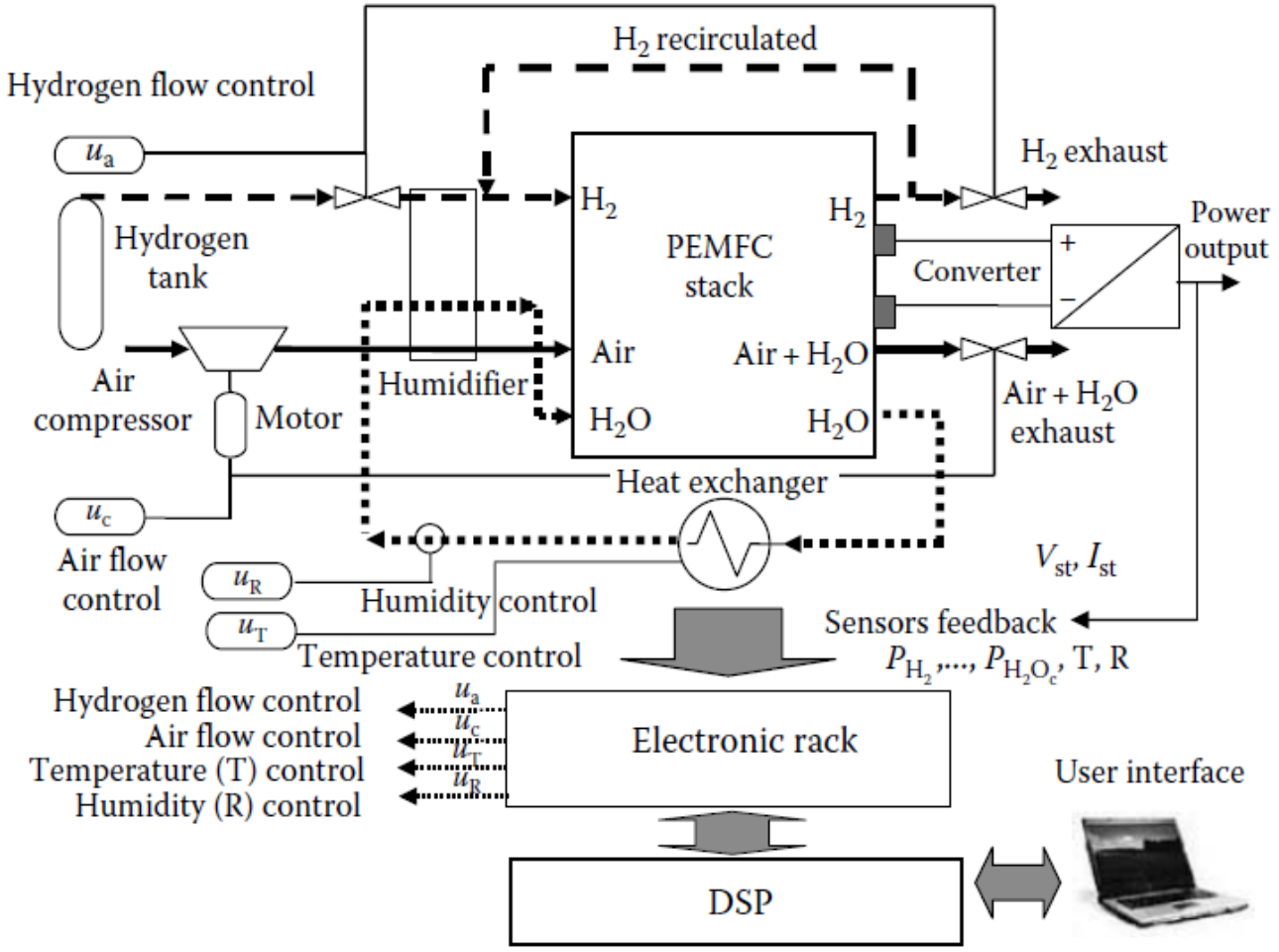

Figure 3.6 Typical PEM fuel cell stack system layout for a medium-high power stack

3.3.1 Fuel cell stack

The PEM fuel cell stack can be considered the main and most complex block of the entire Simulink model. The stack is made of three sub-blocks (Figure 3.7). The main sub-block is shown in orange in Figure 3.7, and comprises all the fluidic and thermal models of the stack. The red block, instead, comprises the membrane humidification model, while the green one contains the electrochemical model, and it is named "Voltage model". All of these three blocks share data at the same time during the simulation and give output data to other parts of the entire system.

The *stack* block contains the *stack flux* block, the *voltage model* block and the *membrane hydration* block. The only function contained in this block is the computation of the stack temperature obtained as:

$$m_{stack} c_{p_{stack}} \frac{dT_{stack}}{dt} = P_{tot} - P_{el} - \dot{Q}_{loss} - \dot{Q}_{sens} - \dot{Q}_{latent} \tag{3.5}$$

Where m_{stack} is the stack mass (in kg), $c_{p_{stack}}$ is the stack thermal capacity (in J kg^{-1} K^{-1}).

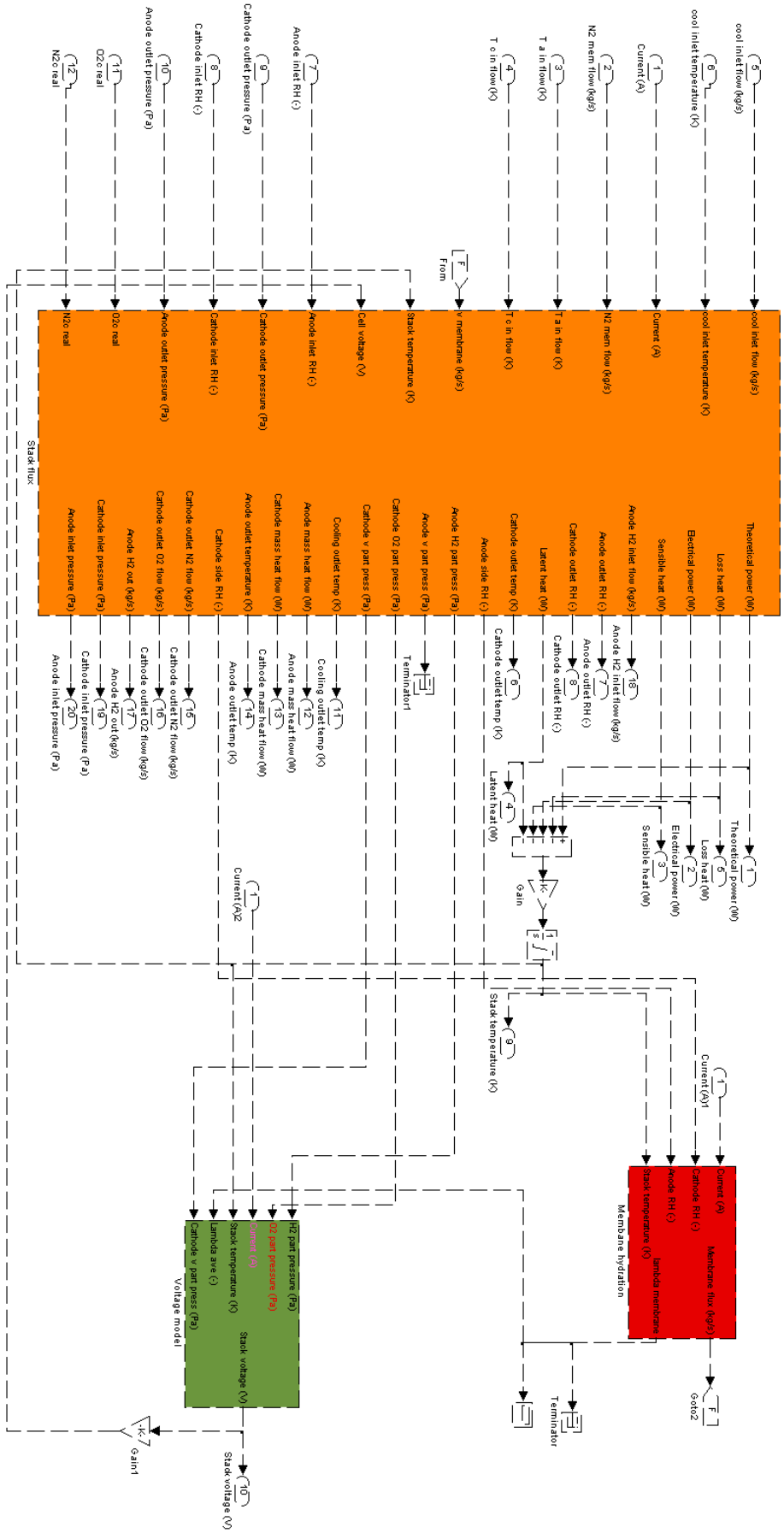

Figure 3.7 Overall PEM fuel cell stack Simulink blocks

The stack flux block is the main and most complex block of the entire system. The following tree shows its main sub-blocks from which it is made:

STACK FLUX BLOCK

- Cooling sensible heat block
- Anode side block
    - Main anode block
        - Anode inlet flux block
            - Electrochem. Reaction block
        - Anode outlet flux block
            - Liquid water accumulation block
    - Anode latent heat block
- Cathode side block
    - Main cathode block
        - Liquid water accumulation block
    - Cathode latent heat block
- Anode mass heat transfer block
- Cathode mass heat transfer block
- Pressure delay block

The *cooling sensible heat* block, the *anode/cathode latent heat* blocks and the *anode/cathode mass heat transfer* blocks are all related to thermal aspects and will be considered together in the following. The *anode side* block and the *cathode side* blocks share some common equations and model assumptions. In the following of this paragraph, the different blocks and their content will be analyzed, but without following the above presented list order to make the explanation of the model more clear.

Electrochemical reaction block

This block simply contains the relation between the electric current demanded to the stack and the consumption of hydrogen and oxygen in terms of mass flow (kg s^{-1}) as well as the production of water. For simplicity, it is assumed the current is all generated by the exact amount of reactants, without considering reactants side reactions or leakage. The reactants consumption is simply given by:

$$H_{2_{react}} = n_c \frac{I}{2F} \mathcal{M}_{H_2} \tag{3.6}$$

$$O_{2_{react}} = n_c \frac{I}{4F} \mathcal{M}_{O_2} \tag{3.7}$$

$$H_2O_{react} = n_c \frac{I}{2F} \mathcal{M}_{H_2O} \tag{3.8}$$

Where $\mathcal{M}$ is the molar mass of the three species expressed in kg mol^{-1}. The by-product water is called *react* for simplicity, even if it is not a reactant but a product. The three terms given in Eq.(3.65) - (3.67) are expressed in kg s^{-1}. All of the quantities expressed in the models are always defined in this manner.

Anode inlet flux block

The anode inlet flux block computes the inlet quantities together with relative humidity and other parameters. Starting from the previous block, the inlet hydrogen (and oxygen) are computed as:

$$H_{2_{a,in}} = \lambda_a H_{2_{react}} \tag{3.9}$$

$$O_{2_{c,in}} = \lambda_c O_{2_{react}} \tag{3.10}$$

Where the term λ denotes the so-called flow stoichiometry, not to be confounded with the membrane humidity (λ_{mem}). The stoichiometry defines the surplus of reactants entering the cell, given a particular current demand. For instance, a stoichiometry value λ_a = 1.6 means the inlet flow of hydrogen is 1.6 times the hydrogen it will react in the stack. Typical values for commercial fuel cells range from 1.4 to 2.5. Usually, the control logic of the stack maintains the stoichiometry value constant, unless very low current generation is demanded. In this case, the stoichiometry rises to a given pre-determined minimum amount of reactants flow. This aspect is implemented in this model with the definition of an *if* function which controls at each time step if the flow computed with Eq.(3.65) - (3.67) is above a minimum value set as a boundary condition (defined with the terms $O_{2_{flow_{min}}}$ and $H_{2_{flow_{min}}}$). If this condition is not met, the model overrides the imposed stoichiometry to guarantee the minimum flow feed.

Inside this block, there is also the computation of the nitrogen inlet flow. The model is able to simulate both air and pure oxygen fuel cells. This can be done simply setting the variable $N_{2_{mole_{ratio}}}$ in the initialization file. In case of pure oxygen cells, this value must be set to zero. In case of air fuel cell, this value can be set to 0.79. The inlet nitrogen is given by:

$$N_{2_{c,in}} = \frac{N_{2_{mole_{ratio}}}}{1 - N_{2_{mole_{ratio}}}} \frac{\mathcal{M}_{N_2}}{\mathcal{M}_{O_2}} O_{2_{in}} \tag{3.11}$$

The electrical output power is simply given by:

$$P_{el} = n_c V_c I \tag{3.12}$$

The total, theoretical power given by the hydrogen oxidation reaction is given by the change in enthalpy:

$$P_{tot} = -\frac{\Delta h_{reaction}}{\mathcal{M}_{H_2}} H_{2_{react}} = -\frac{h_{H_2O} - h_{H_2} - \frac{1}{2} h_{O_2}}{\mathcal{M}_{H_2}} H_{2_{react}} \tag{3.13}$$

This model is also able to consider the presence of nitrogen at the hydrogen side. This can occur in some kinds of fuel cells fed by air at the cathode side, where nitrogen represents the 78% of the gas mixture from a molar basis. In case of fuel cell systems with recirculation at the anode side, it is possible to reach important amount of nitrogen traces at the anode side due to the crossover of nitrogen through the membrane, despite its very low permeability to gas molecules. This

phenomenon is called nitrogen build-up and it is scarcely documented in literature (as in Ahluwalia and Wang 2007), but it is the cause of periodic hydrogen channels venting with pure hydrogen to remove the accumulated nitrogen, representing an extra consumption of hydrogen.

The presence of nitrogen in the anode stream is managed by the variable y_{H_2}, defined at the stack inlet, meaning the mass percentage of hydrogen. To neglect nitrogen presence, it is sufficient to set a value equal to 1.0.

The inlet block is responsible also of computing the water presence at inlet both in gaseous and liquid form. Given the inlet relative humidity ($\phi_{a_{in}}$), the amount of liquid and gaseous water are based on the inlet temperature of the hydrogen. The maximum admissible vapor mass flow at inlet (above which condensation occurs due to relative humidity equal to one) can be calculated as:

$$H_2O_{v_{a,in,max}} = \left(\frac{H_{2_{a,in}}}{\mathcal{M}_{H_2}} + \frac{N_{2_{a,in}}}{\mathcal{M}_{N_2}}\right) \frac{p_{sat}(T_{a,in})}{p_{a,in} - p_{sat}(T_{a,in})} \mathcal{M}_{H_2O} \tag{3.14}$$

Where p_{sat} is the saturation pressure given by Eq.(2.15), and it is function of temperature. In this case, the inlet gas temperature at the anode side is considered. The term $p_{a,in}$ is the inlet pressure at anode side of the entire gas mixture.

In this model, it is considered not only the presence of gaseous water, but also the presence of liquid water. Liquid water is assumed to be transported efficiently through the gas piping of the system. For this reason, the water presence is not given only by the humidity of the inlet gases but also by the possible presence of liquid droplets. A conditional control is then formulated:

If $H_2O_{tot,a,in} \geq H_2O_{v_{a,in,max}}$ then:

$$H_2O_{v_{a,in}} = H_2O_{v_{a,in,max}} \tag{3.15}$$

$$H_2O_{l_{a,in}} = H_2O_{tot,a,in} - H_2O_{v_{a,in}} \tag{3.16}$$

Else:

$$H_2O_{v_{a,in}} = \left(\frac{H_{2_{a,in}}}{\mathcal{M}_{H_2}} + \frac{N_{2_{a,in}}}{\mathcal{M}_{N_2}}\right) \frac{p_{sat}(T_{a,in})\phi_{a,in}}{p_{a,in} - p_{sat}(T_{a,in})\phi_{a,in}} \mathcal{M}_{H_2O} \tag{3.17}$$

$$H_2O_{l_{a,in}} = 0 \tag{3.18}$$

Where the term $H_2O_{tot,a,in}$ is the total amount of water flow (sum of liquid and vapor) entering the cell. The two terms $H_2O_{v_{a,in}}$ and $H_2O_{l_{a,in}}$ are the mass flows of water vapor and liquid water, respectively. The term $H_2O_{tot,a,in}$ is calculated in the same manner of Eq.(3.17), but related to the previous time step of the simulation.

The *anode inlet flux* block is shown in Figure 3.8.

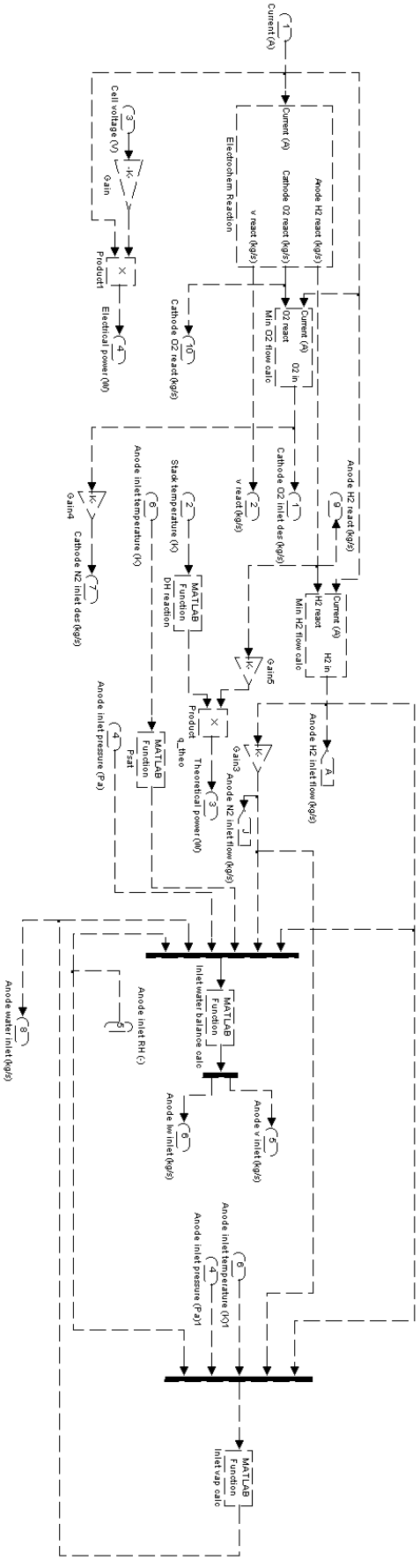

Figure 3.8 *Anode inlet flux* block diagram

Anode outlet flux block

The *anode outlet flux* block computes the stack station and outlet station for the fluidic path of the hydrogen channel. This block is quite complex in its model.

It is assumed the outlet values for the reactants are simply given by the difference between the inlet values and the reacted values. Hydrogen and oxygen crossover through the membrane are neglected. From a practical point of view, there is no possibility of gas accumulation over time, in opposition to the strategy analyzed in Par.3.1.2, where physical discrepancies were easily underlined.

The hydrogen mass flow outlet is given by:

$$H_{2_{a,out}} = H_{2_{a,in}} - H_{2_{react}} \tag{3.19}$$

The intermediate values, i.e. the *stack* values, are computed, for simplicity, using the average values between the inlet and outlet values. In this way, the internal (stack) relative humidity is defined as:

$$\phi_{a,ave} = \max\left[0.0;\ \left(\frac{\frac{H_2O_{v_{a,ave}}}{\mathcal{M}_{H_2O}}}{\frac{H_{2_{a,ave}}}{\mathcal{M}_{H_2}} + \frac{N_{2_{a,ave}}}{\mathcal{M}_{N_2}} + \frac{H_2O_{v_{a,ave}}}{\mathcal{M}_{H_2O}}}\right)\frac{p_{a,ave}}{p_{sat}(T_{a,ave})}\right] \tag{3.20}$$

The average quantities are calculated, as already said, as the average between the inlet and outlet values. These last ones will be introduced later on this paragraph. Given the very low content of nitrogen, the value for $N_{2_{a,ave}}$ is supposed equal to the $N_{2_{a,in}}$ one. The presence of the imposed minimum value of 0.0 is due, also in this case, to prevent numerical errors. The outlet nitrogen mass flow is given taking into account its transport through the membrane, if nitrogen presence and crossover is considered in the simulations, in the form:

$$N_{2_{a,out}} = N_{2_{a,in}} + N_{2_{mem}} \tag{3.21}$$

Where the nitrogen crossover mass flow ($N_{2_{mem}}$), expressed in kg s^{-1}, is assumed positive in the oxygen to hydrogen direction.

The outlet relative humidity is given in the same manner of Eq.(3.20), substituting the outlet quantities to the average ones:

$$\phi_{a,out} = \max\left[0.0;\ \left(\frac{\frac{H_2O_{v_{a,out}}}{\mathcal{M}_{H_2O}}}{\frac{H_{2_{a,out}}}{\mathcal{M}_{H_2}} + \frac{N_{2_{a,out}}}{\mathcal{M}_{N_2}} + \frac{H_2O_{v_{a,out}}}{\mathcal{M}_{H_2O}}}\right)\frac{p_{a,out}}{p_{sat}(T_{a,out})}\right] \tag{3.22}$$

The outlet value for the water vapor requires a different approach from the one adopted for the hydrogen in Eq.(3.19). Since three different temperatures are used in the model, namely the inlet, stack and outlet stations, possible phase change can occur. The maximum water vapor admissible at the stack station is given when relative humidity reaches unity. In this case its value is:

$$H_2O_{v_{a,out,max}} = \left(\frac{H_{2_{a,out}}}{\mathcal{M}_{H_2}} + \frac{N_{2_{a,out}}}{\mathcal{M}_{N_2}}\right)\frac{p_{sat}(T_{a,out})}{p_{a,out} - p_{sat}(T_{a,out})}\mathcal{M}_{H_2O} \tag{3.23}$$

A conditional execution is then performed:

If $\left[(H_2O_{tot,a,in} - H_2O_{mem}) \geq H_2O_{v_{a,out,max}}\right]$ then:

$$H_2O_{v_{a,out}} = H_2O_{v_{a,out,max}} \tag{3.24}$$

$$H_2O_{l_{a.out}} = H_2O_{tot,a,in} - H_2O_{mem} - H_2O_{v_{a,out}} \tag{3.25}$$

Else:

$$H_2O_{v_{a,out}} = H_2O_{tot,a,in} - H_2O_{mem} \tag{3.26}$$

$$H_2O_{l_{a.out}} = 0.0 \tag{3.27}$$

In the case of $(H_2O_{tot,a,in} - H_2O_{mem}) \leq 0$, this means that all of the water entering the anode side is transported through the membrane to the cathode side. In this case, the software implemented forces the value of $H_2O_{v_{a,out}}$ to zero, since it should assume a negative value from Eq.(3.26). The membrane water flow here introduced (H_2O_{mem}) is calculated from the *membrane hydration* block, and will be modelled in Par.3.3.1.4. This value is assumed positive when the flow moves from anode to cathode side.

Two more functions are calculated within the *anode outlet flux* block. The first one is the calculation of the hydrogen side sensible heat produced. The formula is implemented as:

$$\begin{aligned}\dot{Q}_{sens_a} = {} & H_{2_{a,out}} c_{p_{H_2}} (T_{a,out} - T_0) + H_2O_{v_{a,out}} c_{p_{H_2O_v}} (T_{a,out} - T_0) \\ & + N_{2_{a,out}} c_{p_{N_2}} (T_{a,out} - T_0) + H_2O_{l_{a,out}} c_{p_{H_2O_l}} (T_{a,out} - T_0) \\ & - H_2O_{l_{a,in}} c_{p_{H_2O_l}} (T_{a,in} - T_0) - H_2O_{v_{a,in}} c_{p_{H_2O_v}} (T_{a,in} - T_0) \\ & - H_{2_{a,in}} c_{p_{H_2}} (T_{a,in} - T_0) - N_{2_{a,in}} c_{p_{N_2}} (T_{a,in} - T_0)\end{aligned} \tag{3.28}$$

The sensible heat is in this case measured in W. The T_0 value is the reference temperature (298.15 K).

The second and last aspect contained in this block is a "delay" block used to simulate the transient behavior of the fluid flow path. Despite this aspect is not one of the slowest transients, some seconds of delay between the change in the inlet data and the corresponding change in the outlet data might occur. The delay block has also the very important function to avoid the presence of algebraic loops inside the model. Algebraic loops are defined in the Simulink guide as:

"An algebraic loop in a Simulink model occurs when an input port depends on the output. Typically, algebraic loops occur by direct feedthrough, within the block or through a feedback path through other blocks with direct feedthrough. Some Simulink blocks have input ports with direct feedthrough. These blocks can cause algebraic loops in your model. The software cannot compute the output of these blocks without knowing the values of the signals entering the blocks at these input ports. Some examples of blocks with direct feedthrough inputs are m*ath function* block, *gain* block, *integrator* block, when the initial condition port depends on the block output, *product* block, *state-space* block, when the D matrix coefficient is nonzero, *sum* block, *transfer fcn* block, when the numerator and denominator are of the same order, *zero-pole* block, when the block has as many zeros as poles. An example of an algebraic loop is the following simple scalar loop:

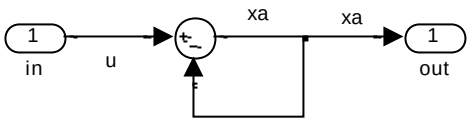

Figure 3.9 Example of algebraic loop

Mathematically, this loop implies that the output of the *sum* block is an algebraic state *xa* that is constrained to equal the first input *u* minus *xa* (for example, *xa = u – xa*). The solution of this simple loop is *xa = u/2* [...]". Theoretically, algebraic loops could be considered as differential algebraic equations. "Simulink solves the algebraic equations (the algebraic loop) numerically for *xa* at each step of the solver [...]. Algebraic loops occur when modelling physical systems, often due to the conservation laws of mass and energy. You can also use algebraic constraints to impose design constraints on system responses in a dynamic system. Choosing a particular coordinate system for a model can also result in an algebraic constraint. In most cases, you can eliminate algebraic loops [...] to produce an ordinary differential equation. However, this technique is not always practical".

The delay block implemented in this model is placed in series to the exit of the outlet gaseous water ($H_2O_{v_{a,out}}$). This block avoid the generation of an algebraic loop, since the delay block contains an integrator. The delay block, moreover, simulates the transient response of the fluidic line, as it is in the real case. In this manner, the delay block does not interfere with the real physics of the fuel cell, representing a real phenomena. The delay block is implemented in Simulink as:

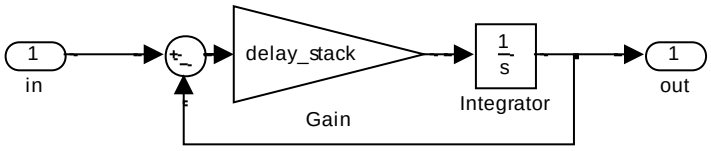

Figure 3.10 Delay block in Simulink

This model simply represents a first order model. The *delay_stack* gain helps in controlling the time constant of the transient. The delay block behavior is shown in Figure 3.12. The starting value of the simulations is given equal to 0.0, with the goal value of 1.0.

One of the most important assumptions of the fuel cell model is the fact that the liquid water formation inside the fuel cell is actively transported out of the stack. This assumption is strong, since liquid water accumulation might influence the performance of the cell. However, given the mono-dimensionality of the model, the modeling of liquid water accumulation in certain points of the stack becomes not practical.

To partially consider liquid water accumulation, an anode and cathode liquid removal percentage is defined. In this way, the liquid water calculated at the outlet station ($H_2O_{l_{a.out}}$) is multiplied by this factor, and this quantity is the liquid water effectively exiting from the stack. The remaining liquid water, instead, will accumulate inside the cell and will sum to the liquid water remaining quantity defined in the following paragraph. Figure 3.11 shows the outlet portion of the *Anode outlet flux* block, depicting the liquid water accumulation model.

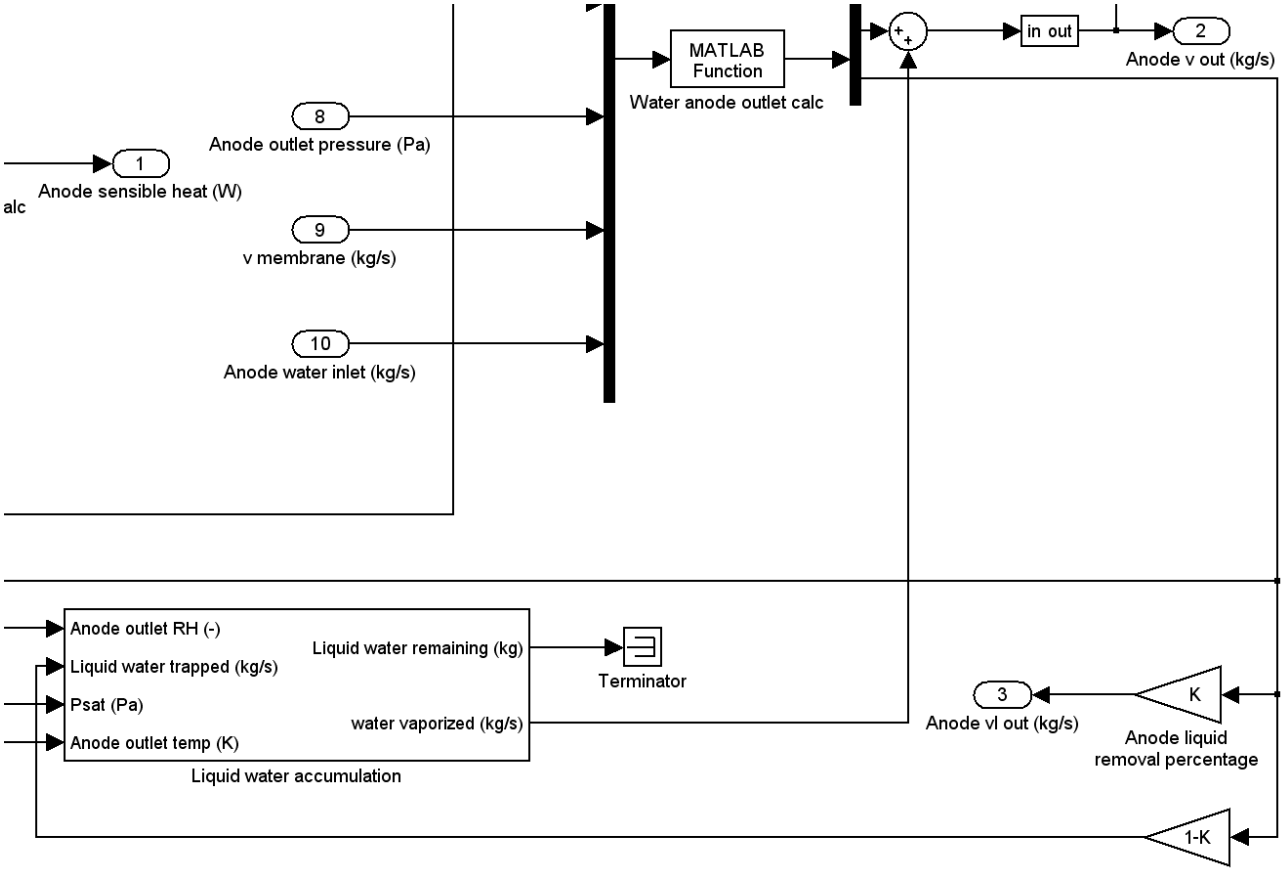

Figure 3.11 Liquid water accumulation and removal portion

Main anode block

This block simply puts together all of the blocks listed below it. It does not contain model equations.

Anode latent heat block

The anode latent heat block computes the heat (in W) related to the phase change of water. It simply operates computing the difference between the inlet and outlet vapor mass flow and taking into account the transport of water through the membrane. It is defined as:

$$\dot{Q}_{latent,a} = \left(H_2O_{v_{a,out}} - H_2O_{v_{a,in}} - H_2O_{mem}\right)\Delta H_{vap} \tag{3.29}$$

The latent heat is considered negative when heat is absorbed by water evaporation. The heat of vaporization (in J kg^{-1}) is modeled as temperature dependent as (Yu et al. 2005):

$$\begin{aligned}\Delta H_{vap} = \frac{1}{\mathcal{M}_{H_2O}}[&45070 - 41.9(T_{stack} - 273.15) + 3.44 \\ &\times 10^{-3}(T_{stack} - 273.15)^2 + 2.54 \times 10^{-6}(T - 273.15)^3 - 8.98 \\ &\times 10^{-10}(T_{stack} - 273.15)^4]\end{aligned} \tag{3.30}$$

The heat of vaporization is here calculated at the intermediate, stack station.

Anode side block

This block contains the *main anode* and the *anode latent heat* blocks, plus few other model equations used to interface the anode side to the cathode and other ones. The anode outlet temperature is calculated as a separated quantity with respect to the stack temperature. The anode outlet temperature refers to the temperature of gases, while the stack temperature refers to the "solid" portion of the stack. The anode outlet gas temperature is here defined as a sort of heat exchanger in the way:

$$T_{a,out} = T_{a,in} + \left(T_{stack} - T_{a,in}\right)\left[1 - \exp\left(-\frac{hA_a}{\dot{m}c_p}\right)\right] \tag{3.31}$$

The term hA_a is the heat conductivity defined in W K^{-1}, and it is the product of the heat exchange area (A) and the thermal conductivity constant (h) given in W K^{-1} m^{-2}. This last value is dependent upon different quantities and it is difficult to determine exactly for a fuel cell stack. For this reason, the term hA_a is used as a tuning parameters to control the thermal behavior of the stack. The term $\dot{m}c_{p_a}$ is the product of the gas species mass flow and their specific heat, given by:

$$\dot{m}c_{p_a} = H_2O_{v\,a,in}c_{p_{H_2O_v}} + H_{2\,a,in}c_{p_{H_2}} + N_{2\,a,in}c_{p_{N_2}} \tag{3.32}$$

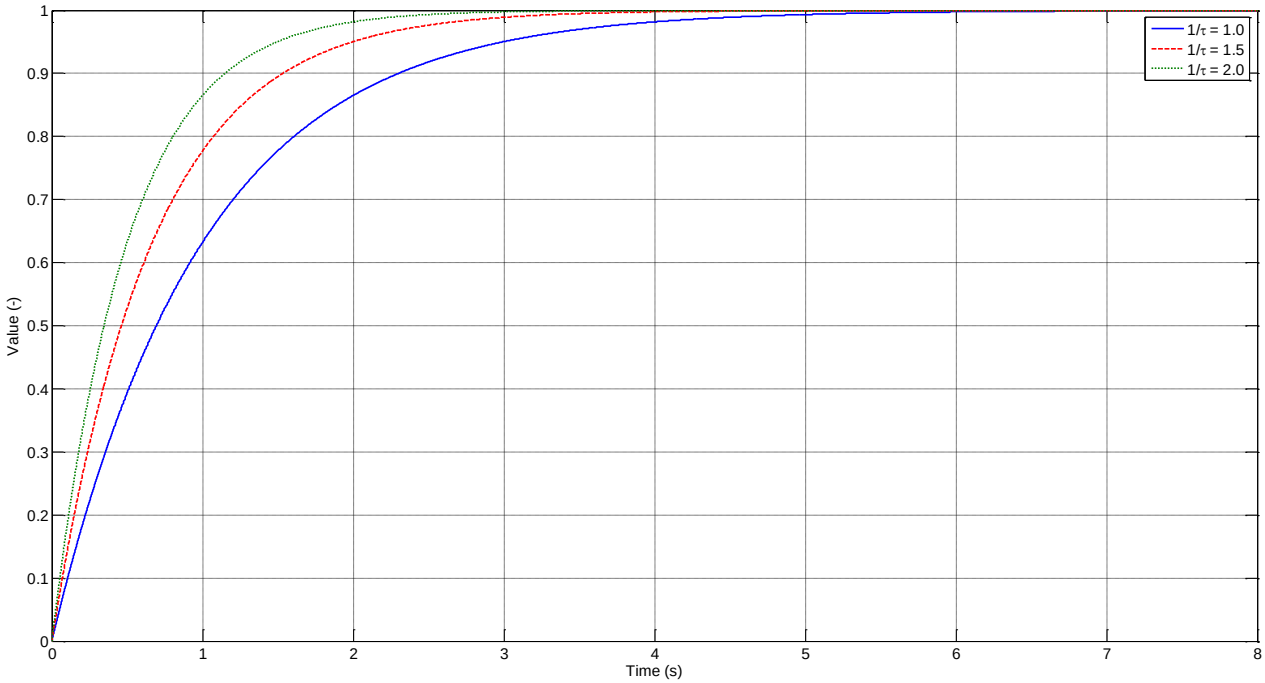

Figure 3.12 Delay block behavior

The *anode side* block gives also information about the gases partial pressures using the following equation:

$$p_x = p_{ave}\frac{\frac{X_{a,in}}{\mathcal{M}_X}}{\frac{H_{2\,a,in}}{\mathcal{M}_{H_2}} + \frac{N_{2\,a,in}}{\mathcal{M}_{N_2}} + \frac{H_2O_{v\,a,in}}{\mathcal{M}_{H_2O}}} \tag{3.33}$$

Where *X* represents the *x*-species. The partial pressures (given in Pa) are calculated at the inlet station for simplicity. Given the fact that the main mass of gases entering the stack is made of hydrogen (considering nitrogen will be present only in traces and that water vapor pressure is usually in the order of few thousands of Pascal), the error committed using these partial pressures also at the stack and outlet stations should be minimal. Moreover, the average pressure contains the average of the inlet and outlet station pressures. The average pressure (p_{ave}) is calculated at the level of the *stack flux* block, detailed later.

Liquid water accumulation block

This block takes into account the presence of liquid water within the fluid channels of the hydrogen side. In presence of liquid water and with relative humidity lower than unity, water passes from liquid to gaseous phase, reducing the amount of liquid water and rising the amount of vapor in the fluid stream and vice-versa. This block is modelled in Simulink with two *if* blocks:

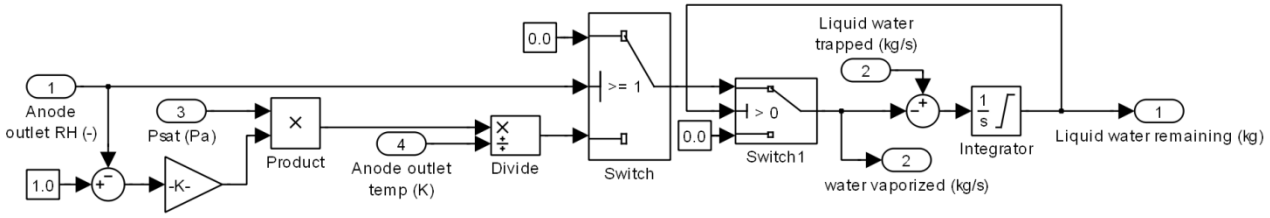

Figure 3.13 *Liquid water accumulation* block diagram

The first control is made on the presence of liquid water inside the anode channels. In case of liquid water presence, the second condition verifies the relative humidity value. For this block, it was chosen to use the outlet relative humidity value. If the relative humidity is equal to one, the quantity of water vapor produced is zero, since under this condition condensation takes place, and the amount of liquid water inside the anode side rises. In case of relative humidity lower than one, then evaporation occurs in the case of presence of liquid water remaining inside the channels.

The difference between the liquid water "trapped" and the water vaporized (given both in kg s^{-1}) is then integrated over time to obtain the mass of liquid water remaining (given in kg). The saturation condition present inside the *integrator* block is used to prevent negative values, in order to prevent numerical problems.

The amount of liquid water evaporating is defined as:

$$H_2O_{a,evap} = c_r \frac{(1-\phi_{a,out})Vol_a \mathcal{M}_{H_2O}}{T_{a,out}} p_{sat}(T_{a,out}) \tag{3.34}$$

Eq.(3.34) is the same used in fluid-dynamics models implemented for multi-phase flows, as in ANSYS (2011). The c_r quantity is the condensation/evaporation rate (equal to 100 s^{-1} in ANSYS 2011). *Vol* indicates the void space volume (in m^3) inside the fuel cell sides.

Anode mass heat transport block

This block computes the heat ($\dot{Q}_{mass,a}$) removed from the anode side due to the transport of mass from the anode to the cathode side or vice/versa. This heat is given by the mass transport of

three species: hydrogen consumption, water transport through the membrane and nitrogen crossover. This heat is given by:

$$\dot{Q}_{mass,a} = \left[H_2O_{mem} c_{p_{H_2O}} + \frac{H_{2_{a,in}}}{\lambda_a} c_{p_{H_2}} - N_{2_{mem}} c_{p_{N_2}} \right] (T_{stack} - T_0) \tag{3.35}$$

In addition, it is considered positive when removed from the anode side. The signs of the three terms depend on the convention adopted in this model (water membrane transport positive from anode to cathode and nitrogen crossover positive from cathode to anode). Since the transport or reaction of these species occur at the membrane/catalyst interface, it is assumed to use the temperature of the solid, i.e. the stack temperature, at which the membrane is exposed.

3.3.1.1 Cathode side block

This block contains all the other blocks belonging to the cathode side already described previously, and some few other functions.

The cathode outlet temperature ($T_{c,out}$) is calculated as:

$$T_{c,out} = T_{c,in} + \left(T_{stack} - T_{c,in}\right) \left[1 - \exp\left(-\frac{hA_c}{\dot{m} c_p} \right) \right] \tag{3.36}$$

The term hA_c is the heat conductivity defined in W K^{-1}, and it is the product of the heat exchange area (A) and the thermal conductivity constant (h) given in W K^{-1} m^{-2}. This last value is dependent upon different quantities and it is difficult to determine exactly for a fuel cell stack. For this reason, the term hA_c, together with the corresponding hA_a is used as a tuning parameters to control the thermal behavior of the stack. The term $\dot{m} c_{p_c}$ is the product of the gas species mass flow and their specific heat, given by:

$$\dot{m} c_{p_c} = H_2O_{v_{c,in}} c_{p_{H_2O_v}} + O_{2_{c,in}} c_{p_{O_2}} + N_{2_{c,in}} c_{p_{N_2}} \tag{3.37}$$

The complete sensible heat transported from the fluid flow passing through the stack is computed as the sum of the sensible heats associated with the anode, cathode and cooling streams:

$$\dot{Q}_{sens} = \dot{Q}_{sens_a} + \dot{Q}_{sens_c} + \dot{Q}_{sens_{cool}} \tag{3.38}$$

The heat lost by the stack ($\dot{Q}_{loss}$) due to the thermal contact between the stack outer surfaces and the ambient air is simplified with a unique thermal conductivity coefficient (hA_{stack}), and it is modelled as:

$$\dot{Q}_{loss} = hA_{stack}(T_{stack} - T_{room}) \tag{3.39}$$

It is assumed the stack internal temperature used as the reference temperature of the membrane (T_{stack}) is the same of the outer surfaces for simplicity. T_{room} is the ambient temperature and it is considered constant. hA_{stack} can be considered as another tuning factor.

Main cathode block

The *main cathode* block contains all the most important model equations for the cathode side, and it collects the inlet, stack and outlet station variables in a unique block. Its layout in Simulink is given in Figure 3.14. The fact that for that anode side three species were considered, namely hydrogen, nitrogen and water, simplifies the cathode modeling, since also at this side three

species will be considered. Moreover, only oxygen and hydrogen species are substituted, making the cathode side model quite similar to the anode one. Nevertheless, the transport through the membrane is opposite, so particular attention must be paid for the signs. Also for the cathode side, three stations are identified: inlet, stack and outlet. Also in this case, the gases temperature is kept separate from the stack temperature. This last one, anyway, is assumed equal on both sides.

The inlet data (water vapor and liquid water) are computed in the same way given in Eqs. (3.14)-(3.18):

$$H_2O_{v_{c,in,max}} = \left(\frac{O_{2_{c,in}}}{\mathcal{M}_{O_2}} + \frac{N_{2_c,in}}{\mathcal{M}_{N_2}}\right)\frac{p_{sat}(T_{c,in})}{p_{c,in} - p_{sat}(T_{c,in})}\mathcal{M}_{H_2O} \tag{3.40}$$

In this model, it is considered not only the presence of gaseous water, but also the presence of liquid water. Liquid water is assumed to be transported efficiently through the gas piping of the system. For this reason, the water presence is not given only by the humidity of the inlet gases but also by the possible presence of liquid droplets. A conditional control is then formulated:

If $H_2O_{tot,c,in} \geq H_2O_{v_{c,in,max}}$ then:

$$H_2O_{v_{c,in}} = H_2O_{v_{c,in,max}} \tag{3.41}$$

$$H_2O_{l_{c,in}} = H_2O_{tot,c,in} - H_2O_{v_c,in} \tag{3.42}$$

Else:

$$H_2O_{v_{c,in}} = \left(\frac{O_{2_{c,in}}}{\mathcal{M}_{O_2}} + \frac{N_{2_c,in}}{\mathcal{M}_{N_2}}\right)\frac{p_{sat}(T_{c,in})\phi_{c,in}}{p_{c,in} - p_{sat}(T_{c,in})\phi_{c,in}}\mathcal{M}_{H_2O} \tag{3.43}$$

$$H_2O_{l_{c,in}} = 0 \tag{3.44}$$

Where the term $H_2O_{tot,c,in}$ is the total amount of water flow (sum of liquid and vapor) entering the cell. The two terms $H_2O_{v_{c,in}}$ and $H_2O_{l_{c,in}}$ are the mass flows of water vapor and liquid water, respectively. The term $H_2O_{tot,c,in}$ is calculated in the same manner of Eq.(3.43), but related to the previous time step of the simulation.

It is assumed the outlet values for the reactants are simply given by the difference between the inlet values and the reacted values as for the hydrogen side. Hydrogen and oxygen crossover through the membrane are neglected. From a practical point of view, there is no possibility of gas accumulation over time, in opposition to the strategy analyzed in Par.3.1.2, where physical discrepancies were easily underlined.

The oxygen mass flow outlet is given by:

$$O_{2_{c,out}} = O_{2_{c,in}} - O_{2_{react}} \tag{3.45}$$

The intermediate values, i.e. the *stack* values, are computed, for simplicity, using the average values between the inlet and outlet values also for the cathode side. In this way, the internal (stack) relative humidity is defined as:

$$\phi_{c,ave} = \max\left[0.0;\ \left(\frac{\frac{H_2O_{v_{c,ave}}}{\mathcal{M}_{H_2O}}}{\frac{O_{2_{c,ave}}}{\mathcal{M}_{O_2}} + \frac{N_{2_{c,ave}}}{\mathcal{M}_{N_2}} + \frac{H_2O_{v_{c,ave}}}{\mathcal{M}_{H_2O}}}\right)\frac{p_{c,ave}}{p_{sat}(T_{c,ave})}\right] \tag{3.46}$$

The average quantities are calculated, as already said, as the average between the inlet and outlet values. These last ones will be introduced later on this paragraph. The presence of the imposed minimum value of 0.0 is due, also in this case, to prevent numerical errors. The outlet nitrogen mass flow is given taking into account its transport through the membrane, if nitrogen presence and crossover is considered in the simulations, in the form:

$$N_{2_{c,out}} = N_{2_{c,in}} - N_{2_{mem}} \tag{3.47}$$

Where the nitrogen crossover mass flow ($N_{2_{mem}}$), expressed in kg s^{-1}, is assumed positive in the oxygen to hydrogen direction.

The outlet relative humidity is given in the same manner of Eq.(3.66), substituting the outlet quantities to the average ones:

$$\phi_{c,out} = \max\left[0.0;\ \left(\frac{\frac{H_2O_{v_{c,out}}}{\mathcal{M}_{H_2O}}}{\frac{O_{2_{c,out}}}{\mathcal{M}_{O_2}} + \frac{N_{2_{c,out}}}{\mathcal{M}_{N_2}} + \frac{H_2O_{v_{c,out}}}{\mathcal{M}_{H_2O}}}\right)\frac{p_{c,out}}{p_{sat}(T_{c,out})}\right] \tag{3.48}$$

The outlet value for the water vapor requires a different approach from the one adopted for the hydrogen. Since three different temperatures are used in the model, namely the inlet, stack and outlet stations, possible phase change can occur. The maximum water vapor possible at the stack station is given when relative humidity reaches unity. In this case its value is:

$$H_2O_{v_{c,out,max}} = \left(\frac{O_{2_{c,out}}}{\mathcal{M}_{O_2}} + \frac{N_{2_c,out}}{\mathcal{M}_{N_2}}\right)\frac{p_{sat}(T_{c,out})}{p_{c,out} - p_{sat}(T_{c,out})}\mathcal{M}_{H_2O} \tag{3.49}$$

A conditional execution is them performed:

If $\left[(H_2O_{tot,c,in} + H_2O_{mem} + H_2O_{react}) \geq H_2O_{v_{c,out,max}}\right]$ then:

$$H_2O_{v_{c,out}} = H_2O_{v_{c,out,max}} \tag{3.50}$$

$$H_2O_{l_{c.out}} = H_2O_{tot,c,in} + H_2O_{mem} - H_2O_{v_{c,out}} + H_2O_{react} \tag{3.51}$$

Else:

$$H_2O_{v_{c,out}} = H_2O + H_2O_{mem} + H_2O_{react} \tag{3.52}$$

$$H_2O_{l_{c.out}} = 0.0 \tag{3.53}$$

In the case of $(H_2O_{tot,c,in} - H_2O_{mem} + H_2O_{react}) \leq 0$, this means that all of the water entering the cathode side is transported through the membrane to the anode side by back diffusion. In this case, the software implemented forces the value of $H_2O_{v_{c,out}}$ to zero, since it should assume a negative value. The membrane water flow here introduced (H_2O_{mem}) is calculated from the *membrane*

hydration block, and will be modeled in Par.3.3.1.4. This value is assumed positive when the flow moves from anode to cathode side. The difference of these equations from the anode side ones consists only in the presence of the additional term H_2O_{react}, representing the by-product water. Another difference is the change of the sign of the H_2O_{mem} term.

Also for the cathode flux there is a delay block to avoid the algebraic loop presence and to simulate the internal fluid flow transient. The delay block here used is the same of the anode flow one, with the same time constant. Also in this case, the delay block is placed in series to the exit of the outlet station water vapor value ($H_2O_{v_{c,out}}$).

The cathode sensible heat is computed as follows:

$$\begin{aligned}\dot{Q}_{sens_c} = {} & O_{2_{c,out}} c_{p_{O_2}} (T_{c,out} - T_0) + H_2O_{v_{c,out}} c_{p_{H_2O_v}} (T_{c,out} - T_0) \\ & + N_{2_{c,out}} c_{p_{N_2}} (T_{c,out} - T_0) + H_2O_{l_{c,out}} c_{p_{H_2O_l}} (T_{c,out} - T_0) \\ & - H_2O_{l_{c,in}} c_{p_{H_2O_l}} (T_{c,in} - T_0) - H_2O_{v_{c,in}} c_{p_{H_2O_v}} (T_{c,in} - T_0) \\ & - O_{2_{c,in}} c_{p_{H_2}} (T_{c,in} - T_0) - N_{2_{c,in}} c_{p_{N_2}} (T_{c,in} - T_0)\end{aligned} \tag{3.54}$$

The partial pressures of the gases at the stack level are computed in the same manner of the anode side. In particular:

$$p_x = p_{ave} \frac{\frac{X_{c,in}}{\mathcal{M}_X}}{\frac{O_{2_{c,in}}}{\mathcal{M}_{O_2}} + \frac{N_{2_{c,in}}}{\mathcal{M}_{N_2}} + \frac{H_2O_{v_{c,in}}}{\mathcal{M}_{H_2O}}} \tag{3.55}$$

Liquid water accumulation block

This block computes the liquid water accumulation inside the cathode channels in the same way of the anode one.

In presence of liquid water and with relative humidity lower than unity, water passes from liquid to gaseous phase, reducing the amount of liquid water and rising the amount of vapor in the fluid stream and vice-versa. This block is modelled in Simulink with two *if* blocks. The first control is made on the presence of liquid water inside the cathode channels. In case of liquid water presence, the second condition verifies the relative humidity value. For this block, it was chosen to use the outlet relative humidity value. If the relative humidity is equal to one, the quantity of water vapor produced is zero, since under this condition condensation takes place, and the amount of liquid water inside the cathode side rises. In case of relative humidity lower than one, then evaporation occurs in the case of presence of liquid water remaining inside the channels.

The difference between the liquid water "trapped" and the water vaporized (given both in kg s^{-1}) is then integrated over time to obtain the mass of liquid water remaining (given in kg). The saturation condition present inside the *integrator* block is used to prevent negative values, in order to prevent numerical problems.

The amount of liquid water evaporating is defined as:

$$H_2O_{c,evap} = c_r \frac{(1 - \phi_{c,out}) Vol_c \mathcal{M}_{H_2O}}{T_{c,out}} p_{sat}(T_{c,out}) \tag{3.56}$$

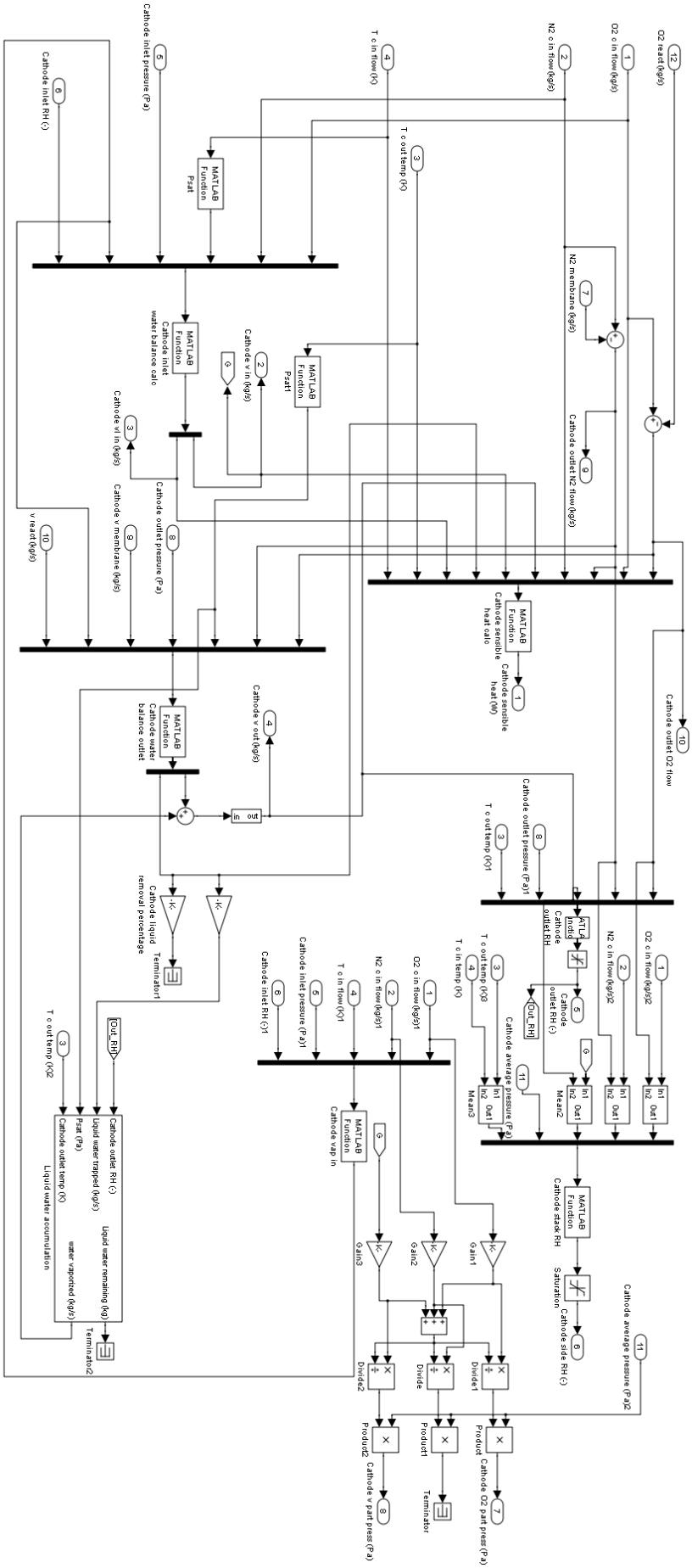

Figure 3.14 Main cathode block

Cathode latent heat block

This block differs slightly from the anode side one, given the presence of the by-product water. In this block, two possibilities can be encountered for the computation of the latent heat:

If $H_2O_{l_{c,in}} \geq \left(H_2O_{v_{c,out}} - H_2O_{mem} - H_2O_{v_{c,in}}\right)$ then:

$$\dot{Q}_{latent_c} = \left(H_2O_{v_{c,out}} - H_2O_{mem} - H_2O_{v_{c,in}}\right)\Delta H_{vap,in} \tag{3.57}$$

Else

$$\dot{Q}_{latent\_c} = \left(H_2O_{v_{c,out}} - H_2O_{mem} - H_2O_{v_{c,in}} - H_2O_{l_{c,in}}\right)\Delta H_{vap,stack} + H_2O_{l_{c,in}}\Delta H_{vap,in} \tag{3.58}$$

The heat of vaporization is calculated as in Eq.(3.30), using the inlet or the stack temperature.

Cathode sensible heat block

The cooling fluid flow is considered in a simple way in this model. It is assumed the fluid is always liquid, without phase change. The cooling sensible heat ($\dot{Q}_{sens_{cool}}$) is given by:

$$\dot{Q}_{sens_{cool}} = c_{p_{H_2O_l}}\left(T_{cool,out} - T_{cool,in}\right)H_2O_{l_{cool}} \tag{3.59}$$

Where the $T_{cool,in}$ and $T_{cool,out}$ are the inlet and outlet temperature (in K) of the cooling fluid. $H_2O_{l_{cool}}$ is the cooling mass flow, measured in kg s^{-1} and considered constant along the whole channel.

The outlet temperature is computed as a heat exchanger as:

$$T_{cool,out} = T_{cool,in} + \left(T_{stack} - T_{cool,in}\right)\left[1 - \exp\left(-\frac{hA_{cool}}{\dot{m}c_{p_{cool}}}\right)\right] \tag{3.60}$$

Also for this latter case, the hA_{cool} variable can be used as a thermal tuning parameter. The term at the denominator of the exponential is simply given by the product $H_2O_{l_{cool}}c_{p_{H_2O_l}}$.

3.3.1.2 Anode and cathode mass heat transport block

This block computes the heat ($\dot{Q}_{mass,a}$) removed from the cathode side due to the transport of mass from the anode to the cathode side or vice/versa. This heat is given by the mass transport of three species: hydrogen consumption, water transport through the membrane and nitrogen crossover. This heat is given by:

$$\dot{Q}_{mass,c} = \left[-H_2O_{mem}c_{p_{H_2O}} + \frac{O_{2_{c,in}}}{\lambda_c}c_{p_{O_2}} - N_{2_{mem}}c_{p_{N_2}}\right](T_{stack} - T_0) \tag{3.61}$$

The signs of the three terms depends on the convention adopted in this model (water membrane transport positive from anode to cathode and nitrogen crossover positive from cathode to anode). Since the transport or reaction of these species occur at the membrane/catalyst interface, it is assumed to use the temperature of the solid, i.e. the stack temperature, at which the membrane is exposed.

Anode and cathode delta pressure blocks

The pressure loss due to the viscous friction force inside the stack and experienced by the anode and cathode fluid streams is modelled here as linear dependent on the mass flow. The Simulink model is built with a user function where the user can change the law relating the pressure loss with the total mass flow inlet. In this way the outlet pressure (sum of the partial pressures) is given as:

$$p_{a,out} = p_{a,in} - \Delta p_a = p_{a,in} - \hat{f}\left(H_{2_{a,in}} + H_2O_{v_{a,in}} + N_{2_{mem}}\right) \tag{3.62}$$

$$p_{c,out} = p_{c,in} - \Delta p_c = p_{c,in} - \hat{f}\left(O_{2_{c,in}} + H_2O_{v_{c,in}} + N_{2_{c,in}}\right) \tag{3.63}$$

It is important to define the pressure loss (Δp) in term of Pascal units.

The average pressure used in the *anode* and *cathode* blocks is then obtained as the average between the inlet and outlet pressures:

$$p_{ave_{a,c}} = \left(\frac{p_{in_{a,c}} - p_{out_{a,c}}}{2}\right) \tag{3.64}$$

A pressure delay block is placed at the exit of the pressure loss calculation to simulate the transient of the pressure variation inside the stack channels. This avoid also the generation of an algebraic loop. Two delay blocks are placed both at the anode and cathode pressure loss quantities. Two time constants (*pressure_delay_stack*) are used to calibrate the transient response of the stack.

The total latent heat of the stack ($\dot{Q}_{latent}$) is simply given by the sum of the cathode and anode latent heats (Eqs. (3.29), (3.57), (3.58)).

3.3.1.3 Voltage model block

The voltage model block is shown in Figure 3.15. In this model, five aspects are considered:

- Ideal voltage.
- Activation voltage loss and crossover currents loss.
- Ohmic voltage loss.
- Concentration voltage loss.
- Double layer effects.

Ideal voltage

The ideal voltage model is simply the same adopted for the electrolyser one. The Nernst voltage varies with temperature and pressure, and it is computed with Eq.(2.4) and Eq.(2.24). In Eq.(2.24) the activity of water (*acty*) is simply given by the partial pressure of water, computed by the stack flux block.

Activation voltage and crossover currents loss

The activation voltage losses of anode and cathode (hydrogen and oxygen sides, respectively, for a PEM fuel cell) are computed as:

$$V_{act} = \frac{RT_{stack}}{n_e F} \sinh^{-1}\left(\frac{i + i_n}{2i_0}\right) \tag{3.65}$$

Where the exchange current densities (i_0) are computed with Eq.(2.22) and Eq.(2.23), taking into account the influence of temperature (positive) on the reduction of the voltage loss. The i_n term is the crossover current density (measured in A m^{-2}), already mentioned in Par.1.3.1.1. The activation voltage loss is expressed making use of the arcsine function.

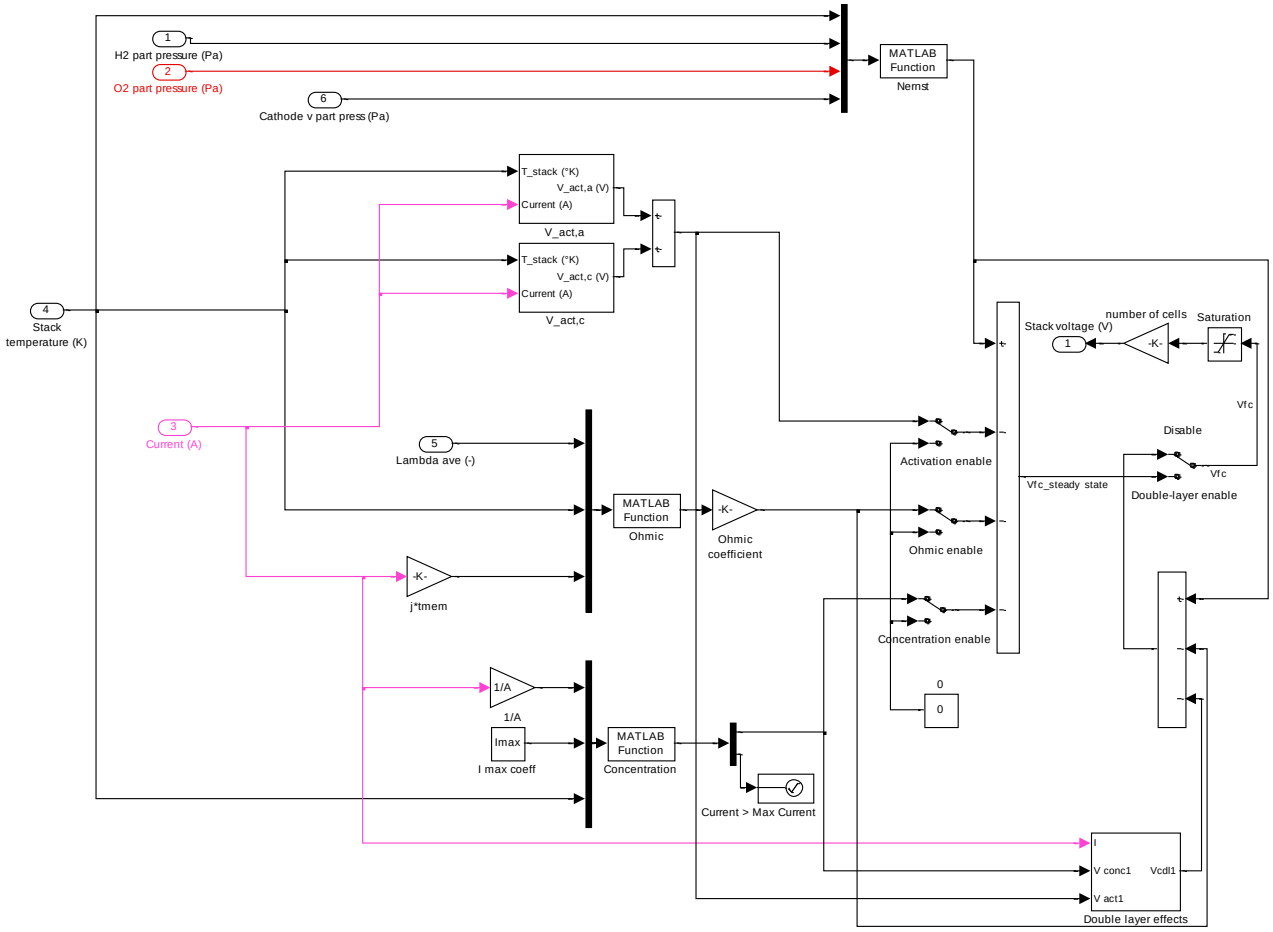

Figure 3.15 Voltage model block

Ohmic voltage loss

The ohmic voltage loss model used here makes use of the same model adopted in literature for the computation of the membrane electric conductivity. As already mentioned, all of the available literature makes use of the same equations, obtained semi-empirically by Springer et al (1991).

The membrane conductivity (measured in S m^{-1}) is calculated for a Nafion® membrane in the form:

$$\sigma_{mem} = \max\left\{0.001;\quad 100(0.00514\lambda_{ave} - 0.00326)exp\left[1268\left(\frac{1}{303} - \frac{1}{T_{stack}}\right)\right]\right\} \qquad (3.66)$$

The presence of the *max* function is a numerical condition used to avoid the possibility to obtain negative values – not physically possible, for the conductivity at very low membrane humidification. The term λ_{ave}, in fact, is the membrane average humidity (dimensionless) and will be explained later. Its value is passed form the *membrane hydration* block. The stack temperature (T_{stack}) is computed at the *overall PEM stack* block level. The membrane conductivity equation could become negative in the case of $\lambda_{ave} < 0.634$. This value, although it is very low and difficult

to be encountered in present cases, might be obtained during the initial steps of the simulation, where initial conditions and the first steps of the computation might lead to very low values of λ_{ave}.

The voltage loss due to ohmic resistance is given by the inverse of conductivity, multiplied by the membrane thickness (t_{mem}) and the current density:

$$V_{ohm} = Ohm_{coeff} \frac{t_{mem}}{\sigma_{mem}} \frac{I}{A} \tag{3.67}$$

The ohmic voltage loss (V) is here multiplied by a tuning factor, the Ohm_{coeff}, used later in the simulations to control the steepness of the polarization curve.

Concentration voltage loss

The concentration voltage losses are responsible of the "knee" visible in the right-hand side of the polarization curve, occurring at high current densities. The concentration voltage losses are given by the finite diffusivity values of the reactants at the catalyst surface, limiting their maximum mass flux toward the reaction sites to a finite value. The concentration losses appear when the maximum amount of current density is approached and have a typical logarithmic shape. Concentration losses are modeled here in the following way:

$$V_{conc} = \frac{RT_{stack}}{2F} \ln\left(\frac{i_{max}}{i_{max} - i}\right) \tag{3.68}$$

Where the i_{max} value represents the maximum current density (in A m^{-2}) obtainable from the cell, corresponding to a concentration level of reactants equal to zero at the catalyst surface. I is the actual current density of the cell.

A conditional control implemented in the model avoids the reaching of zero at the denominator of the logarithm. This might happen in case of a bad current command to the fuel cell stack. In case of $i \geq i_{max}$, the simulation stops with a dedicated warning message.

Double layer effects

The charge double layer is important in understanding the dynamic electrical behavior of fuel cells.

Whenever two different materials are in contact, there is a build-up of charge on the surfaces or a charge transfer from one to the other. In electrochemical systems, the charge double layer forms in part due to diffusion effects, as in semiconductors, and also because of the reactions between the electrons in the electrodes and the ions in the electrolyte, and also as a result of applied voltages. For example, the situation in Figure 3.16 might arise at the cathode of an acid electrolyte fuel cell.

Electrons will collect at the surface of the electrode and H^+ ions will be attracted to the surface of the electrolyte. These electrons and ions, together with the O_2 supplied to the cathode will take part in the cathode reaction. However, any collection of charge, such as of these electrons and H^+ ions at the electrode/electrolyte interface will generate an electrical voltage. The layer of charge on or near the electrode–electrolyte interface is a store of electrical charge and energy, and as such behaves much like an electrical capacitor.

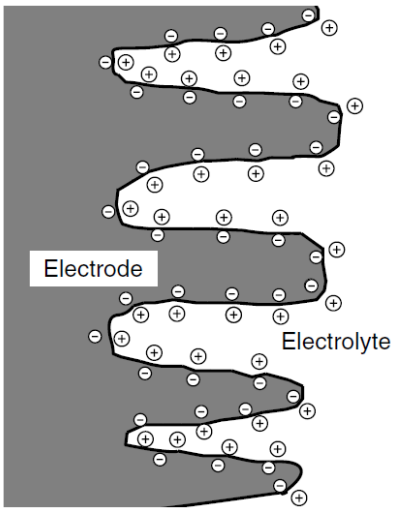

Figure 3.16 Charge double layer formation at the electrode/electrolyte interface

If the current changes, it will take some time for this charge (and its associated voltage) to dissipate (if the current reduces) or to build up (if there is a current increase). Therefore, the overvoltage does not immediately follow the current in the way that the ohmic voltage drop does. The result is that if the current suddenly changes, the operating voltage shows an immediate change due to the internal resistance, but moves slowly to its final equilibrium value. One way of modelling this is by using an equivalent circuit, with the charge double layer represented by an electrical capacitor. The capacitance (measured in F) of a capacitor is given by the formula:

$$C = \varepsilon \frac{A_{real}}{d} \tag{3.69}$$

where ε is the electrical permittivity (about 8.85×10^{-12} F m^{-1} in vacuum), A is the surface area, and d is the separation of the plates. In this case, A is the real surface area of the electrode, which is several thousand times greater than its length × width. Also d, the separation, is very small, typically only a few nanometers. The result is that, in some fuel cells, the capacitance will be of the order of a few Farads, which is high in terms of capacitance values. The connection between this capacitance, the charge stored in it, and the resulting activation overvoltage, leads to an equivalent circuit as shown in Figure 3.17 (Adzapka et al. 2008).

The resistor R_{ohm} models the ohmic losses. R_{act} and R_{conc} model the series of the activation and concentration voltage losses. A change in current gives an immediate change in the voltage drop across this resistor. The effect of this capacitance resulting from the charge double layer gives the fuel cell a good dynamic performance in that the voltage moves gently and smoothly to a new value in response to a change in current demand. It also permits a simple and effective way to distinguish between the main types of voltage drop, and hence to analyze the performance of a fuel cell.

The voltage given by the double layer effect (ΔV_{dl}) is obtained in the model integrating over time the following equation thanks to Simulink.

$$C_{dl}\frac{dV_{dl}}{dt} = I - \frac{\Delta V_{dl}}{\left(\frac{\Delta V_{conc} + \Delta V_{act}}{I}\right)} \tag{3.70}$$

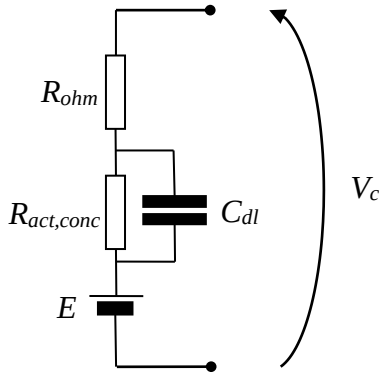

Figure 3.17 Cell equivalent circuit considering the charge double layer effect

The charge double layer effect is implemented in the model with the capability to include it or not in the simulation. A manual switch in the *voltage model* block allows its activation. It is also possible to disable the different voltage losses (activation, ohmic and concentration) one by one, allowing the study of their effects on the polarization curve. The overall fuel cell stack voltage (V_{stack}) is implemented in the same block in the following form without considering the double layer effects:

$$V_{stack} = n_c(E - \Delta V_{act} - \Delta V_{ohm} - \Delta V_{conc}) \tag{3.71}$$

where n_c stands for the number of cells in the stack. In presence of the double layer effects, V_{stack} takes the form:

$$V_{stack} = n_c(E - \Delta V_{ohm} - \Delta V_{dl}) \tag{3.72}$$

In the model, a saturation block prevents the cell stack voltage to reach negative values, which could be encountered during the initial simulation steps due to numerical approximations. In real fuel cells, negative cell voltage might be encountered in damaged cells or during severe system failures. These situations are here not implemented.

3.3.1.4 Membrane hydration block

The membrane hydration block is responsible of the computation of the overall membrane humidification. The membrane humidification, as already said, plays a key role in the correct fuel cell operation and lifetime. The immediate effect of humidification is the variation of the membrane electrical conductivity. Consequently, a proper humidification keeps the polarization curve less steep in the central region.

Membrane humidification model

The membrane humidification model used in this work made use of the finite differences method to compute an average value of membrane hydration. Since its dynamics could strongly influence the behavior of the transient response of the stack (Par.3.1.1), this more detailed membrane model should help in giving better results. The finite differences method allows to discretize the membrane thickness into an arbitrary number of elements. At the same time, it was important to keep the computational time of this sub-model at acceptable levels.

The water concentration (C_{mem}) inside the membrane, measured in mol m^{-3} can be expressed as a convection-diffusion problem as:

$$\frac{\partial C_{mem}}{\partial t} = -\frac{\partial J_{mem}}{\partial z} = D_{mem}\frac{\partial^2 C_{mem}}{\partial z^2} - \frac{\xi}{F}\frac{\partial i}{\partial z} \tag{3.73}$$

Where J_{mem} is the membrane water flow (expressed in mol $m^{-2}s^{-1}$) and z is the spatial dimension along the membrane thickness. D_{mem} is the diffusivity of water through water, and it is here calculated with the improved semi-empirical relations given by Motupally et al. (2000):

$$D_{mem} = \begin{cases} 3.1 \times 10^{-7}\lambda_{mem}[\exp(0.28\lambda_{mem}) - 1]\exp\left(-\frac{2346}{T_{stack}}\right), & \lambda_{mem} < 3 \\ 4.17 \times 10^{-8}\lambda_{mem}[1 + 161\exp(-\lambda_{mem})]\exp\left(-\frac{2346}{T_{stack}}\right), & \lambda_{mem} \geq 3 \end{cases} \tag{3.74}$$

The membrane humidification (λ_{mem}) is usually defined in all the available literature, starting from the work by Springer et al. (1991) as a power law relating it to the water activity:

$$\lambda_{mem} = 0.043 + 17.81a_{H_2O} - 39.85a_{H_2O}^2 + 36.0a_{H_2O}^3 = \frac{C_{H_2O}}{\frac{\rho_{mem}}{\mathcal{M}_{mem}}} \tag{3.75}$$

Where ρ_{mem} is the membrane dry density (in kg m^{-3}) and $\mathcal{M}_{mem}$ is the membrane equivalent weight expressed in kg mol^{-1}. Both these two values are constants. The water activity at the membrane catalyst layer interface can be exchanged with the relative humidity (Sivertsen and Djilali 2005). The first term in the right hand side portion of Eq.(3.73) is the conductive flux, while the second one is the convective flux generated by the electro-osmotic drag, discussed later. i is the current density and ξ is the electro-osmotic drag constant. Since the current density through the stack can be considered always constant along the membrane thickness, apart from almost instantaneous current transients, the term $-\frac{\xi}{F}\frac{\partial i}{\partial z}$ can be neglected. Moreover, considering Eq.(3.75), it is possible to substitute λ_{mem} and C_{mem}, obtaining the following equation:

$$\frac{\partial \lambda_{mem}}{\partial t} = D_{mem}\frac{\partial^2 \lambda_{mem}}{\partial z^2} \tag{3.76}$$

D_{mem} is here considered constant and not dependent upon the membrane thickness, calculating an average value of it to avoid excessive computational cost.

The last equation was solved numerically using the finite differences method, adopting a non-uniform Dirichlet boundary condition, in the way:

$$\begin{cases} \frac{\partial \lambda_{mem}}{\partial t} = D_{mem}\frac{\partial^2 \lambda_{mem}}{\partial z^2} \\ \lambda_{mem}(0,t) = \lambda_{an}(t) \\ \lambda_{mem}(n,t) = \lambda_{cat}(t) \\ \lambda_{mem}(x,0) = \lambda_{ini}(x) \end{cases} \tag{3.77}$$

The derivatives discretization was done with a centered difference approach giving the following equations for a generic i point:

$$\left(\frac{\partial \lambda_{mem}}{\partial z}\right)_i \approx \frac{\lambda_{mem_{i+\frac{1}{2}}} - \lambda_{mem_{i-\frac{1}{2}}}}{h}$$
$$\left(\frac{\partial^2 \lambda_{mem}}{\partial z^2}\right)_i \approx \frac{\lambda_{mem_{i+1}} - 2\lambda_{mem_i} + \lambda_{mem_{i-1}}}{h^2} \quad (3.78)$$

Where h is the length of the segment considered. This discretization is referred to a 1-D situation, obviously. Substituting the equations in Eq.(3.78), the following expression was obtained:

$$\frac{\partial \lambda_{mem}}{\partial t} = \frac{D_{mem}}{h^2}\begin{bmatrix} -2 & 1 & 0 & \cdots & \cdots & 0 \\ 1 & -2 & 1 & \cdots & \cdots & 0 \\ 0 & 1 & -2 & 1 & \cdots & 0 \\ 0 & \cdots & \cdots & \ddots & \cdots & \vdots \\ \vdots & \cdots & \cdots & \cdots & \ddots & \vdots \\ 0 & \cdots & \cdots & 0 & 1 & -2 \end{bmatrix}\{\lambda_{mem}\} + \frac{D_{mem}}{h^2}\begin{bmatrix} \lambda\_an \\ 0 \\ \vdots \\ \vdots \\ 0 \\ \lambda\_cat \end{bmatrix} \quad (3.79)$$

The left hand side of Eq.(3.79) was not discretized directly, since its discretization, being part of the Simulink solver, did not require any kind of discretization. The model was implemented in Simulink simply implementing the right hand side of Eq.(3.79) and then integrating it with the integrator block. The Simulink solver allows the selection of both implicit and explicit solving methods for the time derivative. A similar approach can be found in Ahmed and Chmielewsi (2011).

Membrane water transport model

Considering PEM fuel cells performance dramatically affected by water management, it is possible to focus on two macro-scale effects, namely two phenomena able to modify the polarization curve and consequently the power output of the cell and the stack. As previously underlined, excessively dry reactant gases will cause a rapid membrane dehydration with the worst situation of a membrane irreversible failure: the main impact is a rising of the membrane electrical resistance – the main form of voltage ohmic loss in the cell –, this making the polarization curve steeper. Membrane dehydration is very rapid in time, since the membrane is really thin, in the order of tenths or hundredths of microns.

On the other hand, with excessive water content, water removal is penalized. The worst case will be humidity equal to one, causing condensation not compensated by evaporation yet, hence the beginning of flooding phenomenon. Flooding has two serious effects:

- At the porous gas diffusion layer level, water droplets will partially or completely occlude the pores: this implies that the reactants will encounter difficulties in reaching the chemical reaction sites, since they are forced to pass through smaller volumes and/or longer paths, this causing both higher pressure drops or lower oxygen and hydrogen concentrations. The reduced mass flow of reactants gases at minor pressure will reduce also the capacity to remove liquid water.
- At the catalyst layer, instead, platinum particles could be covered with water droplets, avoiding reactants contact with the catalyst.

In both cases, flooding will reduce power output, lowering polarization curves, especially at high current densities, where higher water production occurs.

It has to be remarked that the cell performance drops with water accumulation and drying-out could be time-dependent, hence immediately observable if water balance is strongly not in an equilibrium condition, or after sufficiently long operating times, as underlined in experimental studies (e.g. in Urbani et al. 2008), where steady state conditions are reached not sooner than few hours. On the other hand, if water flooding reaches an equilibrium point, the performance of the cell will not show any other oscillation in the time domain.

In this work, both the electro-osmotic and back-diffusion terms are considered. Figure 3.18 shows water movements across the membrane.

A third, almost negligible form of transport through the membrane is the so-called crossover, regarding both electrons and reactant gases, not investigated here.

Electro-osmotic drag flow (n_d, in kg s^{-1}) is found to be equal to:

$$n_d = \frac{2.5}{22}\frac{I}{F\mathcal{M}_{H_2O}} \tag{3.80}$$

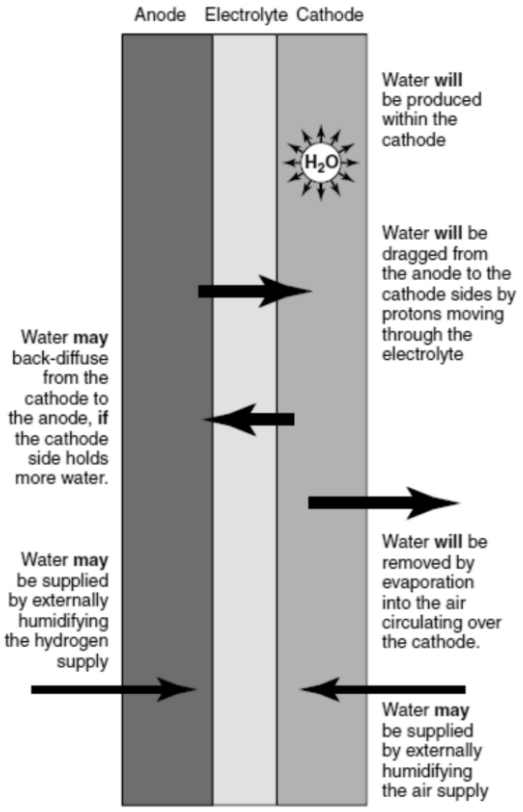

Figure 3.18 The different water movements to, within, and from the electrolyte of a PEM fuel cell

The second transport phenomenon, the back-diffusion, requires the definition of the water diffusion coefficient, D_{H_2O}, measured in m^2/s, already introduced by Eq.(3.74).

Using the Fick's law of diffusion and integrating it linearly, it is possible to define the back-diffusion flow, n_{bd}, in the form:

$$n_{bd} = \frac{D_{H_2O}\left[C_{H_2O_{cat}} - C_{H_2O_{an}}\right]}{t_m \mathcal{M}_{H_2O}} A \tag{3.81}$$

The two terms C_{H_2O} (mol m^{-3}) represent the water molar content at membrane-CL interfaces, and it is expressed as in Eq.(3.75). The net water flux across the membrane, H_2O_{mem}, has the following formula:

$$H_2O_{mem} = (n_d - n_{bd})n_c \tag{3.82}$$

Where the minus sign indicates a positive flux for water moving from the anode to the cathode side and vice-versa.

3.3.2 Air/oxygen compressor

The air/oxygen compressor model is quite simple. This model contains a sub-model consisting of the electric motor powering the compressor. This model is essentially based on Pukrushpan et al. (2004). Since the information relevant to the stack are essentially the mass flow, electric power input, outlet temperature and pressure, it was considered sufficient to maintain the compressor model to a basic level. Nevertheless, the transient behavior of the compressor and engine are modelled, given the importance of transient phenomena for the fuel cell model.

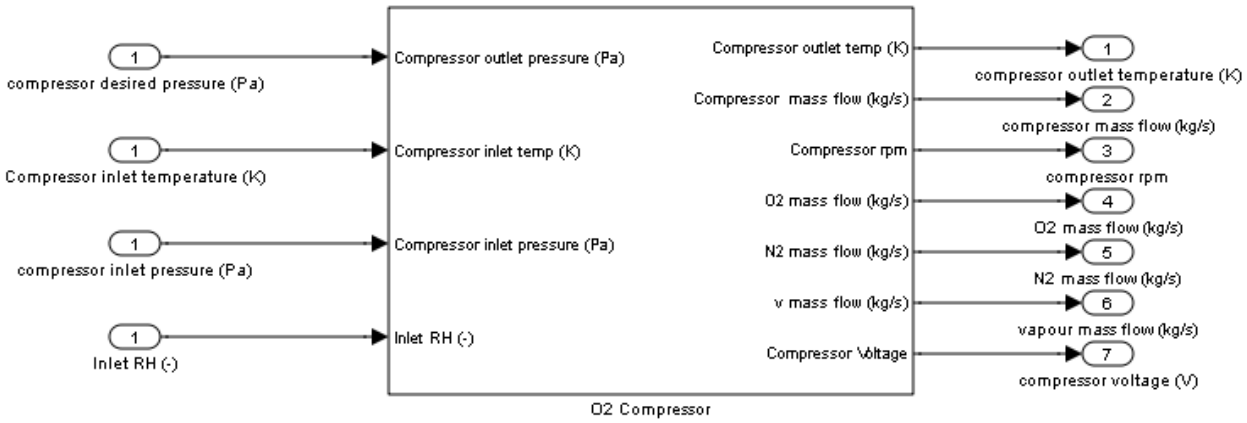

Figure 3.19 Air/oxygen compressor model block

The compressor is modeled using as input three ambient conditions: temperature, pressure and relative humidity and the *compressor desired pressure*. This value corresponds to the pressure loss of the cathode side (Δp_c) and is used in the model to vary the compressor mass flow and pressure to meet the requirements of the stack. The ambient variables could be obtained in different way and can be set as constant or variable.

The compressor model has only two stations, namely the inlet and outlet. It contains also a compressor *flow controller* block made of a simple PID logic. The internal structure of the compressor model can be seen in Figure 3.20.

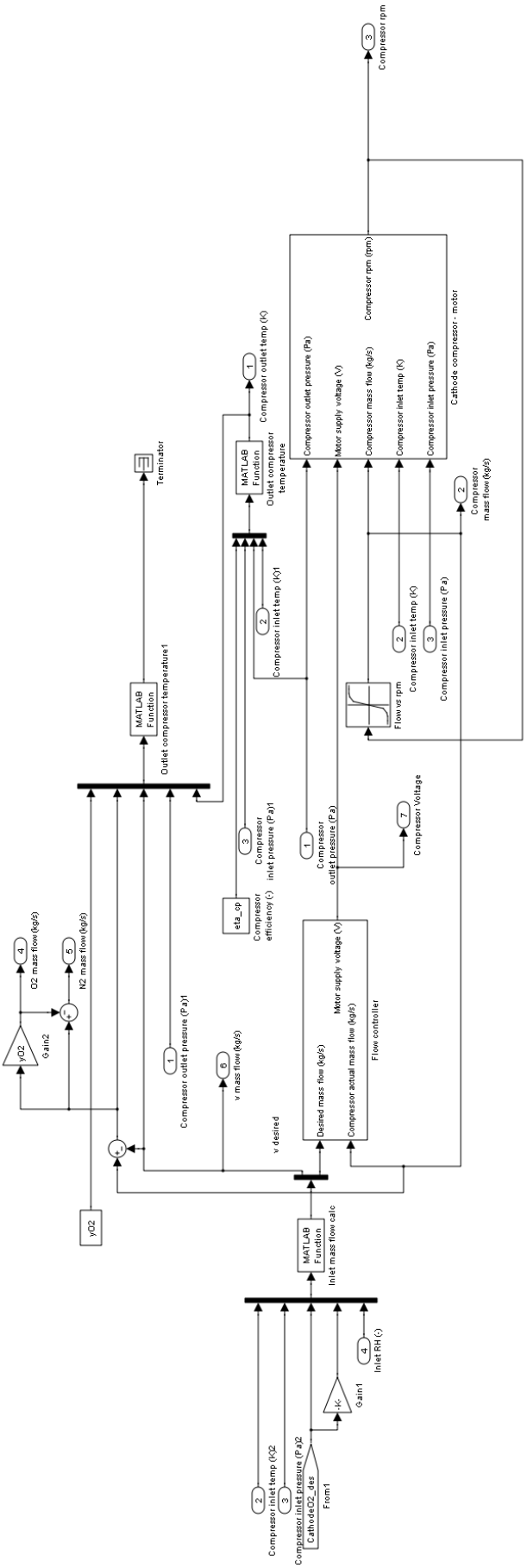

Figure 3.20 Internal structure of the air/oxygen compressor

Given the inlet quantities and the desired oxygen mass flow (obtained from the *stack flux* block with Eq.(3.10) at every time step), Simulink computes the so-called *desired* input mass flow. This value will be compared with the actual mass flow given by the compressor outlet to change the compressor speed in order to meet the desired values. The desired input mass flow of water vapor is calculated in the following way:

$$H_2O_{v_{in,des}} = \left(\frac{O_{2_{in,des}}}{\mathcal{M}_{O_2}} + \frac{1 - y_{O_2}}{y_{O_2}} \frac{O_{2_{in,des}}}{\mathcal{M}_{O_2}} \right) \frac{p_{sat}(T_{in})\phi_{in}}{p_{in} - p_{sat}(T_{in})\phi_{in}} \mathcal{M}_{H_2O} \tag{3.83}$$

The total desired mass flow will be given by the sum of the desired oxygen, nitrogen and water vapor, where the quantity y_{O_2} is the oxygen mass fraction (dimensionless) of the air entering the compressor. The *des* quantities are the desired quantities required by the fuel cell stack for the operation. Since in the stack model the variation of the reactants mass flow ($H_{2_{react}}$ and $O_{2_{react}}$) is considered instantaneous with the current demand (Eq.(3.6), (3.7)), a variation in electric current immediately gives a variation in the desired values. Nevertheless, the compressor will spend some time to modify its operating point satisfying the new desired values.

The flow controller is made up of a simple PID controller. The PID logic simply compares the desired values with the actual ones (whose description is given later), and change the voltage applied to the motor moving the compressor. The schematic of the PID controller is shown in Figure 3.21. The controller uses three different gains for the proportional, derivative and integral command. The saturation blocks simulates the maximum output voltage the controller can give to the motor.

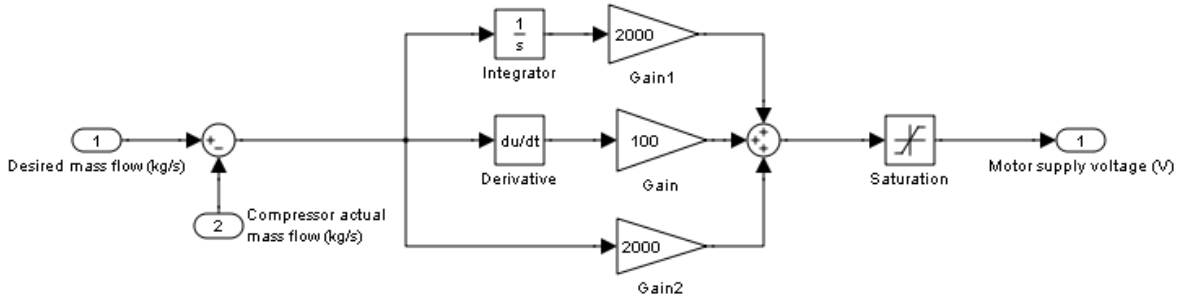

Figure 3.21 Simple PID controller block

Compressor motor block

The compressor electric motor uses a simple model, made up of lumped parameters. The model representation in Simulink is given in Figure 3.22.

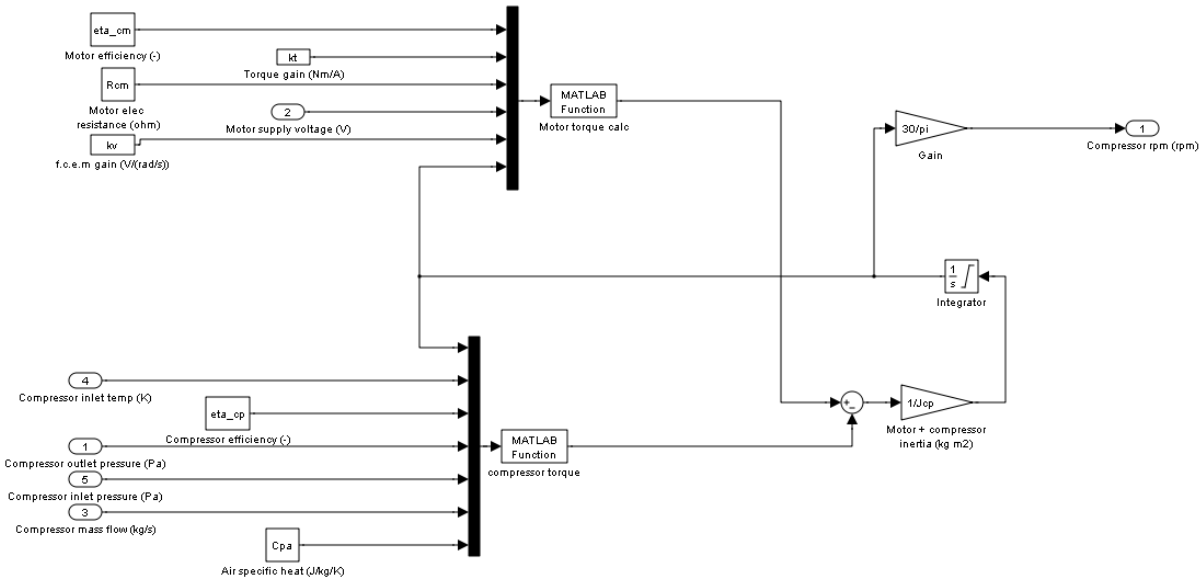

Figure 3.22 Compressor electric motor block

The model is made of two main elements calculating the compressor torque and the electric motor torque, and giving as output the compressor speed (in rpm). Given the compressor speed, a look-up table is used to relate the map of the compressor, i.e. its hydraulic head and mass flow, with its speed.

The electric motor torque (τ_m) is given by:

$$\tau_m = \eta_m \frac{k_T(V_m - k_V \omega_m)}{R_m} \tag{3.84}$$

The torque given by the electric motor is given by two main parameters, namely the torque gain (k_T) and the electromotive force (EMF) gain (k_V). The first one is given in Nm A^{-1}, while the second one is given in $V(rad\ s^{-1})^{-1}$. V_m is the voltage applied to the motor and R_m is the motor electric resistance (given in Ω). The rotational speed of the motor, considered here directly connected to the compressor is represented by ω_m. The term η_m is the efficiency of the motor.

The torque given by the compressor (τ_{com}) is given by (Pukrushpan 2004):

$$\tau_{com} = \frac{\dot{m}_{in}}{\omega_m \eta_{com}} c_{p_{in}} T_{in} \left[\left(\frac{p_{out}}{p_{in}} \right)^{\frac{\gamma-1}{\gamma}} - 1 \right] \tag{3.85}$$

Where $\dot{m}_{in}$ is the total mass flow entering the compressor, η_{com} is the compressor efficiency and $c_{p_{in}}$ is the gas specific heat. This value is equal to 1006 J kg^{-1} K^{-1} for standard air and 920 J kg^{-1} K^{-1} for pure oxygen. The constant γ is independent from the use of air or pure oxygen.

The motor speed is simply given by:

$$\frac{d\omega_m}{dt} = \frac{\tau_m - \tau_{com}}{J_{cm}} \tag{3.86}$$

Where J_{com} is the compressor and motor inertia (in kg m^{-2}). The integration over time of Eq.(3.86) gives the motor and compressor speed in rad s^{-1}.

The compressor mass flow ($\dot{m}_{in}$), representing the actual mass flow, is obtained from a look-up table correlating mass flow to pressure rise and speed. In this way, the desired vs. actual mass flow is compared to give a command voltage. The variation in the commanded voltage modifies the motor speed and hence its mass flow. The pressure rise required will be given instead by the stack model.

The compressor outlet temperature is given by:

$$T_{out} = T_{in} + \frac{T_{in}}{\eta_{com}}\left[\left(\frac{p_{out}}{p_{in}}\right)^{\frac{\gamma-1}{\gamma}} - 1\right] \tag{3.87}$$

It is important to point out that the compressor outlet pressure is given by the system considered.

3.3.2.1.1 Model setup and simulation results

The parameters used for the model of the motor and air compressor are mainly taken from Bird (2002), where the transient phenomena of the air feed system of a 20 kW fuel cell designed for terrestrial vehicles are addressed. The values for both the electric brushless motor and the screw compressor are given, together with the compressor map. Given the rated power of 20 kW, coincident with the Ballard Mark9 SSL stack analyzed in this work, the system considered by Bird (2002) can be considered fully compatible with the one considered in this work. The values for the electric motor are given in Table 3.1. The motor used in this case is a Unique Mobility motor.

Table 3.1 Electric motor parameters used for the compressor motor

Parameter	Value
Parameters taken from Bird (2002)	
Motor electric resistance (R_m)	36 Ω
Torque gain (k_t)	0.191 (N m)A^{-1}
EMF gain (k_v)	0.191 V(rad s^{-1})$^{-1}$
Motor+compressor inertia (J_{cm})	0.014 kg m^2
Other parameters	
Motor efficiency (η_m)	0.97
Compressor efficiency (η_{com})	0.6

The other parameters in Table 3.1 were not given, and were estimated considering typical high efficiency brushless motors and the average compressor efficiency given in Figure 3.23. The compressor efficiency (η_{com}) is not considered variable, for simplicity.

The compressor used by Bird (2002) is an Opcon screw compressor designed for fuel cells. Its map is given in Figure 3.23.

The points used for the present model are interpolated from the compressor map using Matlab interpolation functions. The resulting function expressing the mass flow as output is function of both the pressure increase and compressor rotational speed (in RPM).

Using the data just shown to calibrate the model, the PID controller parameters were varied to obtain a desirable mass flow output. The parameters used in the PID controller are parameters chosen by the system designer, and can be selected quite arbitrarily. Information about the control logic of the system modeled by Bird (2002) was not given, unfortunately. The PID constants directly affect the transient response and steady-state response of the system.

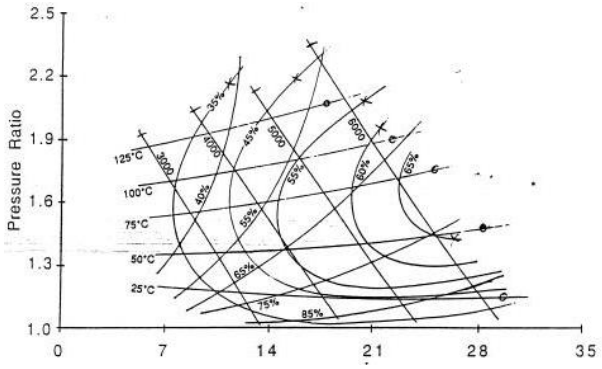

Figure 3.23 Opcon compressor map used for the air compressor model

In the following simulations, the desired pressure rise is kept constant at 50000 Pa (the maximum pressure rise present in the Ballard stack (Par.3.3.1). The inlet temperature is fixed at 30°C (303 K) as well as the inlet relative humidity (95%) and the inlet pressure was taken equal to the standard ambient pressure of 101325 Pa. Keeping constant these variables, the desired mass flow was set at the response of the system was analyzed.

Figure 3.24 shows the response of the system to a request of 0.015 kg s^{-1} (720 l min^{-1} at standard conditions), being this value higher than the maximum mass flow required by the Ballard stack at maximum current simulated, equal to almost 0.01 kg s^{-1} or 480 l min^{-1} (Par.4.1.1). The parameters used for the PID controller are equal to 60000, 30000 and 30000 for the proportional, derivative and integrator gains, respectively. As can be seen, the motor speeds up for about 4 seconds, reaching a higher than required mass flow output. The controller then responds reducing the motor speed to obtain the desired mass flow of 720 l min^{-1}. The steady state condition is reached in about 10-12 seconds starting from zero. The error at steady state between the commanded (720 l min^{-1}) and the actual flow (760 l min^{-1}) is of the 5.6 percent, and is directly related to the PID parameters, and can be considered sufficiently precise. The temperature reached at the outlet of the compressor is shown in Figure 3.25. The temperature is constant because it is calculated using the difference between outlet and inlet temperature, and are both fixed in this simulation. The input voltage commanded by the control logic is also reported in Figure 3.25. The maximum input voltage is limited at 600 V. The high voltage here shown is given by the constant k_v, equal to 0.191 V (rad s^{-1})$^{-1}$, corresponding to a value of 20 Volts every 1000 RPM. Anyway, the voltage input given can be simply scaled varying the k_v value, without modifying the behavior of the compressor.

The minimum flow and pressure required by the Ballard stack are equal to 1.8×10^{-4} kg/s (8.64 l min^{-1}) and 150 Pa. These can be considered the minimum values the compressor-motor will have to satisfy, in opposition to the values just shown. The results are shown in Figure 3.30 and Figure 3.31, and are comparable with the previous ones. In this case, the compressor required more time to reach the desired mass flow, since for about 10 seconds, the initial condition set for the compressor speed was higher than the required one. The temperature increase is very low (about 0.5 K) given the low mass flow, as well as the voltage input. The steady-state error in this case is equal to about 5.9%.

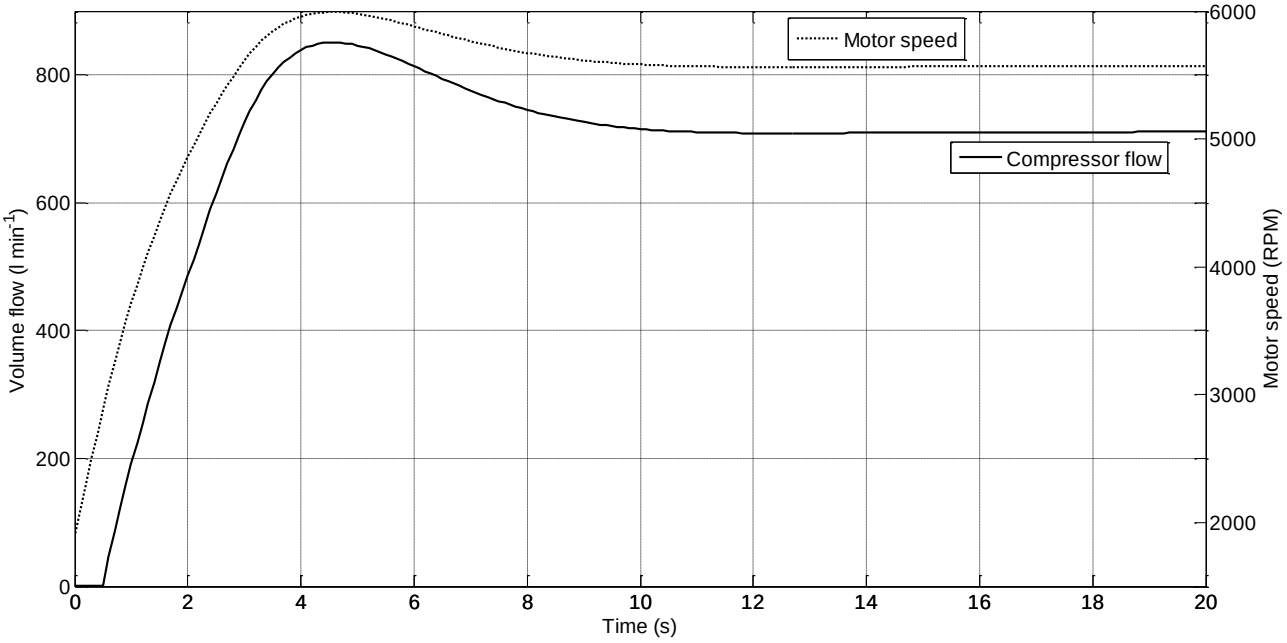

Figure 3.24 Compressor volume flow and motor speed. Transient response. Maximum pressure and flow

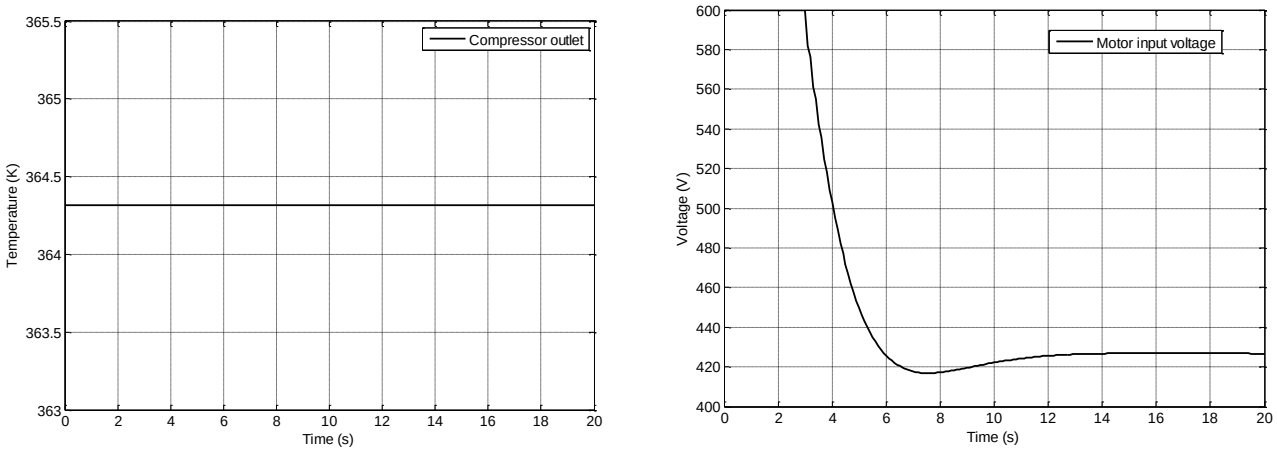

Figure 3.25 Compressor outlet temperature (left side) and motor input voltage (right). Maximum pressure and flow

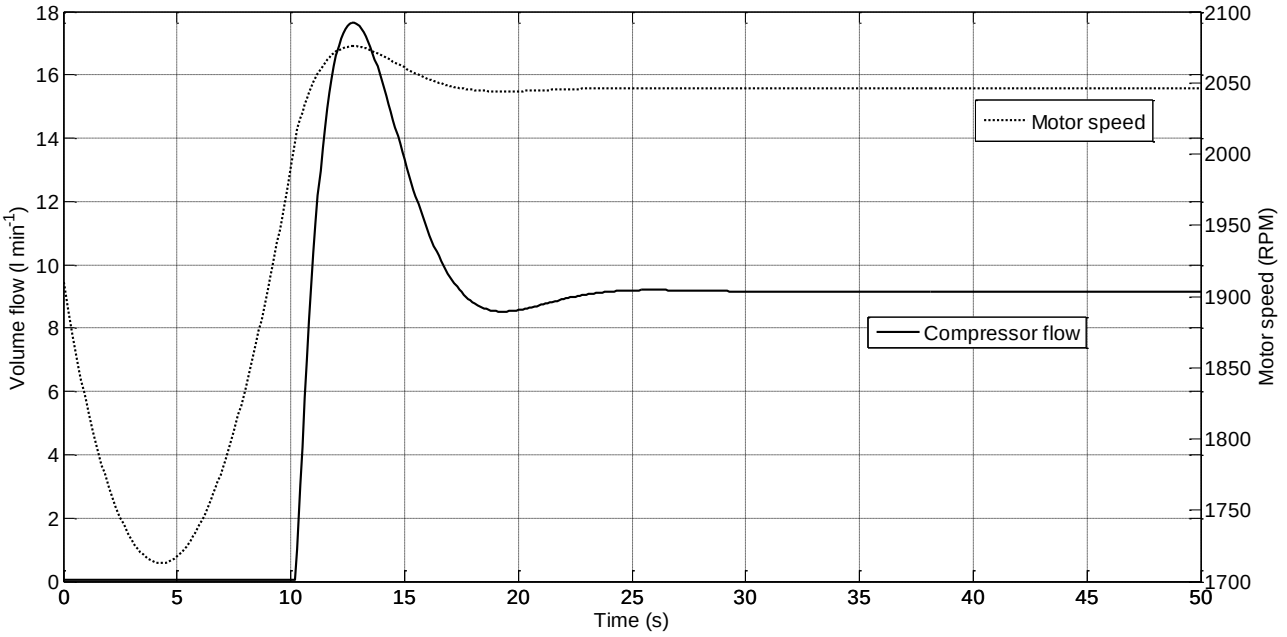

Figure 3.26 Compressor volume flow and motor speed. Transient response. Minimum pressure and flow

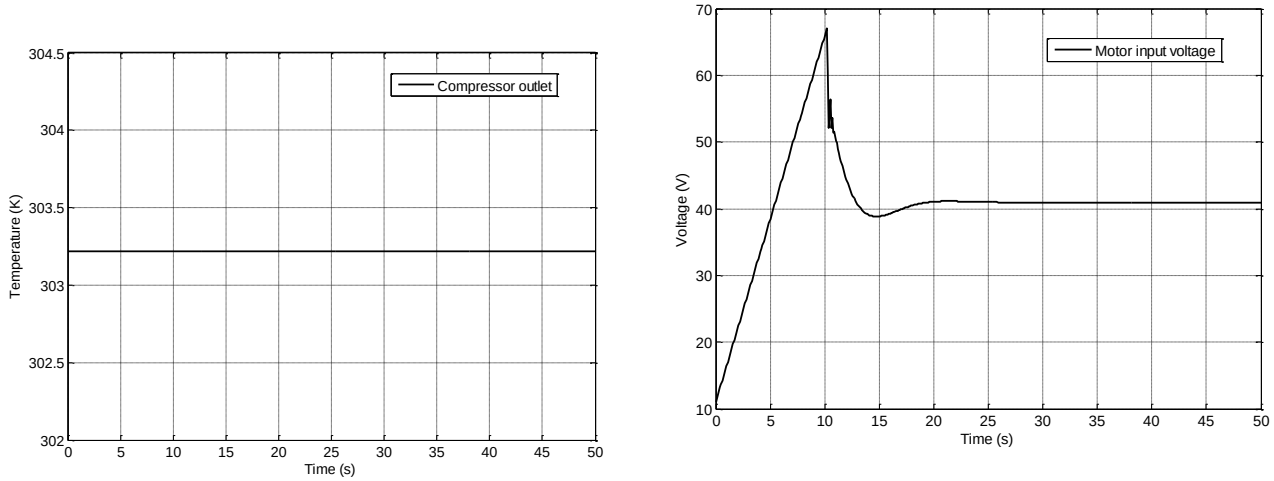

Figure 3.27 Compressor outlet temperature (left side) and motor input voltage (right). Minimum pressure and flow

The next two figures show the combination of the two previous test cases, with a step increase in the flow and pressure demand from the minimum to the maximum values required, and just simulated, imposed at 30 seconds of simulation. The results are given in Figure 3.28 and Figure 3.29, and can be considered a sort of superimposition of the two previous test cases. The temperature rise is a step, since the temperature is modeled here as instantaneous, without time delays. Other test cases will be presented in the complete fuel cell system setup and simulation (Par.4.2).

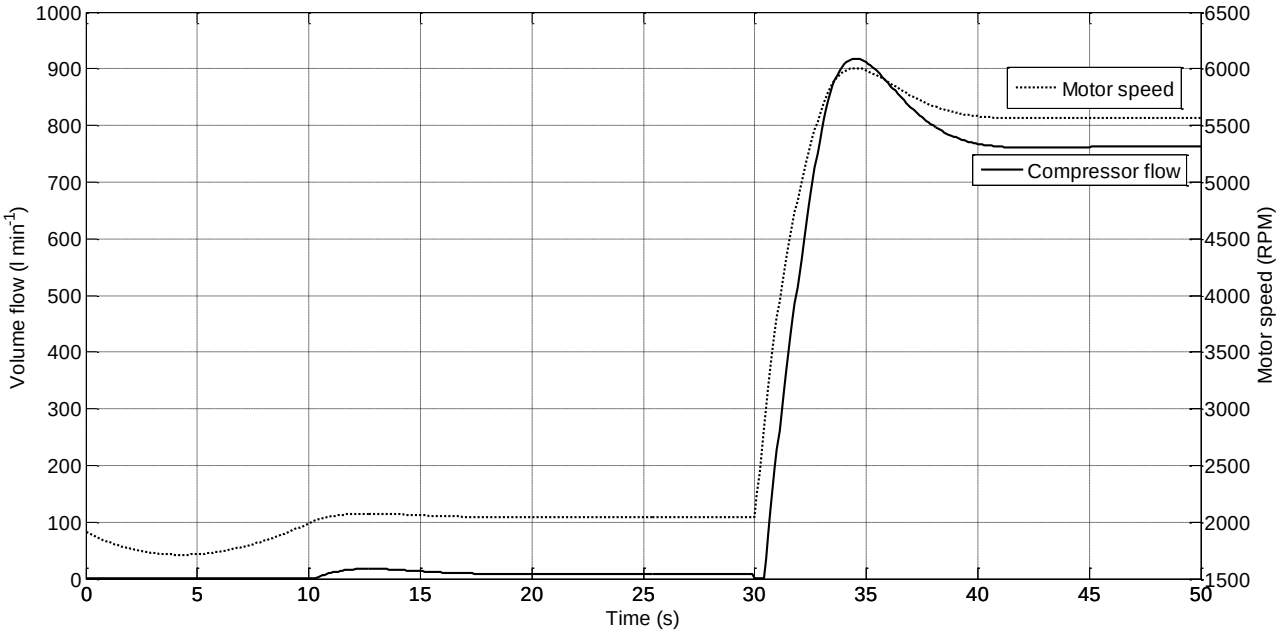

Figure 3.28 Compressor volume flow and motor speed. Transient response. Step increase from minimum to maximum volume flow and pressure.

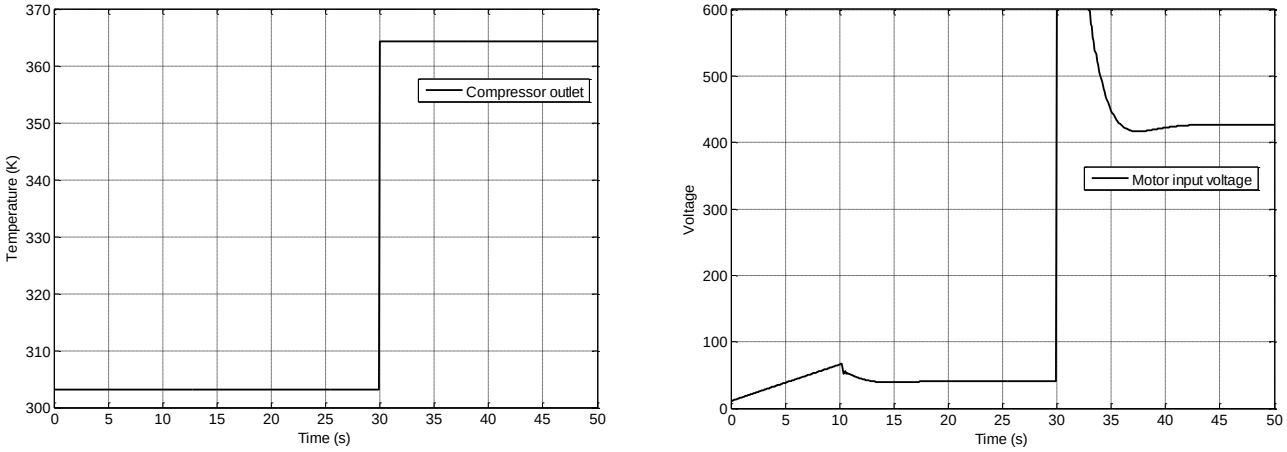

Figure 3.29 Compressor outlet temperature (left side) and motor input voltage (right). Step increase from minimum to maximum volume flow and pressure.

3.3.3 Cathode intercooler

Given the high temperature of the gases exiting the compressor, and the relatively low temperature at which the fuel cell stack operates (usually between 50-80 °C), it might be necessary to cool down the temperature of the gases prior to entering the stack and/or humidifiers.

The intercooler here adopted is considered to be a counter-flow heat exchanger made of two separate sides, namely the hot and cold ones, with a metallic wall interfacing the heat exchange between them. The model implemented is identical to the one developed by Smedsrud (2007).

The intercooler model is formulated using ten segments representing ten stations along the fluid flow path. In this model, the intercooler used is assumed to be a counter-flow one. At each station, the inlet and outlet temperatures of the hot and cold flow, denoted with the subscripts *H* and *C* respectively, are computed together with the temperature of the metallic wall separating the two

sides. Figure 3.30 shows an enlargement of the Simulink model used, depicting two of the intercooler stations. The overall intercooler model is given in Figure 3.31.

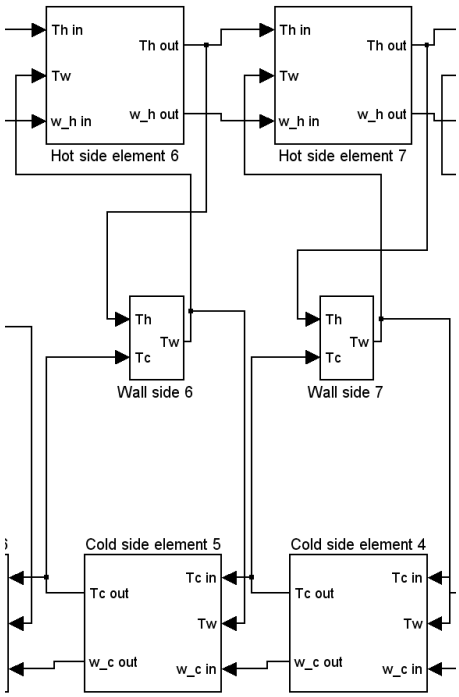

Figure 3.30 Detail of the intercooler Simulink model

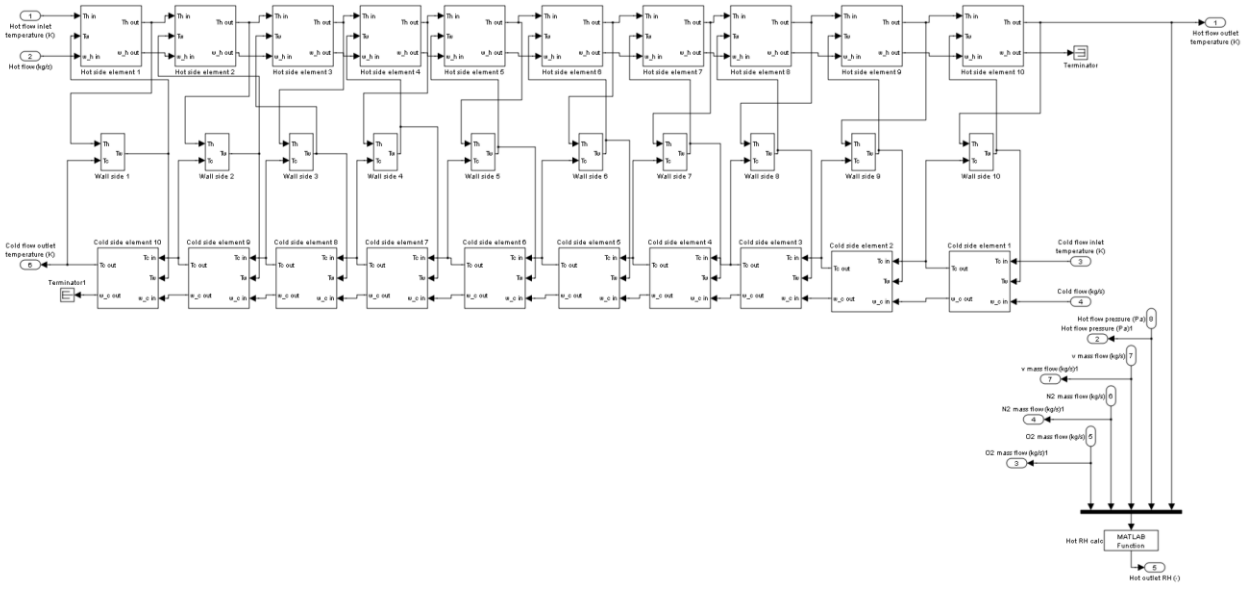

Figure 3.31 Overall intercooler Simulink model

At each of the intercooler station, it is assumed the inlet and outlet flows are the same. At each of the hot flow station, the outlet temperature ($T_{H_{out}}$) is computed integrating the following differential equation:

$$\frac{dT_{H_{out}}}{dt} = K_{1H_{ic}}\left[\dot{m}_{H\,in}\left(T_{H_{in}} - T_{H_{out}}\right)\right] - K_{2H_{ic}}\left(T_{H_{out}} - T_W\right) \tag{3.88}$$

Where $T_{H_{in}}$ is the inlet hot flow temperature, $\dot{m}_{H_{in}}$ is the inlet mass flow (kg s^{-1}) and the T_W variable is the hot-cold wall interface temperature. Two thermal coefficients, used as tuning parameters, are used, namely $K_{1H_{ic}}$ and $K_{2H_{ic}}$, given in kg^{-1} and s^{-1}, respectively.

The cold flow is resolved in the same way of the hot one with the following, symmetrical equation:

$$\frac{dT_{C_{out}}}{dt} = K_{1C_{ic}}\left[\dot{m}_{C\,in}\left(T_{C_{in}} - T_{C_{out}}\right)\right] - K_{2C_{ic}}\left(T_{C_{out}} - T_W\right) \tag{3.89}$$

Two new calibration parameters are defined, namely $K_{1C_{ic}}$ and $K_{2C_{ic}}$, defined in the same way of $K_{1H_{ic}}$ and $K_{2H_{ic}}$.

The wall temperature is assumed equal on both sides of the hot-cold interface, for simplicity. Its value (T_W) is given by:

$$\frac{dT_W}{dt} = K_{1W_{ic}}\left(T_{H_{out}} - T_W\right) - K_{2W_{ic}}\left(T_W - T_{C_{out}}\right) \tag{3.90}$$

The six thermal constants introduced in Eqs. (3.88), (3.89) and (3.90) can be expressed as:

$$K_{1H_{ic}} = \frac{N_{ic}}{\rho_H V_H} \qquad K_{2H_{ic}} = \frac{h_{H_{ic}} A_{ic}}{c_{p_H} \rho_H V_H} \tag{3.91}$$

$$K_{1C_{ic}} = \frac{N_{ic}}{\rho_C V_C} \qquad K_{2C_{ic}} = \frac{h_{C_{ic}} A_{ic}}{c_{p_C} \rho_C V_C} \tag{3.92}$$

$$K_{1W_{ic}} = \frac{h_{H_{ic}} A_{ic}}{c_{p_W} \rho_W V_W} \qquad K_{2W_{ic}} = \frac{h_{C_{ic}} A_{ic}}{c_{p_W} \rho_W V_W} \tag{3.93}$$

Where A_{ic} is the contact surface between the fluid and the wall interfacing the two sides, ρ_W is the density of the material of the wall, c_{p_W} is its thermal capacity (in J kg^{-1} K^{-1}) and V_W is the wall volume (in m^3). The variables $h_{H_{ic}}$ and $h_{C_{ic}}$ are the convective heat transfer coefficients on the two wall sides of the intercooler (in W m^{-2} K^{-1}). N_{ic} are the number of elements used in the exchanger (10 in this case). All of the other variables with the subscripts "*H*" and "*C*" refer to the hot and cold sides. The volume and area variables are referred to the whole heat exchanger and are then divided by the number of cells used in the model.

In this model, it is assumed to use liquid water as cooling fluid, as is usually done for medium and high power fuel cell stack. Nevertheless, it is possible to use gas, simply modifying the heat exchange parameters in the model.

Since the gases exiting from the compressor are cooled, there will be a change in the relative humidity. The intercooler model computes the outlet relative humidity in the following way:

$$\phi_{ic_{out}} = \frac{\dfrac{p_{ic_{out}}}{p_{sat}\left(T_{H_{out}}\right)} \dfrac{H_2O_v}{\mathcal{M}_{H_2O}}}{\dfrac{O_2}{\mathcal{M}_{O_2}} + \dfrac{N_2}{\mathcal{M}_{N_2}} + \dfrac{H_2O_v}{\mathcal{M}_{H_2O}}} \tag{3.94}$$

The inlet and outlet mass flows (H_2O_v, O_2 and N_2) are passed to the intercooler model from the compressor one and are considered constant for simplicity (no leakage considered). It is also assumed there is no pressure loss due to the irreversibility.

3.3.3.1.1 Model setup and simulation results

The intercooler model calibration with experimental data is very difficult to obtain, given the geometric and thermal properties of the intercooler used, usually not given by the manufacturer. While the volume of the hot and cold sides could be determined injecting water, and the wall volume could be determined estimating the mass of metal used from the exchanger mass and metal density, the other thermal variables show a great variability. In particular, the heat transfer coefficients, for instance, can vary greatly. For water, the $h_{C_{ic}}$ value could be comprised between 50 and 10000 W m^{-2} K^{-1}, while for the air side, the $h_{H_{ic}}$ value could be in the interval 10 – 200 W m^{-2} K^{-1} (Lienhard and Lienhard, 2003).

For these reasons, the six thermal constants in Eqs.(3.91), (3.92) and (3.93) are roughly estimated for the purposes of this work and used as calibration parameters to obtain a plausible thermal difference between the inlet and outlet temperatures of the water and air flows.

A preliminary estimation of the thermal power removed from the air flow can be obtained using the rated values of the air mass flow used in Par.3.3.2.1.1 (0.015 kg s^{-1}) and assuming a maximum temperature difference between the inlet and outlet temperature of 20 K. Using the heat law, it is possible to estimate the thermal power as:

$$\dot{Q}_{ic} = \dot{m}_{air} c_{p_{air}} \Delta T = 0.015 \cdot 1005 \cdot 20 \approx 300\ W \tag{3.95}$$

where $c_{p_{air}}$ = 1005 J kg^{-1} K^{-1}. This value can be considered low if compared to conventional heat exchangers. Using this value, it is possible to obtain a first estimate of the heat exchanger area (A_{ic}) from the definition of the heat transfer coefficient (h):

$$\dot{Q}_{ic} = h_{H_{ic}} A_{ic} \Delta T_{H_{ic}} \ \rightarrow A_{ic} = \frac{\dot{Q}_{ic}}{h_{H_{ic}} \Delta T_{H_{ic}}} \approx 0.14\ m^2 \tag{3.96}$$

where the value used here for $h_{H_{ic}}$ is equal to 105, considered as the average of the interval given by Lienhard and Lienhard (2003). The temperature difference is equal to 20 K also in this case. Using the same approach for the water side, and using the area just find in Eq.(3.96), together with a temperature increase of 5 K, the corresponding cold side heat transfer coefficient can be determined as:

$$\dot{Q}_{ic} = h_{C_{ic}} A_{ic} \Delta T_{C_{ic}} \ \rightarrow h_{C_{ic}} = \frac{\dot{Q}_{ic}}{A_{ic} \Delta T_{C_{ic}}} \approx 428 \frac{W}{m^2 K} \tag{3.97}$$

This value, despite not being the average of the interval given by Lienhard and Lienhard (2003), is comprised in the interval itself.

The heat transfer coefficient for wall pipes ($h_{W_{ic}}$) can be determined in several ways, for instance, it can be used the following formula (Welty et al. 2007):

$$h_{W_{ic}} = \frac{2 k_{W_{ic}}}{d_i \cdot \ln\left(\frac{d_o}{d_i}\right)} \tag{3.98}$$

Where the $k_{W_{ic}}$ term is the thermal conductivity of the material used (about 16 W m^{-1}K^{-1}), while d_o and d_i are the outer and inner diameter of the tube. For a 5 mm (internal diameter) pipe, and with a thickness of 0.1 mm, the corresponding values of $h_{W_{ic}}$ would be of about 163,000 W m^{-2} K^{-1}, given the argument of the logarithm at the denominator near to one.

Apart from the thermal properties estimated here, the geometrical parameters (area and volume) involved are still important in the determination of the *K* constants. These values cannot be known and will be used as tuning parameters.

Considering a tube of 5 mm of diameter, the length of the tube required to obtain a total surface area equal to the one given in Eq.(3.96) should be of 8.9 meters. With these values, the internal volume of the cylinder of 5 mm of diameter and 8.9 meters long will be of about 0.175 liters. This value can help in giving the order of magnitude of the volumes involved. The volume of solid of this kind of tubing would be equal, instead, to 0.0143 liters, equal to an order of magnitude less than the gas volume.

The six values obtained using the data just introduced can be estimated in:

$$K_{1H_{ic}} = \frac{N_{ic}}{\rho_H V_H} = 46{,}700 \qquad K_{2H_{ic}} = \frac{h_{H_{ic}} A_{ic}}{c_{p_H} \rho_H V_H} = 68 \tag{3.99}$$

$$K_{1C_{ic}} = \frac{N_{ic}}{\rho_c V_C} = 57 \qquad K_{2C_{ic}} = \frac{h_{C_{ic}} A_{ic}}{c_{p_C} \rho_C V_C} = 0.082 \tag{3.100}$$

$$K_{1W_{ic}} = \frac{h_{H_{ic}} A_{ic}}{c_{p_W} \rho_W V_W} = 0.269 \qquad K_{2W_{ic}} = \frac{h_{C_{ic}} A_{ic}}{c_{p_W} \rho_W V_W} = 1.1 \tag{3.101}$$

Where for the wall material, stainless steel is used as reference, with a density (ρ_W) of 7800 kg m^{-3} and a specific heat (c_{p_W}) of 490 J kg^{-1} K^{-1}.

For simplicity, the volumes of the hot (air) and cold (water) sides are assumed equal to each other. The following simulations were done using these values.

The first set of simulations were done using constant values of inlet mass flows and temperatures to understand the transient behavior of the whole intercooler.

The first simulation was done using the maximum mass flow considered for the fuel cell at the cathode side (0.015 kg s^{-1}) at a temperature of 90°C (363 K). The water (coolant) flow was set at about 2.0 l min^{-1}, equal to 0.033 kg s^{-1} and entering at a temperature of 45°C (318 K). The initial outlet temperature of the hot and cold sides are of 60°C (333 K) and 27°C (300 K).

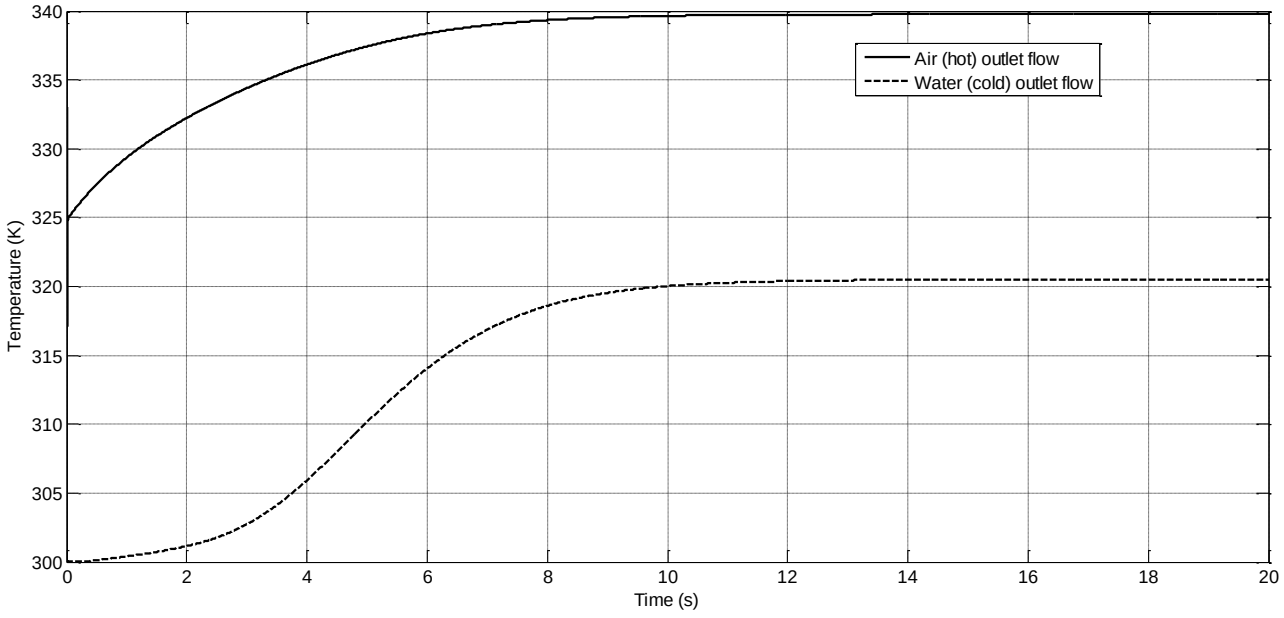

Figure 3.32 Intercooler outlet temperatures. Baseline values

As can be seen from Figure 3.32, the transient time can be estimated in about 11 seconds, with a steady-state asymptotic behavior. The temperature difference between the air inlet and outlet is equal to 23.2 K (363 – 339.8), while the water temperature rise is equal to 2.5 K (320.5 – 318). These temperature values can be considered compatible with the temperature differences used in the previous equations to estimate the thermal constants, which were set to 20 and 5 K for the air and water flows, respectively.

A step response is considered in Figure 3.33, where the inlet temperature is varied at T=20 s with a step, passing from the value of 50°C (323 K) to the value of 90°C (363 K).

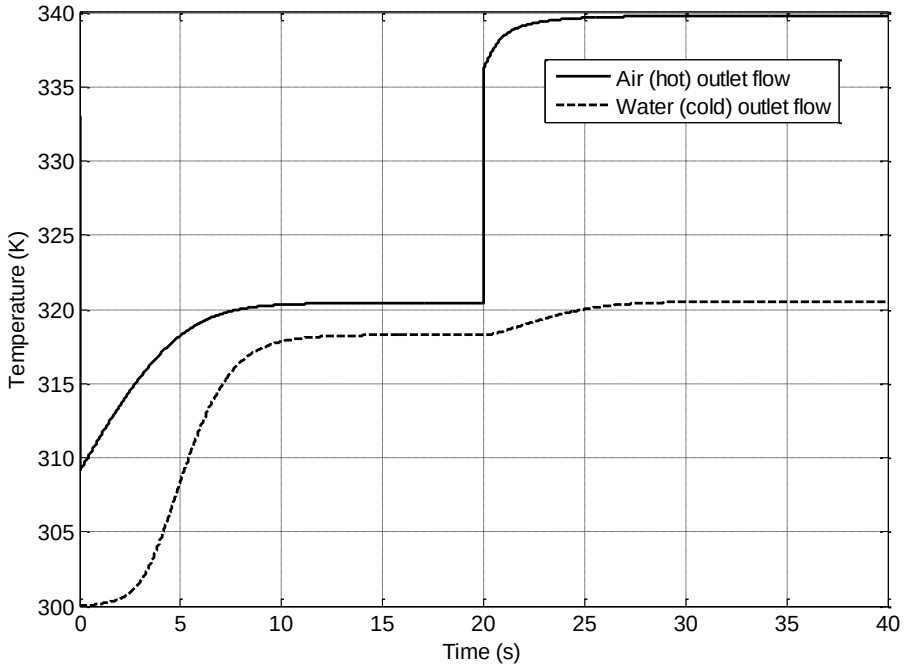

Figure 3.33 Intercooler outlet temperatures. Baseline values. Step response to air inlet temperature increase

In the case of a step command, the temperature of the two streams at the outlet changes with the temperature, since the mass flow of the two streams are kept equal. In this case, the temperature difference for the two streams are different for the 50°C inlet temperature portion, and equal to 2.6 K (323 - 320.4) and 0.3 K (318.3 – 318.0). The transient response for the step input is equal to the standard test case, obviously. The temperature values along the ten segments of the intercooler are given in Figure 3.35 for both the air and water flows. The stations identify the inlet and outlet values across the ten stations. Station 1 coincides with the inlet point, while station 11 is the outlet station for both the two streams. The baseline values for the simulation given in Figure 3.32 are used.

In case of a step variation in the mass flow of one of the two flows, the response is still similar to the previous analyses. The flow of the coolant water was reduced from 2.0 to 1.0 l min^{-1} with a step command. The plot of the outlet temperatures is given in Figure 3.34. A ramp increase in the air inlet temperature from 50°C to 90°C is also given in Figure 3.34, with a ramp slope of 1.0 K s^{-1} from T=20 s, and keeping the water mass flow cosnt6ant to 2.0 l min^{-1}.

Modifying the six thermal constants it should be possible to obtain, for a given mass flow and inlet temperature, a desired outlet temperature (and hence a temperature differential). Since the hot and cold flows are coupled together, as well as the wall, the modification of one of the thermal parameters should impact the thermal response of the two fluids.

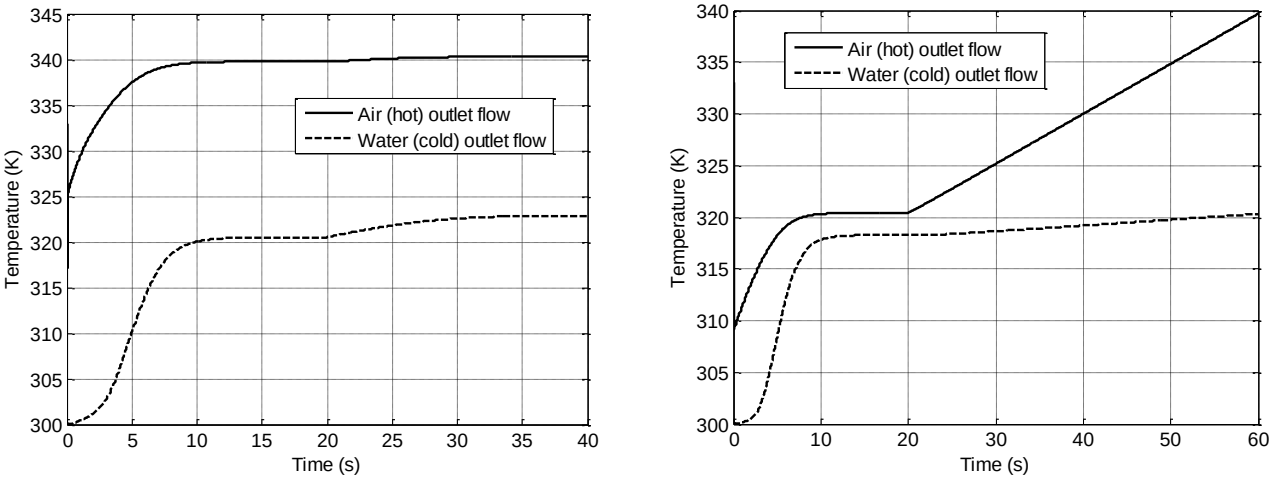

Figure 3.34 Intercooler outlet temperatures. Baseline values. Step response to water inlet mass flow decrease (Left side). Ramp response to air inlet temperature increase (right side)

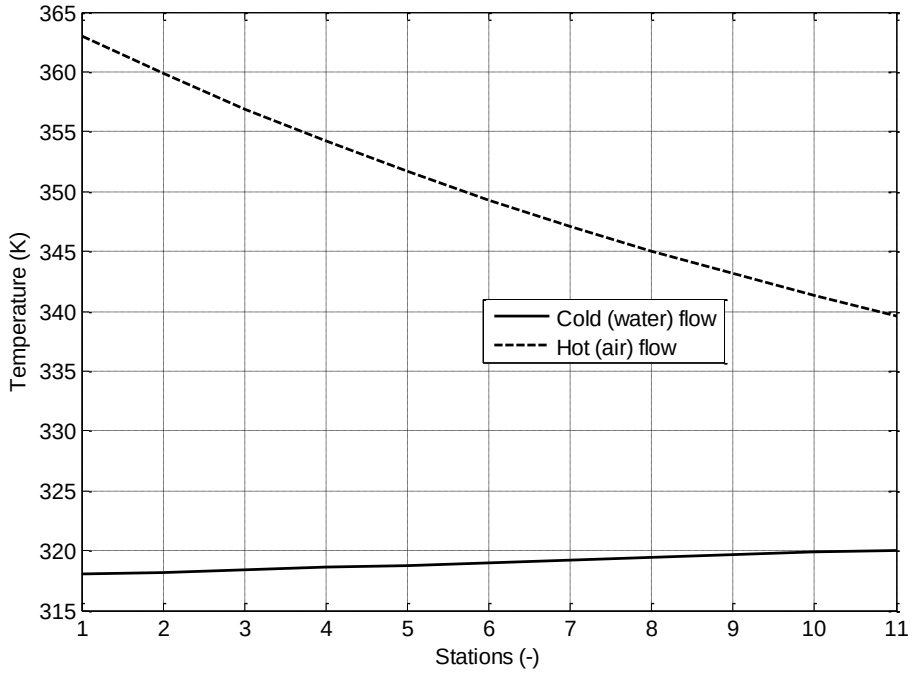

Figure 3.35 Intercooler hot and cold flow temperature profiles along the channels. Baseline values

The variation of the ±25% of the variables $K_{1H_{ic}}$ and $K_{2H_{ic}}$ gave results comparable with the baseline values for the hot air flow, and are not reported here for brevity. The variation of the cold side variables, instead, gave different results. The variation of the ±25% of $K_{1C_{ic}}$ and $K_{2C_{ic}}$, in fact, modified the transient response of the intercooler, but giving at the same time, the same steady-state behavior. This is shown in Figure 3.36, where the outlet temperatures for the air and water side are given. The behavior for the two sides is identical. Different steady-state values were instead reached varying together the variables involved at the two sides. Respectively, the $K_{1C_{ic}}$ and $K_{1H_{ic}}$. This can be seen in Figure 3.37. The variation given in the air side was more visible than the water side.

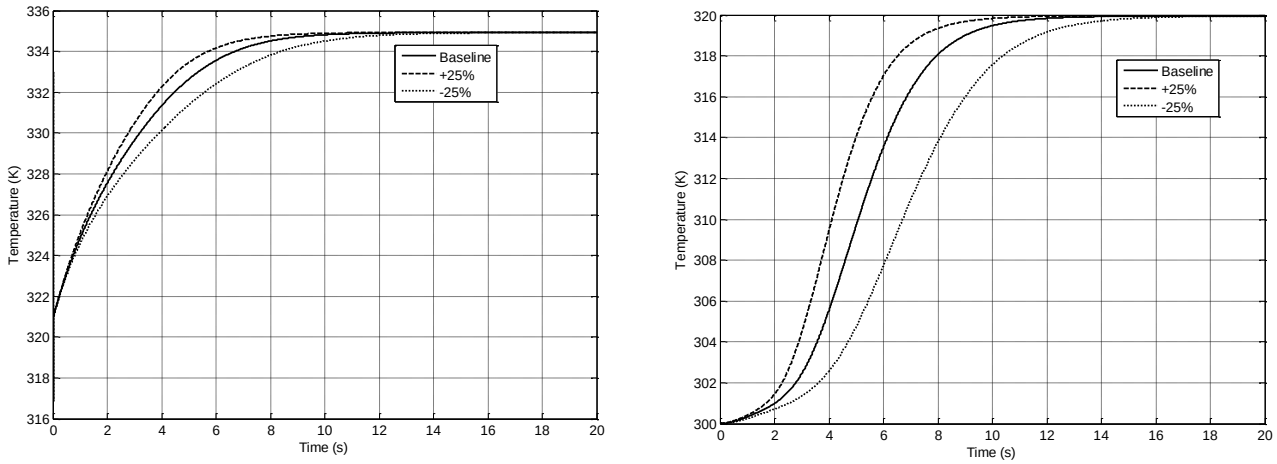

Figure 3.36 Outlet temperature variation obtained varying the $\boldsymbol{K_{1C_{ic}}}$ and $\boldsymbol{K_{2C_{ic}}}$ variables. Air side (left). Water side (right)

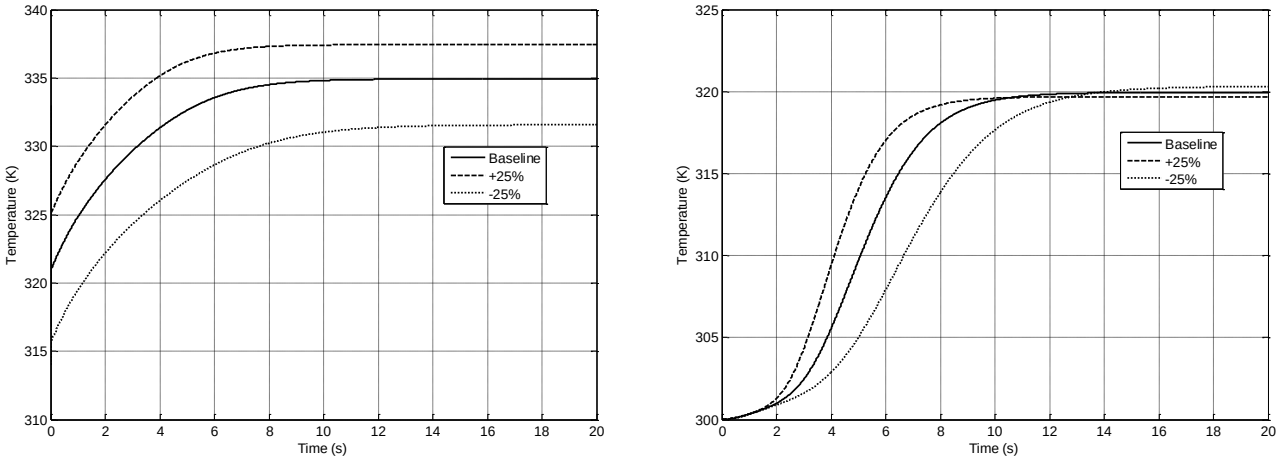

Figure 3.37 Outlet temperature variation obtained varying the $\boldsymbol{K_{1C_{ic}}}$ and $\boldsymbol{K_{1H_{ic}}}$ variables. Air side (left). Water side (right)

Similar results were obtained varying the other couple of variables, namely the $K_{2H_{ic}}$ and $K_{2C_{ic}}$ variables.

3.3.4 Membrane humidifiers

In the following paragraphs, cathode, anode and water humidifiers will be introduced and their model will be shown.

3.3.4.1 Cathode humidifier

The cathode humidifier implemented in this model is a membrane humidifier. Membrane humidifiers are humidifiers widely used in fuel cell applications, being compact, lightweight and without moving parts. Moreover, the humidification process is completely passive, i.e. it does not require any control to maintain the relative humidity level of the reactants.

Two main kinds of humidifiers are widely used, membrane humidifiers and bubble humidifiers. Bubble humidifiers are generally used for big power levels, requiring many kilowatts of power, and

hence requiring a high quantity of oxygen and hydrogen mass flows. Membrane humidifiers are instead suitable for small and medium power fuel cell stacks. In this work, membrane humidifiers are modelled.

The cathode humidifier is made of three blocks, representing the three regions in which the humidifier is made up of. Three domains are identified: the dry air duct, representing the air needing humidification (*dry air duct* block), the humid air duct, responsible for the humidification of the flow (*humid air duct* block) and the one devoted to the computation of the membrane humidification (*membrane flow* block).

Membrane humidifiers are made of an external barrel (in plastic or metallic material) containing a great amount of polymer channels, usually Nafion. Figure 3.38 shows the layout and principles of functioning of a membrane humidifier. The "exhaust air outlet" is usually the air/oxygen exiting from the cell stack, given the fact that exhaust gases are usually at high temperature and relative humidity, and represents the humid air duct in the model. It is also possible to substitute the exhaust air with other moisture rich flows coming from other parts of the systems. It is also possible to feed this duct with liquid water. The "dry air inlet" coincides with the flow that must be humidified. As can be seen, a large amount of Nafion tubes are present inside the humidifier (up to few thousands). Table 3.2 shows some data taken from one manufacturer. As can be seen, the number of tubes rises with the fluid flow needing humidification. Moreover, a single humidifier model allows for a wide variation of mass flow in terms of liters per minute.

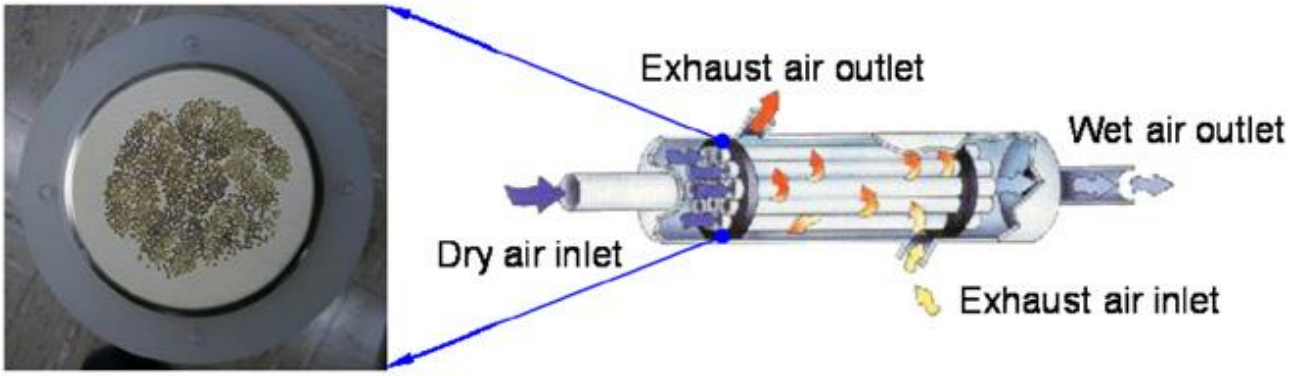

Figure 3.38 Membrane humidifier layout

Table 3.2 Membrane humidifiers flow data (PermaPure 2013)

Model	Number of Nafion tubes	Maximum delta pressure (bar)	Gas to gas flow range (slpm)	Water to gas flow range (slpm)
FC125	240	1.72	15-75	< 150
FC150	480	1.03	35-150	200-300
FC200	780	0.70	50-300	300-450
FC300	1660	0.35	120-625	450-1000
FC300HP	1660	3.0	120-625	450-1000
FC400	2500	0.35	200-1000	1000-1500
FC600	7000	0.35	500-2500	> 1500

The model of the cathode humidifier can be considered similar to a counter-flow heat exchanger, but with the important difference of allowing a selective mass flow of water through the walls of the heat exchanger. The model here presented is based essentially on the works by Park et al. (2008) and Chen et al. (2008). The model is modified to fit it in the Simulink environment. One of the main differences of this model from the others consist in the transient formulation of the membrane hydration done also for the PEM fuel cell (Par.3.3.1.4). The complete Simulink layout of the humidifier with its three main blocks is given in Figure 3.39.

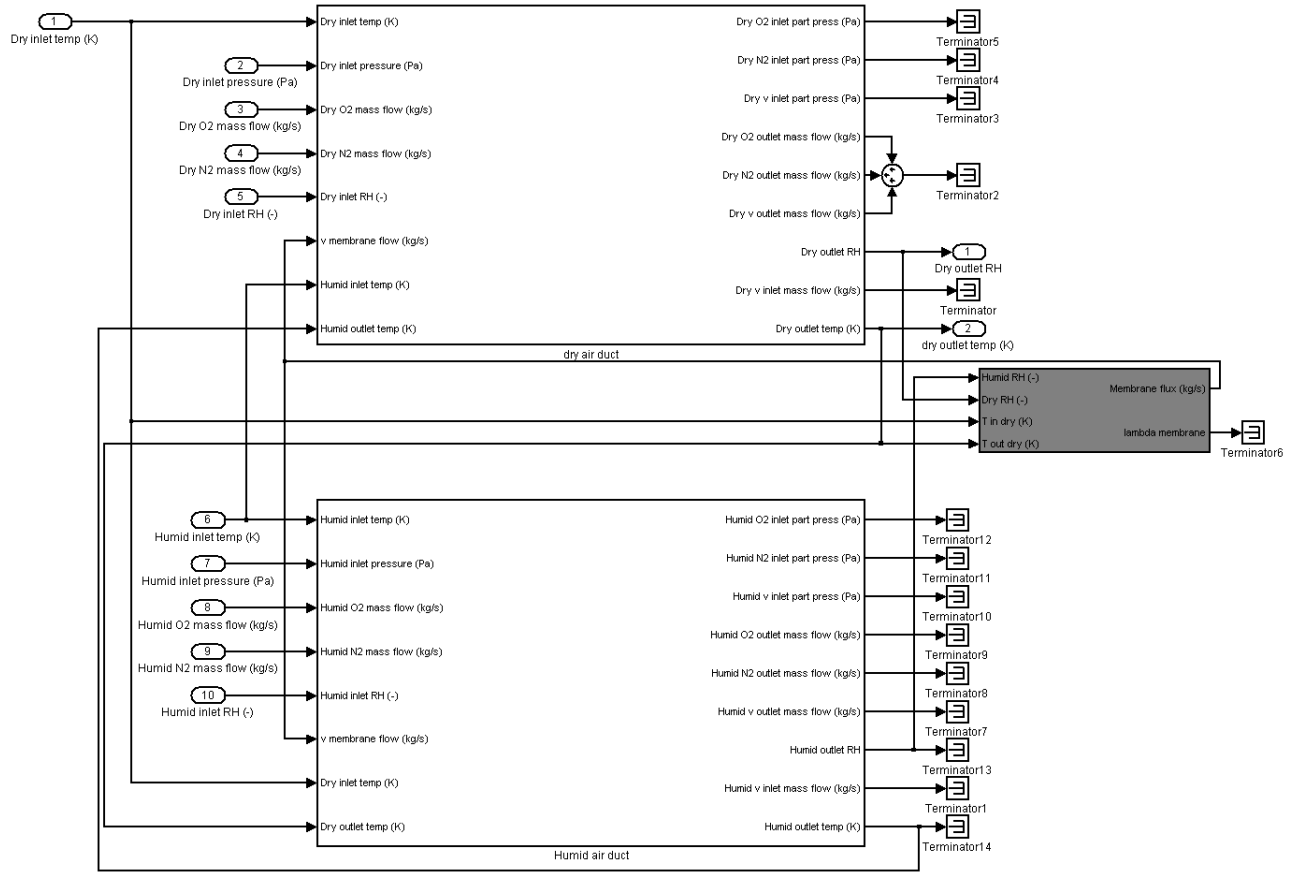

Figure 3.39 Cathode humidifier layout

The inlet data required by the humidifier are the inlet temperature, pressure, oxygen and nitrogen mass flows and relative humidity for both the dry and humid flows. All of these data comes from the other main blocks of the system (fuel cell stack outlet or compressor/intercooler, for instance). The output of the humidifier block is the outlet relative humidity and temperature, being them the only two data required by the fuel cell stack (humidifiers are usually placed just before the stack inlet).

Dry air duct block

The dry air duct block is shown in Figure 3.40. At the inlet, given temperature, pressure, relative humidity and mass flows of oxygen and nitrogen, the partial pressures of the three species involved (oxygen, nitrogen and water vapour) are calculated in the following way. The oxygen and nitrogen partial pressures are given by:

$$p_{O_{2_{in,dry}}} = p_{in,dry} \frac{\frac{O_{2_{in,dry}}}{\mathcal{M}_{O_2}}}{\frac{O_{2_{in,dry}}}{\mathcal{M}_{O_2}} + \frac{N_{2_{in,dry}}}{\mathcal{M}_{N_2}} + \frac{H_2O_{v_{in,dry}}}{\mathcal{M}_{H_2O}}} \tag{3.102}$$

$$p_{N_{2_{in,dry}}} = p_{in,dry} \frac{\frac{N_{2_{in,dry}}}{\mathcal{M}_{N_2}}}{\frac{O_{2_{in,dry}}}{\mathcal{M}_{O_2}} + \frac{N_{2_{in,dry}}}{\mathcal{M}_{N_2}} + \frac{H_2O_{v_{in,dry}}}{\mathcal{M}_{H_2O}}} \tag{3.103}$$

Where $p_{in,dry}$ is the inlet dry air side total pressure (given by the compressor block, for instance). O_2, N_2 and H_2O_v are the mass flows (kg s^{-1}) of oxygen, nitrogen and water vapor, respectively. Liquid water is not considered in this model. It is assumed the possible presence of liquid water can be neglected. The mass flow of water vapor is obtained directly from the inlet relative humidity. It can be calculated in terms of the inlet variables with the formula:

$$H_2O_{v_{in,dry}} = \left(\frac{O_{2_{in,dry}}}{\mathcal{M}_{O_2}} + \frac{N_{2_{in,dry}}}{\mathcal{M}_{N_2}}\right) \frac{p_{sat}(T_{in,dry})\phi_{in,dry}}{p_{in,dry} - p_{sat}(T_{in,dry})\phi_{in,dry}} \mathcal{M}_{H_2O} \tag{3.104}$$

The saturation pressure is calculated at the inlet temperature. All of the variables given in Eq.(3.104) are part of the input variables. The water vapor partial pressure is simply given by the product of saturation pressure and humidity:

$$p_{H_2O_v} = \phi_{in,dry} p_{sat}(T_{in,dry}) \tag{3.105}$$

The outlet mass flows at the dry side are computed considering the oxygen and nitrogen do not cross the membrane tubes, despite the Nafion membrane has a very small permeability to oxygen and nitrogen. In this way, the outlet nitrogen and oxygen flows coincide with the inlet ones. The only difference will be represented by the water vapour. Water vapour transport through the membrane is given by the permeability of the membrane to water. The outlet water vapour mass flow will be the given by:

$$H_2O_{v_{out,dry}} = \max\left(0.0;\ H_2O_{v_{in,dry}} + H_2O_{mem,humid}\right) \tag{3.106}$$

The term $H_2O_{mem,humid}$ is the membrane flow, assumed positive from the humid to the dry air side. In case of negative flows, the total value of the outlet mass flow could reach non-physical negative values. For this reason, it was implemented a max control in the Simulink model to keep the outlet value to a minimum value of 0.0 kg s^{-1}.

Due to the variation in temperature and water presence inside the humidifier, the dry outlet relative humidity changes. Since the mass flows at the outlet are given, it is possible to know the outlet molar flow (mol s^{-1}) and hence the molar fraction of each species. The partial pressures of oxygen, nitrogen and water vapour are simply given by:

$$p_{x_{out,dry}} = p_{out,dry} \frac{\frac{\dot{m}_x}{\mathcal{M}_x}}{\frac{O_{2_{out,dry}}}{\mathcal{M}_{O_2}} + \frac{N_{2_{out,dry}}}{\mathcal{M}_{N_2}} + \frac{H_2O_{v_{out,dry}}}{\mathcal{M}_{H_2O}}} \tag{3.107}$$

Where *x* is the *x-species*. The outlet pressure ($p_{out,dry}$) is considered equal to the inlet pressure, since most of the pressure drop occurring in the fuel cell system is given by the fuel cell stack. The relative humidity is given by the ratio between the vapor pressure and saturation pressure:

$$\phi_{out,dry} = \frac{p_{v_{out,dry}}}{p_{sat}(T_{out,dry})} \tag{3.108}$$

The outlet temperature ($T_{out,dry}$) is calculated in the following.

The thermal balance inside the dry air duct is written in the following way:

$$\begin{aligned} &\dot{Q}_{humid} + c_{p_{N_2O_2}}\left(N_{2_{in,dry}} + O_{2_{in,dry}}\right)T_{in,dry} + c_{p_{H_2O_v}}H_2O_{in,dry}T_{in,dry} \\ &- c_{p_{N_2O_2}}\left(N_{2_{out,dry}} + O_{2_{out,dry}}\right)T_{out,dry} - c_{p_{H_2O_v}}H_2O_{out,dry}T_{out,dry} \\ &+ c_{p_{H_2O_v}}H_2O_{mem,humid}\left(\frac{T_{in,dry} + T_{out,dry}}{2}\right) \\ &= c_{v_{N_2O_2}}m_{N_2O_{2dry}}\frac{d}{dt}\left(\frac{T_{in,dry} + T_{out,dry}}{2}\right) \\ &+ c_{v_{H_2O_v}}m_{H_2O_{v_{dry}}}\frac{d}{dt}\left(\frac{T_{in,dry} + T_{out,dry}}{2}\right) \end{aligned} \tag{3.109}$$

Eq.(3.109) is the thermal balance inside the dry air duct. On the left hand side of the equation, there is the thermal contribution ($\dot{Q}_{humid}$) due to the heat transfer between the dry and humid regions, detailed in the following. The heat transport given by the mass flow of nitrogen and oxygen, as well as water vapor is given by the second, third, fourth and fifth terms. It is conventionally assumed to have positive heat when entering the dry air channel. The term $c_{p_{N_2O_2}}$ is the specific heat of the mixture of nitrogen and oxygen and is calculated in the following. The heat transport is simply given by the balance between the energy entering in the duct at the inlet temperature ($T_{in,dry}$) minus the energy exiting from it at the outlet temperature ($T_{out,dry}$). It is here considered also the thermal transport given by the passage of water from the humid to the dry air duct (or vice-versa), and it is represented by the last term on the left hand side of the equation. Since water transport might occur along the full length of the dry air duct, and hence at different temperatures, it was assumed to consider the average between the inlet and outlet temperature, since this model is a mono-dimensional one. Eq.(3.109) balances the heat mass transport and the heat conduction with the variation in the internal energy of the duct, represented by the right hand side terms of the equation. The term $c_{v_{N_2O_2}}$ is the specific heat of the nitrogen and oxygen mixture at constant volume (in J kg^{-1} K^{-1}), while the two terms $m_{N_2O_2}$ and $m_{H_2O_v}$ are the mass (in kg) of nitrogen/oxygen and water vapour, respectively, contained in the dry air domain. Also in this case, the derivative of temperature is substituted by the average between the inlet and outlet temperature, for the same reason given above. Since the only unknown term in Eq.(3.109) is the outlet temperature ($T_{out,dry}$), it is possible to explicit its derivative from Eq.(3.109) and to integrate it over time using the Simulink *Integrator* block.

The mixture specific heats ($c_{P_{N_2O_2}}$ and $c_{v_{N_2O_2}}$) are calculated through the mass average using their mass flows:

$$c_{p_{N_2O_2}} = y_{O_2}c_{p_{O_2}} + y_{N_2}c_{p_{N_2}} \equiv \left(\frac{O_{2_{in,dry}}}{O_{2_{in,dry}} + N_{2_{in,dry}}}\right)c_{p_{O_2}} + \left(\frac{N_{2_{in,dry}}}{O_{2_{in,dry}} + N_{2_{in,dry}}}\right)c_{p_{N_2}} \tag{3.110}$$

$$c_{v_{N_2O_2}} = y_{O_2} c_{v_{O_2}} + y_{N_2} c_{v_{N_2}} \equiv \left(\frac{O_{2_{in},dry}}{O_{2_{in},dry} + N_{2_{in},dry}} \right) c_{v_{O_2}} + \left(\frac{N_{2_{in},dry}}{O_{2_{in},dry} + N_{2_{in},dry}} \right) c_{v_{N_2}} \quad (3.111)$$

Where the specific heats of oxygen and nitrogen are considered constant with temperature. The mass of the three species ($m_{N_2O_2}$ and $m_{H_2O_v}$) are calculated using the ideal gases law and using the inlet partial pressures:

$$m_{N_2O_2} = \frac{Vol_{dry,humid}}{RT_{in,dry}} \left(p_{N_2,in,dry} \mathcal{M}_{N_2} + p_{O_2,in,dry} \mathcal{M}_{O_2} \right) \quad (3.112)$$

$$m_{H_2O_v} = \frac{Vol_{dry,humid}}{RT_{in,dry}} p_{H_2O_v,in,dry} \mathcal{M}_{H_2O} \quad (3.113)$$

The term $Vol_{dry,humid}$ refers to the volume (in m^3) of the entire dry air duct of the humidifier. Its value can be easily obtained from the datasheets of commercial manufacturers (PermaPure® 2013).

The heat transfer between the dry and humid ducts ($\dot{Q}_{humid}$) is calculated using the following relation taken form, and it is quite complex.

In the case of the validity of the following relation:

$$\left| T_{in,hum} - T_{out,dry} \right| - \left| T_{out,hum} - T_{in,dry} \right| \cong 0 \quad (3.114)$$

Then the heat transfer is given by:

$$\dot{Q}_{humid} = UA_{humid} \frac{\left| T_{in,hum} - T_{out,dry} \right| - \left| T_{out,hum} - T_{in,dry} \right|}{\ln \left(\frac{\left| T_{in,hum} - T_{out,dry} \right|}{\left| T_{out,hum} - T_{in,dry} \right|} \right)} sgn\left(T_{out,hum} - T_{out,dry} \right) \quad (3.115)$$

Alternatively, the following relation holds:

$$\dot{Q}_{humid} = UA_{humid} \left| T_{in,hum} - T_{out,dry} \right| sgn\left(T_{out,hum} - T_{out,dry} \right) \quad (3.116)$$

The terms with the *hum* subscript refer to the humid air duct. UA_{humid} is the heat exchange coefficient (in W K^{-1}) of the humidifier and must be intended as a possible calibration coefficient. *sgn* is the sign function.

Humid air duct block

The *humid air duct* block is almost completely identical and symmetrical to the *dry air duct* block just discussed. Anyway, there are few differences. The outlet water vapor mass flow is given by:

$$H_2O_{v_{out,hum}} = \max \left(0.0;\ H_2O_{v_{in,hum}} - H_2O_{mem,humid} \right) \quad (3.117)$$

The plus sign of Eq.(3.106) is substituted by the minus sign. Another double sign change is in the heat equation of Eq.(3.109) at the heat and water membrane flow ($\dot{Q}_{hum}$ and $H_2O_{mem,humid}$):

$$
\begin{aligned}
-\dot{Q}_{humid} &+ c_{p_{N_2O_2}}\left(N_{2_{in,hum}} + O_{2_{in,hum}}\right)T_{in,hum} + c_{p_{H_2O_v}}H_2O_{in,hum}T_{in,hum} \\
&- c_{p_{N_2O_2}}\left(N_{2_{out,hum}} + O_{2_{out,hum}}\right)T_{out,hum} \\
&- c_{p_{H_2O_v}}H_2O_{out,hum}T_{out,hum} \\
&- c_{p_{H_2O_v}}H_2O_{mem,humid}\left(\frac{T_{in,hum} + T_{out,hum}}{2}\right) \\
&= c_{v_{N_2O_2}}m_{N_2O_{2hum}}\frac{d}{dt}\left(\frac{T_{in,hum} + T_{out,hum}}{2}\right) \\
&+ c_{v_{H_2O_v}}m_{H_2O_{vhum}}\frac{d}{dt}\left(\frac{T_{in,hum} + T_{out,hum}}{2}\right)
\end{aligned}
\tag{3.118}
$$

All the other equations are the same, except the *hum* subscript substituting the *dry* one, since all of the variables are related to the humid air duct.

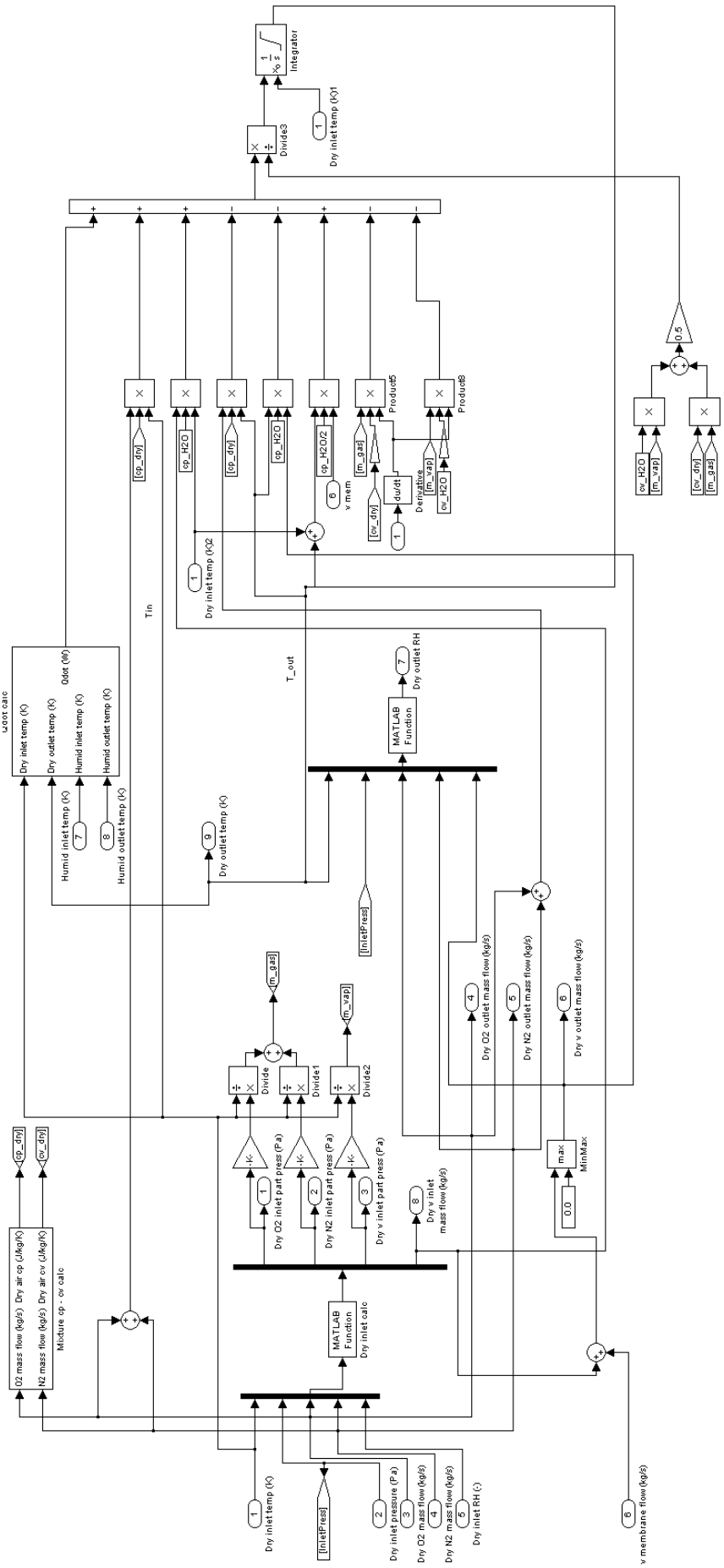

Figure 3.40 Humidifier dry air duct block

Membrane flow block

The *membrane flow* block merges the information coming from the dry and humid air ducts. This block uses the dry and humid relative humidity and the inlet and outlet dry air duct temperatures, and gives as output the membrane flux used by both the humid and dry air duct blocks. As can be seen, an algebraic loop would be present. A delay block, nevertheless, is placed at the exit of the outputted membrane flow, avoiding the algebraic loop. This delay allows the user to set some additional transient response of the humidifier membrane. Nevertheless, the transient response of it is already modelled in the block, and the delay constant should be set to a minimum. The modelling of water transport through the membrane is identical to the modelling given for the fuel cell stack. Some important differences are present, anyway. The membrane thickness (t_{mem}) is in this case substituted by the channel wall thickness (t_{humid}) and the fuel cell area (A) is replaced by the external surface of the channels (A_{humid}). Moreover, in the case of the humidifier, no current is present, so the electro-osmotic drag from the anode to the cathode side looses physical validity. In the case of the humidifier, the only relevant force for the transport of water from the dry to the humid air duct is the concentration gradient imposed on the two sides by the difference in relative humidity at the two sides.

Apart from these differences, the membrane model of the humidifier uses the same equations of its counterpart for the stack membrane (Par.3.3.1.4).

A last consideration must be done for the choice of the relative humidity values. Since the model is lumped, three possible choices for the computation of the relative humidity can be done: the use of the RH at inlet, at outlet or a possible average between inlet and outlet. The second choice was done for this model, i.e. the outlet relative humidity values are used for the computation of the membrane water presence at the two sides of the Nafion channels. This choice was done performing several simulations and comparing the outlet humidity values of the dry and humid sides. The same trials were done maintaining the temperature constant (UA_{humid} and temperature differences equal to zero) and with a great variety of temperature and thermal exchange differences.

Considering the physical nature of the humidifier, in the case of a humid air duct rich in water vapour and the dry air duct poor in water vapour, it is logical to suppose the humid air duct will lose water vapour through its path – from the inlet to the outlet, in a progressive way. On the other hand, the dry air duct will receive water in the same manner from the inlet to the outlet. In the extreme case, when the relative humidity of the humid side would reach the sale value of the dry one, water passage from the humid side to the dry one will stop in an asymptotic way. Apart from some numerical fluctuations, the relative humidity of the dry side will be always less or equal to the humid one, always considering channels with blended temperature variations. Using the inlet values for humidity, it was possible to note in the plot of the relative humidity that the dry air duct humidity at the exit was higher than the relative humidity of the humid side, not consistent with the physical laws governing the humidifier. Even using the average between the inlet and outlet similar results were observed. Instead, the choice of the outlet relative humidity maintains the relative humidity on the two sides at the exit consistent with a physical explanation.

3.3.4.1.1 Model setup and simulation results

The overall model testing is now presented. For this test, the model PermaPure® membrane humidifier (FC300-1666-15ABS) is chosen. Its characteristics are reported in Table 3.3. Some data used for the simulation are directly derived from these data and presented in the same table.

Table 3.3 PermaPure humidifier physical properties (PermaPure 2013)

Characteristics	FC300-1660-15ABS humidifier	FC200-780-10PP humidifier
Manufacturer data		
Tube length (m)	0.381	0.264
Number of tubes (-)	1660	780
Inner tube diameter (m)	0.97×10^{-3}	0.97×10^{-3}
Tube wall thickness (m)	0.025×10^{-3}	0.025×10^{-3}
External shell diameter (m)	0.1	0.0545
Derived data		
Outer tube diameter (m)	1.020×10^{-3}	1.020×10^{-3}
Transverse inner total area (m^2)	1.226×10^{-3}	5.764×10^{-4}
Transverse outer total area (m^2)	6.469×10^{-3}	1.696×10^{-3}
Humid side available volume (m^3)	2.475×10^{-3}	4.462×10^{-4}
Dry side available volume (m^3)	4.673×10^{-4}	1.517×10^{-4}
Dry-humid duct exchange area (m^2)	2.0267	0.6577

The manufacturer provides also the relation (Figure 3.41) between mass flow (in slpm) and the temperature difference between the humid inlet flow temperature and the dry outlet flow temperature (i.e. the approach temperature).

Model Number	Approach Temperature*		
	4 Deg.	6 Deg.	9 Deg.
FC125-240-5PP	13	30	40
FC125-240-7PP	18	42	56
FC125-240-10PP	25	60	80
FC150-480-7PP	35	84	112
FC150-480-10PP	50	120	160
FC200-780-7PP	57	137	182
FC200-780-10PP	80	195	260
FC300-1660-7ABS	121	291	387
FC300-1660-10ABS	173	415	553
FC300-1660-10HP	173	415	553
FC300-1660-15ABS	259	623	830
FC400-2500-10ABS	260	625	833
FC400-2500-12ABS	312	750	1000
FC400-2500-15ABS	390	938	1250
FC400-2500-20ABS	520	1250	1667
FC600-7000-8PP	583	1400	1860
FC600-7000-14PP	1020	2450	3267

Figure 3.41 PermaPure membrane humidifier mass flow (in slpm) vs. approach temperatures

In the following simulation tests, the average value of 623 slpm is used. This corresponds to a dry inlet mass flow of 0.014 kg s^{-1} of air at standard conditions. This value will be kept constant, while the other variables will be changed.

The first test consider the exchange in water content due to the sole difference in the humidity content in the two streams. Humid inlet flow is set at $\varphi=1.0$, and dry inlet flow at $\varphi=0.5$. Using the same mass flow (0.014 kg s^{-1}) and the same temperature at the two sides (340 K), posing the UA_{humid} value equal to 0.0 and neglecting the latent heat of vaporization, it is possible to understand the behavior of the humidifier in absence of phase change and thermal exchange between the two sides. This can be seen in Figure 3.42, where the relative humidity values of the two outlets is plotted vs. time. The transient can be considered a sort of first order. In this case, the

difference in humidity at the two sides is responsible of water transfer from one side to the other. The rise in water content from one side corresponds to the lowering on the other one. Since temperatures are the same and are kept constant, the relative humidity and absolute humidity coincide in this case. If the dry inlet temperature is lowered, instead, the outlet relative humidity will obviously change, as can be seen in Figure 3.43. Here, the temperature of the dry inlet flow is varied in decrements of ten degrees from 340 to 300 °C. In this case, the different temperature between the humid and dry flow, makes the coincidence of absolute and relative humidity no longer valid. The lower the temperature of the dry flow, the lower its ability to absorb water, the higher its relative humidity. Vice-versa for the humid flow, always kept at 340°C.

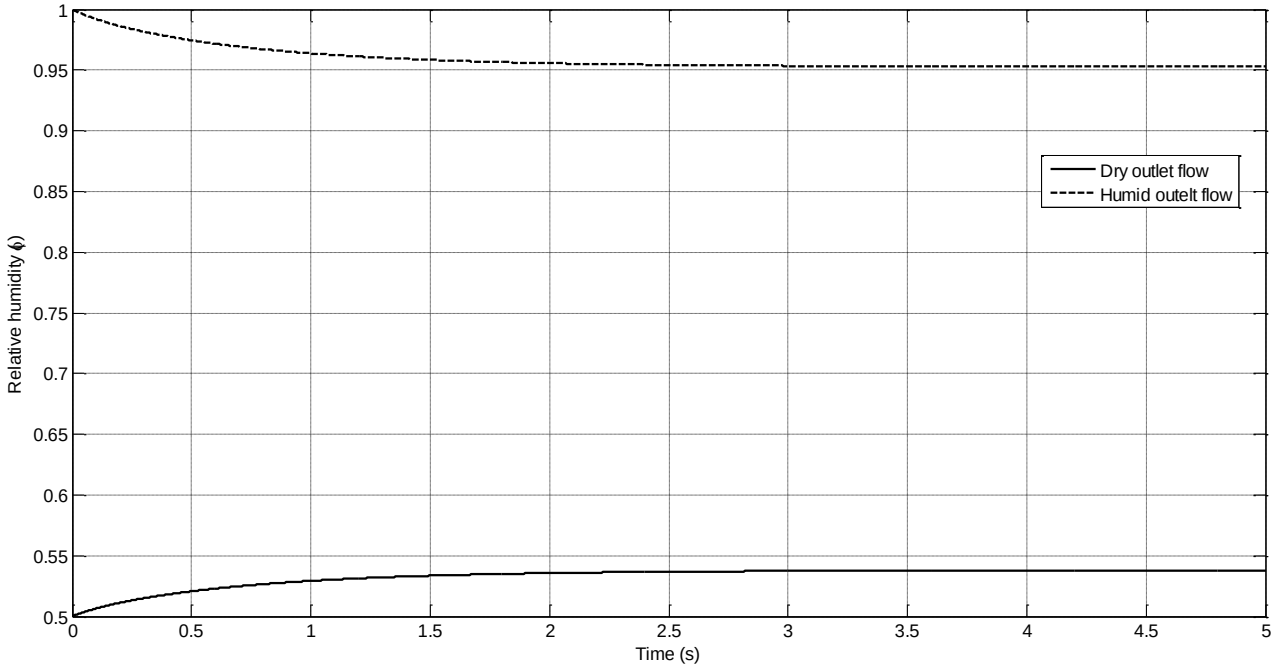

Figure 3.42 Cathode humidifier outlet flow relative humidity

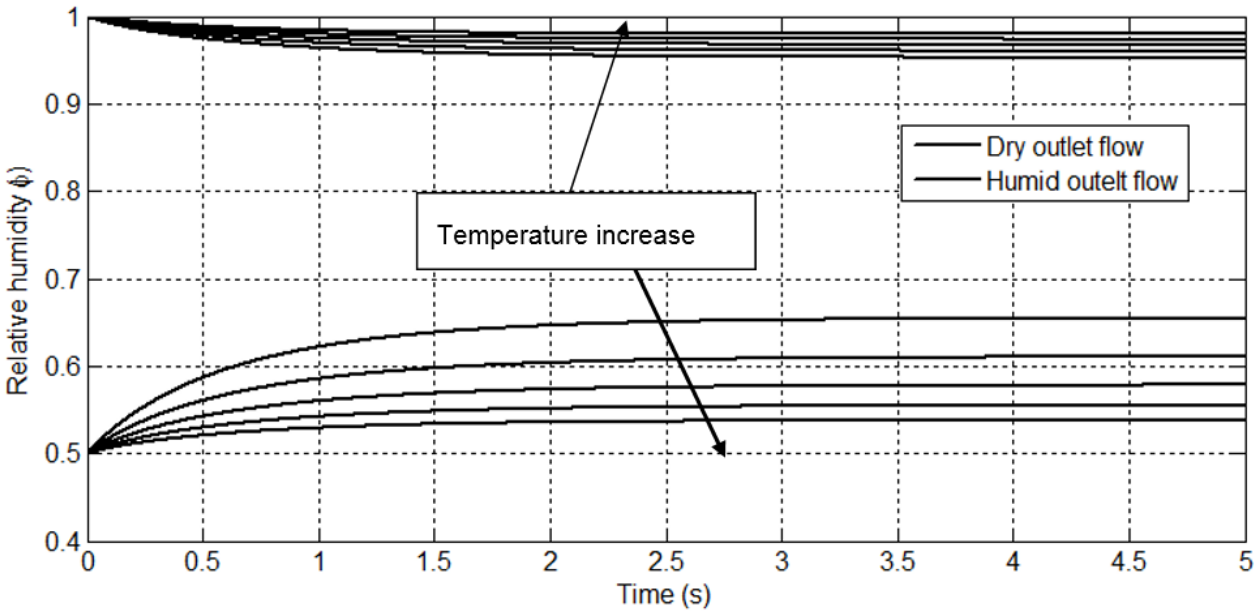

Figure 3.43 Variation in outlet relative humidity with temperature. Null heat exchange. Uniform flows.

A variation of the mass flow value of the humid duct does not have any consequence, and it is not reported here for brevity.
When all the thermal phenomena involved in the humidifier are considered, the temperature variations in the two streams play a more important role. Considering the present humidifier, the humid air duct is fed directly by the exhaust gas stream coming from the outlet. For this reason this stream is about at the same temperature of the stack and it is made of high relative humidity content, given by the by-product water. Moreover, its mass flow can be easily calculated if the stoichiometric value is known. Supposing a value of about 1.5, the outlet flow will be one third of the inlet flow (0.5/1.5). In the next simulations a temperature of 70°C for both the dry and humid flow were used. The dry inlet flow corresponds to a total mass flow of 0.014 kg s^{-1}, the humid inlet flow was taken equal to one third of this value (0.005 kg s^{-1}), with a relative humidity value equal to 1.0. The dry air flow humidity was set at 0.3, given the high temperature of the gases. A trial value of $UA_{humid} = 2.0$ W K^{-1} was used.

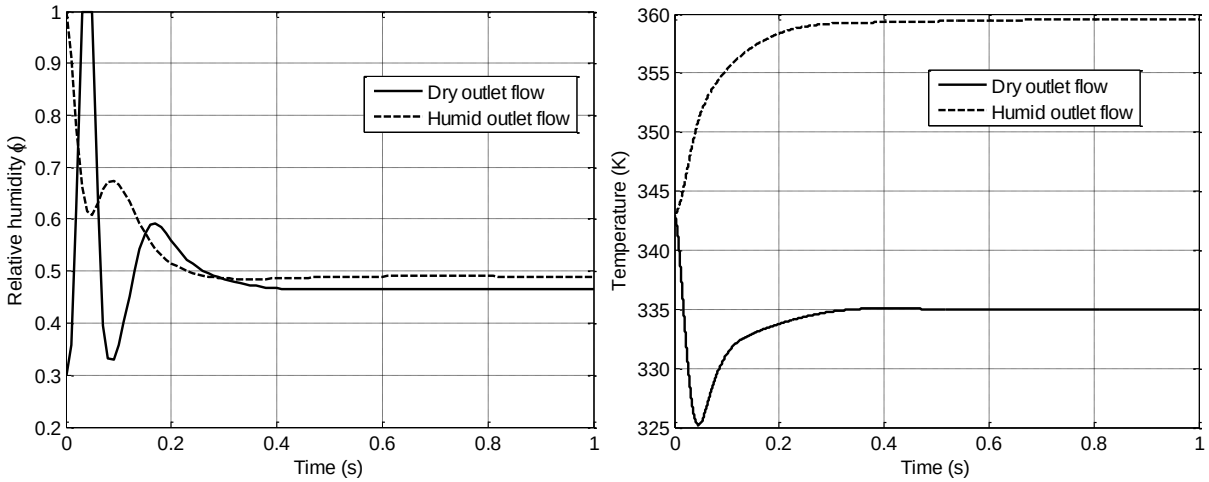

Figure 3.44 Humidifier outlet humidity and temperature values

Figure 3.44 shows the temperature and relative humidity transient behaviour for the dry and humid air duct. As can be seen, the transient phenomena are in the order of 0.5 seconds and show some pronounced oscillations for the relative humidity. At the end of the transient, the humidity values of the two streams are quite similar to each other, reaching an equilibrium condition with the humid air duct slightly more wetted than the dry one. The temperature plot, instead, shows a peculiarity of membrane humidifiers. Despite the equal initial temperature of the two streams, the passage of water from one side to the other lowers the temperature of the dry air side and rises the temperature of the humid one, acting not only as a humidifier but also as a cooler for the fluid needing humidification. This can be easily explained considering the heat of vaporization of water. At the dry side, water passes from liquid form, from the surface of the membrane, to gaseous form in the fluid stream, absorbing heat from the dry side (thus lowering the temperature) and releasing it when passing from gaseous to liquid on the humid side (increasing the humid side temperature). In this case there is a decrease of 8 K on the dry side. This value coincides with the definition of approach temperature, given the fact that the two sides used the same inlet temperature.

An important aspect coming from Figure 3.44 consists in having only a slight increase in the relative humidity of the dry side, passing from 0.3 to about 0.45, despite the maximum value (1.0) at the humid side. This can be explained considering that the humid side rises its temperature, thus lowering its relative humidity. Moreover, water passes from this side to the other one, lowering the

amount of content in it. These two effects lower the relative humidity at the humid side rapidly, bringing to an equilibrium value between the two sides at a low level. Another aspect to take into account is the mass flow of the fluid stream, being about one third.

In the practical case, given the high relative humidity content at the stack outlet, the flow is usually over-saturated with water, which is transported in aerosol liquid form inside the humidifier, where a small amount of water usually accumulates, providing a reservoir of liquid water. In this model, this aspect is not directly simulated, but can be easily obtained imposing a relative humidity value always equal to 1.0 in the whole humid duct. Doing in this way, the relative humidity at the exit of the dry air duct increases, as can be seen in Figure 3.45.

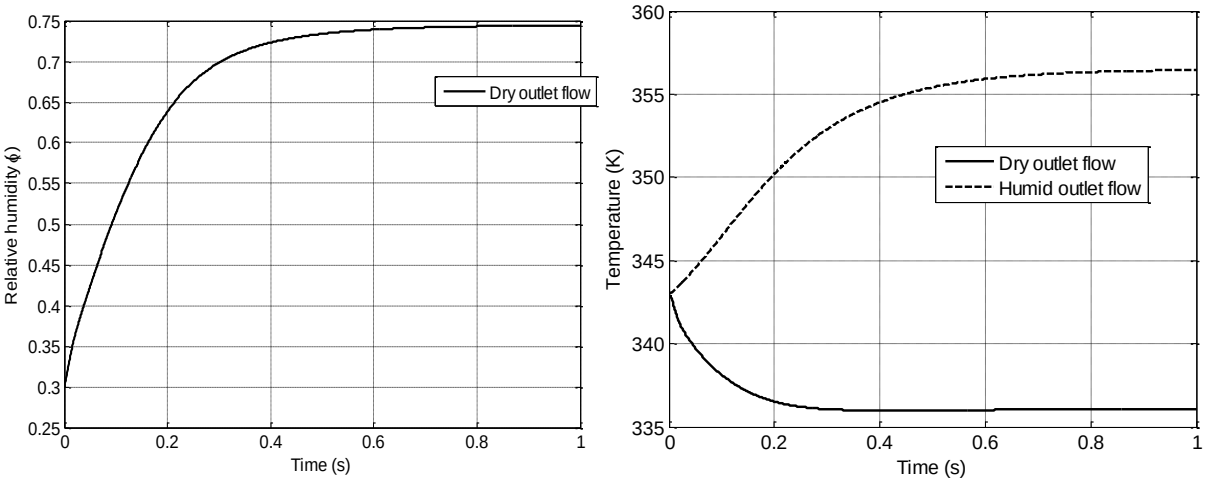

Figure 3.45 Humidifier outlet humidity and temperature values using constant humid side relative humidity

The membrane humidification (λ_{mem}) and water flow for this second test case is shown in Figure 3.46. The transient response of these two variables are the same of temperature and relative humidity reported in Figure 3.45, indicating that thermal and fluid-dynamics evolve at the same time.

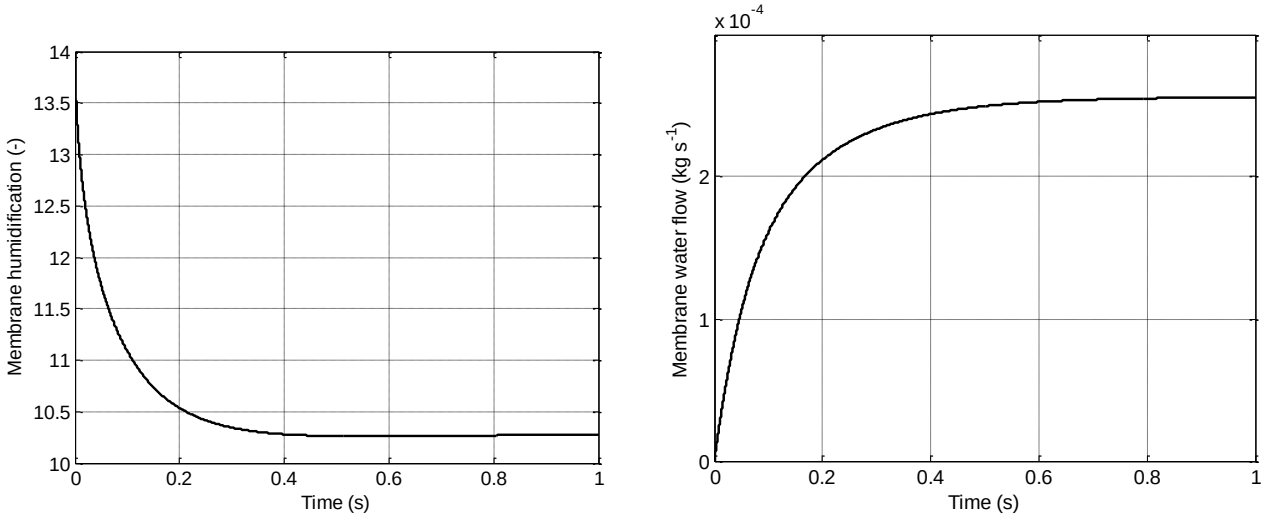

Figure 3.46 Humidifier membrane humidification and water flow

The variation of relative humidity at the dry inlet is reported in Figure 3.47. As can be seen, a great variation in the inlet relative humidity has a low effect on the corresponding outlet humidity. Increasing the inlet humidity from 0.0 to 0.7, the variation at the outlet passes from about 0.729 to about 0.784, indicating a good response of the humidifier to variations in the inlet conditions. An even more compact distribution of values can be seen when varying the inlet mass flow requiring humidification (Figure 3.48). In this latter case, the inlet mass flow was varied of minus/plus 20 and 30 percent from the baseline value (0.011 kg s^{-1}), with a dry inlet humidity equal to 0.3.

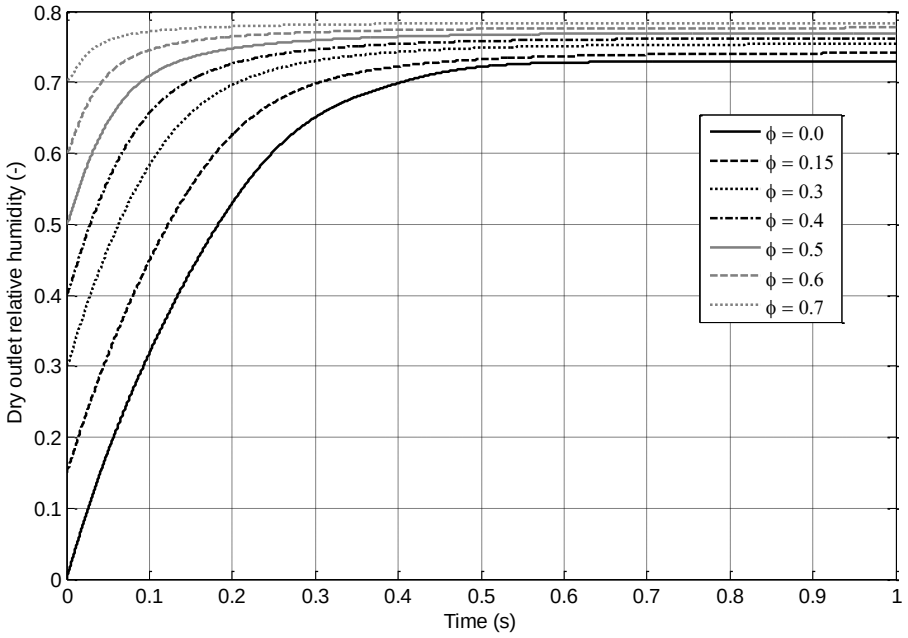

Figure 3.47 Dry outlet relative humidity vs. time. Different dry inlet relative humidity values

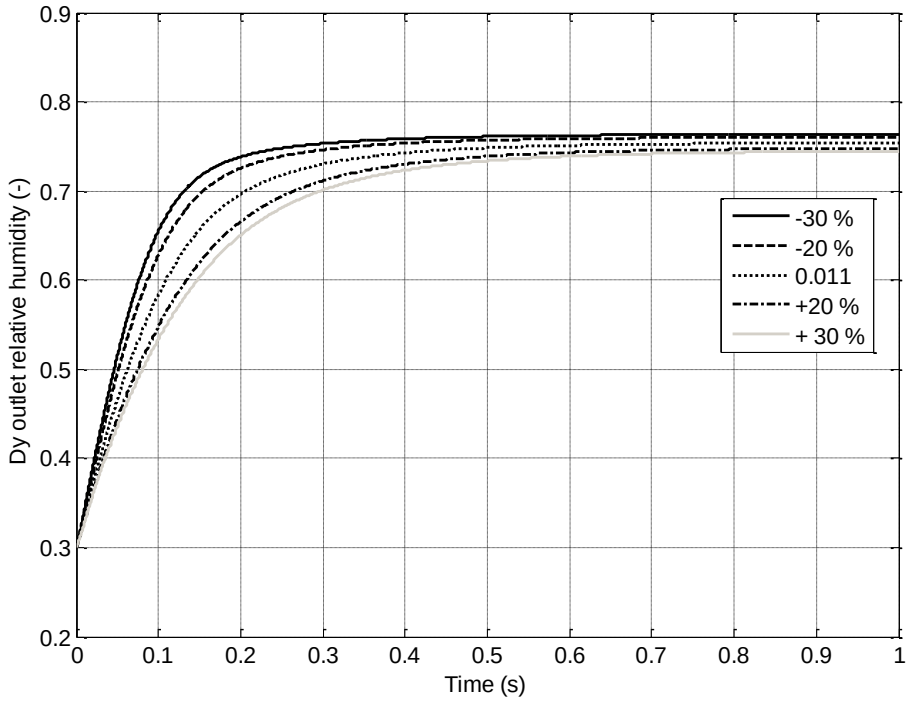

Figure 3.48 Dry outlet relative humidity vs. time. Different mass flow inlet values. Baseline value: 0.011 kg s^{-1}

The calibration and validation of the model for the cathode membrane humidifier is based on the available data given by PermaPure® (2013). In particular, PermaPure gives the values of the dry outlet temperature and relative humidity, evaluable from Figure 3.41. The validation of the model was based on three different mass flow values (Figure 3.41). Using the value of UA_{humid} and the membrane diffusion constant (k_{mem}) as calibration parameters, related to the thermal exchange and membrane water diffusion constant, the first operating point (259 slpm) was chosen. The mass flow of the humid air flow was set equal to the dry air mass flow. Table 3.4 shows the three mass flow values and their related temperature and humidity at the dry air outlet, as indicated by the manufacturer. The variation of the two calibration parameters allowed a perfect correspondence of relative humidity and temperature. The other two points were then simulated varying the inlet mass flow, and the corresponding errors in simulated and manufacturer data (i.e. the empirical data) are given in Table 3.4. As can be seen, the temperature error is very small, with a maximum relative error of about the 0.6%, while the relative humidity error is instead higher, but it can be considered still acceptable, being of about the 7.8%. This result can be considered a good one, since some geometrical and physical data were not known from the manufacturer.

Table 3.4 Cathode humidifier model validation and calibration

Mass flow	**Empirical data**		**Model data**		**Error**	
(slpm)	Temperature (K)	Relative humidity (%)	Temperature (K)	Relative humidity (%)	Relative humidity (%)	Temperature (%)
259	339	83.5	339.0	83.5	0	0
623	337	76.0	337.7	70.1	7.763	0.208
830	334	65.3	336.0	64.5	1.225	0.599

The values of UA_{humid} and k_{mem} used to obtain the data in Table 3.4 are equal to 155 W K^{-1} and 0.134.

3.3.4.2 Anode humidifier

The anode humidifier model is completely symmetrical to the cathode humidifier. Membrane humidifiers, in fact, works in the same way for both air (or oxygen) and hydrogen without any difference. The only main difference comes from the different mass flows occurring at the anode side (less than the cathode ones), implying the use of smaller humidifiers for the anode if compared to the cathode ones. Also the different thermal properties of hydrogen compared to air (or oxygen) can produce some different results in the thermal behavior of the humidifier. The model of the anode humidifier is therefore identical to the cathode humidifier just presented (Par.3.3.4.1). Thanks to the use of nitrogen on both the hydrogen and oxygen sides, it was possible to maintain the same model, with the only substitution of hydrogen species (and its physical and thermal properties) to the oxygen one, in a way similar to the anode and cathode models of the fuel cell stack.

For brevity, the equations for the anode side humidifier are not reported.

3.3.4.2.1 Model setup and simulation results

This model is similar to the cathode humidifier, except for the gas and dimensions used. All of the data and discussions presented in Par.3.3.4.2.1 are therefore valid also for this second case. The validation process was done in the same way of the previous one, selecting as a possible candidate as anode humidifier the version FC-200-780-10PP (Figure 3.41). The same procedure of the cathode humidifier was followed, using air instead of hydrogen, given the fact that the operating

parameters given by the manufacturer are related to air flow. The results are similar to the cathode ones and are presented in Table 3.5.

Table 3.5 Anode humidifier model validation and calibration

Mass flow	**Empirical data**		**Model data**		**Error**	
(slpm)	Temperature (K)	Relative humidity (%)	Temperature (K)	Relative humidity (%)	Relative humidity (%)	Temperature (%)
80	339	83.5	339.0	83.5	0	0
195	337	76.0	337.5	69.6	8.421	0.148
260	334	65.3	337.3	64.4	1.378	0.089

The values of UA_{humid} and k_{mem} used to obtain the data in Table 3.5 are equal to 52 W K^{-1} and 0.144. The maximum error in relative humidity can be considered comparable to the cathode humidifier (8.421 vs. 7.763) and acceptable, as well as the temperature one. The difference in the k_{mem} value can be considered part of the uncertainties and errors in the model and empirical data. The difference in the *UA* value can be easily explained considering the fact that this value is directly related to the thermal exchange (*U* term) and interface area (*A* term) between the dry and humid ducts. Since the thermal exchange term should be the same in case of the same fluid, the only variable is the *A* term. If the thermal exchange area of the two humidifiers reported in Table 3.3 are compared, their ratio give a value of 3.08. This value is practically identical to the ratio between the two UA_{humid} values, corresponding to 2.98. This last result confirms the validity of this model. Using these data it is also possible to estimate the *U* term, which can be calculated in the range 76.4 - 79.1 W.

3.3.4.2.2 Water-gas membrane humidifiers

Given the possibility to use water or another moisture-rich gas as a humidification media for the membrane humidifiers, a model of a water-gas humidifier was also developed. The water-gas humidifier is quite similar to the gas-gas humidifiers just presented in the above paragraphs (Par.3.3.4.1 and Par.3.3.4.2). The main difference consists in the humid side of the channel, which is completely filled with liquid water. Hence, the relative humidity of the humid side will be always placed to 1.0. In this model, water evaporation inside the humid duct is not contemplated. Another difference comes from the thermal balance equation in this side.

The water-gas humidifier is developed only for the hydrogen side, given the fact that at the oxygen side it is usually more convenient to use exhaust gases from the stack instead of a liquid. Anyway, it would be possible to modify its model simply substituting oxygen to hydrogen, as for the case of cathode and anode humidifiers just introduced.

The model is made up of three blocks, namely the *dry air duct* block, the *water duct* block and the *membrane hydration* block.

Dry air duct block

This block is identical to the same block already seen in the cathode humidifier *dry air duct* block.

Water duct block

This block results simplified if compared to the corresponding block (the *humid air duct* block) of the cathode humidifier. Since liquid water is present, it is not necessary compute any of the partial pressures given by gases. Moreover, the relative humidity is here fixed to 1.0 (even if the relative humidity concept for liquid flows looses physical sense). This un-physical value is simply used to fix the water presence at the Nafion membrane wall to its maximum level.

The outlet liquid water mass flow is simply given by:

$$H_2O_{l_{out,hum}} = \max\left(0.0;\ H_2O_{l_{in,wat}} - H_2O_{mem,wat}\right) \tag{3.119}$$

The *l* subscript stands for "liquid" water, while *wat* means the water side of the humidifier.

The thermal balance equation modifies in the following form:

$$\begin{aligned} &-\dot{Q}_{humid} + c_{p_{H_2O_l}} H_2O_{l_{in,wat}} T_{in,wat} - c_{p_{H_2O_l}} H_2O_{l_{out,wat}} T_{out,wat} \\ &\quad - c_{p_{H_2O_l}} H_2O_{mem,humid} \left(\frac{T_{in,wat} + T_{out,wat}}{2}\right) \\ &\quad = c_{p_{H_2O_l}}\, m_{H_2O_{l_{wat}}} \frac{d}{dt}\left(\frac{T_{in,wat} + T_{out,wat}}{2}\right) \end{aligned} \tag{3.120}$$

Membrane hydration block

This block is identical to the block seen for the cathode gas-gas humidifier. The only difference is given by the use of a constant value (1.0) for the relative humidity of the water side.

3.3.1 Hydrogen flow mixer

This model was developed to allow the mixture of two flows coming from different sources at different temperatures and compositions. In this particular case, the mixer here developed was used to model the combination between the hydrogen coming from the hydrogen tank with the one coming from the outlet of the stack anode, containing a high amount of hydrogen and water vapor. This model can be almost considered a sort of "sum" block, since it introduces only some simple equations. Its layout is shown in Figure 3.49. It is here assumed the hydrogen coming from the tank consists of pure hydrogen, without water vapor or other contaminants.

This model operates summing the nitrogen, hydrogen and water vapor coming from two inlets. The temperature given by the two temperatures of the two streams is calculated in a sort of average. The first operation consists in calculating the specific heat of the gas mixture coming from the stack outlet, given as the mass flow averaged specific heat of hydrogen, nitrogen and water vapor, given by:

$$c_{p_{stack}} = \frac{H_{2_{stack,out}} c_{p_{H_2}} + N_{2_{stack,out}} c_{p_{N_2}} + H_2O_{stack,out} c_{p_{H_2O}}}{\dot{m}_{tot_{stack,out}}} \tag{3.121}$$

Where $\dot{m}_{tot_{stack,out}}$ is the total mass flow exiting from the stack. The specific heat are considered constant with temperature.

The temperature exiting from the mixer is calculated with the mass flow and specific heat averaged temperature of the two streams, since the specific heats are not dependent upon temperature, and obtained from the conservation of energy:

$$T_{mix} = \frac{c_{p_{stack}} T_{stack,out} \dot{m}_{tot_{stack,out}} + c_{p_{H_2}} H_{2_{tank}} T_{tank}}{c_{p_{stack}} \dot{m}_{tot_{stack,out}} + c_{p_{H_2}} H_{2_{tank}}} \tag{3.122}$$

Given the mixer outlet temperature and mass flow, the relative humidity is computed and passed to the following block as in Eq.(3.48). The pressure of the two mixing streams is considered to be the same and coincident with the stack inlet pressure.

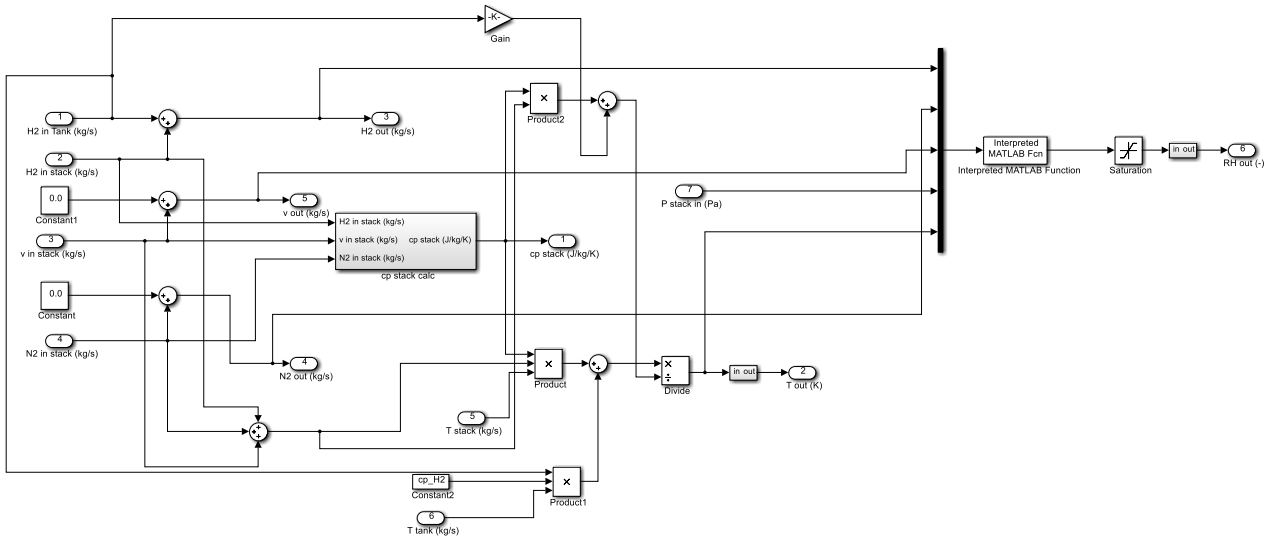

Figure 3.49 *Flow mixer* model block

4. FUEL CELL AND ELECTROLYSER SYSTEM VALIDATION AND SIMULATION

4.1 Fuel cell stack model validation

The validation of the fuel cell stack model must be considered the most important step to assess the goodness and fidelity of the whole model.

4.1.1 Experimental setup

The validation of the fuel cell stack model was obtained comparing the stack model with empirical results derived from direct experiments. The validation was performed comparing the model with the system layout given in Figure 4.1.

As can be seen in Figure 4.1, the stack is fed directly by a laboratory air and hydrogen line, and it is quite simple. Considering the air line, the air passes from a pressurized duct (about 15 bar) through a mass-flow regulator, which reduces the pressure and mass flow to the required stoichiometric and recommended pressure values. The air then passes through a controlled evaporator and heater to rise temperature and relative humidity up to about 65°C and 95%, respectively. Then, the air is fed directly to the stack and vented at the cathode exit, without recirculation. Hydrogen is fed in the same way of air. The temperature of the stack is controlled through a coolant loop cycle. This cycle senses the stack and coolant temperatures and varies the mass flow of a coolant fluid (de-ionized water) kept at constant temperature (61°C) through the stack.

In this validation, the electrical heaters and humidifiers are not directly modelled. These two elements are part of the laboratory equipment and are designed to maintain very precise humidity and temperature values. Moreover, the coolant loop cycle is not directly simulated. The model system layout for the validation of the Ballard stack comprises only the fuel cell stack model (Par.3.3.1). All of the other equipment and ancillary elements are modelled using look-up tables reporting the empirical data sensed at each second during the experiment on the test rig.

The Ballard stack considered was the Ballard Mark9 SSL model, made up of 110 cells, and shown in Figure 4.2. Its main characteristics are a mass of 17 kg and a rated power of 19.3 kW. Its external dimensions are 326 x 760 x 60 mm.

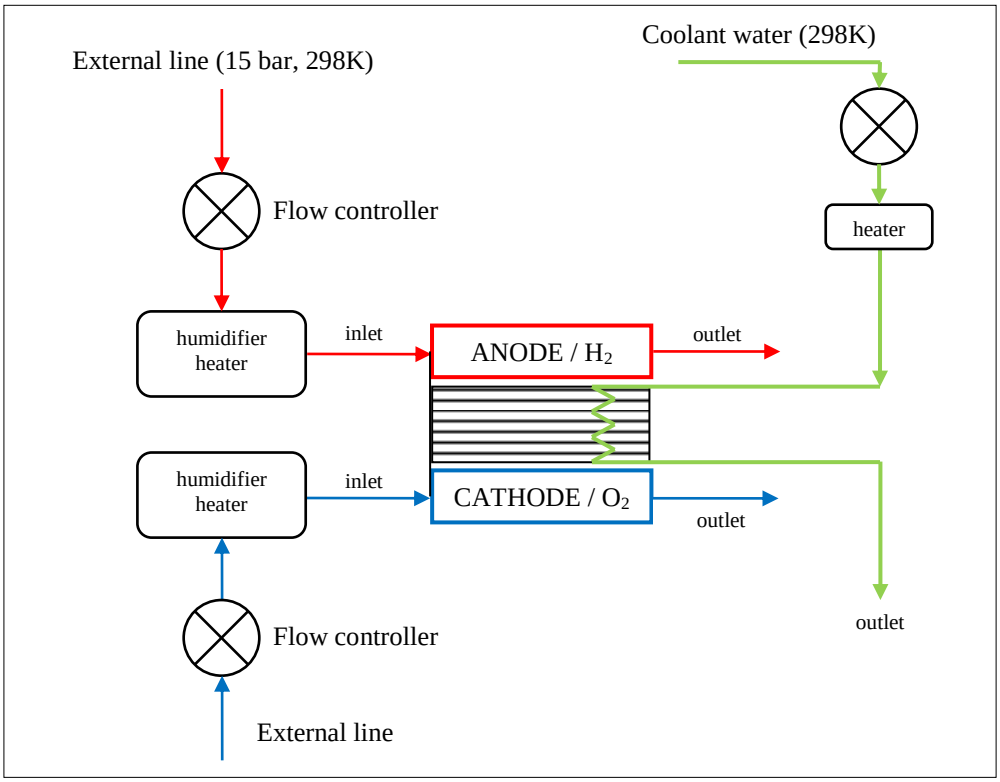

Figure 4.1 Ballard fuel cell stack test rig layout

4.1.2 Model assumptions and setup

All of the physical quantities used in this validation are given in Table 4.1. The most uncertainties come from the quantities labelled "estimated", since manufacturer data were not available. The cell active area (A) was determined considering the exterior dimensions transverse to the stack: 760 x 60 mm, giving an area of 0.0456 m^2. This area was reduced to the 75% to take into account the area of the cell not involved in the reaction of hydrogen. This value was chosen as a reasonable value, obtained confronting other fuel cell bipolar plates, since the Ballard stack cannot be opened for patents reasons. This gave an active cell area of 0.034 m^2. Also the stack thermal capacity, expressed as the product of mass and specific heat was evaluated. It was considered a stack mass of 17 kg, coming from datasheets (Ballard 2005, 2007). The specific heat of graphite was considered (710 J kg^{-1} K^{-1}), being graphite the main and heavier component of the stack, since all of the 111 bipolar plates making the 110 cells are made of this material. The stack, moreover, does not comprise other elements apart from the stack itself. All of the stack mass was attributed to graphite. The resulting heat capacity ($c_{p_{stack}}$) is of about 12000 J K^{-1}. Another value estimated a priori was the maximum current (i_{max}) attainable from the stack before the stack voltage reaches a 0.0 V value (Eq.(3.68)). The Ballard steady-state polarization curve is shown in Figure 4.3. This plot shows the cell voltage vs. current at two different inlet pressures. In both cases, the polarization curve does not show the typical knee and decrease of voltage at high current density, even at 300 A. Considering the cell area (A), this means a current density of about 8800 A m^{-2}. Since the concentration losses are not present up to 300 A and since the fuel cell stack was not tested at these current values, the i_{max} values was set at very high current densities to make the concentration losses negligible.

Figure 4.2 Ballard MARK9 SSL fuel cell stack

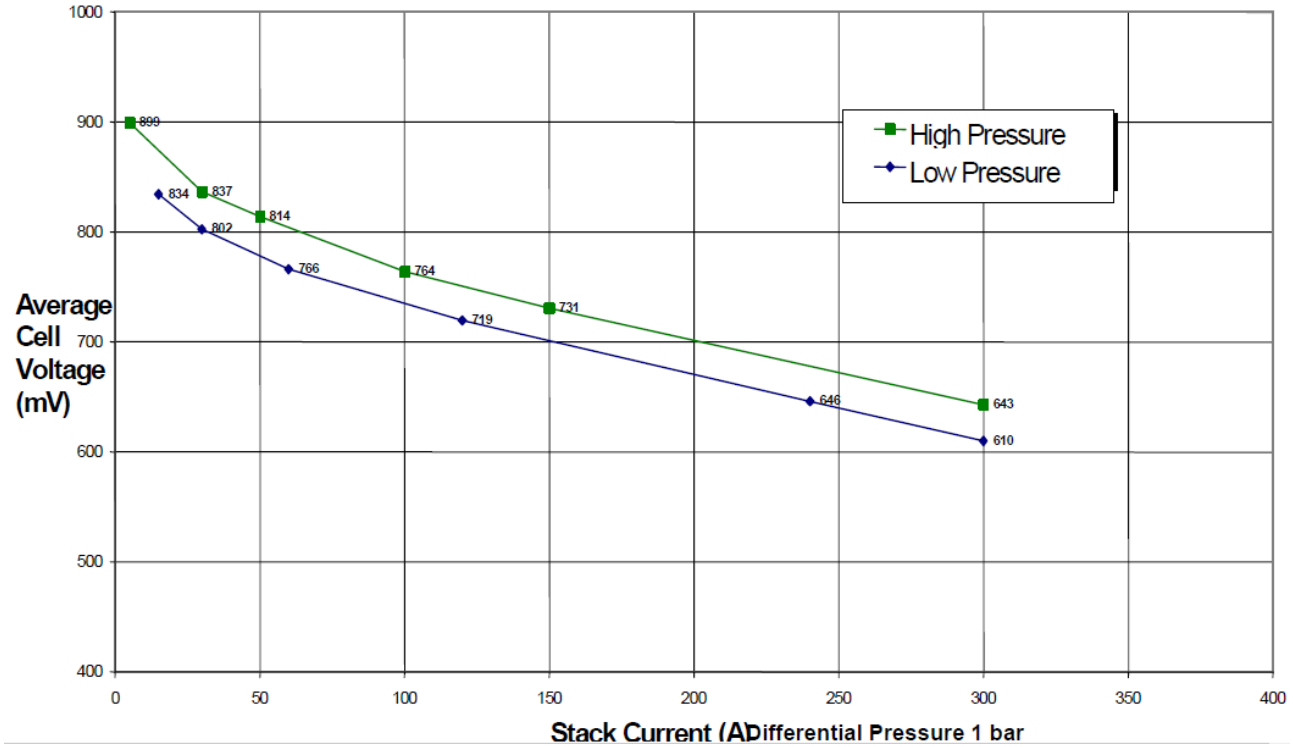

Figure 4.3 Ballard Mark 9™ SSL polarization curve

The double-layer capacitance (C_{dl}) was also estimated. Since the double-layer capacitance shows some effects only for few milliseconds, the real value of this parameter was not important for the purposes of the validation. The value of 3.0 F was taken from Larminie and Dicks (2003).

All of the other parameters of Table 4.1 were obtained from the manufacturer manual or are part of the experimental and calibration setup.

The ambient conditions of the laboratory test are standard conditions, and the cell was fed with air and pure hydrogen.

4.1.1 Experimental results and model validation

Figure 4.4 shows the Simulink model of the corresponding system tested for the validation (Figure 4.1). The main inlet data required by the stack can be seen as input to the block *Ballard Mark9 SSL*. The current profile and output voltage experimentally tested is shown in Figure 4.5 and Figure 4.6.

The current profile was made up of increasing and decreasing steps, starting from about 4.9 A and up to 170 A. The current steps were sharp and immediate, without transients. The voltage plot shows typical undershoots with the increase of current and overshoots with the decrease of current. Moreover, the high spikes in the right hand-side portion of the graph in Figure 4.6 (see the circled area), and highlighted in Figure 4.7, are partially due to the classic overshoot of fuel cells, but are also caused by the reactants feed line controller. The controller used, in fact, in response to a variation in the current demand, responded first with an increase in the mass flow and then it allowed the increase in current after a short time. This behavior was responsible of the "squared" overshoot of Figure 4.7.

Table 4.1 Ballard fuel cell stack model validation. Parameters and physical variables.

Property	Value	Notes
Ambient conditions		
Ambient temperature (T_{amb})	298.15 K	Lab temperature
Ambient pressure (P_{amb})	101325 Pa	Lab pressure
Ambient RH (φ_{amb})	0.5	Lab relative humidity
Ambient air density (ρ_{amb})	1.225 kg m^{-3}	Lab density
Oxygen/nitrogen mix	0.79/0.21	Lab standard air
Fuel cell stack properties		
Cell area (A)	0.034 m^2	Estimated
Number of cells (n_c)	110	From (Ballard 2005)
Membrane thickness (t_{mem})	127x10^{-5} m	From (Ballard 2007)
Stack thermal capacity ($c_{p_{stack}}$)	12000 J K^{-1}	Estimated
Anode fluid volume (Vol_{an})	0.44x10^{-3} m^3	From (Ballard 2007)
Cathode fluid volume (Vol_{cat})	0.78x10^{-3} m^3	From (Ballard 2007)
Electrochemical properties		
Maximum current (i_{max})	18000 A m^{-2}	Estimated
Double-layer capacitance (C_{dl})	3.0 F	Estimated
Reference anode exchange current density ($i_{0_{ref,a}}$)	1.8x10^8 A m^{-2}	Calibration
Reference cathode exchange current density ($i_{0_{ref,c}}$)	1.8x10^7 A m^{-2}	Calibration
Crossover current (I_n)	15 A m^{-2}	Calibration
Ohmic coefficient tuning parameter (Ohm_{coeff})	0.8 (-)	Calibration
Initial and boundary conditions		
Initial stack temperature ($T_{stack_{ini}}$)	308 K	Experiment setup
Nitrogen crossover	0.0 kg s^{-1}	Crossover neglected
Stack heat exchange constant (hA_{stack})	2.0 J kg^{-1}	Calibration
Anode heat exchange constant (hA_a)	27.6 J kg^{-1}	Calibration
Cathode heat exchange constant (hA_c)	28.6 J kg^{-1}	Calibration
Cooling fluid heat exchange constant (hA_{cool})	1760 J kg^{-1}	Calibration
Anode inlet temperature ($T_{in,an}$)	Look-up table	Experiment setup
Cathode inlet temperature ($T_{in,cat}$)	Look-up table	Experiment setup
Anode inlet RH ($RH_{in,an}$)	0.95	Experiment setup
Cathode inlet RH ($RH_{in,cat}$)	0.95	Experiment setup
Coolant flow inlet temperature ($T_{cool,in}$)	334 K	Experiment setup

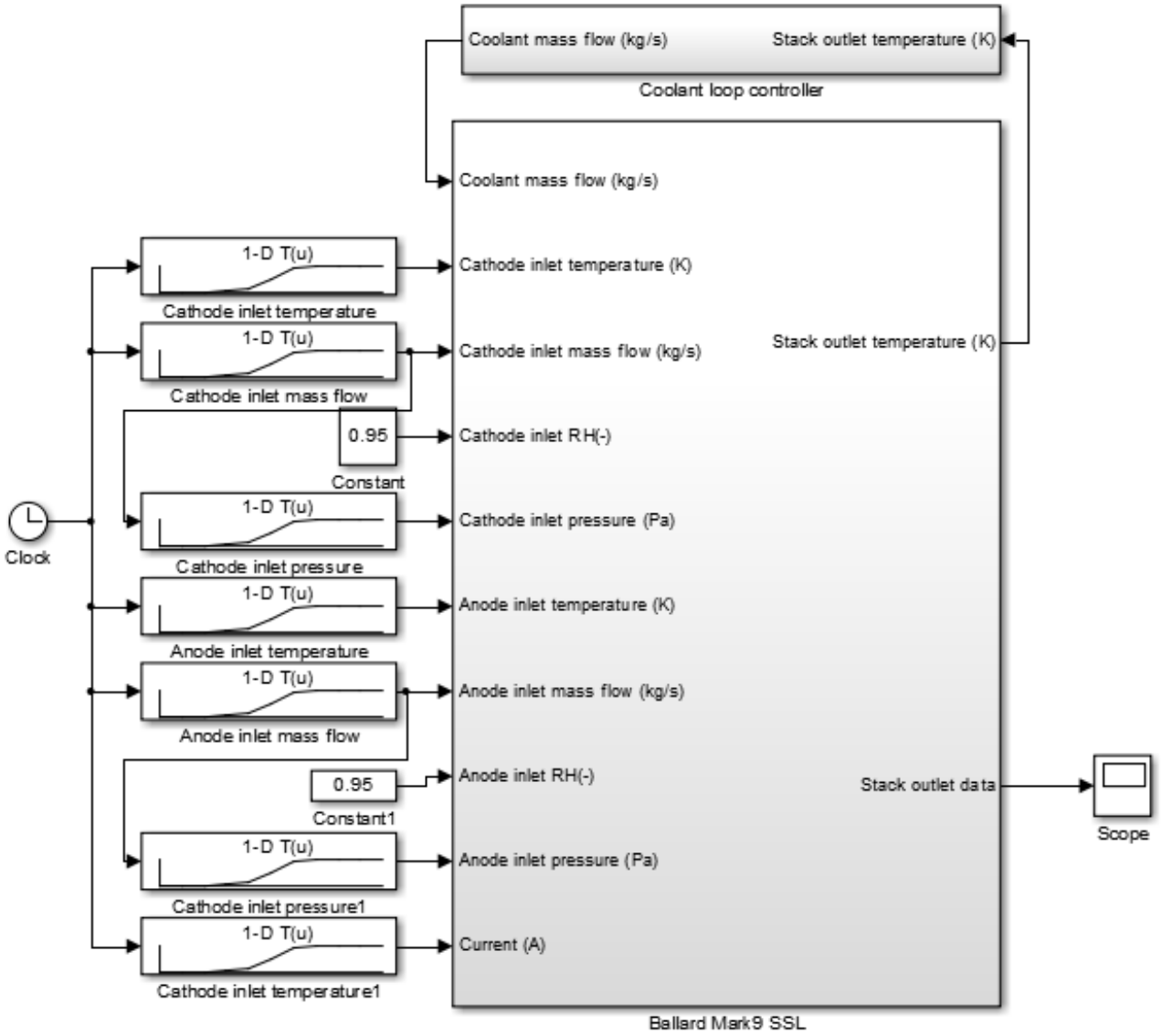

Figure 4.4 Simulink model representation of the Ballard test rig

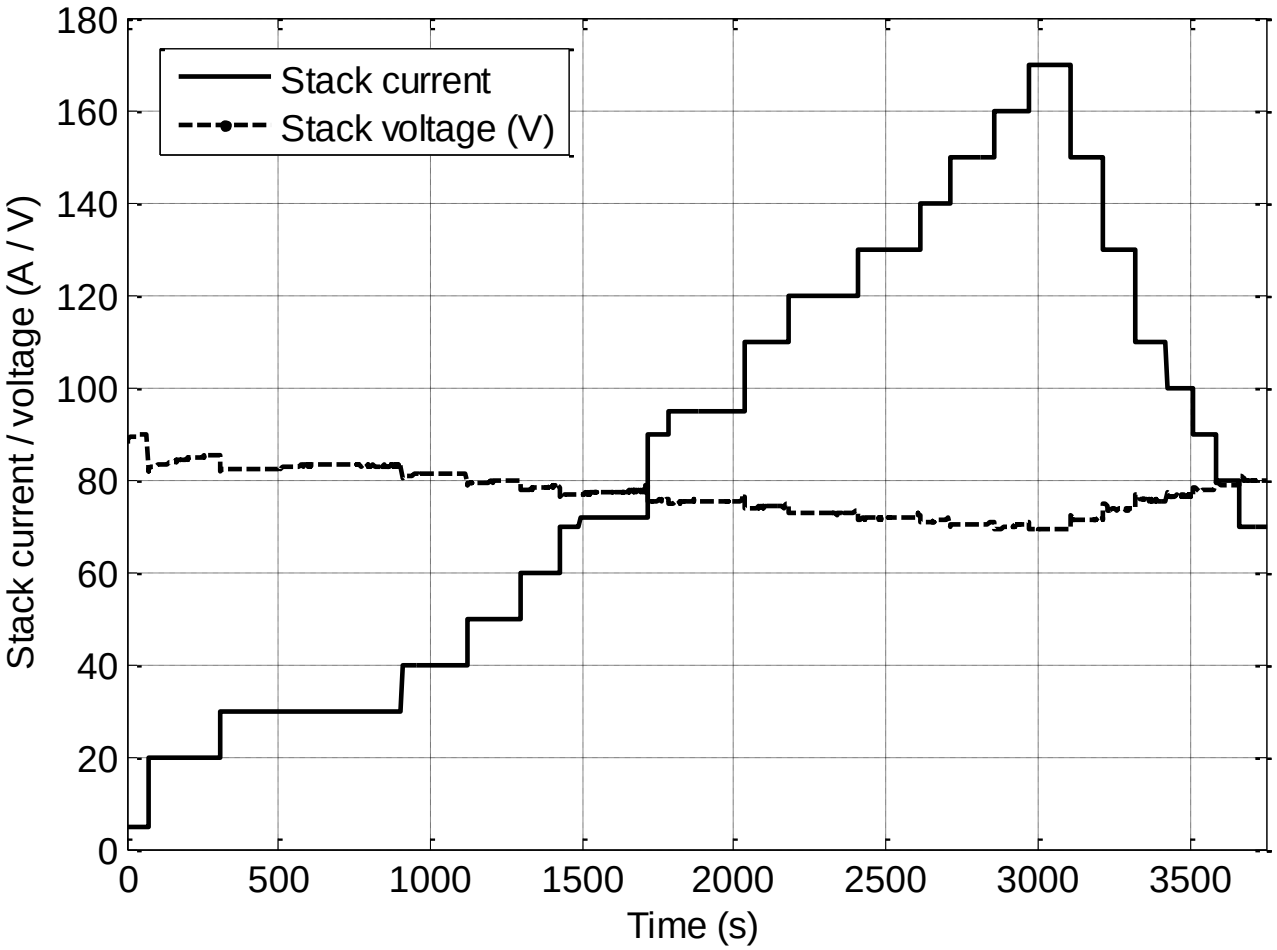

Figure 4.5 Ballard Mark9 SSL experimental current load profile and stack output voltage

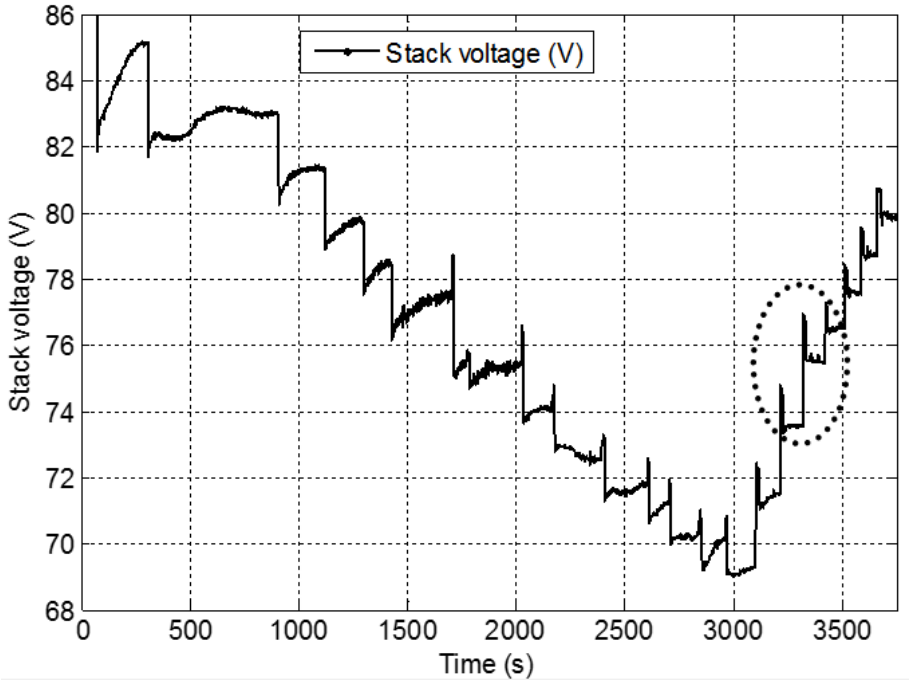

Figure 4.6 Ballard Mark9 SSL experimental stack output voltage

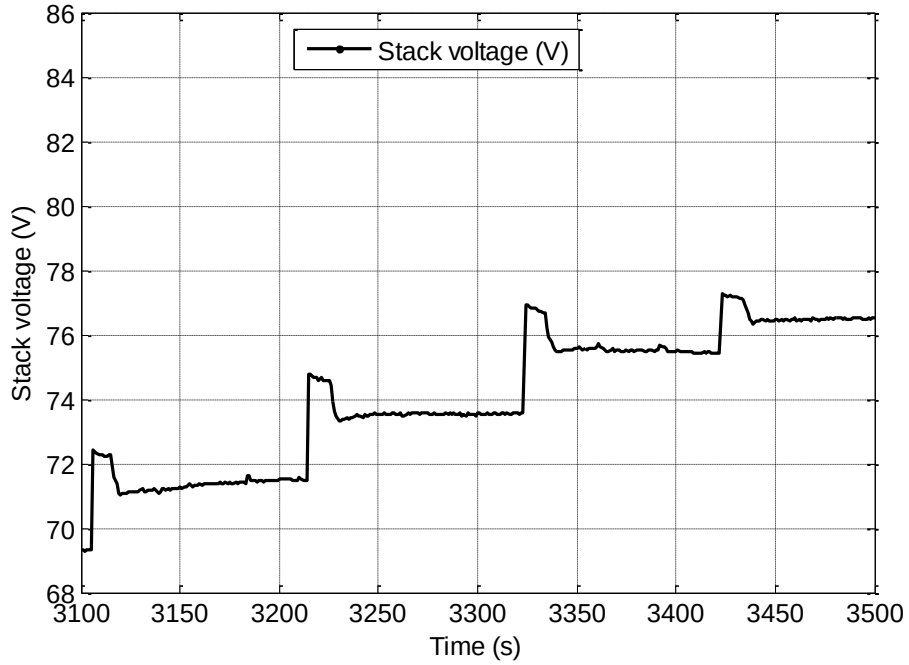

Figure 4.7 Ballard Mark9 SSL experimental stack output voltage. Zoomed area

As already said, the elements external to the stack were not modeled for this validation. In particular, the experimental stack inlet temperature and mass flows were monitored for both the anode and cathode side, and are shown in Figure 4.8. As can be seen, the temperature inlet for both the anode and cathode sides were not constant during the test, showing blended variations with the current demand. The inlet mass flows, instead, show a profile similar to the current one, since the inlet mass flow is directly proportional to the stoichiometric value. Anyway, in this case, up to about 2500 s the mass flows are fixed to a minimum value imposed by the controller used on the test rig, and only from about 100 A the mass flow becomes proportional to current.

The inlet relative humidity, instead, showed a more compact and uniform distribution around the value of 95%.

To make the validation of the model more precise and coincident with the experimental data, the temperature profiles and mass flows in Figure 4.8 were used, using a look-up table in Simulink, relating each time instant with a particular value of these quantities. The same was done, obviously, for the current load profile. The look-up tables used in Simulink can be clearly seen in Figure 4.4.

The inlet relative humidity was instead set as a constant and equal to 95%. The same approach was done for the pressure drop inside the stack. As a reference, the outlet pressure was obviously set at the atmospheric conditions (101325 Pa), since the stack outlet was directly connected with the ambient. Pressure transducers were mounted at the stack inlet to sense the pressure drop across the stack. The relation between mass flow and pressure drop was then plotted (Figure 4.9) as a function of mass flow (in kg s^{-1}). A linear relation was obtained and then used as a look-up table for the pressure loss inside the Simulink model.

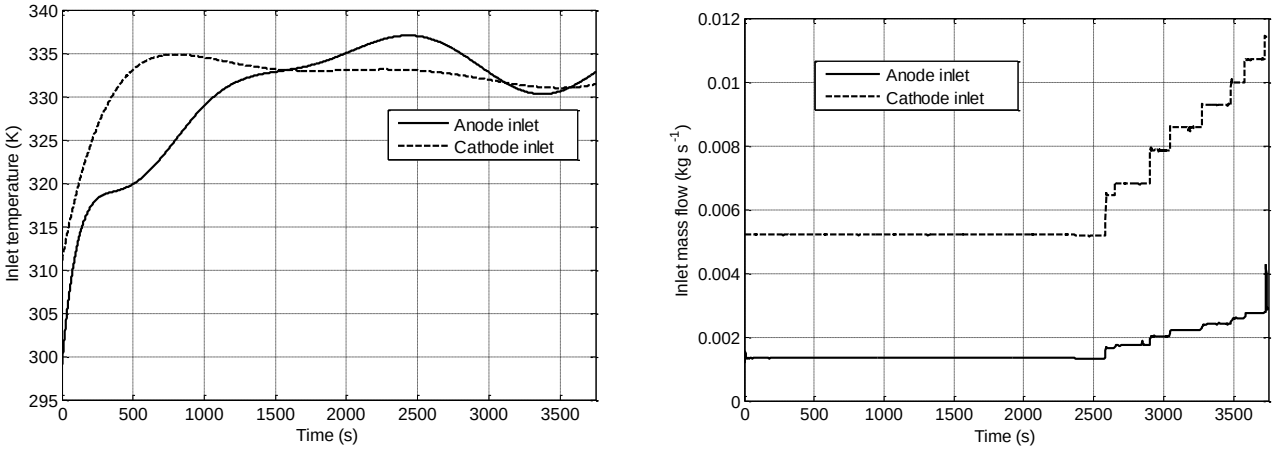

Figure 4.8 Stack inlet temperatures and mass flows for the anode and cathode sides. Anode inlet flow x 10

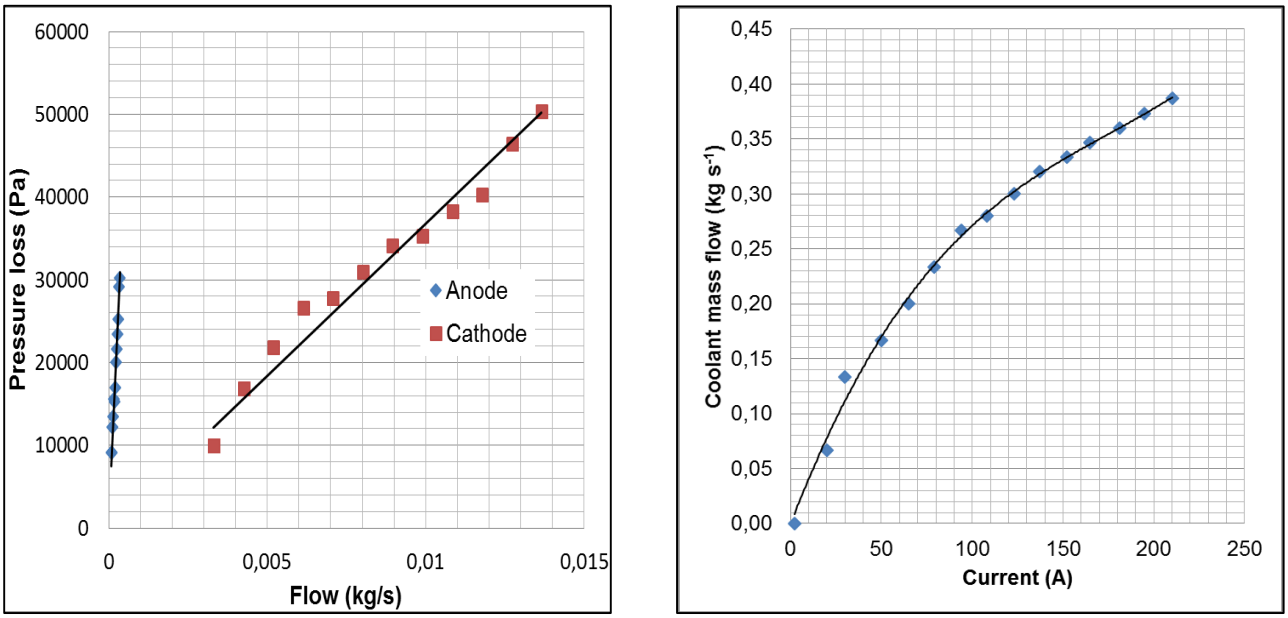

Figure 4.9 Ballard Mark9 SSL anode and cathode pressure loss data and linear interpolation (left hand side). Coolant flow function of current (right hand side)

4.1.1.1 Thermal model calibration

Unfortunately, only few thermal data were measured during the test. The coolant mass flow and temperature were monitored. While the coolant flow temperature showed few oscillations, and remained near to the value of 334 K (equal to the maximum inlet coolant flow temperature given by the manufacturer (Ballard 2007)), the mass flow obviously varied with the current demand. The plot of mass flow vs. current is given in Figure 4.9. A cubic interpolation was used to obtain a function relating mass flow and current, and the resulting equation was used to model the *coolant loop* in Simulink (Figure 4.4).

The temperature of air and hydrogen at the outlet, unfortunately, were not monitored. These quantities would have been useful to calibrate the anode and cathode side thermal exchange constants hA_a and hA_c. Knowing the inlet and outlet temperatures at a specific steady-state current load, it would have been possible to calibrate them very easily, varying them and the stack thermal exchange constants (hA_{stack}) together to reach the coincidence between the measured and the

calculated outlet temperatures. Since these data were not available, the two quantities hA_a and hA_c were set to obtain at the outlet the same temperature of the stack. This result was obtained with a series of trial and error simulations until their values matched the stack temperature. This assumption is not far from the real scenario. In fact, the gases inside the stack move for a long pattern inside the bipolar plates channels, up to some meters in some compact configurations. Despite the speed of the gases, this long distance and contact with the surrounding stack, together with a usually small difference in temperature between the stack and the inlet gases make possible to have similar temperatures at the outlet of the reactants gas. The values for hA_a and hA_c were then set at 55.1 and 57.1 J kg^{-1}. Using these values it was possible to have coincidence between stack and reactants gases temperature, as can be seen in Figure 4.10, where the tree curves are superimposed and not distinguishable. This simulation was performed using the values of Table 4.1.

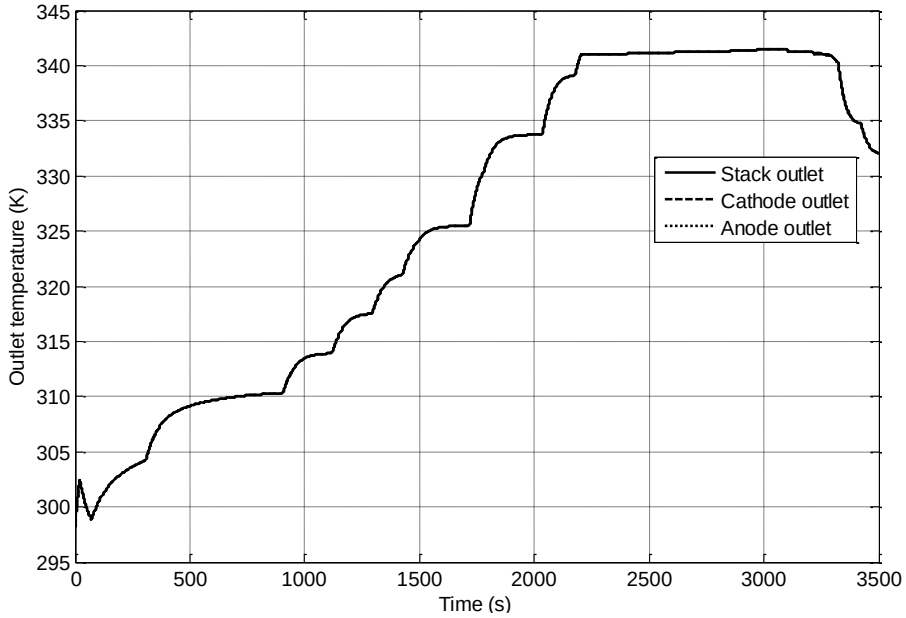

Figure 4.10 Coincidence between stack, anode and cathode outlet temperatures

The stack temperature, on the other hand, was not known, despite the coolant flow controller monitored it for the water flow. The coolant flow was set to maintain a certain difference between the inlet and the outlet coolant flow temperature. This constant difference was maintained varying the mass flow with current, i.e. the thermal dissipation required. Given the temperature difference, the heat removed from the stack can be directly determined by the heat law:

$$\dot{Q} = \dot{m}_{cool} c_{p_{H_2O_l}} \Delta T \tag{4.1}$$

In this way, the stack temperature control can be done in an indirect way. The real system was tested using a temperature difference of 5 degrees for the first 2400 seconds (corresponding to less than 120 A) and 10 degrees for the successive time. The predicted stack temperature was 342 K (69°C) and 346 K (73°C) for the two time intervals. These values are summed up in Table 4.2.

The calibration of the thermal model was done using the coolant mass flow vs. current law of Figure 4.9 for the coolant inlet mass flow, and a fixed value of 334 K for the inlet temperature of the coolant flow. These values were the input quantities. The output monitored values were the stack and coolant flow outlet temperatures.

The calibration was done varying the two remaining thermal parameters, namely the hA_{stack} and hA_{cool}. The first one is related to the thermal exchange between the stack and the surrounding environment, while the second one is related to the thermal exchange between the coolant fluid and the stack.

Table 4.2 Temperature values used for the coolant loop calibration

Current value / time (A/s)	**Coolant temperature (K)**		**Predicted stack temperature (K)**
	Inlet	Outlet	
< 120 / 2400	334	339	342
> 120 / 2400	334	344	346

The calibration was done keeping all of the other variables constant. The electrochemical constants were set at $i_{0_{ref,a}} = 1x10^8$ A m^{-2}, $i_{0_{ref,c}} = 1x10^7$ A m^{-2} and Ohm_{coeff} = 1.0. Using these values, the voltage vs. current curve was not superimposed to the experimental one, with an average and maximum error between model and experimental voltage of 4.31 and 13.24 percent, respectively. Anyway, this was considered a good result for the calibration of the thermal parameters. Using a trial and error approach, the final values chosen for the hA_{stack} and hA_{cool} variables were 2.0 and 1760 J K^{-1}, respectively. As can be seen, a clear influence on the stack thermal behavior is given by the active cooling and not by the thermal radiation and natural convection between the external walls of the stack and the surrounding environment. With these data it was possible, varying the current load, to obtain a rise in the coolant fluid comprised always between 5 and 10 K and, and the same time, maintain the stack temperature inside the interval 342-348 K quite easily. The results of the calibration can be seen in Figure 4.11. The solid line shows the stack temperature, and it is always comprised above the coolant flow temperature and in the interval 338-348.5 K. The dotted line, representing the coolant flow outlet temperature is always maintained in the interval 339-344, indicating the temperature rise of 5-10 K are sufficiently maintained, apart from the initial portion of the graph.

Despite the small discrepancies of 1-2 K between the margins of Table 4.2 and the results shown in Figure 4.11, the thermal calibration can be considered done and sufficiently reliable. In fact, 2 K in the order of 340 K represent only a relative error of the 0.6%. Moreover, the response of the stack to variations of few kelvin degrees can be considered quite negligible if compared to the influence of other parameters (i.e. the relative humidity and electrochemical parameters).

4.1.1.1 Electrochemical model calibration and model validation

The electrochemical model calibration, consisting of the definition of $i_{0_{ref,a}}$, $i_{0_{ref,c}}$, i_n and Ohm_{coeff}, namely the reference exchange current densities, the crossover current density and the ohmic losses calibration coefficient can be considered the stack model validation itself, since all of the other variables are fixed and the electrochemical parameters play a fundamental role in the electrical response of the stack.

The validation of the stack model was performed comparing the stack output voltage with the experimental output voltage (shown in Figure 4.6), and calculating the relative error of the two curves for each time instant.

The first calibration process regarded the steady-state response of the stack. The variation of the delay constants will be considered later to attain a transient response possibly similar to the experimental one. The four calibration constants were varied considering their effects on the polarization curve. After some tentative trials and comparisons with the Ballard experimental data,

the final values for them were fixed, and are shown in Table 4.1. The resulting polarization curve representing the validation of the stack model is shown in Figure 4.12 and Figure 4.13.

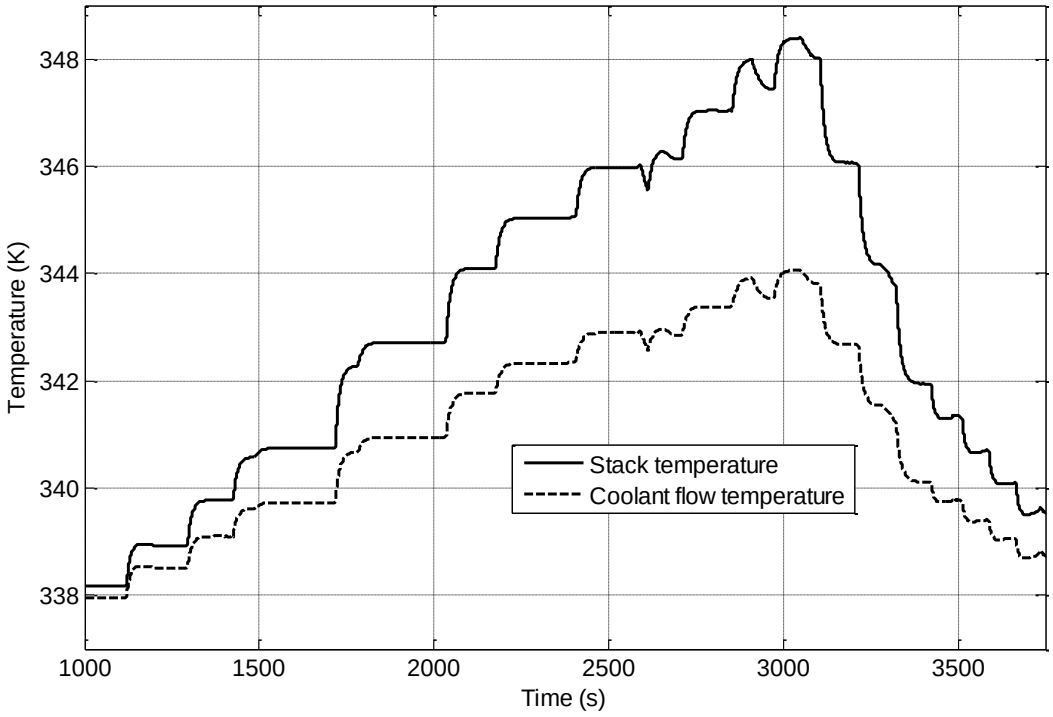

Figure 4.11 Stack and coolant flow outlet temperature vs. time

The curve is drawn in the interval 0 - 3750 seconds. As can be seen, the main discrepancies can be underlined in the initial portion of the two graphs. These discrepancies can be related both to the experimental bench and the model itself. During the startup of the stack, in fact, the cells require some amount of time to reach their full operating capabilities. This is also the reason for which the current output is kept at low values, to avoid stresses to the cells. The model also requires a sort of startup time, since the initial conditions set in the model itself might be different from the real ones.

Nevertheless, apart from this initial variation between the two models, it is possible to affirm the two curve as sufficiently close to each other.

The relative error between experimental and model data, obtained confronting the two stack voltage values at each second, showed a *maximum error equal to 3.18% and an average error of 0.70%*.

These values are calculated in the range 100-3570 seconds – keeping out the initial discrepancy from the error computation. This result can be considered fully acceptable and the model can be considered sufficiently realistic.

Zooming at the graph of Figure 4.12, shown in Figure 4.13, it is possible to consider the transient phenomena involved. During the progressive increase in the current drain - left hand side of the graph, the experimental data showed a continuous presence of undershoots at each current increase. The high frequency variations in the experimental curve are given by the acquisition system and variations in the boundary conditions. The model curve, on the other hand, showed at the same time undershoots at each current step, but of different entity.

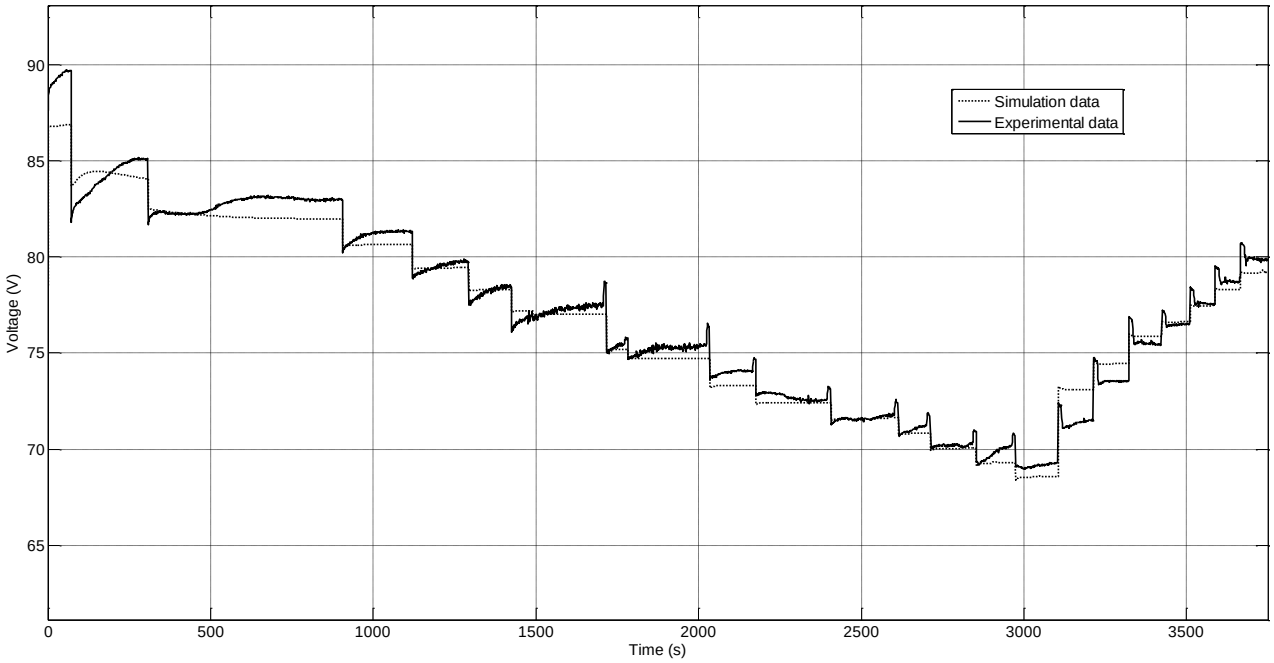

Figure 4.12 Validation of the stack model. Experimental and simulation voltage vs. time

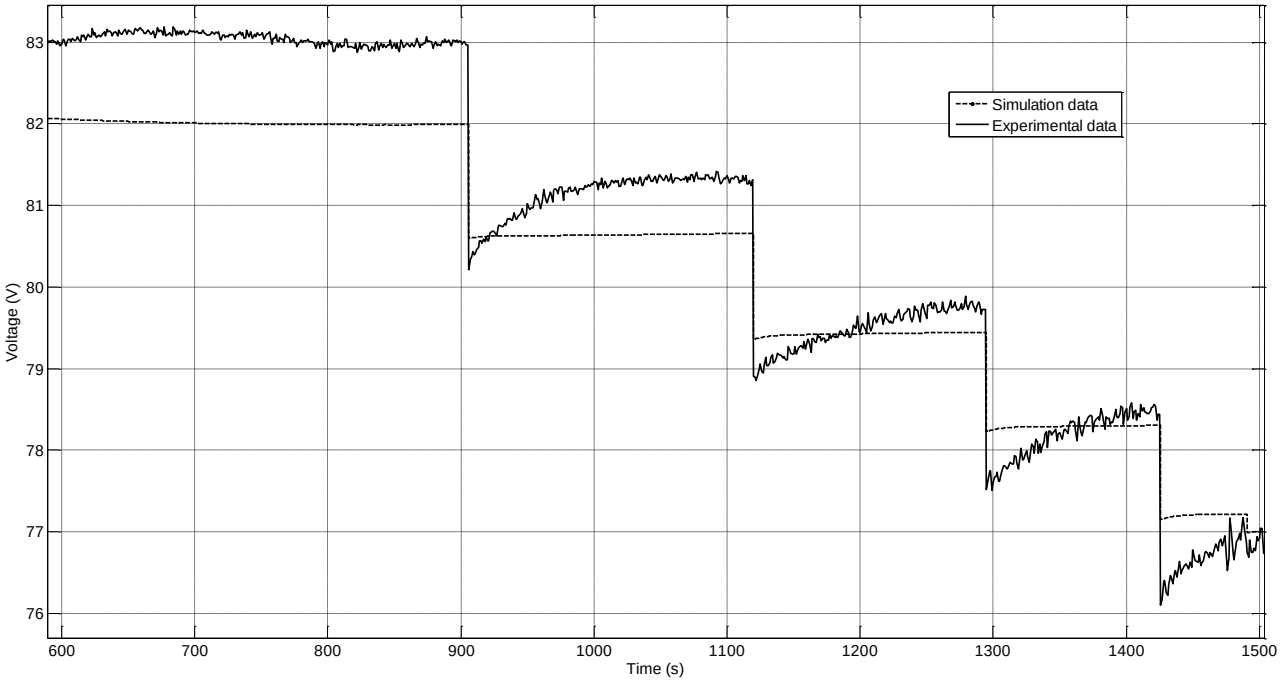

Figure 4.13 Validation of the stack model. Experimental and simulation voltage vs. time. Zoomed area at the left hand side

The time constant for the experimental curve is much higher – i.e. the transient lasts for more time than the experimental one. At the other side of the curve, when the current is reduced at each step, both the experimental and the model curves showed overshoot responses at each step. Also in this case the transient response is different between the two curves. The transient of the model data is variable and in the order of 45-50 seconds for the step response at 2035 s, as can be seen in Figure 4.14, while the transient response can be considered about the double for the experimental data,

considering it extinguished at about 2140 s. It is also important to note the higher abrupt loss of voltage in the experimental curve, i.e. the vertical lines in Figure 4.13, if compared to the simulation one when the current increases.

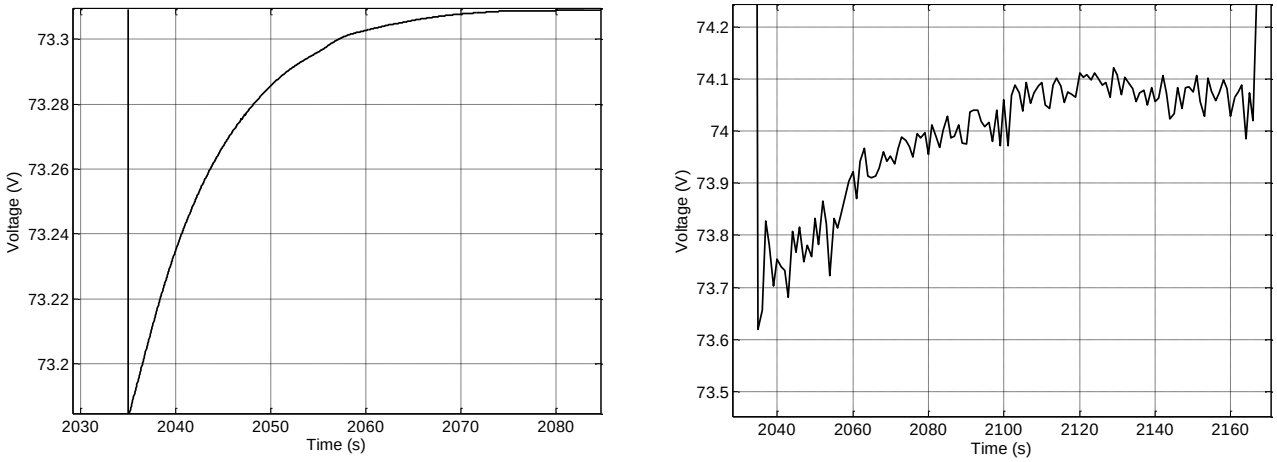

Figure 4.14 Simulation (left) and experimental (right) transient response. Zoom of the voltage vs. current curves

Figure 4.15 shows a zoomed area of the right hand side of the curve, where the current decreases step by step. As can be seen, the curves here are more "flat", both in the experimental and in the model curve. The flat spikes visible in the experimental curve, already mentioned before, are not well simulated by the model, despite these data are passed to the model in the form of look-up table for the mass flows. The transient response of the models, in this second case can be considered comparable. The discrepancy in the steady-state voltage values are part of the small error of 0.70% encountered, but in this case are in the order of few units or tenths of milli-volts.

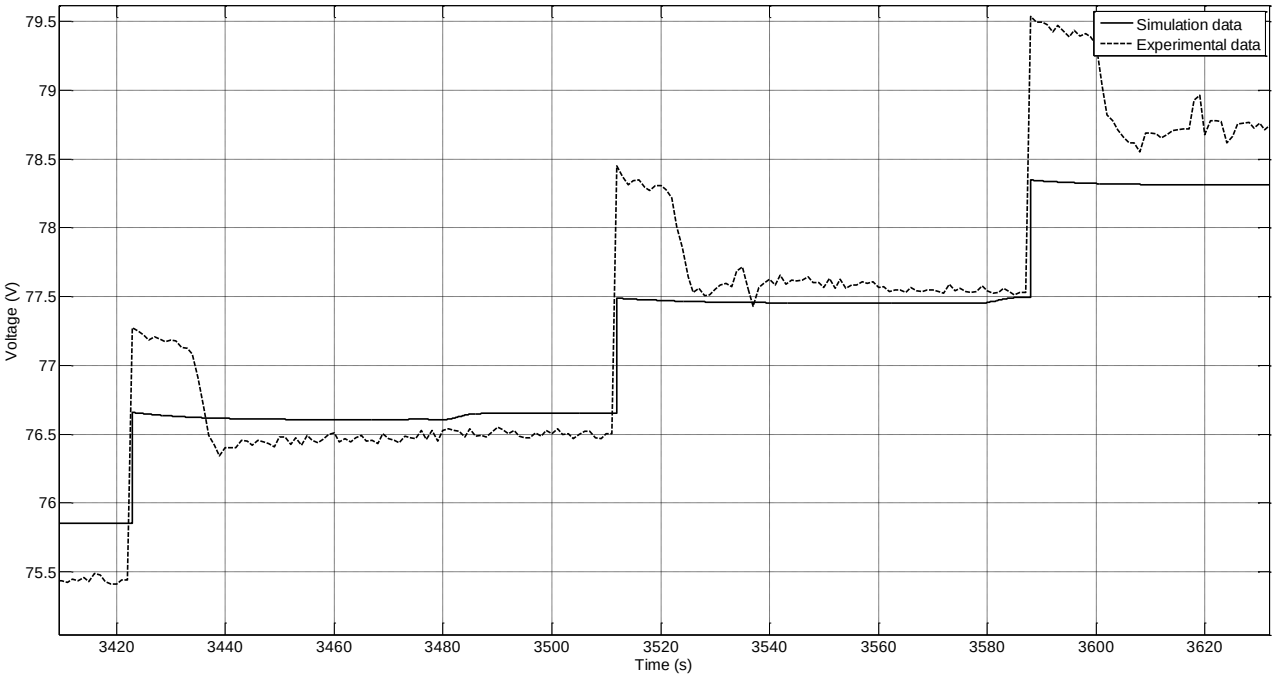

Figure 4.15 Validation of the stack model. Experimental and simulation voltage vs. time. Zoomed area at the right hand side

The pressure delay and stack delay constants were then varied, keeping the other variables constant. The variation of these quantities produced no appreciable effect on the time constant of the transient response of the system. They only slightly modified its value.

The discrepancy in the transient response of the system can be explained considering the fact that the fuel cell stack tested for the validation of the model used a fuel cell which was inactive for a long period. One of the main effects of the inactivity of fuel cells are the progressive dry-out of the PEM membrane. This dry-out modifies the molecular structure of the membrane, and a successive use of the cell would require, in the worst scenario, a sort of re-vitalization procedure of the cells. This consists in flooding the cells injecting de-ionized water on the anode and/or cathode sides of the stack instead of its conventional gaseous reactants, and keeping it inside the cell for some hours or even days. This procedure repeated over time allows the membrane to re-absorb its natural content of water and allow its original ionic conductivity and chemical structure.

Taking into account the last consideration done, the long transient time exhibited by the experimented Ballard stack can be at least partially explained. Since the stack was inoperative for a long time, the membrane ability to respond to rapid variation in the current demand was degraded by a partial dry-out of the membrane. The progressive capability of the tested system to reach better performances can be clearly seen when the two sides of the experimental curve (increasing and decreasing current steps) are compared. This is shown in Figure 4.16, where the current profile is divided by 2 to obtain the same y-axis scale. The arrows of different shape and length in this figure compare four couples of the same current output. As can be clearly seen, comparing the corresponding voltage values for each couple of current value, the voltage value on the right hand side is always higher (when steady-state condition is reached) than its corresponding value on the left hand side. This behavior can be explained if it is considered the progressive re-hydration of the membrane during the test, partially revitalizing the membrane.

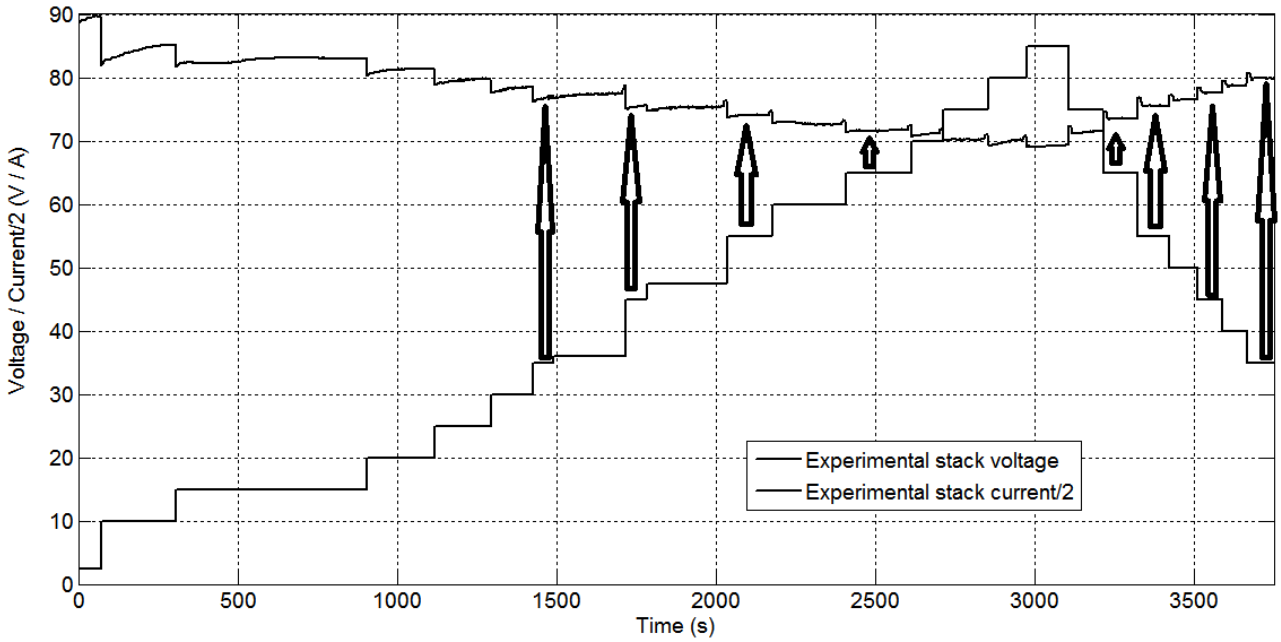

Figure 4.16 Experimental voltage and current vs. time comparison

At this point, several trials and modifications to the stack model were performed in order to obtain a stack voltage curve showing the effects of the just-mentioned membrane dry-out. First of all, the

maximum membrane water content was reduced from 14.4 to 8.0 to simulate the reduced capability of the membrane to contain water. This produced only slightly effects. The second tentative modification to the model was the re-formulation of the membrane water diffusivity, affecting both the membrane water content and its response to the variation in the surrounding humidity. Its definition (Eq.(3.74)) was modified in the D_W term, adding a calibration constant (k_{D_w}) in the way:

$$D_{w_{eff}} = D_w \cdot k_{D_w} \tag{4.2}$$

Where $D_{w_{eff}}$ is the effective water diffusivity, and D_w is the "standard membrane" water diffusivity constant. In this second case, the time constant of transients in the model were modified in a better way, but without showing the values expected. The variation in the maximum water content in the membrane and the variation in water diffusivity were the two main and only modeled aspects considered for the membrane hydration model.

Given the discrepancy in the transients between the model and experimental data, the phenomena involved in the transient response of fuel cells were reconsidered (Par.3.1.1). In particular, the GDL gaseous and liquid species transport from the channels to the reaction sites was re-analyzed. Given the complexity in modeling a multi-phase and multi-gas mixture, a different method to model the variation of reactants concentration at the catalytic surface was at this point developed.

The Simulink block of the GDL formulation is shown in Figure 4.17, where the oxygen partial pressure model is given. The formulation for the anode side is identical.

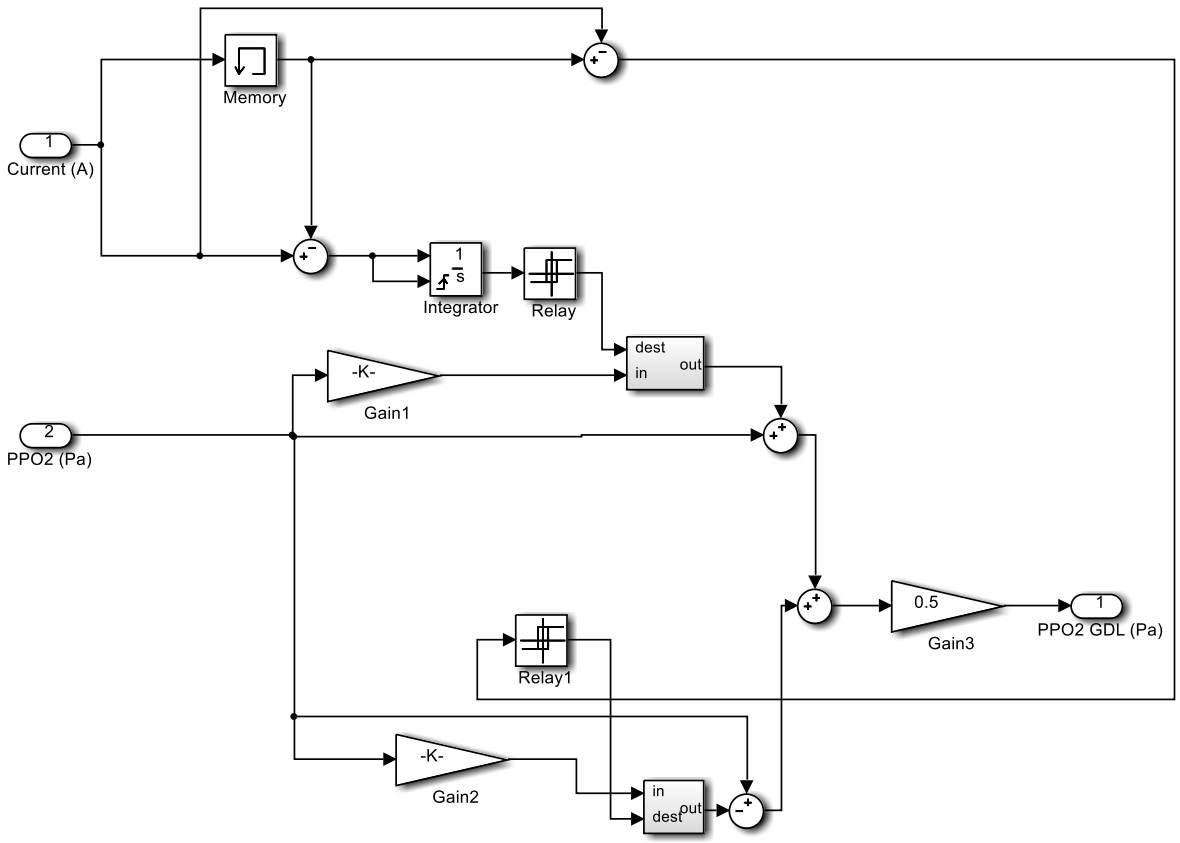

Figure 4.17 GDL model block in Simulink

The GDL model operates in the following way. When a variation in the current demanded is sensed (given by the *Memory* block), an integrator is reset to zero and starts again. The reset in the integrator activates a *Relay* block which starts the generation of a first order transient (indicated by the gray block and identical to the *delay* blocks already discussed before. This transient response is added or subtracted to the partial pressure present at that time inside the gas channels, and it is computed by the *pressure delay* block introduced in Par.3.3.1. As can be seen in Figure 4.17, there are two symmetrical elements. The upper one computes the transient response in the case of a current increase, while the lower one is used for current decreases. The response of these two blocks are then summed, and divided by two to avoid a double output value. The constants used in this block are only two. The first one, inside the two *Gain* blocks, regulates the height of the step at the current variation, and was indicated as $V_{GDL_{step}}$ and named as "GDL step transient constant". The other one is the constants inside the gray blocks, and regulating the transient time of the first order dynamics. This second value was called $V_{GDL_{time}}$, and named as "GDL time transient constant". As an example, the current steps used for the Ballard stack were used as input to this new block, and the output of the relay and oxygen partial pressure is shown in Figure 4.18. On the left hand side, the current steps and the relative positive relay output is superimposes. As can be seen, at each current variation, the relay generates a spike, resetting the integrator and starting the delay in the oxygen partial pressure variation, which is reported on the right hand side of Figure 4.18. When current increases, the local oxygen (and hydrogen) concentration locally reduces suddenly, given the higher demand in current. This produces a membrane partial pressure decreasing suddenly. When current decreases, instead, the situation reverses, creating a local accumulation of unused reactant.

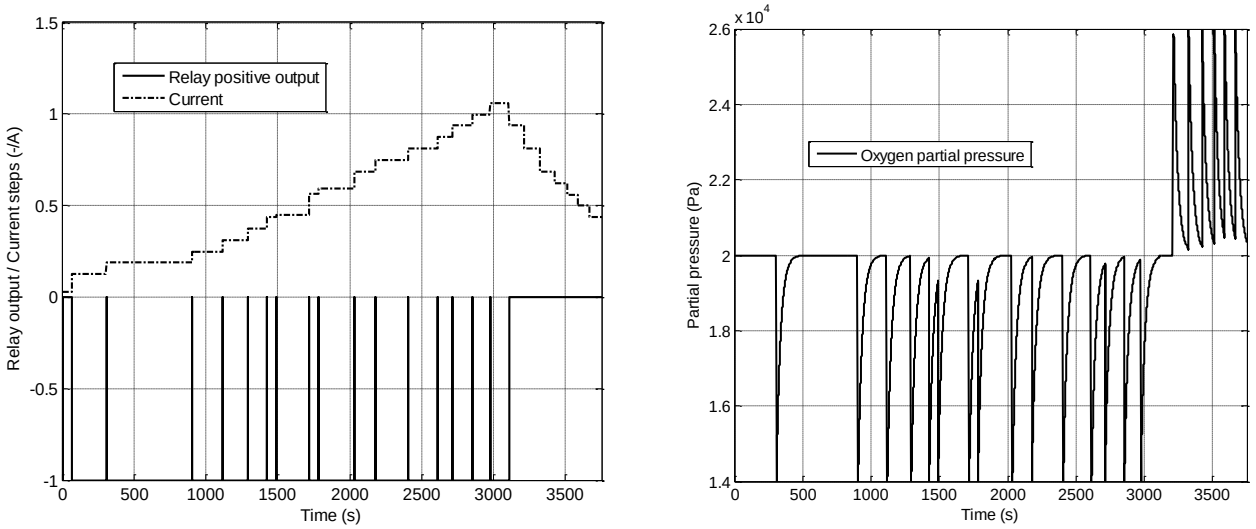

Figure 4.18 GDL model block output. Relay output and currents steps (left side). Oxygen partial pressure transient at GDL catalyst layer interface (right side)

This new model of the GDL was the included in the stack model, between the model calculating the channels partial pressure of oxygen and hydrogen and the voltage model block, computing the Nernst potential based on the partial pressure values (Eq.(1.20)).

The results obtained were impressive. The membrane de-hydration was considered limiting its value to 7.0 (with a saturation block) instead of 14.4. Some trials were done to modify both the electrochemical calibration parameters and the two new constants introduced. The first attempt considered the left hand side of the polarization curve. As can be seen in Figure 4.19, the

experimental and simulation data are very similar to each other, both in terms of steady-state and transient response. A zoomed area can be seen in Figure 4.20, where in some cases, the two curves are even not distinguishable. *The error is estimated in an average value of the 0.65% and a maximum error of the 3.06%*. A great discrepancy can be seen in the right hand side portion of the curves, when the current is decreased. Given the possibility of a partial membrane re-hydration and the considerations shown in Figure 4.16, the simulation was done another time, but giving a higher maximum membrane humidification when the current starts to decrease. In particular, the maximum value of membrane hydration equal to 7.0 was brought linearly to 10.0 from 3100 s to 3750 s.

Another parameters calibration was done. The final values are given in Table 4.3. The final results are shown in Figure 4.21 and Figure 4.22. The results are even better than the previous test case. The other delay constants apart from the GDL ones, were left to unity.

The thermal calibration parameters were left to the same values used for the previous thermal model calibration. The stack and gas temperatures, in fact, despite the variations in the model remained mostly equal to the previous case.

The average error for the final validation is equal to 0.44%, with a maximum error equal to 1.87%

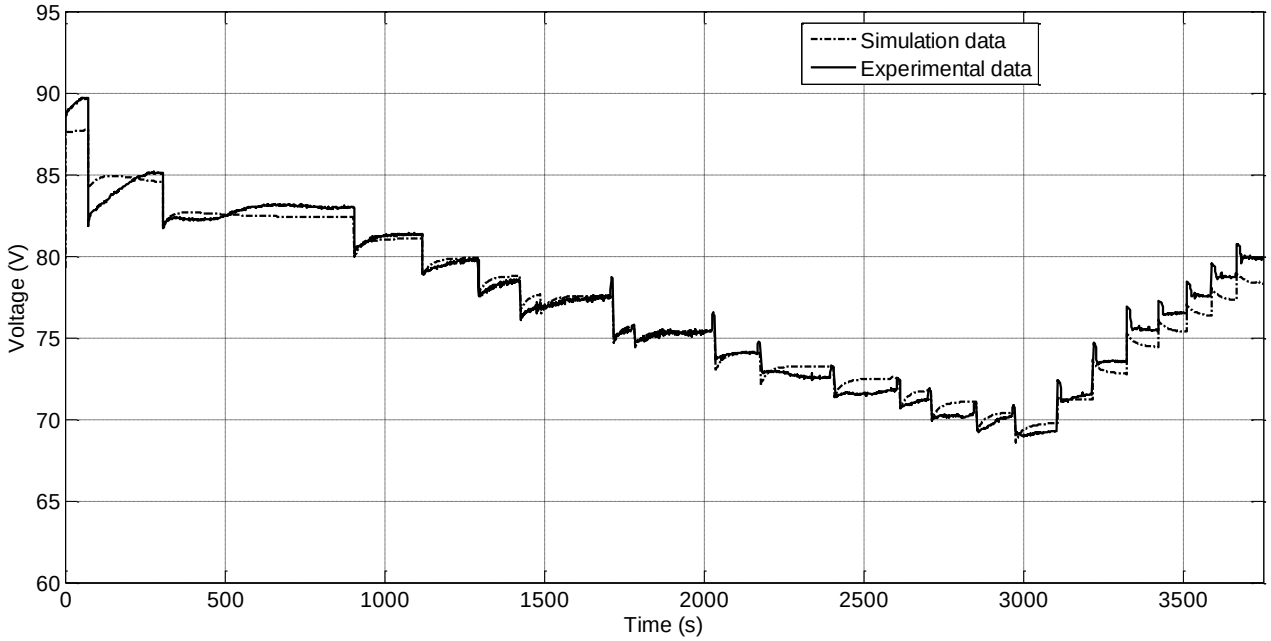

Figure 4.19 Comparison between experimental and simulation voltage data using degraded membrane and new GDL formulation

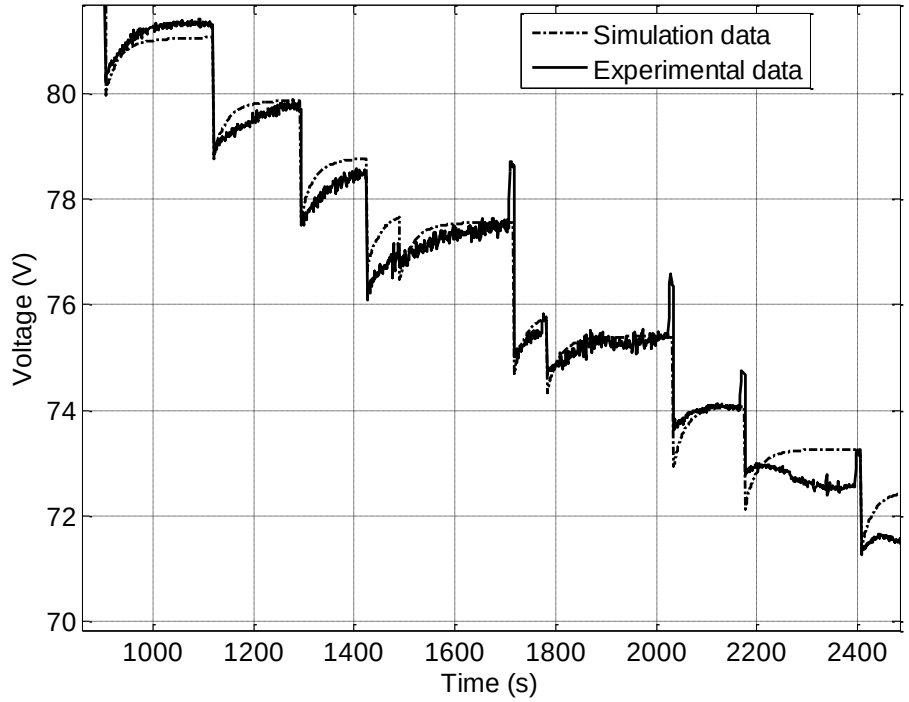

Figure 4.20 Comparison between experimental and simulation voltage data using degraded membrane and new GDL formulation. Zoomed area of Figure 4.19

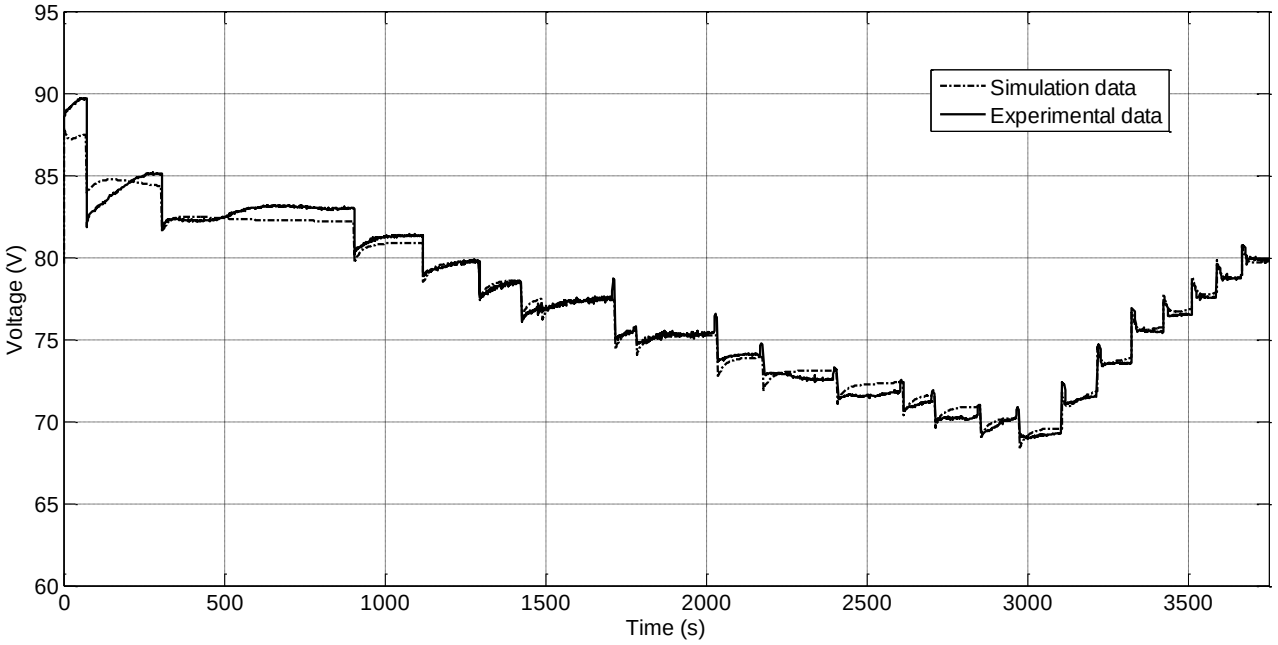

Figure 4.21 Final validation plot of the Ballard Mark9 SSL stack system

Table 4.3 Calibration parameters used for the final model validation

Validation parameters	Value
Electrochemical parameters	
Maximum current (i_{max})	18000 A m^{-2}
Double-layer capacitance (C_{dl})	3.0 F
Reference anode exchange current density ($i_{0_{ref,a}}$)	1.8x10^{8} A m^{-2}
Reference cathode exchange current density ($i_{0_{ref,c}}$)	5.8x10^{7} A m^{-2}
Crossover current (I_n)	9.0 A m^{-2}
Ohmic coefficient tuning parameter (Ohm_{coeff})	0.78 (-)
Thermal parameters	
Stack heat exchange constant (hA_{stack})	2.0 J kg^{-1}
Anode heat exchange constant (hA_a)	27.6 J kg^{-1}
Cathode heat exchange constant (hA_c)	28.6 J kg^{-1}
Cooling fluid heat exchange constant (hA_{cool})	1760 J kg^{-1}
Transient parameters	
Pressure delay constant	1.0 (-)
Stack delay constant	1.0 (-)
GDL transient step constant ($V_{GDL_{step}}$)	0.6 (-)
GDL transient time constant ($V_{GDL_{time}}$)	1/30 (-)

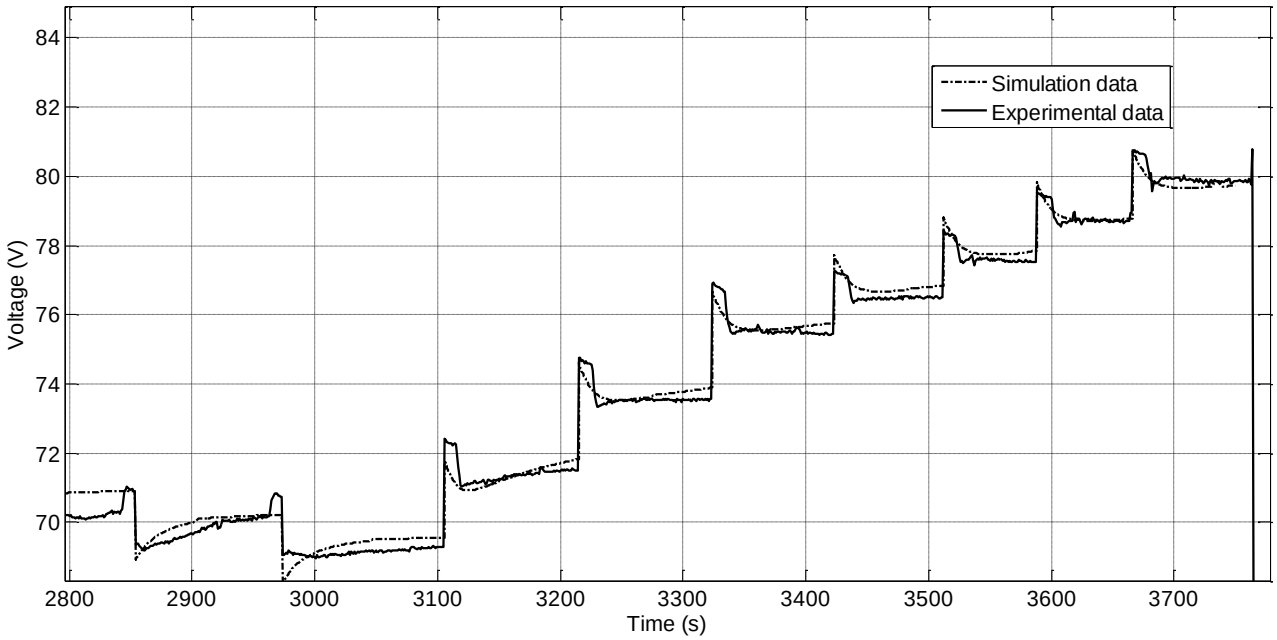

Figure 4.22 Final validation plot of the Ballard Mark9 SSL stack system. Zoomed area of the right side portion

4.2 Fuel cell system model simulation

In this paragraph, the overall fuel cell system will be simulated using most of the elements developed in this work. The stack model used the same calibration and validation parameters used for the validation just seen. The system layout is given in Figure 4.23. The system consists of a motor-compressor block providing the air mass flow required. The air flow is then passed through an intercooler to reduce the temperature of the air exiting from the compressor-motor. Then, the air flow enters a cathode membrane humidifier, where the dry air flow is humidified and partially

cooled down by the cathode outlet flow coming from the stack. The humid flow exiting from the membrane humidifier is vented. The humidified air flow then enters the Ballard stack.

On the anode side, the hydrogen in pure form is taken from a pressurized bottle at ambient temperature. The flow is controlled with a mass flow controller and a pressure reducer (these elements are not modeled). The hydrogen flow is then mixed with the flow exiting from the anode outlet flow. The exhaust flow requires a small recirculation pump to gain the pressure required at the stack inlet (not modeled). The coolant flow is governed by a mass flow controller to keep the temperature of the stack at the same value varying the mass flow of the coolant fluid. For simplicity, it is considered to use a water flow entering the system always at the same temperature. Also the intercooler liquid fluid is considered in the same way. In real cases, it is usually performed a mixture of fluid flow between the stack coolant flow and the intercooler and/or other elements to use always the same coolant fluid. The hydrogen recirculation pump is not modeled here for simplicity, and the variation in the hydrogen fluid flow is governed instantaneously by the variations in current.

The approach based on a fixed stoichiometric value is used here, as described by the equations in the stack model (Par.3.3.1). A fixed minimum value for hydrogen and air mass flow is used when very low current values would impose very low mass flows of hydrogen and air. This is done with a low level *saturation block* in Simulink. The corresponding Simulink model of the complete system is shown in Figure 4.25.

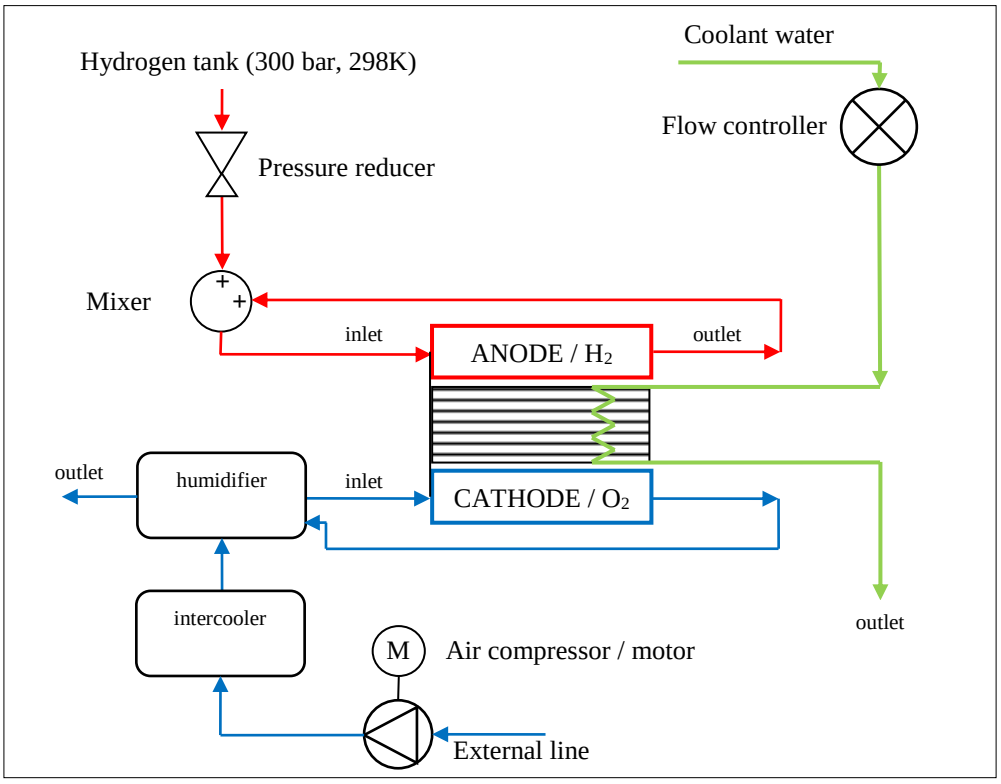

Figure 4.23 Complete fuel cell system layout

This system layout is a typical fuel cell system layout used for terrestrial applications based on fuel cells of several kilowatts of power. Some elements were not considered here. Some air filters and other valves of secondary importance were not modeled. The hydrogen tank, moreover, is not

modeled, and it is assumed the pressure reducer can work instantaneously, maintaining the correct amount of pressure required for the flow to enter the stack.

All of the simulation parameters used in the complete system simulation are the same used previously in the calibration and validation of the single blocks. The Simulink layout given in Figure 4.25 shows the system compressor and motor block in light green, the intercooler in blue, the cathode humidifier in orange, the stack in dark green and the flow mixer in grey.

4.2.1 System simulation under step current variations

The set of simulations considered in this paragraph were performed varying the current demand with several increasing and decreasing steps. Each step was commanded every 100 seconds, with an initial current value of 10 A. The current steps used in the simulations are shown in Figure 4.24. The total simulation time of 600 seconds allowed in containing the computational time.

The only element not simulated was the membrane dehydration given by the stack inactivity discussed in the stack validation paragraph (Par.4.1.1.1).

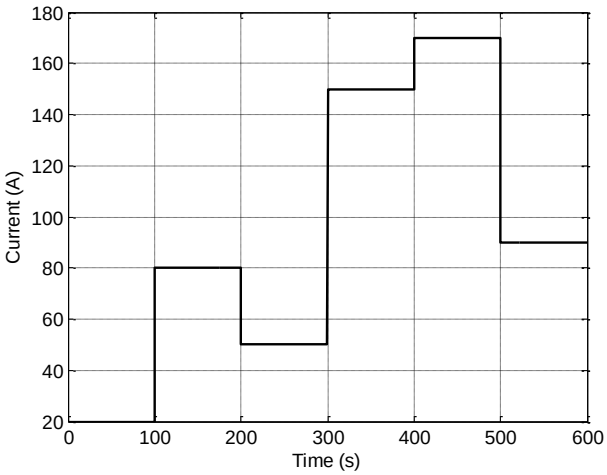

Figure 4.24 Step current profile used for the complete system simulation

The response of the system will be now showed and analyzed from block to block, starting from the compressor-motor block and proceeding towards the stack inlet.

4.2.1.1 Compressor and motor response

The response of the compressor and motor blocks to the step current variations is given in the following images. Figure 4.26 shows the motor rpm values. This plot is similar to the same plots obtained in the motor calibration (Par.3.3.2.1.1). In presence of a higher current demand, the oxygen flow required increases to have more current from the stack. This traduces in a motor command linearly proportional to the current, and dependent upon the stoichiometry. The stoichiometry in these simulations were set equal to 1.6 and 1.8 for the anode (hydrogen) and cathode (oxygen) sides, respectively (based on Ballard recommendations, (Ballard 2007)). The motor response showed some overshoot and undershoot in presence of a commanded increase and decrease, respectively. These overshoots are dependent upon the controller logic and gains used for

the proportional, derivative and integral controllers. On the other hand, the transient time to reach the steady-state condition is fully given by the inertia of the motor and compressor together with the electrical characteristics of the motor. The transient time at each step can be estimated in about 12 seconds. The steady-state condition is met without oscillations.

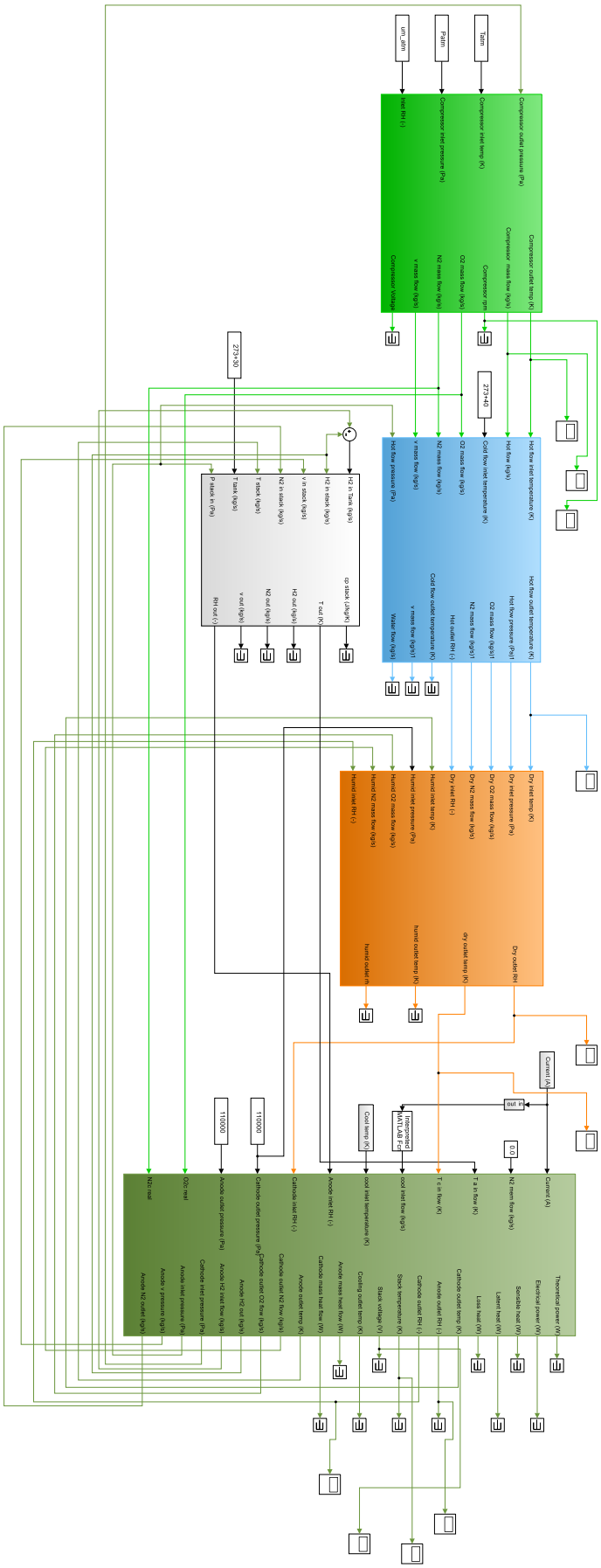

Figure 4.25 Complete fuel cell system layout in Simulink

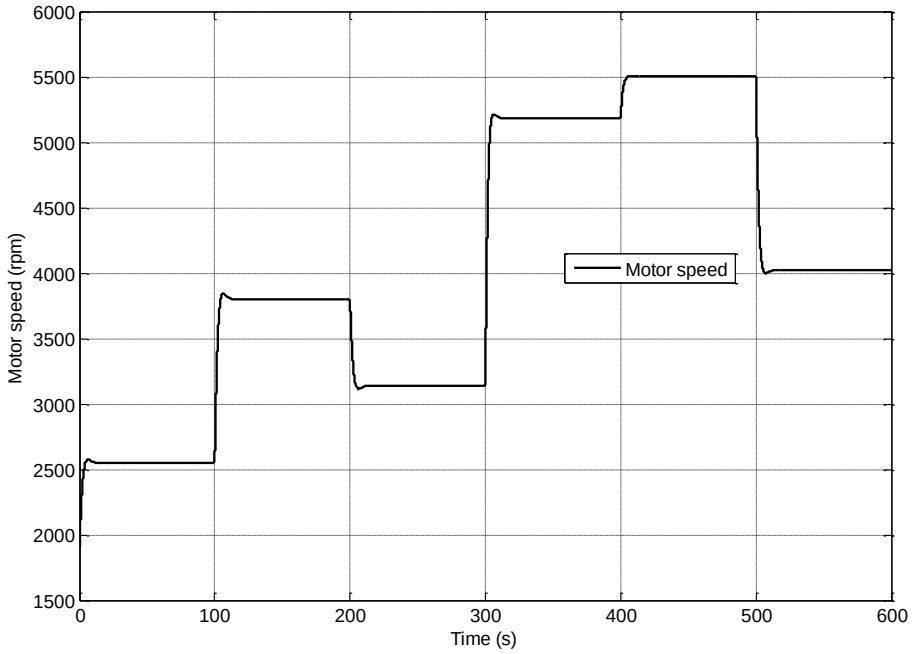

Figure 4.26 Motor speed vs. time. Response to current steps

Given the instantaneous dynamics modeled for the relation between mass flow and motor speed, the mass flow curve is coincident with the rpm plot just discussed and it is not reported here for brevity.

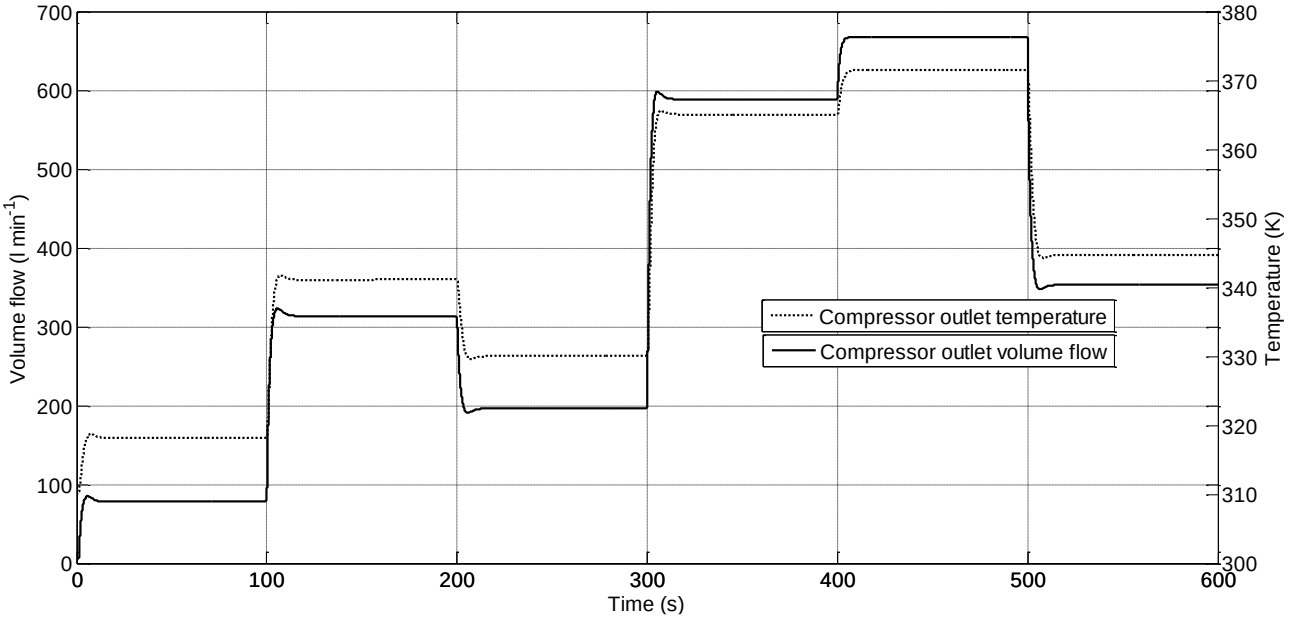

Figure 4.27 Compressor mass flow and outlet temperature vs. time. Response to current steps

Figure 4.27 shows the compressor outlet temperature and volume flow (in l min^{-1}). As can be seen, since the compressor is directly mechanically linked to the motor, the motor speed together with the curves for temperature and flow have the same shape of the rpm one (Figure 4.26). The most important data obtainable from the temperature plot is its maximum temperature reached in correspondence of the maximum flow and current demand, and almost equal to 373 K.

In such cases, the presence of an intercooler would be mandatory for the stack safety. The inlet temperature to the motor (T_{room}) was taken equal to 298.15 K.

4.2.1.2 *Intercooler response*

The intercooler received mainly the mass flow and temperature from the previous compressor block and adapted the coolant water mass flow to maintain the outlet flow temperature to a maximum desired value. For the humidifier inlet temperature, a desired temperature of 60°C (333 K) was chosen.

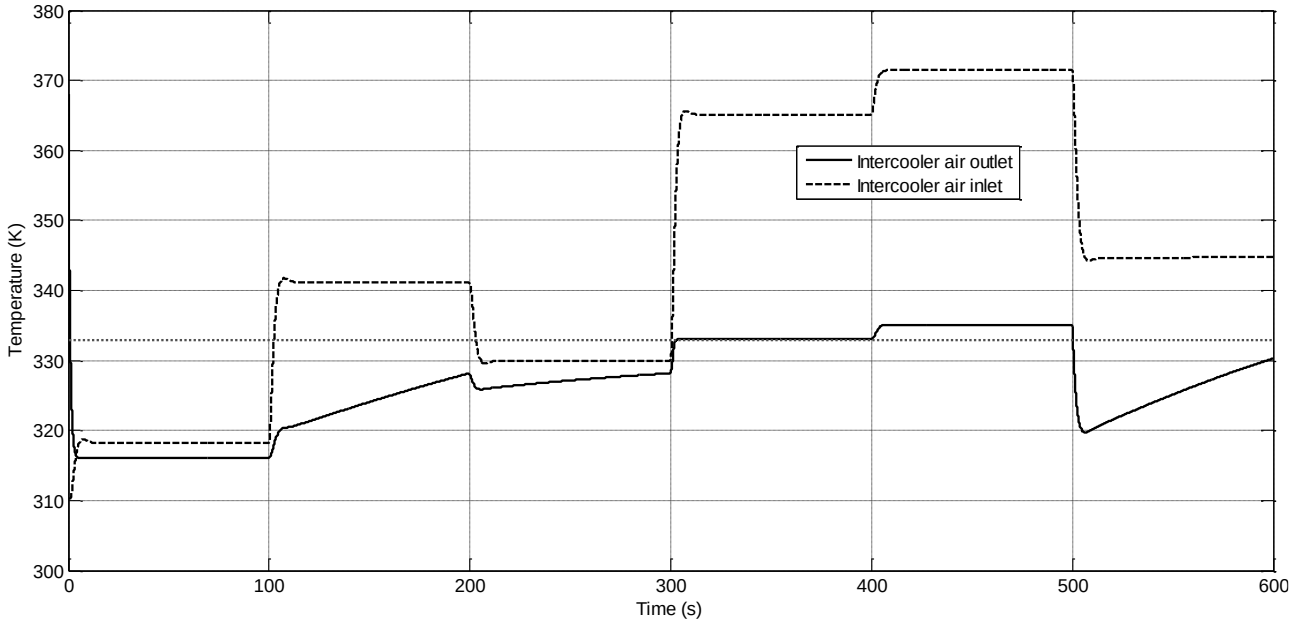

Figure 4.28 Intercooler inlet and outlet temperature vs. time. Response to current steps

Figure 4.28 shows the inlet and outlet temperature of the air flow passing through the stack. The grey dotted line indicate the desired temperature (333 K). As can be seen, the intercooler outlet temperature has a particular shape. For most of the time, the air temperature is always lower than the desired temperature. For this reason, the intercooler does not intervene in cooling the air flow. At T=300 s, instead, the temperature rises too much, and the intercooler intervenes in maintaining the temperature coincident at 333 K. A successive increase in current (T=400 s) makes the temperature to increase further. The temperature at the outlet slightly increases over the desired temperature value, up to about 335.12 K. This excess in temperature is given by the controller gain parameters. Different parameters should be able to modify the response in a better way. It has to be underlined that the intercooler model simply activates when the air flow temperature is excessive. When the temperature is instead below the desired value, the intercooler simply stops. In the practical case, the temperature of the stack is desired to be maintained always at the same level. This implies the use of preheated air flow entering the stack. This is not the case of the intercooler here modeled. The steepness of the curves in Figure 4.28 depends on the temperature difference between the inlet and outlet actual temperature.

The coolant water flow (in l s^{-1}) is shown in Figure 4.29. For most of the time, up to T=300 s, the water flow is equal to zero. The water flow starts after this time instant and keeps to a low value until T=400 s, where the 333 K condition is met. At this point, the successive increase in the current

demand creates a saturation in the intercooler flow. The saturated value of 5.0 l s^{-1} is not shown in Figure 4.29. The simulations at this point were done increasing the intercooler maximum volume flow to 10.0 l s^{-1}. Anyway, the results did not changed substantially, and are reported in Figure 3.26. The maximum water flow raised to about 6.2 l s^{-1}.

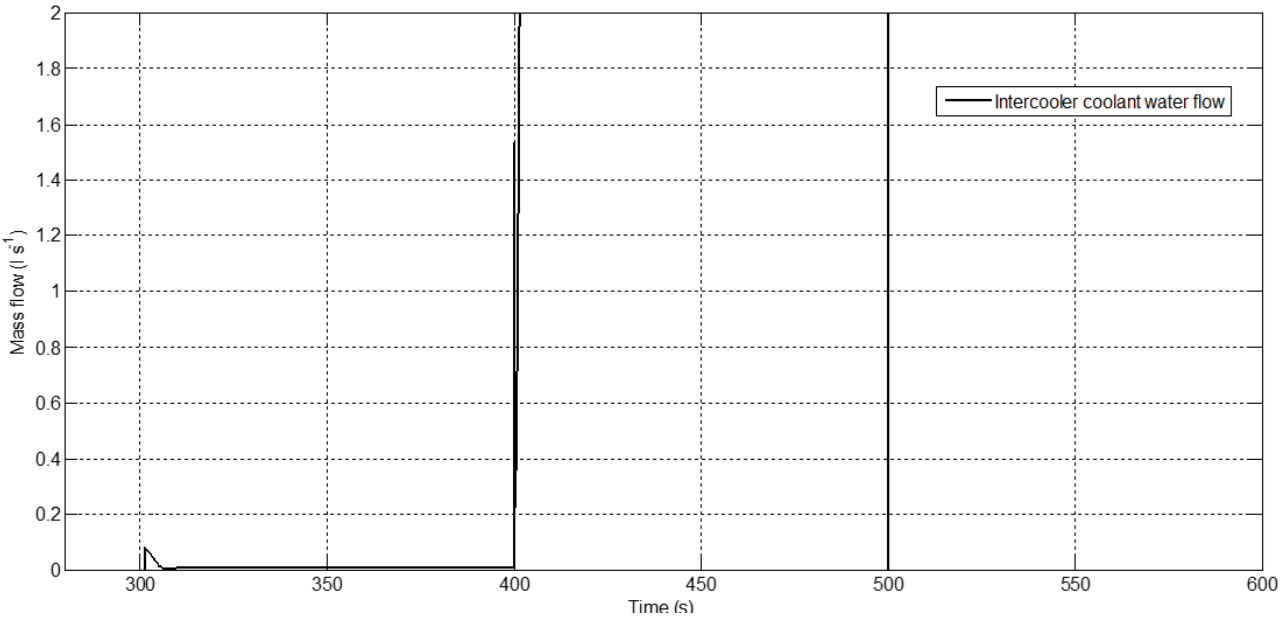

Figure 4.29 Intercooler water flow vs. time. Response to current steps

It is instead more interesting to note the transient response of the water flow. A zoomed area around T = 400 s is given in Figure 4.30. In presence of a step command, the mass flow rapidly increases responding with a positive spike, then lowers immediately and start increasing again towards a steady-state condition. This behavior was given by the derivative gain, responding in presence of rapid variations in the inlet conditions. In the real case, the response of the mass flow would be more relaxed, since the water mass flow would be linked to the water pump dynamics response, not modelled here for these simulations. Considering the transient given in Figure 4.30, it is possible, anyway, to consider a transient of about 7 seconds. This transient response is given by the PID controller gains, and not by a physical delay. The new maximum intercooler water flow was used for all of the following simulations.

A peculiar behavior of the intercooler is represented by the value of the relative humidity at the intercooler air outlet, and shown in Figure 4.31. The relative humidity depends upon several parameters. The combination of the effects given by temperature, mass flow and pressure affected the relative humidity value in this particular way. At each current step the relative humidity shows overshoots and undershoots, as in the case of fuel cells. The behavior is quite similar to the outlet temperature one (Figure 4.28) in terms of shape and steady-state conditions. The relative humidity value, as can be seen, is always quite low if compared to standard ambient air conditions.

This is simply given by the higher temperature of the outlet air, acting in decreasing not the absolute humidity of air, i.e. its partial pressure, but raising the maximum water vapor content allowed, thus lowering the RH value. The inlet ambient relative humidity at the compressor inlet was set to 50%.

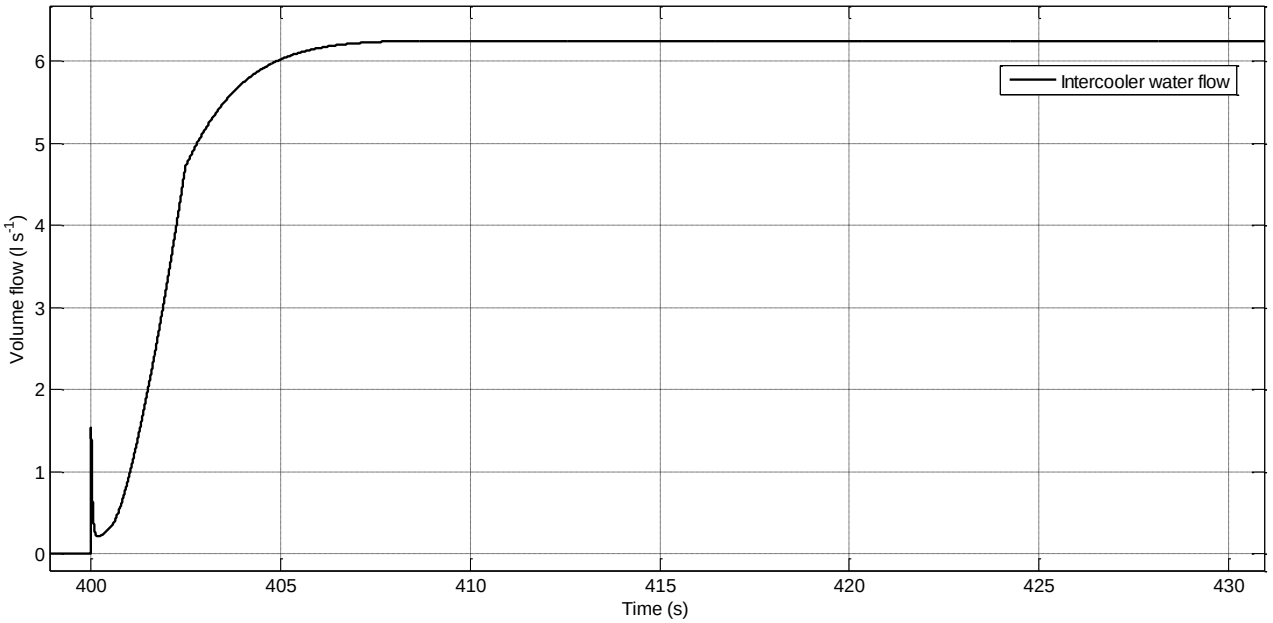

Figure 4.30 Intercooler water flow vs. time. Response to current steps. Zoomed area, increased controller saturation

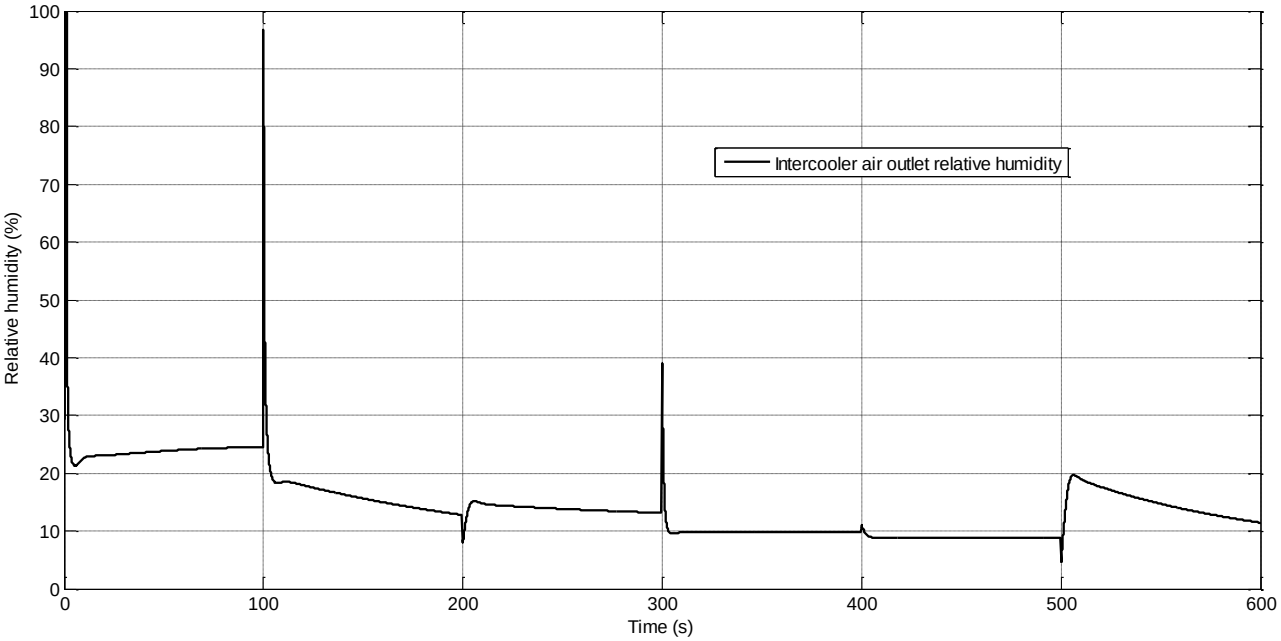

Figure 4.31 Intercooler outlet relative humidity vs. time. Response to current steps

4.2.1.3 Cathode membrane humidifier response

The cathode humidifier receives the humid flow from the stack cathode outlet and uses it to exchange humidity and, secondarily, heat to the dry air coming from the intercooler prior to entering the stack. The flow entering the stack should be always pre-humidified and then injected into the stack. Typical values for the cathode and anode inlet humidity should be quite high. In the case of the anode inlet, the temperature should be higher than the 80% to avoid the anode-side

dehydration due to the water electro-osmotic drag. Also at the cathode, nevertheless, the water flow entering the stack should be maintained at an adequate level.

The relative humidity of air at the humidifier outlet is shown in Figure 4.32. Also this kind of plot shown spikes and related overshoots and undershoots, as already seen in the previous plot of the intercooler humidity (Figure 4.31). Apart from the temporary spikes in this plot, the value of relative humidity is almost always above the 90 percent, indicating a good capacity of the humidifier to maintain adequate levels of water at the stack inlet. The variation in the steady-state values is mainly given by the variation in the mass flow entering the humidifier. As can be seen, when the current demand and the mass flow increase, the relative humidity lowers, since the humidifier must provide water vapor to a higher quantity of mass flow, with the result of a lower relative humidity. Vice-versa in the case of a current reduction. Despite the fact that the temperature of the dry inlet gas and the humidified one varies with time, together with the variation in the relative humidity of both the two streams inside the humidifier, the correspondence between current and relative humidity still remains visible.

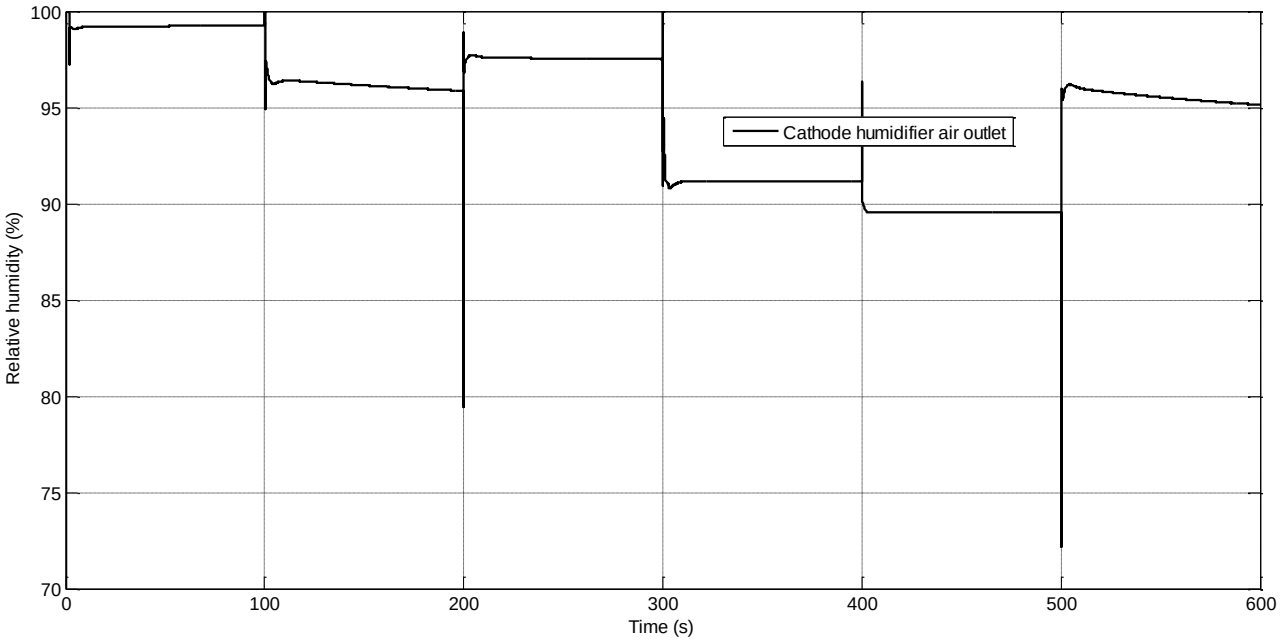

Figure 4.32 Cathode humidifier outlet relative humidity vs. time. Response to current steps

A zoomed portion of the humidity plot is reported in Figure 4.33. As can be seen, together with an undershoot, there is also a small overshoot, or oscillation, around the steady-state value.

The outlet temperature of the flow entering the stack (dry air outlet) and the flow exiting from the humidifier as exhaust flow (humid air outlet) are compared in Figure 4.34. During the first 60 seconds, given by the initial conditions used in the simulations, the flow exiting from the stack is even cooler than the one exiting from the intercooler, given by the transitory stack response to temperature variation.

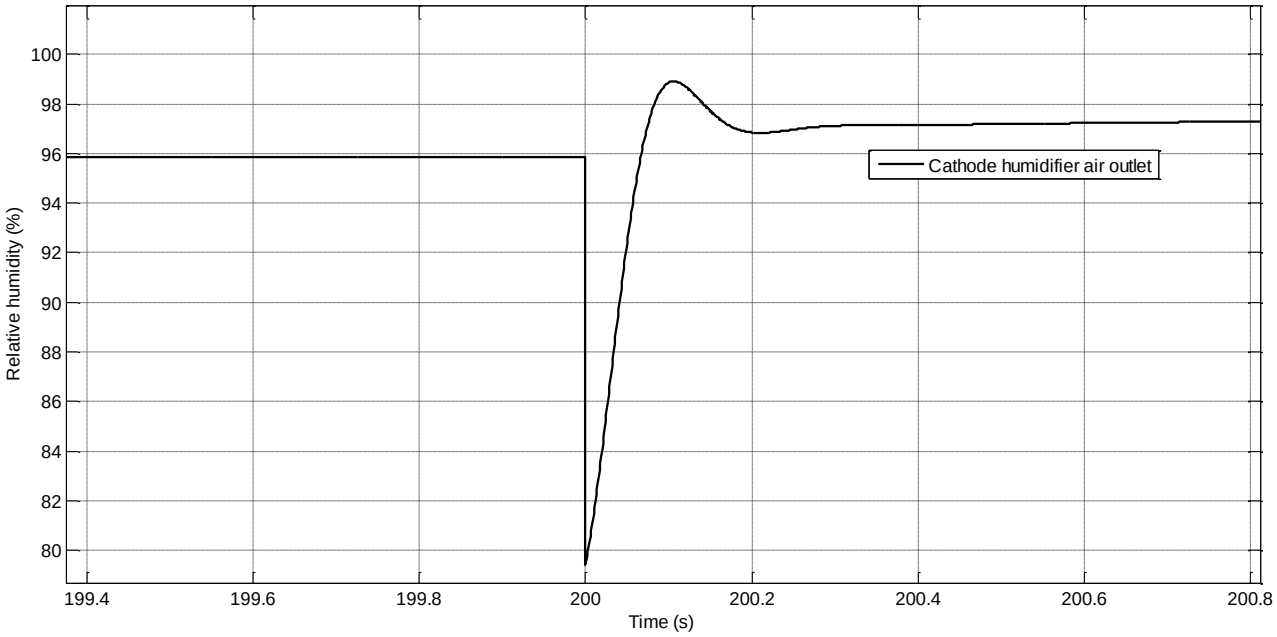

Figure 4.33 Cathode humidifier outlet relative humidity vs. time. Response to current steps. Zoomed area

Apart from this initial condition, the two temperatures are maintained in about 10-15 K for all of the operating time, with the stack inlet temperature (the dry air side) sufficiently constant and around a value of about 325 K (52°C). It is interesting to notice a main difference between the humid and air transient response. The dry air shows some overshoots and undershoots, while this is not the case for the humid one. This can be explained if the two flows are considered from their "origin". In the case of the dry air duct, this flow is "sensible" to the spikes given by the relative humidity plots of the intercooler (Figure 4.31), as well as to the humidity of the humidifier (Figure 4.32), and enters the humidifier with a lower relative humidity and temperature. The humid air flow, instead, comes directly from the stack exit, where the stack thermal response dominates with a sort of first-order response, as it will be shown later (Figure 4.36). The temperature and humidity of this flow are higher, making the influence of the dry air less noticeable.

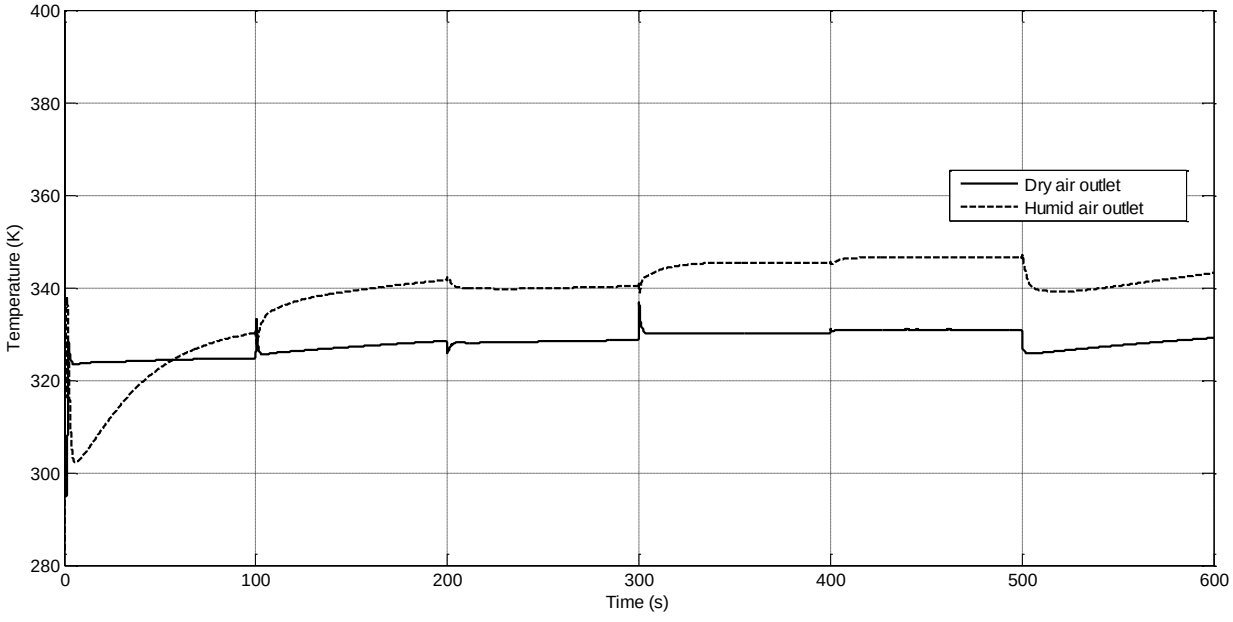

Figure 4.34 Cathode humidifier outlet temperatures vs. time. Response to current steps

The last plot concerning the cathode humidifier is the membrane water flow passing from the humid to the dry air side. As can be seen, the water flow plot has a shape similar to humidity plots. In fact, the main driving force for the water passage in membrane humidifiers is mainly given by the relative humidity value on both sides of the membrane tubes, and secondarily, it depends on temperature.

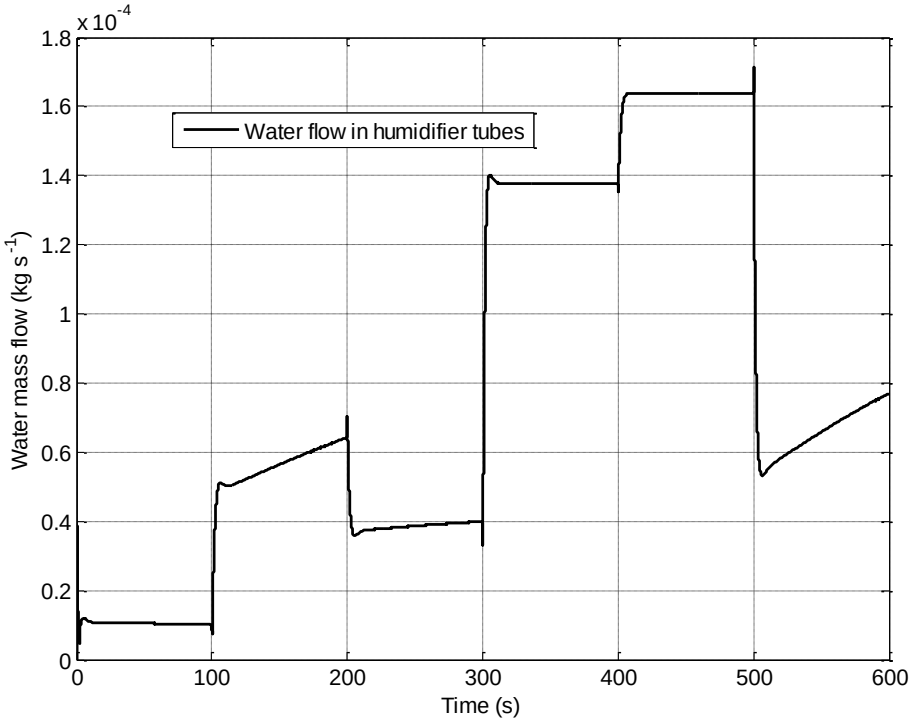

Figure 4.35 Cathode humidifier membrane water flow vs. time. Response to current steps

4.2.1.4 Hydrogen mixer response

The hydrogen mixer simply adds the hydrogen flow coming from the stack with the one coming from the hydrogen tank. The only interesting result obtainable from this block is the relative humidity value and temperature resulting from the flow mixing. These plots are shown in Figure 4.36. As can be seen, the relative humidity of hydrogen is always equal to one, apart around the current steps, where the stack reacts with a temporary drop in the relative humidity before returning to its steady-state condition. The temperature, since it is considered to have the hydrogen entering the mixer at ambient conditions, is always quite low, with a maximum value of less than 330 K (57 °C). At higher current demand, the higher hydrogen flow required from the tank reduces the temperature of the hydrogen exiting from the stack in a more pronounced way. Despite the air temperature at the cathode showed a behavior more similar to the stack one, the hydrogen inlet temperature shows the overshoots and undershoots. The relative humidity at this high level can be explained considering the fact that the hydrogen outlet flow possesses a high temperature (comparable with the stack temperature, Figure 4.38) and humidity. Given the abrupt reduction of temperature when mixed with the cold flow coming from the hydrogen tank, the reduction of temperature makes the gas super-saturated with water vapor, despite the null relative humidity of the tank hydrogen.

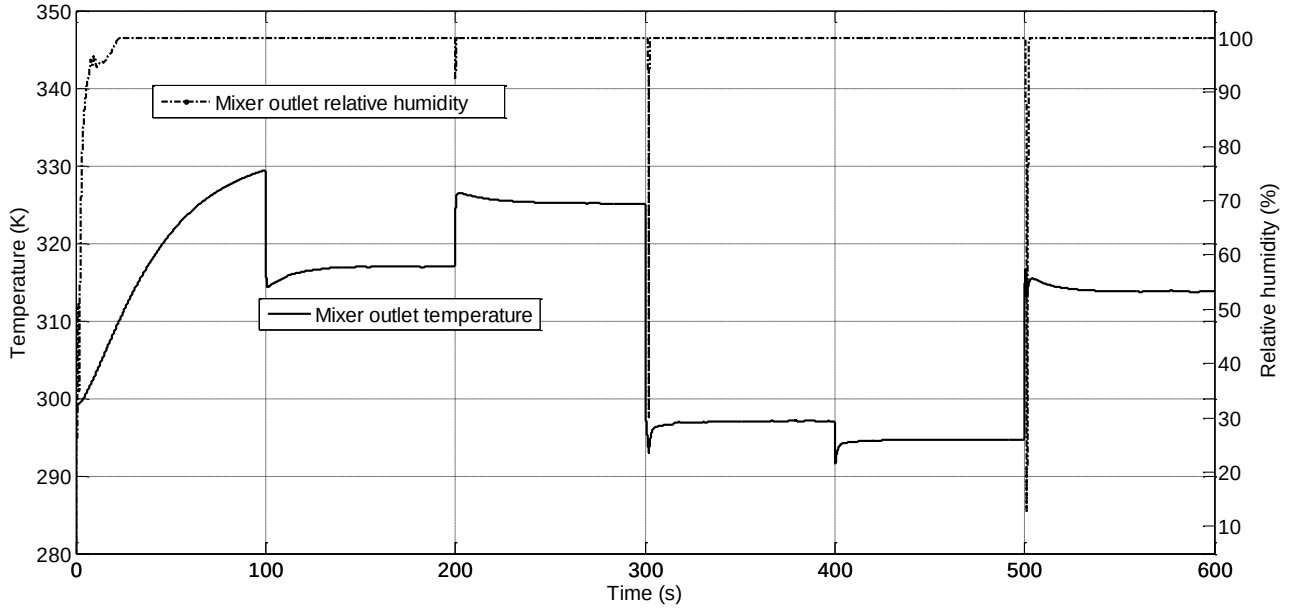

Figure 4.36 Hydrogen mixer outlet temperature and relative humidity vs. time. Response to current steps

4.2.1.5 Fuel cell stack response

The fuel cell stack represents the main core of the simulation model. The step response of the stack is similar to the response already encountered in the previous analyses used for the stack model validation. The voltage plot is shown in Figure 4.37. As can be seen, the voltage plot shows the typical behavior already discussed in depth. The transient time of the voltage plot can be considered comparable to about 100 seconds, since at each step the voltage almost reached the steady-state condition in all cases.

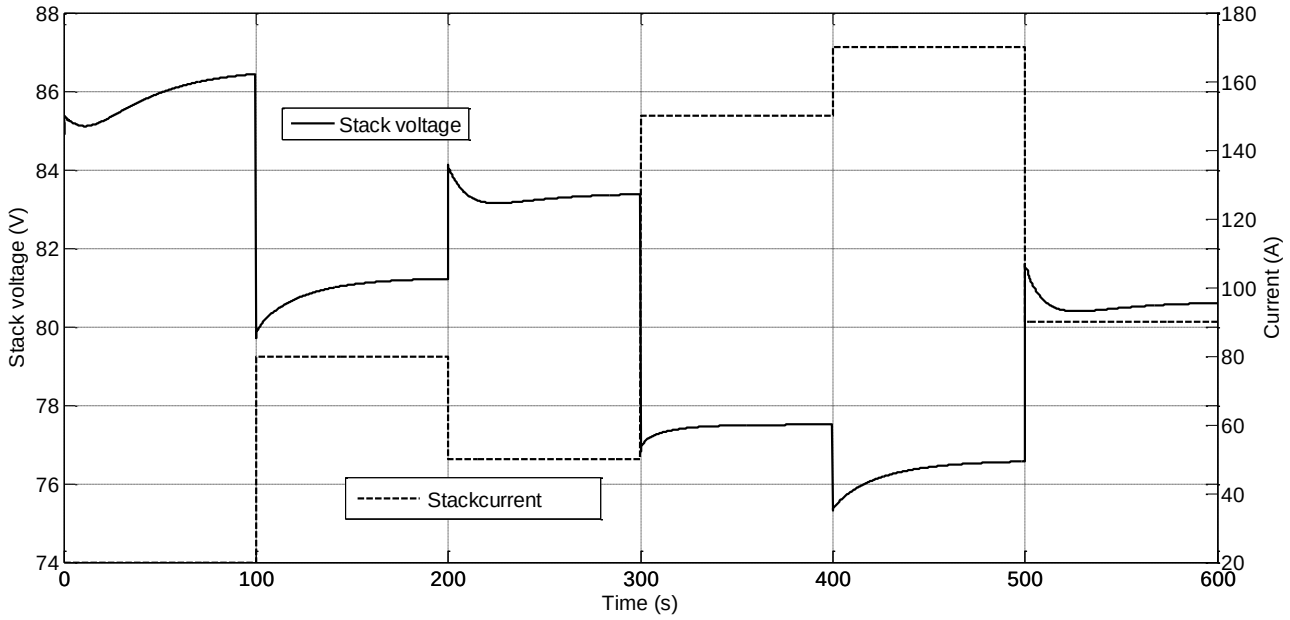

Figure 4.37 Fuel cell stack voltage vs. time. Response to current steps

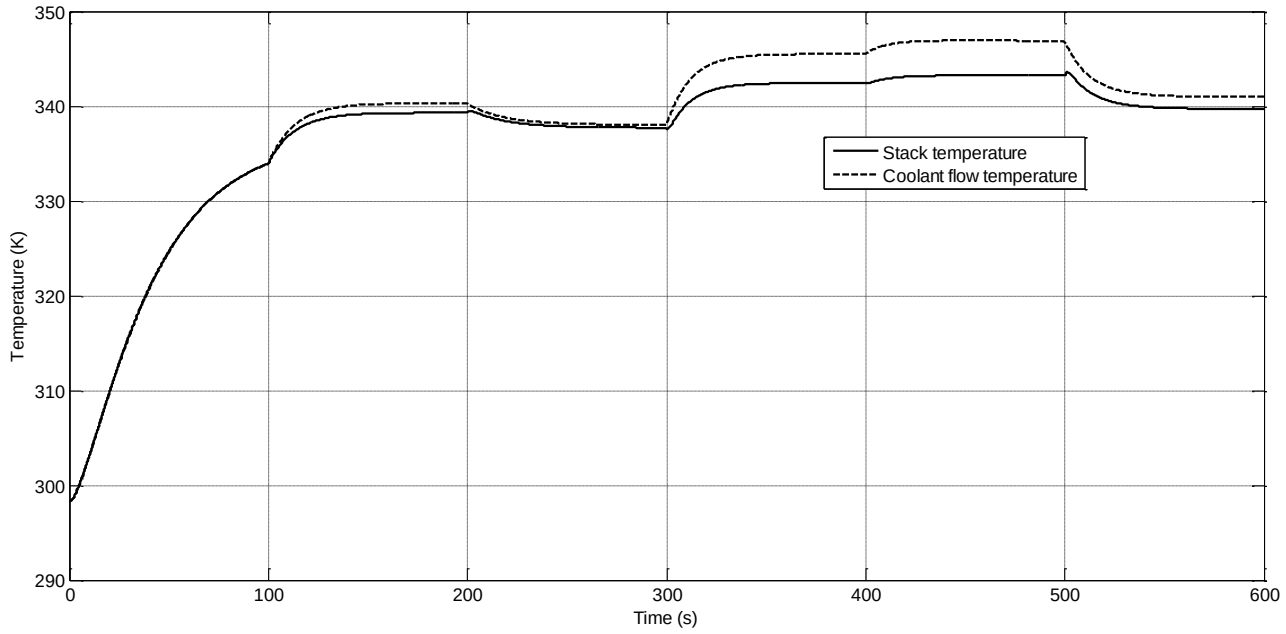

Figure 4.38 Fuel cell stack and coolant flow temperatures vs. time. Response to current steps

The plot of the stack temperature is given in Figure 4.38. The temperature of the stack and of the coolant water at the stack outlet are given. The inlet temperature for the coolant flow was taken equal to the stack validation simulation one. As can be seen, for low values of current, requiring less stack cooling, the two temperatures practically coincide. The maximum in the flow can be seen at high loads. The coolant flow control was taken from the control logic of the Ballard test bench used for the validation of the stack model, and it is simply related to the current demand through a look-up table. The temperature of the stack shows the typical first-order dynamics response, given the nature of the thermal phenomena involved. Moreover, apart from the initial phase (up to T = 100 s) the transient is more rapid of the voltage transient, and can be estimated in about the half of the latter one.

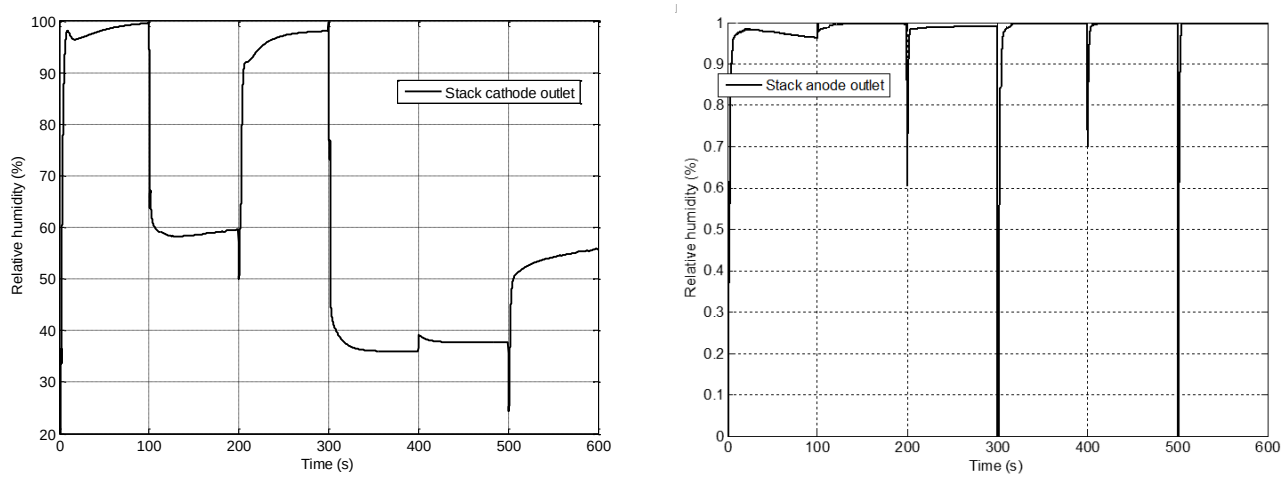

Figure 4.39 Fuel cell stack outlet relative humidity vs. time. Response to current steps

The relative humidity at the anode and cathode outlet sides can be seen in Figure 4.39. Both the cathode and the anode sides showed typical spikes under step current commands, as already seen in all of the other humidity plots already analyzed.

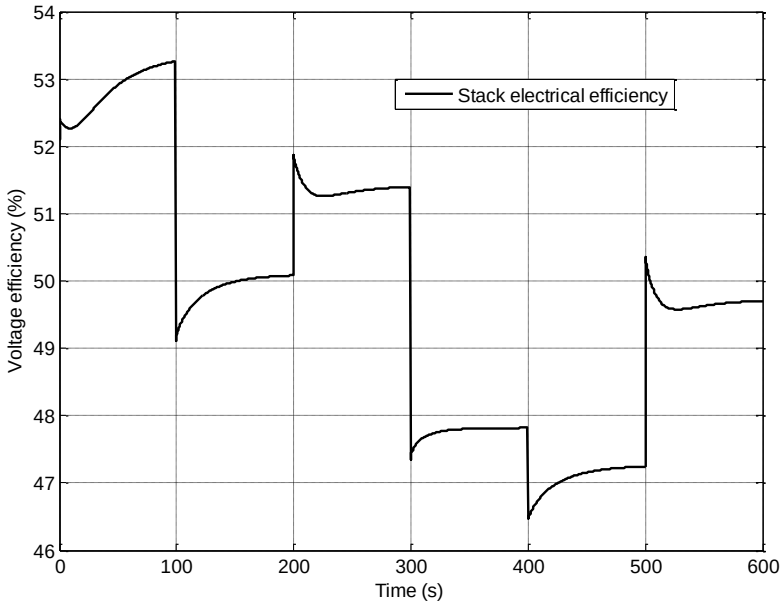

Figure 4.40 Fuel cell stack efficiency vs. time. Response to current steps

The efficiency of the stack is shown in Figure 4.40. Its value is in line with the expected values. The theoretical power output and the real power output changes with time. The theoretical power output showed a quite linear behavior, and can be seen in Figure 4.41. The real power output, instead, showed a slightly curved profile at each step. Their combination (division) gives the efficiency plot of Figure 4.40. The maximum net power in this case is of about 13 kW.

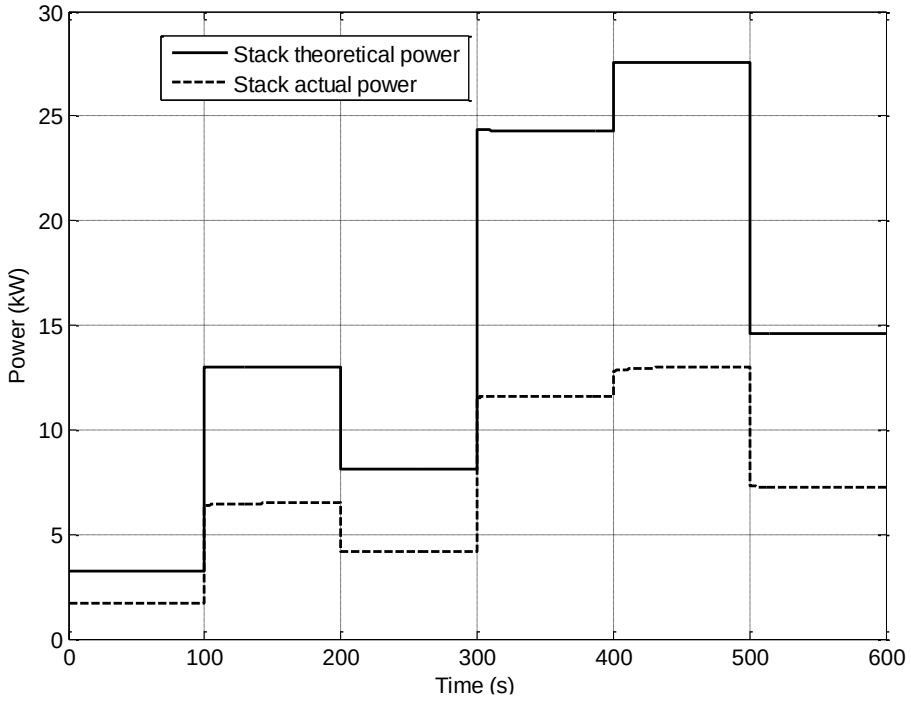

Figure 4.41 Fuel cell stack theoretical and actual power vs. time. Response to current steps

Also the stack membrane hydration showed some undershoots and overshoots. Its plot is reported in Figure 4.42.

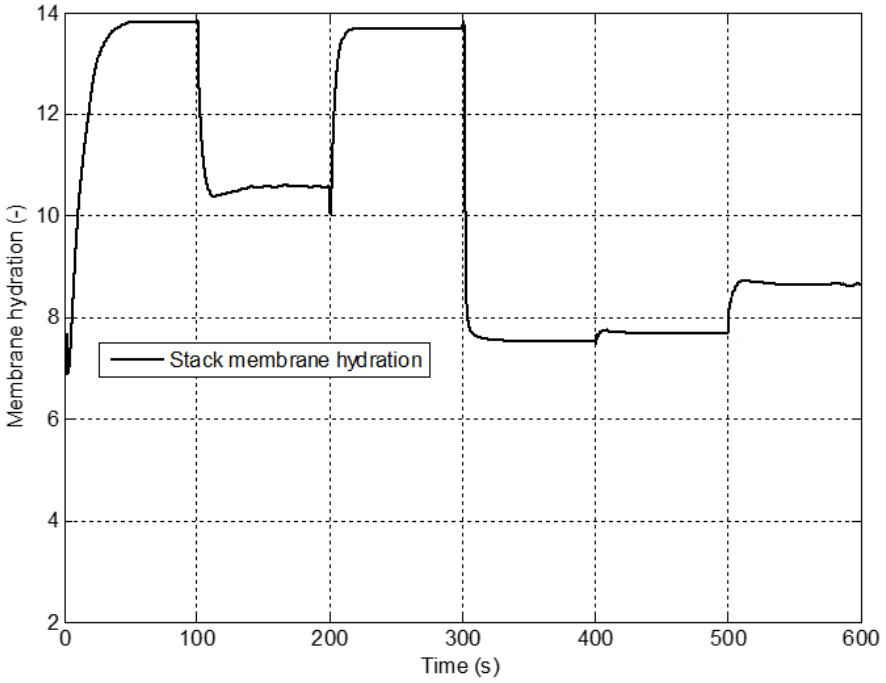

Figure 4.42 Fuel cell stack membrane hydration vs. time. Response to current steps

4.2.1 System response under parameters and boundary conditions variation

The following series of simulations was performed to consider the response to the variation of some relevant parameters and their influence on the stack performance in a sort of sensitivity analysis. In all of these simulations, the polarization curve of the stack is usually drawn. The polarization curve is obtained imposing a blended ramp input current, starting from 5 to 180 A.

4.2.1.1 Influence of temperature

The impact of temperature is now analyzed in the following paragraph. The first set of simulations considered the stack temperature influence on the electrical performance. The stack temperature was fixed at certain values. The curves were plotted in increments of 5°C starting from 45 to 70°C (318-353 K). The results are given in Figure 4.43. As can be seen, a higher stack operating temperature allows a higher voltage output. The increase can be evaluated in about the 2 percent, anyway. The increase in the performance is given by higher energy available for the electrochemical reactions in form of heat. On the other hand, higher temperatures might imply problems in the membrane humidification without an excessive higher performance.

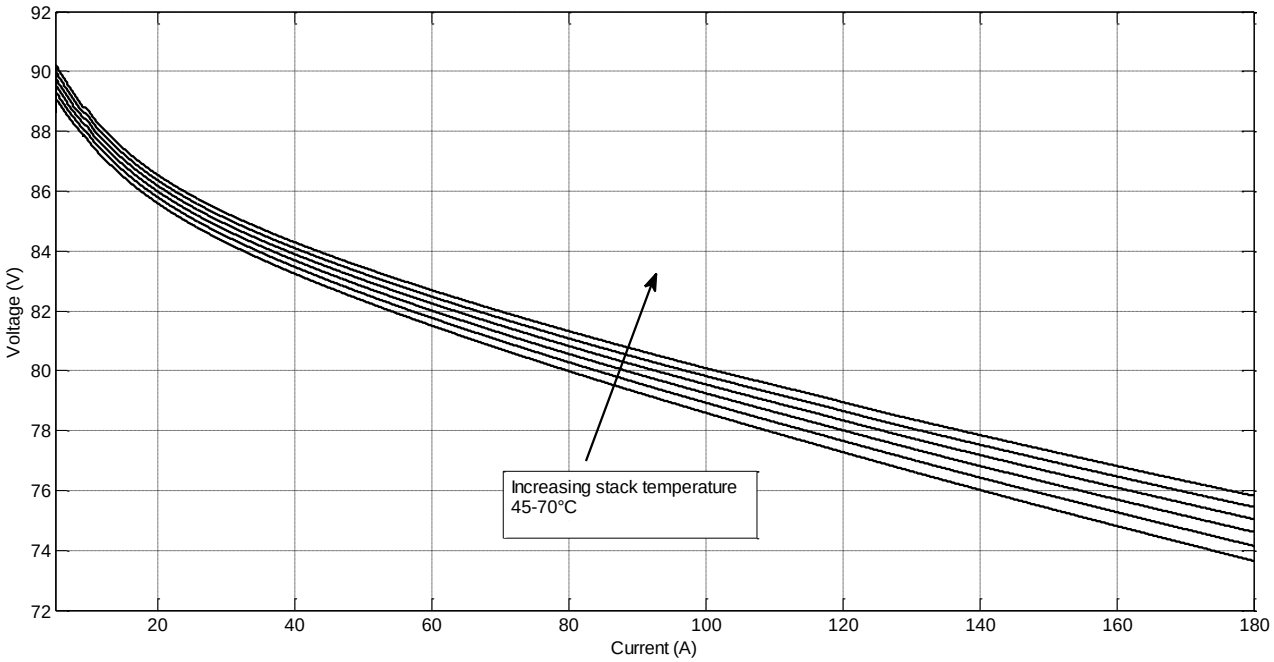

Figure 4.43 Stack voltage vs. current. Stack temperature variation. 45-70°C (318-343K)

Another possible variation in a temperature value might be a different ambient temperature, modifying the heat exchange between the stack and modifying the oxygen flow parameters. The results are given in Figure 4.44. The variation was done from 5 to 30°C. As can be seen, the difference is negligible (notice the zoomed area), and less than the 0.02 percent. This is given by the very low percentage of heat removed from the stack thanks to thermal radiation if compared to the liquid cooling flow. Moreover, the variation in the ambient conditions are controlled and reduced by the thermal control of the air feed line. The same can be said also for the intercooler desired outlet temperature. The results are shown in Figure 4.45. The intercooler outlet temperature was varied from 40 to 65°C (313-338 K). The effect can be considered negligible, since the air flow entering the stack does not affect the stack temperature in a noticeable way, since the electrochemical performance of the stack (and hence the polarization curve) is affected directly by the stack temperature. The same can also be done with the variation in the hydrogen tank temperature. The results show a negligible effect on the stack performance, and are not reported here for brevity.

It is then possible to conclude that the system performance under the variation of temperature values affects the electrical performance only in presence of variations capable to modify actively the stack temperature.

4.2.1.1 Influence of electrochemical parameters

The following series of tests were conducted varying the electrochemical calibration parameters, namely the cathode exchange current density, the ohmic coefficient and the crossover current density. The variation for the ohmic coefficient considered a variation of the ±10 and ±20 percent from the baseline value (0.78) used in the validation. The cathode exchange current density was varied multiplying and dividing it by 2 and 4 to give a better visualization of its influence on the polarization curve. The effect of the reduction of the ohmic voltage loss is given in Figure 4.46.

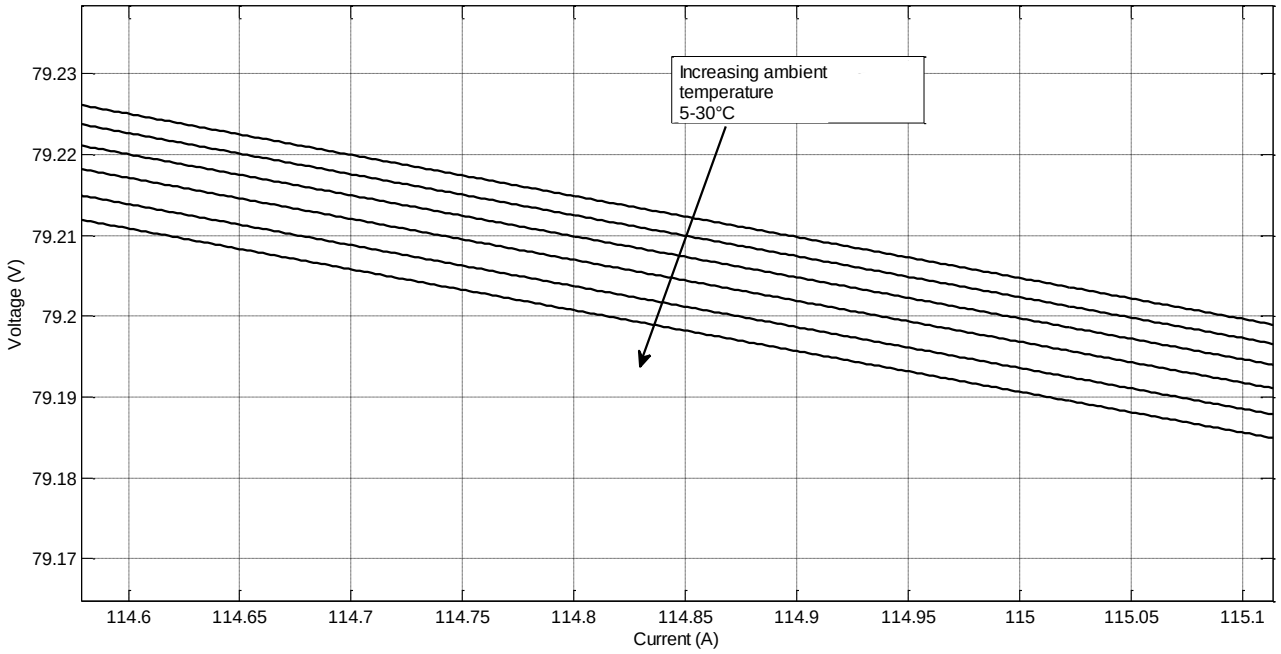

Figure 4.44 Stack voltage vs. current. Ambient temperature variation. 5-30°C (278-303K). Zoomed area

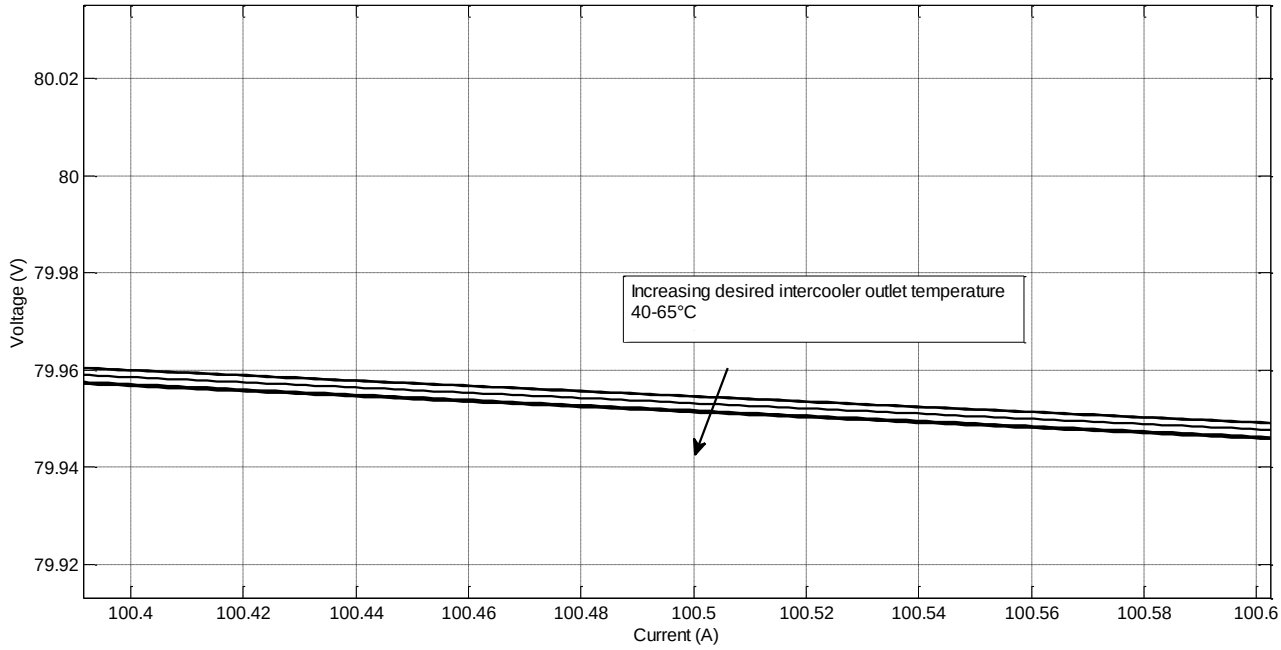

Figure 4.45 Stack voltage vs. current. Intercooler desired outlet air flow variation. 40-65°C (313-338 K)

As can be seen, the reduction in the ohmic coefficient has the effect of varying the curve inclination, and it is more evident in the central portion of the curve, where the ohmic losses prevail on the activation voltage losses.

The effect of varying the activation voltage losses is instead shown in Figure 4.47. The effect of the variation in the exchange current density has the effect of translating all of the polarization curve at lower or higher values. The exchange current density, in fact, acts during the initial portion of the polarization curve, modifying the behavior of the entire curve.

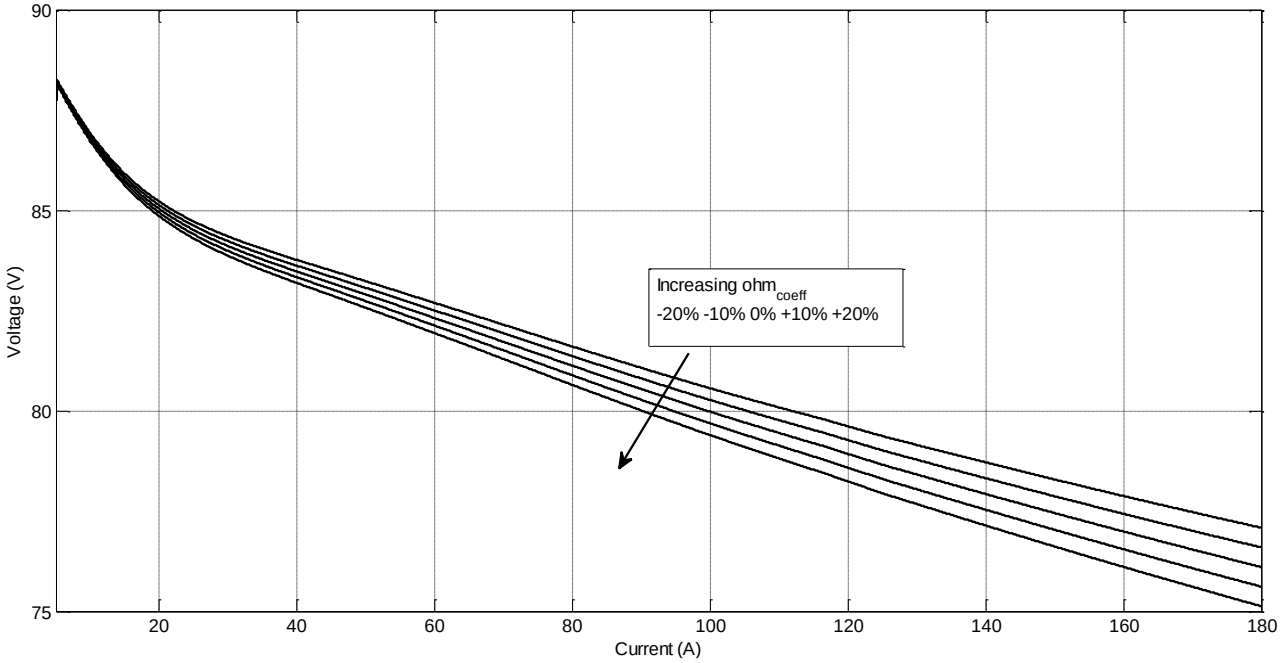

Figure 4.46 Stack voltage vs. current. Ohm_{coeff} variations. -20%; -10%; 0%; +10%; +20%

The crossover current density variation is instead shown in Figure 4.48. The curves were drawn for the initial 20 A, since the crossover current acts in the very initial part of the curve. The crossover currents have the effect of reducing the open circuit voltage below the theoretical open circuit voltage, but extinguish when the current density increases. As can be seen in the figure, the five curves tend to the same value in the right hand side portion of the graph, despite the activation losses keeping the curve well separated from each other.

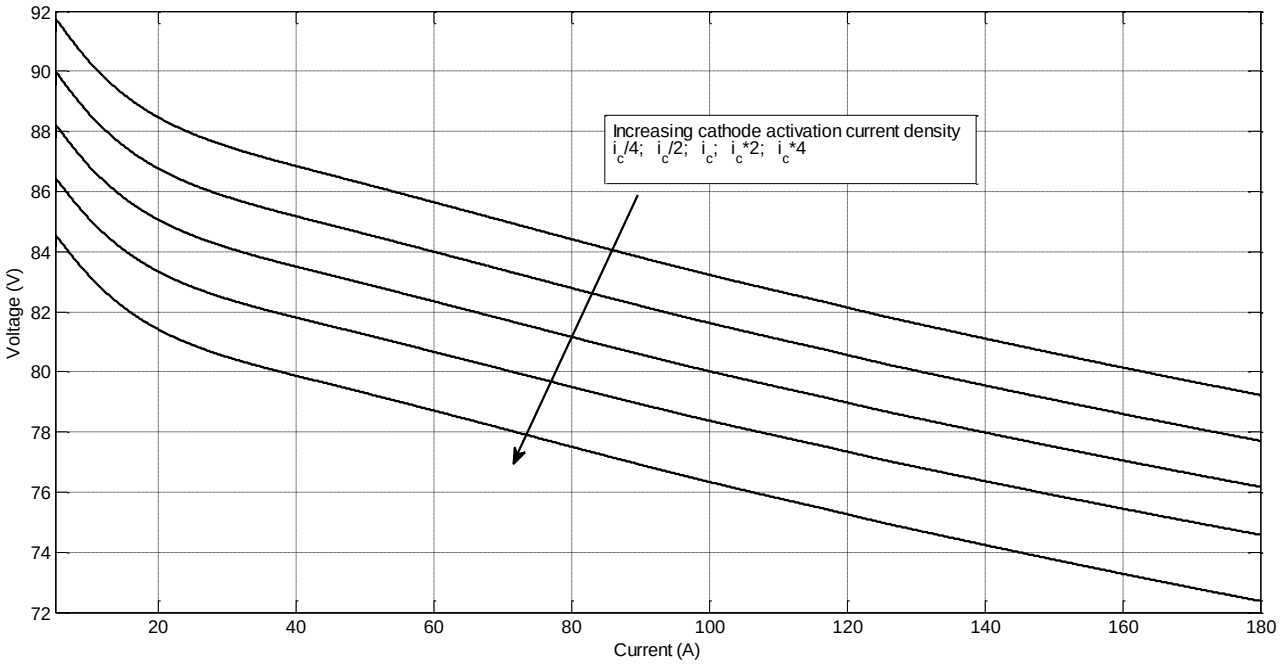

Figure 4.47 Stack voltage vs. current. i_{o_c} variation. Multiplication and division by 2 and 4

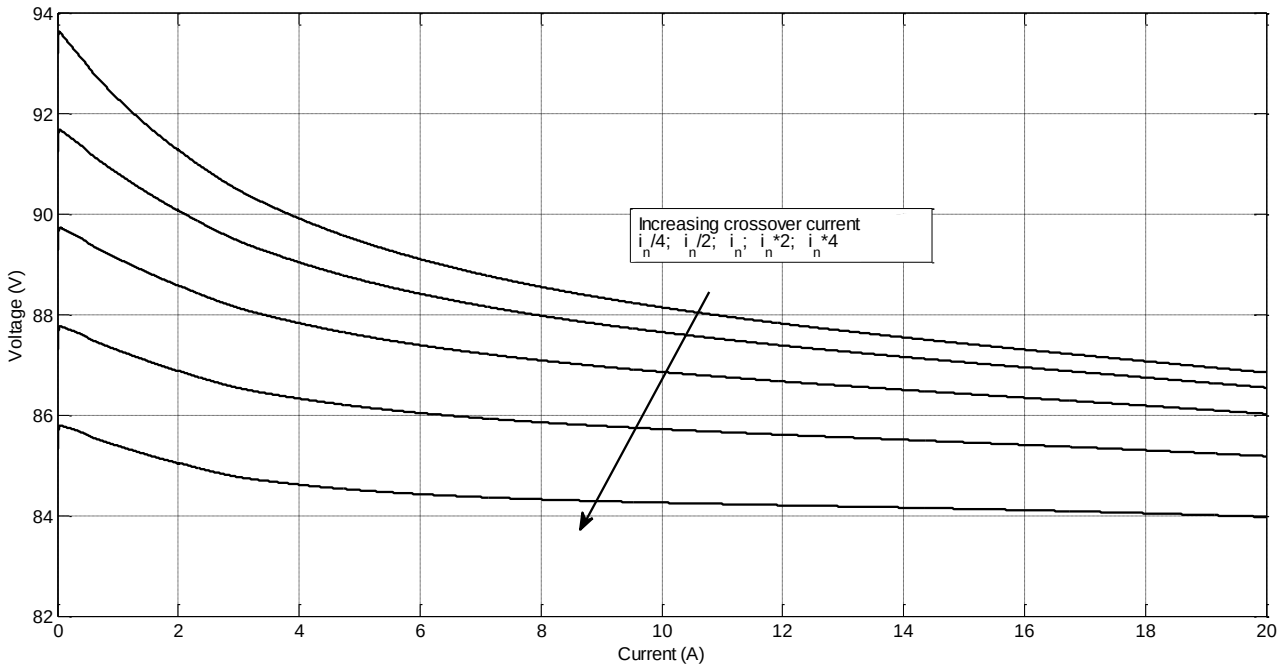

Figure 4.48 Stack voltage vs. current. $\boldsymbol{i_n}$ variation. Multiplication and division by 2 and 4

4.3 Electrolyser system model validation

The electrolyser system model validation consisted in the validation of the stack and the pressure calculation subsystem, together with the coolant flow loop, being these three elements the main elements characterizing the behavior of an alkaline or PEM electrolysis system. Given the poor diffusion of these systems in the market, and being this technology quite well established from the past, only few data can be obtained from the available literature about these technologies. Moreover, there was not an experimental laboratory setup available for the model calibration and comparison with the real data obtained from a dedicated test rig, as in the case of the fuel cell stack, validated before in this chapter (Par.4.1).

The main data used for the validation of the alkaline electrolyser are based on the experimental data used by Nehrir and Wang (2009) for the validation of their models and based on the project given by Meurer et al. (1999) and used also by Ulleberg (2003).

4.3.1 Experimental setup and model assumptions

The experimental setup was taken directly from the publications just mentioned. The pressurized electrolyser used is shown in Figure 4.49. The alkaline electrolyser was a so-called advanced alkaline electrolyser operating at a pressure of 7 bar and at temperatures up to about 80°C (353 K). The cells were circular, bipolar, with a zero spacing geometry, and consisted of NiO diaphragms and activated electrodes. The electrolyte is a stationary 30% KOH solution. Each cell had an electrode area of 0.25 m^2. This gave an operation voltage in the range 30 – 40 V. The hydrogen production and water cooling flow rates for the Phoebus electrolyser was not logged and collected on a regular basis, along with the minutely collected operational data. However, an experiment where this and other pertinent data was sampled for every 5 min was performed by Ulleberg (2003).

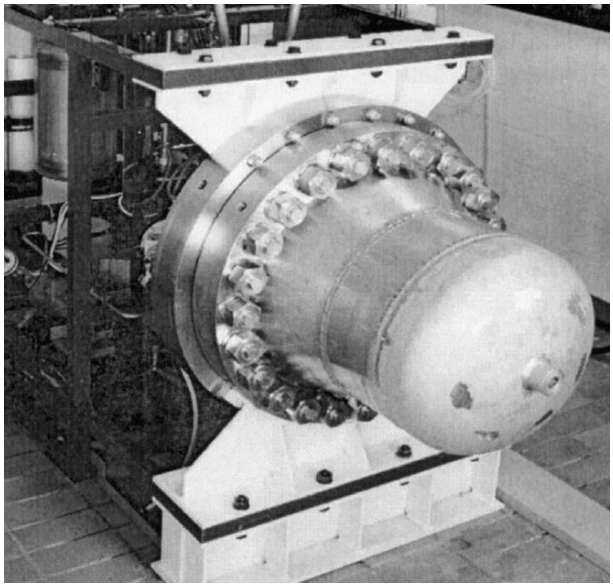

Figure 4.49 Phoebus project pressurized electrolyser used for the validation of the model

Many data used in the present model were available from Nehrir and Wang (2009) and from Ulleberg (2003). These data are given in Table 4.4. Most of the data are obtained from the literature. Few data were taken from the reference work by Evangelista et al. (1975). Few parameters are estimated and not known a priori, and are supposed to be sufficiently reliable. Four variables, namely the reference exchange current densities ($i_{0_{ref,a}}$ and $i_{0_{ref,c}}$), the ohmic coefficient calibration constant (K_{ohmic}) and the crossover current density (i_n) are used in this preliminary stage for the calibration of the model. Given the large amount of available data about the stack thermal properties, the thermal calibration constants are considered fixed at this stage.

Some of the parameters listed as "Experimental data" were derived analytically. More information can be found in Ulleberg (2003) and Nehrir and Wang (2009).

Table 4.4 Calibration parameters used for the electrolyser validation

Parameter	Value	Notes
Stack properties		
Stack thermal resistance (R_{therm})	0.167 K W^{-1}	Experimental data
Stack area (A)	0.25 m^2	Experimental data
Faraday efficiency first constant (k_{f1})	2.5x10^4 A^2 m^{-4}	Experimental data
Faraday efficiency second constant (k_{f2})	0.96	Experimental data
Conductive heat transfer coefficient (h_{cond})	7.0 W K^{-1}	Experimental data
Convective heat transfer coefficient (h_{conv})	0.02 W (K A)$^{-1}$	Experimental data
Electrolyser thermal capacity (C_{ez})	6.252x10^5 J K^{-1}	Experimental data
Number of cells (n_c)	40	Experimental data
Boundary and inlet conditions		
Coolant water mass flow ($\dot{n}_{H_2O}$)	10 l min^{-1} (average)	Experimental data
Coolant inlet temperature	14.5°C (287.5 K)	Experimental data
Stack initial temperature	51.7°C (324.7 K)	Experimental data
Electrolyte concentration (KOH_{conc})	30% weight	Experimental data
Ambient temperature (T_{amb})	25°C (298 K)	Estimated
Separator resistance (R_{sep})	0.17 Ω cm^{-2}	Vermeiren et al. (1997)
Electrolyte bubbles slip ratio (σ_b)	2.0	Evangelista et al. (1975)
Pressure vessels data		

Maximum O_2 pressure	7 bar	Experimental setup
Maximum H_2 pressure	7 bar	Experimental setup
Vessels volume (V_{O_2} and V_{H_2})	0.1 m^3	Estimated

The most important data can be considered the polarization curve of the stack obtained at different stack temperatures kept constant during the operation of the stack. The curve depicting the single cell voltage vs. current density (expressed in mA cm^{-2}) is used and it is shown in Figure 4.50. The dots represent the experimental data at different stack temperatures, while the solid lines indicate the Ulleberg (2003) model results. The translation of this plot from current density to current and from cell voltage to stack voltage is given by Nehrir and Wang (2009) in Figure 4.51. The current range in this figure is reduced if compared to Figure 4.50. The first graph, nevertheless, will be used for the validation.

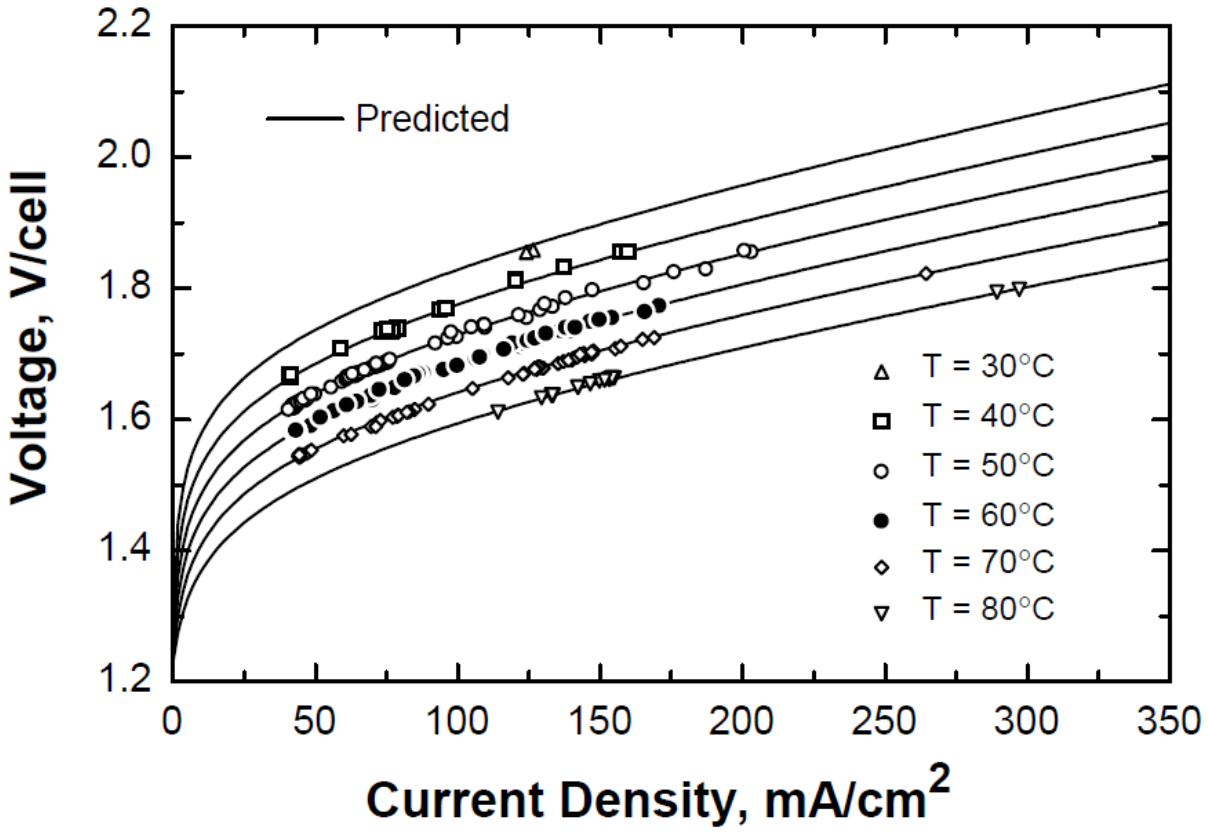

Figure 4.50 Experimental electrolyser polarization curve. Cell voltage vs. current density

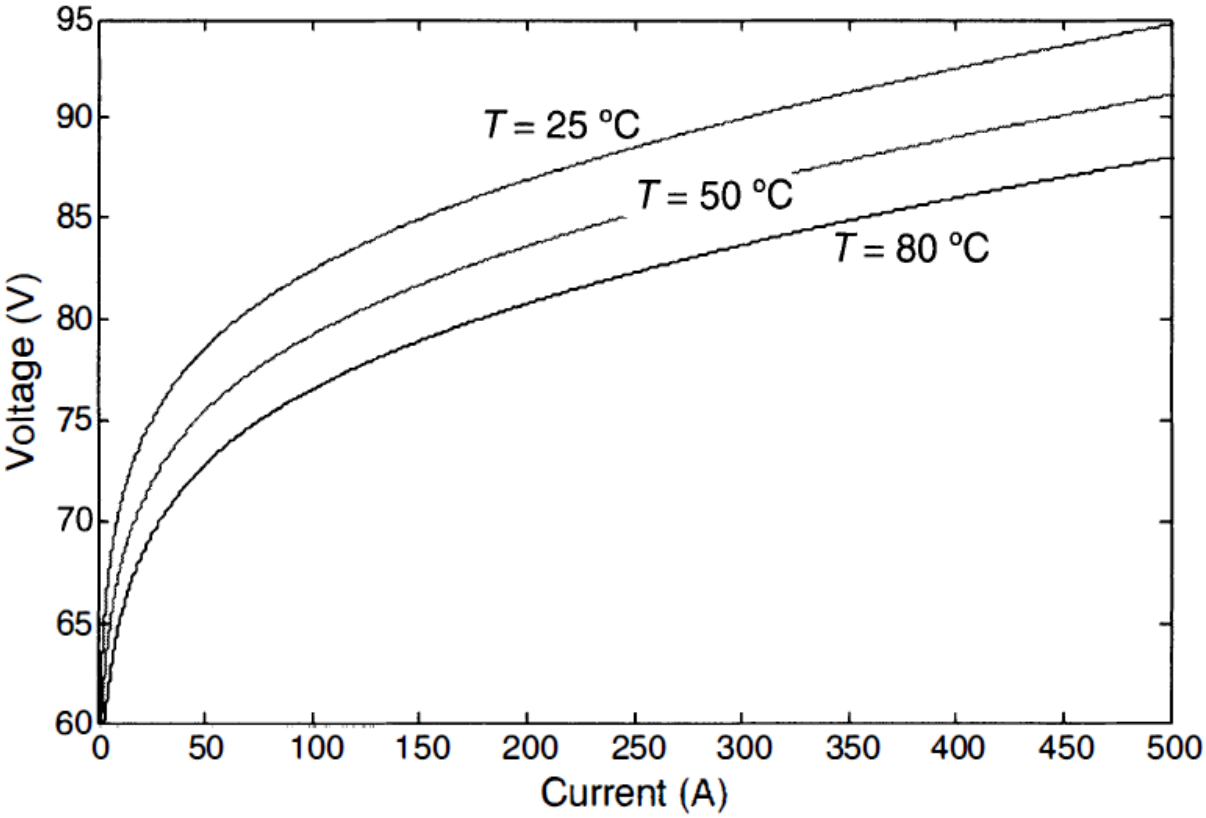

Figure 4.51 Experimental electrolyser polarization curve. Stack voltage vs. current

4.3.2 Experimental results and model validation

4.3.2.1 Thermal model calibration

The thermal model calibration consisted in the determination of the coolant flow controller parameters, namely the proportional, derivative and integrative constants. Given the high amount of thermal data already available, and the correspondence of the thermal model equations with the ones given by Ulleberg (2003) and Nehrir and Wang (2009), the thermal model here presented can be considered comparable with the validation model. The calibration of the coolant flow parameters will be detailed in the following paragraph (Par.4.3.2.2), together with the electrochemical model calibration and validation. The coolant mass flow indicated in Table 4.4 must be considered only as an average value, and cannot be used, since the water mass flow changes widely when passing from few watts to several kilowatts.

4.3.2.2 Electrochemical model calibration and model validation

The validation of the model consisted in keeping the stack temperature at several fixed values, as indicated in Figure 4.50, and recording the steady-state value of current and cell voltage. The calibration and validation was performed point by point. The steady-state condition consisted in the reaching of the maximum pressure inside the pressure vessels (7 bar) and the commanded temperature.

The first trials consisted in the variation of the coolant flow controller parameters to obtain a good coincidence between the commanded and the real stack temperature. The electrochemical calibration parameters were left at the same values used for the fuel cell stack model (Table 4.3).

Despite the two models are completely different, the number and type of electrochemical parameters are the same, given the electrochemical nature of fuel cells and electrolysers. The Ohm_{coeff} coefficient, however, was lowered to $1x10^{-3}$, since the high value of 0.78 gave model divergence.

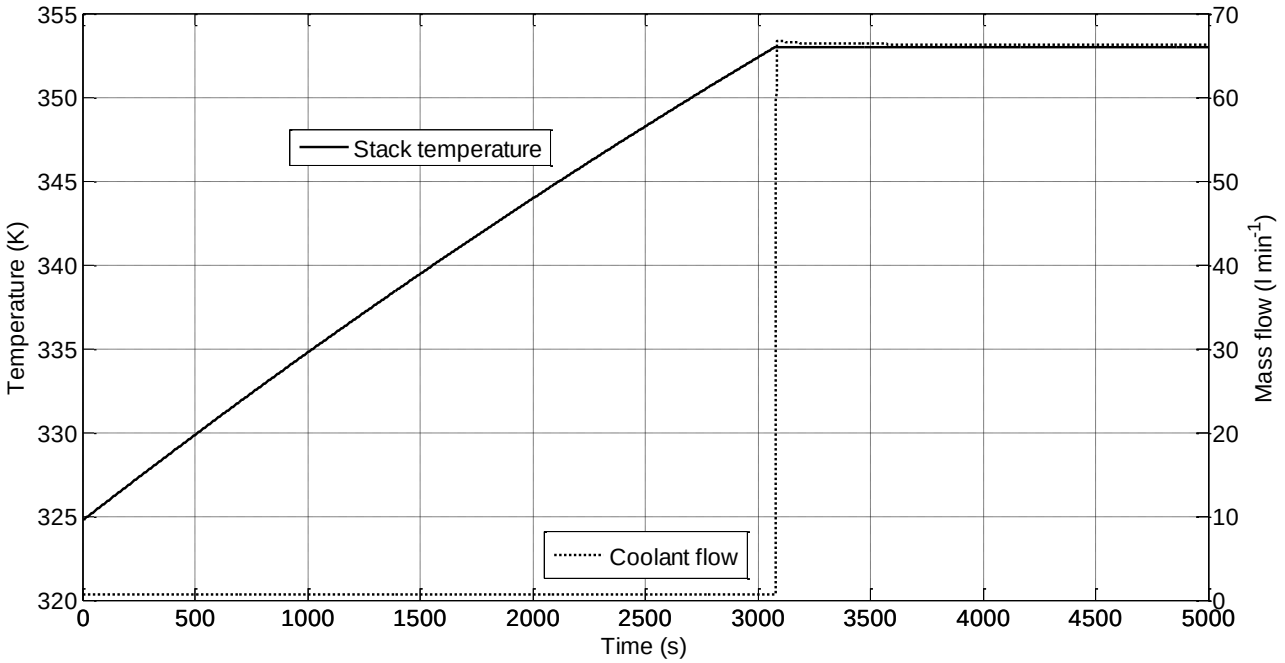

Figure 4.52 Electrolyser thermal control constants calibration. Current = 310 A. Desired temperature = 80°C (353 K)

The calibration of these constants is given in Figure 4.52. This plot shows the stack temperature, starting at 324.6 K (51.6°C) and reaching the value of 353 K (80°C) after 3100 seconds. During this interval, the temperature is left to increase linearly until the temperature reached the commanded value. At this point, the controller rose the coolant mass flow to maintain the temperature at the fixed level. The minimum value of the coolant flow, equal to 0.6 l min^{-1}, was given by Ulleberg (2003) and it is used to maintain a minimum mass flow to keep a small recirculation of the electrolyte to avoid accumulation of ions and impurities. The flow behavior showed a small overshoot when the controller commands its rising. This can be seen in Figure 4.53. The temperature reached by the stack practically coincides with the commanded temperature, indicating the goodness of the thermal model controller. The values used for the coolant flow control are equal to 200.0, 2.0 and 2.0 for the proportional, integrative and derivative portion, respectively.

The calibration of the other parameters was based on a single curve of the experimental data. In particular, the curve drawn at 60°C in Figure 4.50 was used. The calibration was done on the four electrochemical parameters already discussed before. A good correspondence between experimental data and model data can be seen in Figure 4.54. All of the curves are spatially well distributed. The main difference between experimental and model data can be seen in the right hand side portion of the plot, at higher current densities, in particular for the curve drawn at 50°C.

Since the experimental points were available only graphically, without their precise numerical values, the correspondence between the model and experimental data can be done only graphically. It was then not possible to obtain an average or maximum error. Nevertheless, the model can be considered validated in a sufficient manner.

The final electrochemical parameters used for the validation are given in Table 4.5. As can be seen, the ohmic coefficient tuning parameter is very low, indicating a very low influence of the electrolyte parameters model used.

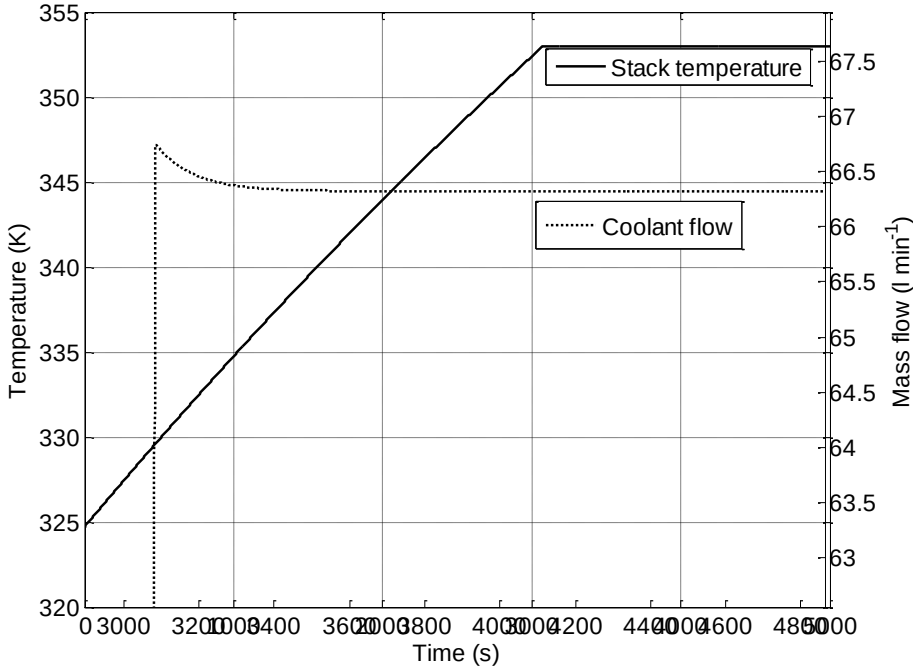

Figure 4.53 Electrolyser thermal control constants calibration. Current = 310 A. Desired temperature = 80°C (353 K). Zoomed view

4.4 Electrolyser system model simulation

In this chapter the system model simulation was performed. Several variables were varied and the results were analyzed.

The first simulation presented considered a fixed value of input current (375 A), and the cell voltage is monitored through time, with a desired stack temperature of 80°C (353 K). All of the variables used are the same given in Table 4.4 and Table 4.5. The transient stack voltage and efficiency are given in Figure 4.55. In this plot, two discontinuities can be easily seen. The first one located at about T = 2775 s, and a greater one at about T = 6000 s. These two discontinuities are given by the pressure inside the pressure vessels and the reaching of the desired stack temperature, enabling the injection of water flow inside the stack. The first discontinuity is given by the reaching of the desired total pressure inside the hydrogen and oxygen vessels of 7.0 bar. The volumes of the two vessels are chosen to reach the same pressure value contemporary on the hydrogen and oxygen sides. This meant the use of a hydrogen vessel volume twice the volume of the oxygen one. While the pressure of the two sides of the stack changes, the voltage and hence the efficiency, measured on a voltage basis rather than on a current basis, changes accordingly. When the system reaches the desired maximum pressure inside the tanks, the system maintains the pressure inside the vessels to a constant value. The second discontinuity is given by the reaching of the operating temperature. When this condition is met, temperature lo longer affects the system response. The stack efficiency, whose values are in line with expected values, has a behavior directly related to the voltage but opposed, since a lowering of the voltage, being the voltage an “input” to the system, means a higher efficiency.

Table 4.5 Electrolyser electrochemical parameters used for the validation of the model

Validation parameters	Value
Electrochemical parameters	
Reference anode exchange current density ($i_{0_{ref,a}}$)	9.0x10^9 A m^{-2}
Reference cathode exchange current density ($i_{0_{ref,c}}$)	9.0x10^9 A m^{-2}
Crossover current (I_n)	7.7 A m^{-2}
Ohmic coefficient tuning parameter (Ohm_{coeff})	0.0005 (-)

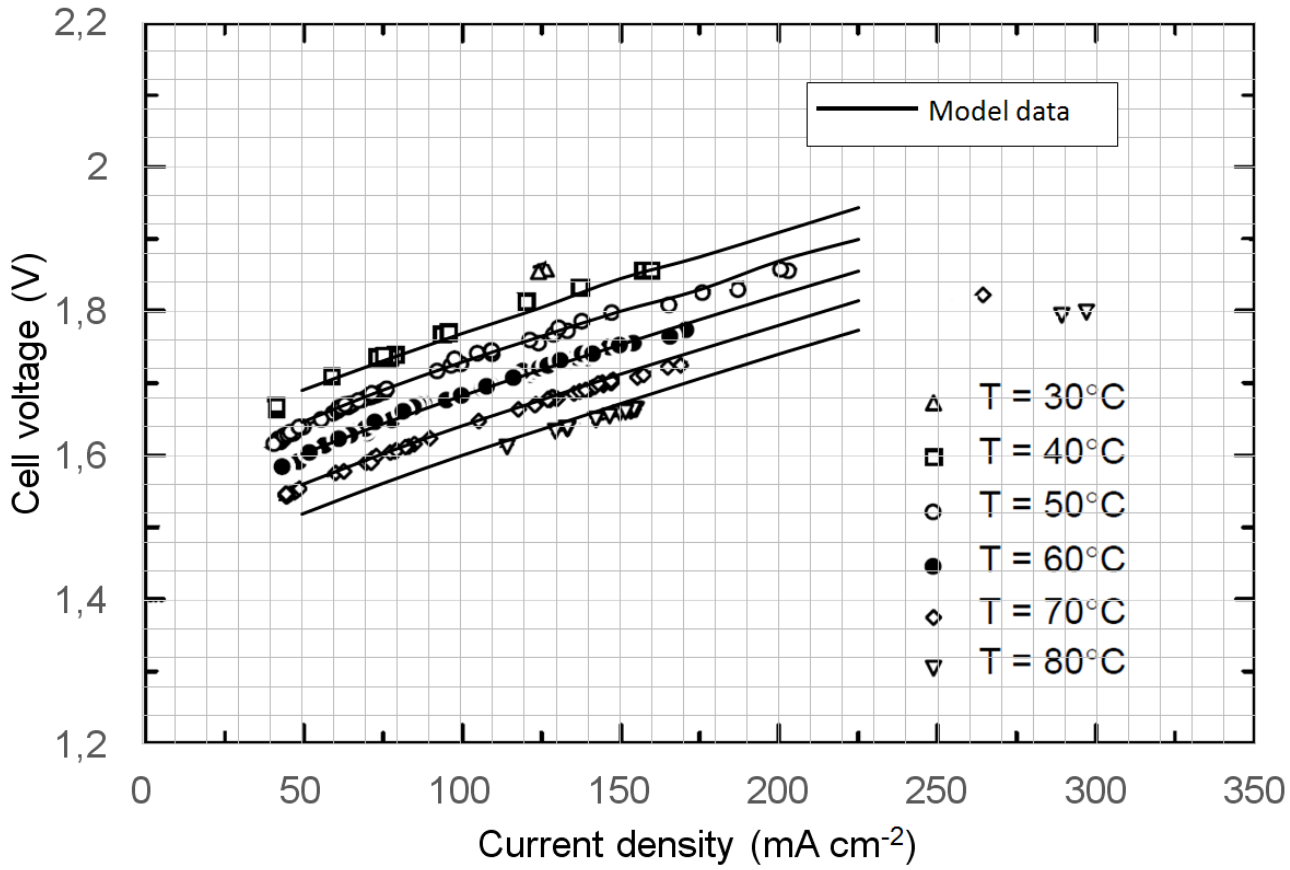

Figure 4.54 Electrolyser model calibration and validation results

In Figure 4.55 there are two main phenomena involved in the resulting curves, namely temperature and pressure, giving some contradictory results with the ones expected. An higher pressure should mean a higher difficulty of the system in providing pressurized gas, following the Nernst law (Eq.(1.20)). The voltage plot just mentioned instead shows a different behavior, with a decrease of voltage until the maximum pressure is reached (T = 2775 s). This can be easily explained considering the fact that the temperature has a beneficial effect on efficiency. Its benefit is higher than the slight voltage increase due to the increase in pressure. The result is a global reduction of voltage with increasing pressure, since the temperature is also increasing contemporarily. If the temperature variation is avoided, in fact, setting the initial stack temperature to the desired value of 80°C, the resulting plot is the one shown in Figure 4.56. In this second case, the voltage rises due to the increase of pressure until the max pressure is reached at T = 2320 s. The knee in this case is no longer caused by the temperature but by the pressure, despite the similarity of the two curves.

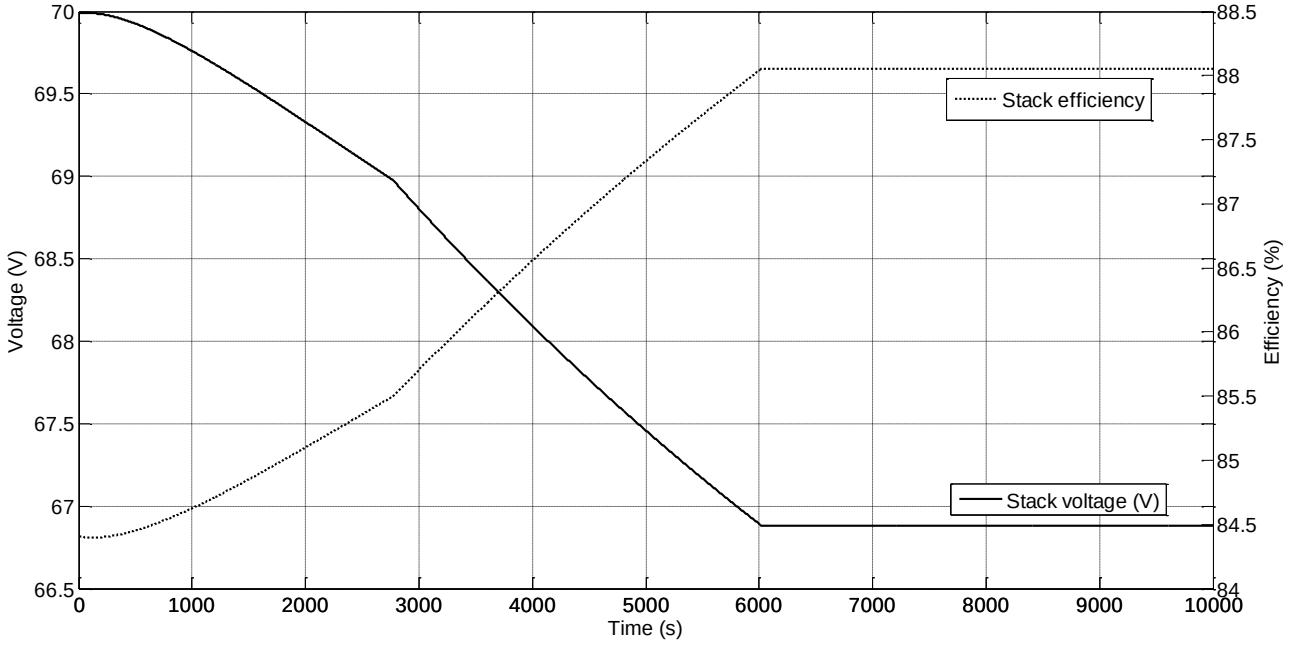

Figure 4.55 Stack voltage and efficiency. Current = 375 A. T = 80°C. P = 7 bar

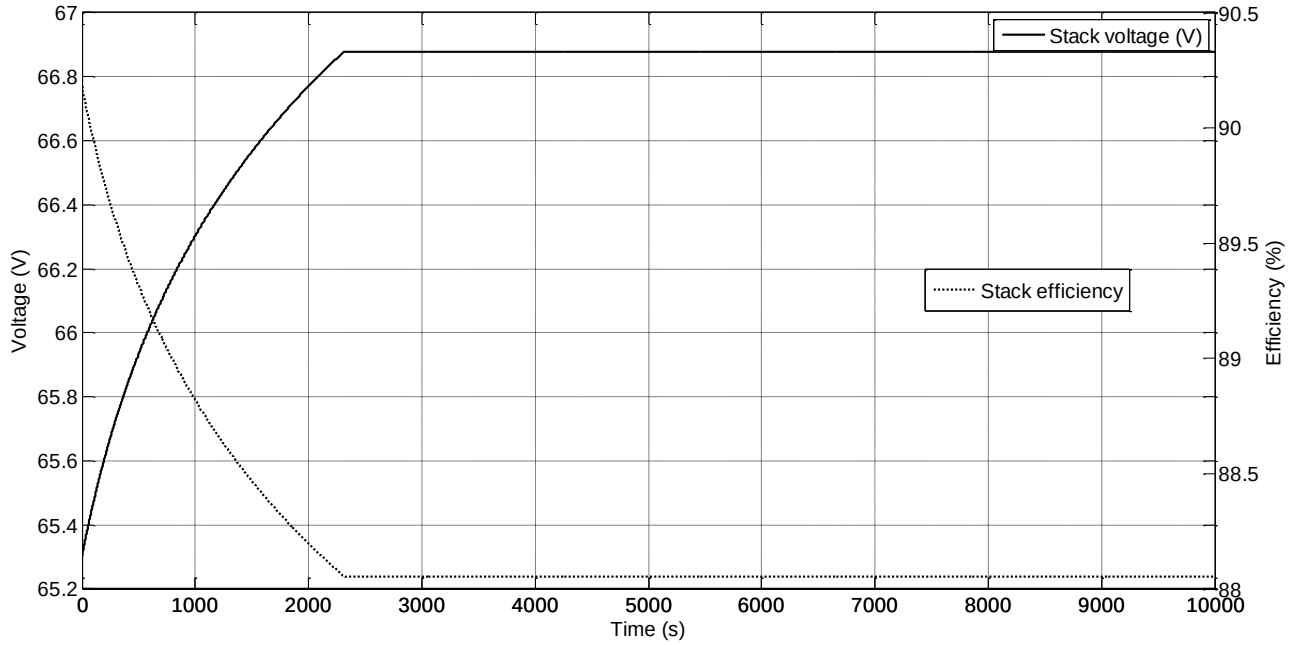

Figure 4.56 Stack voltage and efficiency. Current = 375 A. T = 80°C. P = 7 bar. Initial temperature set at 80°C

The overall increase in voltage is of about 40 mV per cell. The following plot shows the behavior of the voltage stack and efficiency when the other variable, the pressure, is kept fixed, while the temperature varies. Ambient pressure is considered. In this case, the increase in temperature reduces the voltage demand until the set temperature is reached.

In this case, the efficiency at 80°C is higher than the efficiency given in Figure 4.55, given the lower pressure of the stack.

The variation in efficiency given by the variation of the operating, commanded stack temperature is given in Figure 4.58. The maximum pressure was set at this point to 30 bar, a typical value for a

present technology electrolyser. The initial temperature of the stack was lowered to 40°C (313 K) and the temperature varied from 40 to 80°C.

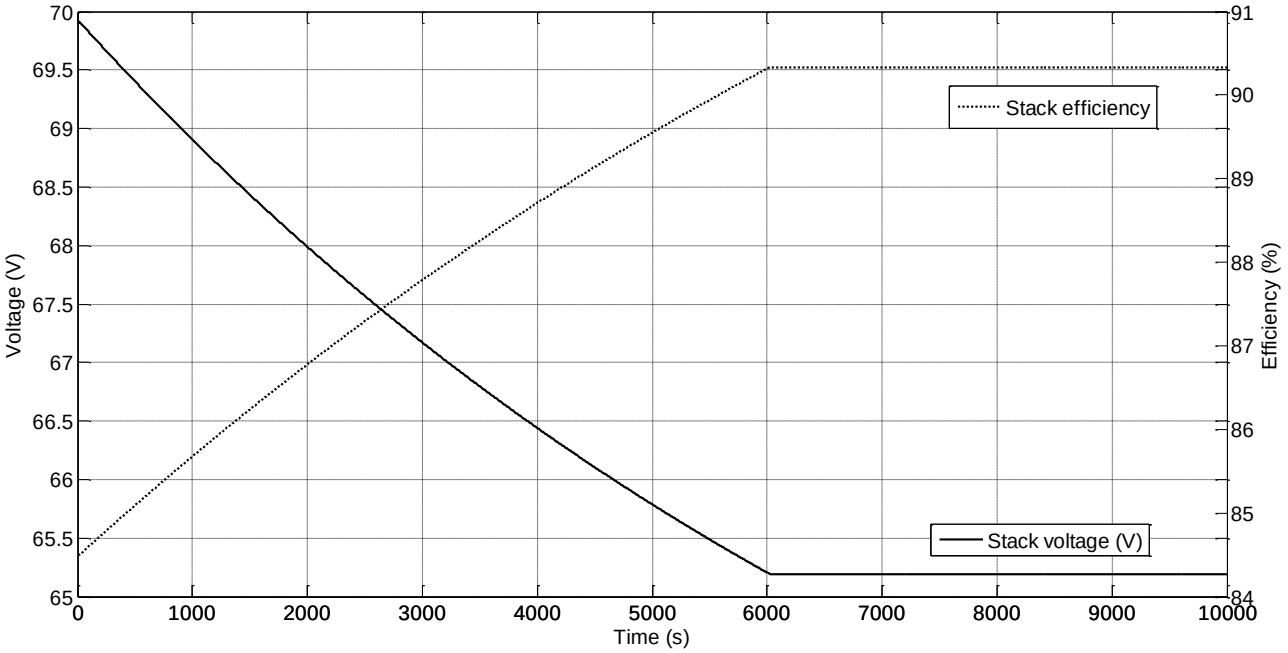

Figure 4.57 Stack voltage and efficiency. Current = 375 A. T = 80°C. P = 1.01325 bar. Initial temperature set at 51.6°C

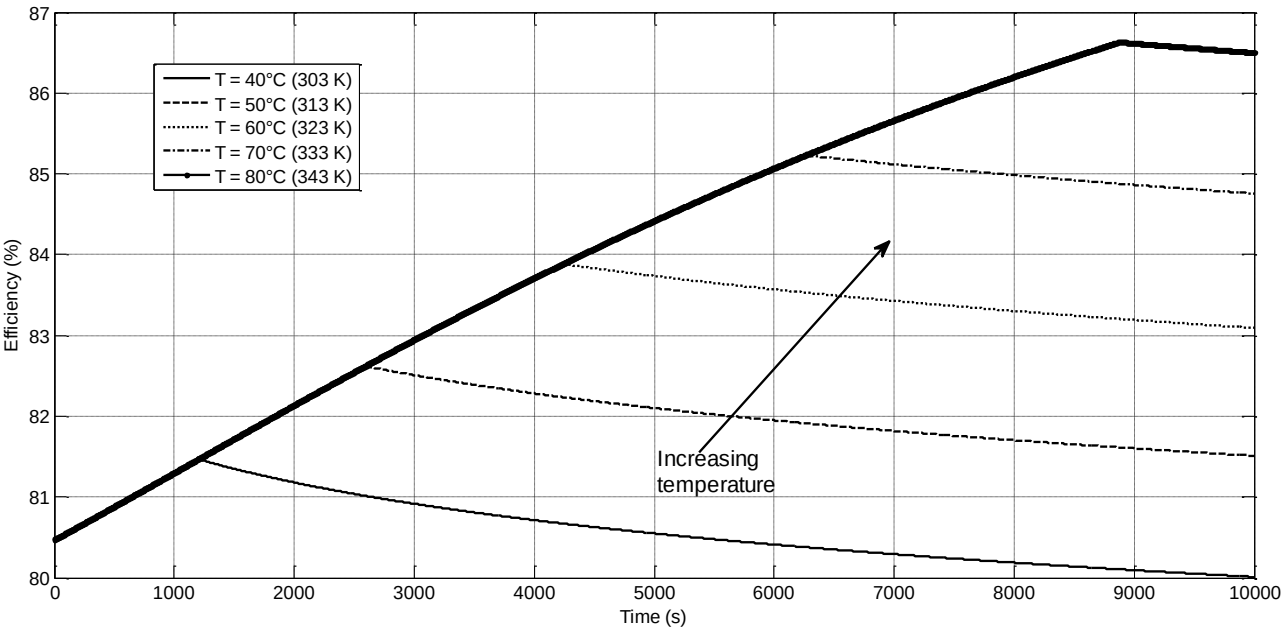

Figure 4.58 Efficiency. Current = 375 A. Increasing temperature. P = 30 bar. Initial temperature set at 35°C (308 K)

The efficiency variation can be clearly seen. The initial increasing line coincides for all of the curves. The difference is encountered when the desired operating temperature is reached. At this point, the efficiency lowers again, due to the increasing pressure. The maximum pressure in this

plot is never reached. When the temperature is increased from 40 to 80°C, the efficiency rises from about 80 to 86.5 percent, meaning a variation of about the 8.2% when the temperature in doubled (in Celsius degrees). A similar behavior can be seen in the relation between efficiency and pressure (Figure 4.59).

The effect of the concentration of KOH can be seen in the ohmic region of the polarization curve, since an increase in the presence of ions help in the current passage. A zoomed area of several polarization curves obtained fixing the temperature to 70°C are given in Figure 4.60. The KOH concentration is varied from 10 to 50 percent. As can be seen, the voltage required reduces the ohmic losses. The variation in voltage passing from 10 to 50 percent can be estimated in about the 1.3 percent.

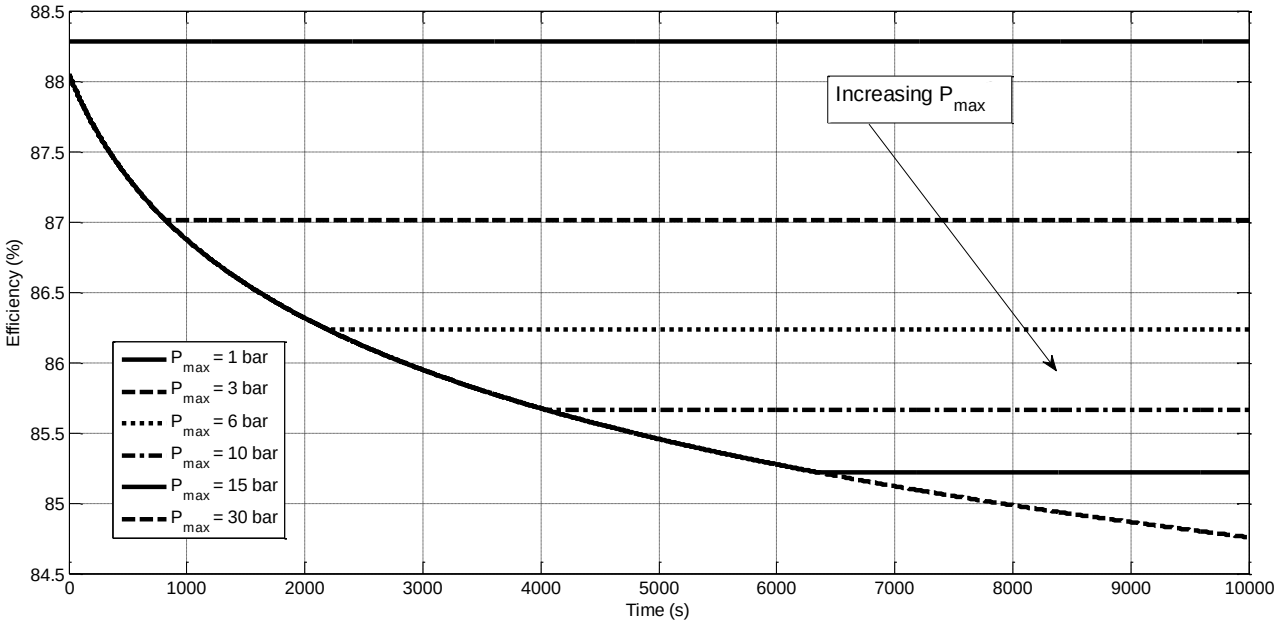

Figure 4.59 Efficiency. Current = 375 A. Increasing maximum pressure. T = 70°C (343 K). Initial pressure set at 1 bar

The next final plots regard the step ramp response and the step response of the system to a variation in current and temperature.

The ramp response of voltage and efficiency when passing from 3 to 600 A is given in Figure 4.61. The variation in current is given in 10000 s, corresponding to about 2.8 hours. The behavior of fuel cell stack and electrolysers to ramp inputs gave results usually similar to polarization curves, in the case of blended ramp slope values.

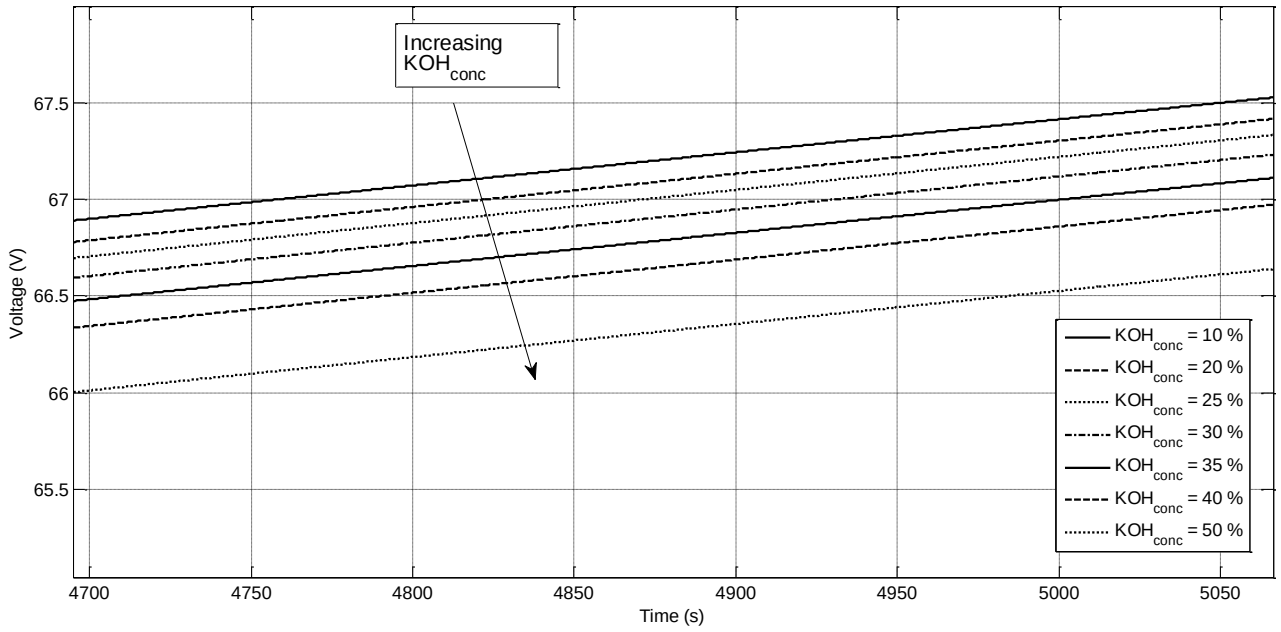

Figure 4.60 Voltage. Ramp response. Increasing KOH_{conc}. T = 70°C (343 K). P_{max} = 30 bar

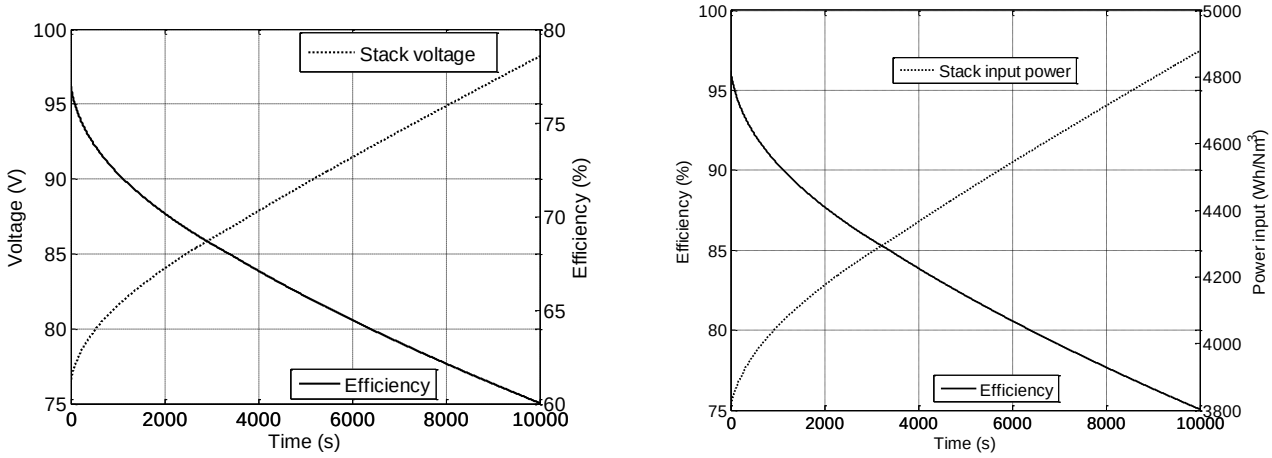

Figure 4.61 Voltage and efficiency (left). Power input and efficiency (right). Ramp response. Pressure fixed at 1 bar. T_{stack} = 70°C (353 K)

The response to a ramp in the desired temperature is not reported, since it does not gave significant results.

The step response of electrolysers is different from the one given by fuel cells. The high thermal resistance of the electrolysers (as can be seen from the long times in the x-axis of all of the previous figures) and their thermal inertia makes the electrolysers transient response very slow if compared to fuel cells. Overshoot and undershoots are practically absent in electrolysers, and the typical plots of variables in electrolysers are usually similar to a line or a first order curve.

The first step response is shown in Figure 4.62. The initial temperature was the same used for the validation (51.6°C) and the final value was set to 70°C. The maximum pressure was set constant to 1 bar, for simplicity. The step in the hydrogen production was increased from 125 to 250 A.

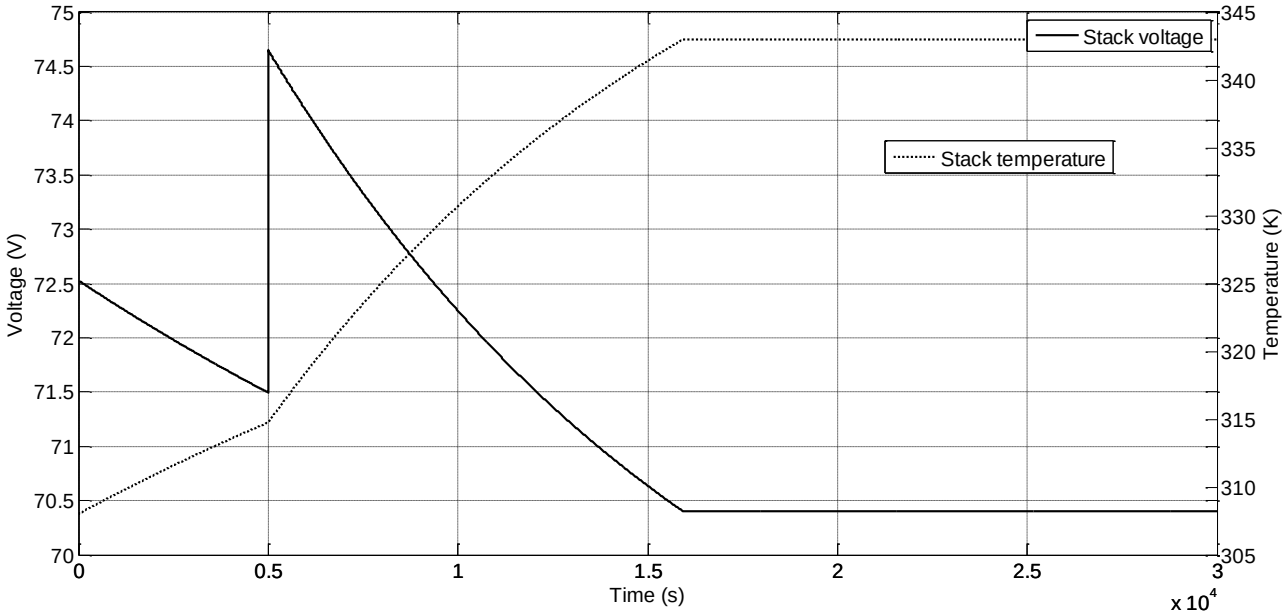

Figure 4.62 Voltage and temperature. Ramp response to current variation. Pressure fixed at 1 bar. T_{stack} = 70°C (353 K). Initial temperature = 51.7°C

The variation in current and voltage occurred at T = 5000 s. As can be seen, the voltage varied abruptly but without showing overshoots or undershoots. The behavior of the voltage variation is in line with the previous analyses, showing a progressive decrease in voltage required, given the increasing temperature increase. The change shown at about T = 16000 s is given by the reaching of the desired temperature.

All of the other variables behave similarly to the plots and variables just seen and are not reported for brevity.

5. FUEL CELL OPTIMIZATION STUDIES

5.1 Fuel cell CFD models and optimization studies

The use of numerical modelling allows a great flexibility in the design and analysis of fuel cells. The first numerical model was developed by Dutta, Shimpalee and Van Zee in 2001 (Dutta et al. 2001), using semi-empirical relations for the fuel cell membrane characterization taken by Springer et al. (1991). All of the other CFD models developed further improved the detail of the phenomenological aspects involved in a PEM fuel cell operation (Lum and McGuirk 2005; Sivertsen and Djilali 2005). The first improvements in the models were the adoption of a multi-phase flow instead of a simpler mono-phase flow – where both presence and effects of liquid water were not taken into account as presented in Siegel et al. (2003), non-isotherm equations and the simulation of a 3D domain (Maher et al. 2009; Falcão et al. 2011) instead of a simpler 2D domain. At present, the most detailed models implement 3D geometries of a complete fuel cell, with non-isotherm and multi-phase flows, capillary pressure, 3D electrochemical and membrane models, and a deeply detailed formulation of the porous media and catalyst layers behaviour. A CFD model of a PEM fuel cell is considered in this paper as a test bench. This model was developed to simulate a 3D complete fuel cell channel, and considering non-isotherm equations, steady-state conditions, compression effects and implementing a pseudo bi-phase flow instead of a fully two-phase flow solution (Dawes et al. 2009).

The design phase of a fuel cell system is extremely important and delicate, as all its features must be correctly identified to comply with the imposed requirements. Therefore, the definition of a suitable design strategy gets crucial. One of the main possible issues consists in adequately managing any design change that could become necessary in a less time consuming manner, while also pointing at setting up a robust and confident simulation framework. One of the most important points is to identify the parameters sensibly affecting the performance, excluding the less relevant ones, to reduce the number of variables to be considered during the successive analyses. Box and Draper (1969) suggested a method to gradually refine a response surface to better capture the real function by screening out unimportant variables. The essential of this method is to reduce the dimensionality of the design space by reducing the number of design variables. Another type of design space reduction tries to reduce the size of the design space, while assuming that the dimensionality cannot be further reduced. Since the combined range of each design variable dictates the size of the design space, the larger the range for each design variable, the larger the design space; the larger the design space, the more difficult and computationally costly the construction of accurate meta-models.

Engineers tend to give very conservative upper and lower bounds for design variables at the initial stage of a design optimization. This is often due to the lack of sufficient knowledge of functions

behaviour and interaction between objective and constraint functions in the early stages of the problem definition. This method is very effective and easy to implement only for some well-known problems (Hu et al. 2008; Chen at al. 2007). The goal of this work was to outline the best suitable approach to perform an MDO process of a PEM fuel cell, starting from its distributed parameters model and resulting in a surrogate model, predicting the cell behavior, as explained in the following paragraphs. Considering the available literature, only few works, dealing mainly with sensitivity analyses, as in Min et al. (2006), can be found. In Guvelioglu and Stenger (2005) it is reported the influence of some cell operating parameters on the current density. Secanell et al. (2010) set up an optimization tool for the Membrane Electrode Assembly (MEA) of a PEM fuel cell together with a sensitivity analysis. The variation of the cell output given by the gas diffusion layer parameters are investigated also in Pourmahmoud et al. (2011) and in Ahmadi et al. (2012). Kim and Sun (2012) dealt with the optimization of the flow channels topology. Anyway, very few works are dedicated to numerical optimization processes, as in Mukhtar et al. (2010). The present work, in addition to performing a sensitivity analysis, combines a CFD model, a Design of Experiment (DoE), surrogate models and optimization algorithms in an automated way with the aim of obtaining a complete optimization loop for PEM fuel cells.

5.2 Optimization methodology

The main structure of the presented work can be summarized below:

- Setup of the PEM fuel cell CFD model.
- Design space evaluation, performed to assess the impact of input values on output parameters, verify the design variables orthogonality and create a data set that can be used to generate approximation models for the design space (surrogate model).
- Surrogate model creation
- Surrogate model-based optimization
- Validation.

Statistics is extensively used at the beginning of this methodology, varying the problem inputs to correctly estimate the system output changes through a sensitivity analysis. Furthermore, a DoE approach is used to create a design matrix required to provide the anchor points of the approximation model, correlating design inputs and objective functions. This approach, better known as Response Surface Methodology (RSM) is extensively adopted to speed up the following MDO processes. An MCS is chosen to evaluate how key parameters affect the final results (Rubinstein and Kroese 2007). The selected variables are sampled through a certain distribution (described later) and a sensitivity analysis is performed. Graphical methods can be adopted to better understand the results (Deb 2001). After evaluating the computational time of a single run of the multidisciplinary PEM fuel cell model, the authors decided to build up a surrogate model, according to literature (Deb 2001; Koehler and Owen 1996). In this paper, some available approximation algorithms are investigated and compared with the aim of selecting the most suitable one, on the basis of the minimum error percentage (Koehler and Owen 1996). As a final point, two unconstrained deterministic single-objective MDO processes are performed to identify the best set of parameters to produce the maximum current density, i.e. the maximum output power. These analyses are obtained recurring to an evolutionary technique, more suitable to find the global optimum than a gradient-based algorithm (Deb 2001).

A commercial tool (*iSight*) is chosen to set up the whole process, embedding both the multidisciplinary fuel cell model (involving CFD and electrochemical codes), the DoE, the surrogate model and the single-objective optimization. The complete process performed in this work is shown briefly in Figure 5.1.

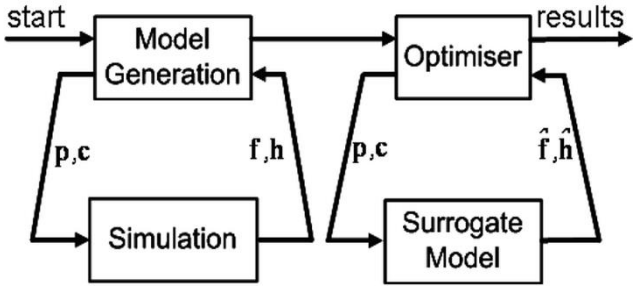

Figure 5.1 Logical scheme of the sequential approach used in this study

5.2.1 PEM fuel cell model used

The fuel cell model used here is based on a work given by Vigna Suria et al. (2011) and validated with empirical values given in literature. The model here used considers all the most important physical aspects involved, and it is based on previous CFD PEM fuel cell models available in literature. The model is implemented in *CD-adapco Star-CCM+* software environment, with an extensive use of user-defined functions. The main characteristics of this model are a 3D simulation domain comprising both fluid and solid regions, a steady-state solution, the adoption of a multi-component gas and non-isotherm conditions. The flow considered is single-phase. The basic equations for the computation of the fluid flow, the diffusivity of the reactants and the ionic conductivity of the membrane are the same that can be found in Pourmahmoud et al. (2011). The electrochemical model uses the standard electrochemical laws implemented in Dawes et al. (2009). The main difference consists in using an arcsine function instead of a logarithmic one for the electrochemical activation losses. The presence of liquid water and its effects on the cell performance (occlusion of catalyst reaction sites and flooding phenomena) are considered despite the single-phase presence. This approach was based on Dawes et al. (2009). The liquid water presence and quantity is calculated from the value of relative and absolute humidity, and the electrochemical and fluid-dynamics performances are scaled (degraded) based on liquid water calculated in each cell of the computational domain. The level of liquid water presence is quantified with the saturation (*s*, dimensionless) value, as in Dawes et al. (2009). The phase-change of vapour into liquid water is considered (imposing gas sinks) and modelled as in ANSYS (2011). The geometrical domain simulated comprised only a single channel of the cell to limit the computational cost. Its geometrical layout is given in Figure 5.2.

The presence of the other fuel cell channels can be also “simulated” varying the starting value of the saturation variable. In this model, the simulation comprises not only the membrane electrode assembly (membrane, catalyst layers and gas diffusion layers), but also the fluid channels, the solid bipolar plates (affecting the heat transfer) and the cooling water flowing on the opposite side of the plates. Together with the indirect liquid water presence simulation, the other main aspect differentiating this model from others is the reduction in the porosity of the gas diffusion layers given by the clamping pressure of the stack, as discussed in Maher et al. (2009).

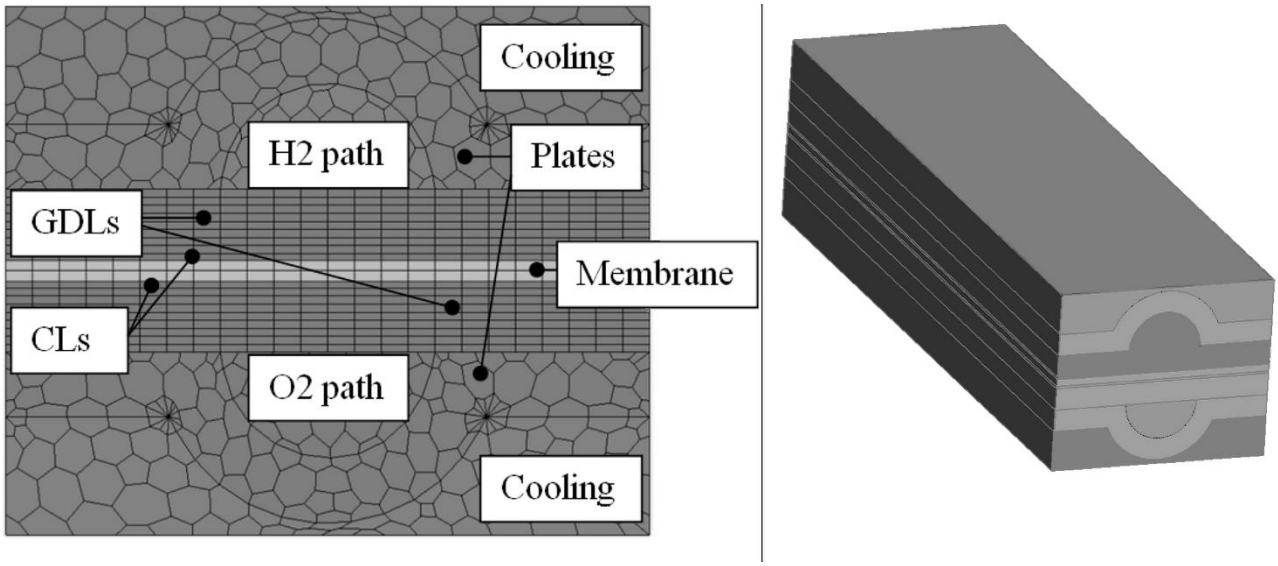

Figure 5.2 Geometrical layout of the fuel cell portion simulated

5.2.2 Design space evaluation

A design space evaluation was performed considering the performance of the fuel cell from a fluid dynamics and electrochemical point of view. A set of parameters was selected, then split into two main sets.

The boundary conditions values (first set of design variables), also defined "uncontrollable input noises" or "noise factors" (D3.4.3 2009; Taguchi 1987), are summarized below:

- Cathode exchange current density, i_{0c}: the exchange current density is an important electrochemical parameter related to the kinetics of the chemical reactions. In the model, it is defined for both the cathode and the anode sides. This variable is usually measured in A/cm^2. The higher its value, the faster the chemical reactions. A quicker chemical reaction has the direct effect of lowering the detrimental voltage losses, since it implies a lower amount of energy absorbed by the reaction itself (in the form of a voltage loss), improving the power output. The cathode exchange current density for a PEM fuel cell is usually in the range of 0.01 – 5 A/cm^2, while the anodic reaction exhibits usually an exchange current density of about 1000 – 3000 A/cm^2 (Dutta et al. 2001). From an electrochemical point of view, the cathode exchange current density produces the well-identifiable initial voltage drop at very low current densities. Therefore, this control factor is expected to have a strong influence on the cell performance.
- Anode exchange current density, i_{0a}.
- Condensation rate, c_r. The condensation rate is a gain factor (measured in 1/s) directly related to the kinetics of water vapor condensation into liquid form. This value is usually defined in the range of 100 – 200 1/s by commercial software, e.g ANSYS Fluent (2011) for the simulation of generic multiphase flows contemplating a transition from vapor to liquid form. In the Fluent PEM fuel cell model this value is set to 100/s.
- Saturation coefficient, sat_{rate}: this parameter is another gain factor used in the definition of the saturation variable (s), implemented for simulating major or minor quantities of liquid water presence inside the porous media. When simulating a portion of fuel cell, it allows the user to take into account the presence of the whole cell, i.e. the liquid water produced by the

part of the cell that is not really considered in the simulation can be modelled by assuming a suitable value of the sat_{rate}. The effects of the presence of liquid water are here considered.

On the other hand, the tuning parameters, also defined "control factors", are summarized below:

- Anode inlet gas temperature, T_a: the temperature of the gas mixture entering the cell at the hydrogen side.
- Anode inlet relative humidity, Rh_a: the relative humidity of the gas mixture entering the cell at the hydrogen side.
- Cathode inlet gas temperature, T_c.
- Cathode inlet relative humidity, Rh_c.
- Compression (of the GDL), *compr*: the effects of the torque applied to clamp the stack. The clamping force, required to prevent reactants leakage and a good contact between the electric conductive parts, has the counteracting effect of reducing the porosity of the gas diffusion layers, directly reducing the void volume available to the reactants. In the model, the gas permeability and diffusivity are reduced as function of the dry porosity of the GDL influenced by the stack clamping pressure.

Geometrical parameters (gas channel width, gas channel length, etc.) are defined as “controllable inputs" since their uncertainty level can be controlled during the manufacturing process (Lum and McGuirk 2005; D3.4.3 2009). They are not involved in the presented sensitivity analysis, since this study is done for a fixed fuel cell geometry.

The design space evaluation is often performed through the use of a DoE technique. The advantage of using a DoE consists in a maximum amount of knowledge gained with a minimum expense of numerical trials. Due to the fact that analysis processes are often time consuming, an efficient exploration of the entire design space requires a systematic samples distribution. The objective is to get many representative details of the correlation between system response and design parameters, while at the same time minimizing the number of design evaluations (Rubinstein and Kroese 2007; D3.4.3 2009; Bernstein and Kuleshov 2009; Barthelemy and Haftka 1993; Cressie 1993; Papadrakakis and Papadapoulos 1996). Several strategies can be used to generate appropriate samples (Siegel et al. 2003; Bernstein and Kuleshov 2009). According to literature references (Papadrakakis and Papadapoulos 1996) and thanks to the low complexity of this model, the MCS approach is used here. For the purposes of this work, a Sample Random Sampling (SRS) technique is used (Rubinstein and Kroese 2007; Koehler and Owen 1996; Papadrakakis and Papadapoulos 1996). A uniform Probability Density Function (PDF) is adopted to model the random behaviour, obtaining in this way a matrix containing the generated values of input parameters. The choice of a uniform PDF is motivated by the fact that a sensitivity analysis is performed evaluating all the values the parameters could assume, without having values with different likelihood, in a range included between upper and lower bounds. The PDF is also allowed thanks to the absence of geometrical parameters considered. Moreover, selected DoE techniques have to ensure the orthogonality of the generated matrix of design variables to ensure a good fit of meta-models (Peraudo et al.2012). An advantage of using orthogonal design variables as a basis for fitting data, is that the inputs can be decoupled in the analysis of variance (Barthelemy and Haftka 1993). Orthogonality implies the estimates of the effects are uncorrelated, where any pair of independent variables is linearly independent. The most familiar measure of dependence between two quantities is the Pearson product-moment correlation coefficient ($\rho_{X,Y}$) also called Pearson's correlation (Tabachnick et al. 2007; Stigler 1989). It is obtained by dividing the covariance of the two variables by the product of their standard deviations:

$$\rho_{X,Y} = \frac{cov(x,y)}{\sigma_X \sigma_Y} = \frac{E[(X-\mu_X)(Y-\mu_X)]}{\sigma_X \sigma_Y} \tag{5.1}$$

The larger the correlation, the less independent the parameters and the less orthogonal the design matrix is. If the design matrix is not orthogonal, a coupling exists in the matrix, so that the interaction effects of independent variables are not distinguishable.

As a second step, a sensitivity analysis was done to evaluate which parameters have the major weight on the system response. This was done thanks to the *iSight* software, providing some useful visual tools. After performing the DoE, a 2nd order polynomial was chosen as approximated function. The function fits the responses on a discrete set of samples after calculating the function coefficients thanks to the least square method. The unknown model function can be approximated by a 2nd order Taylor series.

Moreover, it is possible to use one-dimensional cuts through the response surface to quantify the influence of the parameters separately. The influence of the design parameters is displayed in a classic Pareto plot, where positive effects on the responses are marked in blue, whereas negative effects are colored in red. The last presented representation is more direct than other graphic results, giving the designer a useful tool to better understand which design parameters could be neglected because of their poor effect on global performances (Min et al. 2006). According to common techniques of robust design (D3.4.3 2009), the two sets of parameters are kept separated and two different sensitivity analyses are done to evaluate the influence of each set on the outputs separately. Furthermore, an overall analysis considering all of the parameters at the same time would require a definitely higher number of trials, determining an unacceptable amount of time spent in simulating, as the noise and control factors could sensibly influence each other. Therefore, for the purposes of the present work, two different analyses gave a satisfactory result at a feasible computational cost. The reference output monitored is the current density: at a fixed user defined operating voltage, the higher its value, the higher the power output available from the fuel cell.

Considering the number of trials to be simulated, a good amount should be around 1000. However, splitting the sensitivity analysis into two different ones, 100 simulations can be considered a good compromise between computational cost and sufficiently reliable preliminary results, as already mentioned before. The sensitivity analysis tool provides different graphs and post-processing features. During a preliminary analysis, the most meaningful charts are the scatter plots and the Pareto plots, presented later in the text. Considering the operating conditions at which the cell is investigated, the authors decided to start with the analysis of possible flooding (at low voltage and high current density), opting for 0.2 V. Only a single point of the polarization curve is analyzed, being anyway one of the most representative ones, where the cell is particularly sensible to change in performances. Also a validation of the approach based on the simulation of a single point could better test the goodness of the methodology.

5.2.3 Surrogate modelling

Many engineering analyses consist in running complex computer codes, requiring a vector of design variables *x* (inputs) and computing a vector of responses *y* (outputs). Despite the significant technology advances in the information technology field, the expense of running finite elements analyses is still sensible, as they can take minutes to hours, or even longer, to be completed.

Moreover, this query-and-response technique often leads to a trial and error approach, where the designer will almost never find out the functional relationship between *x* and *y*. This means the best

settings for the input values will be very difficult to be identified (Min et al. 2006; Lindman 1974). Statistics-based techniques are widely used in engineering design to address these concerns. The basic approach is to build approximated models of the analysis codes, able to get the results in a shorter time. If the true behaviour of a computer analysis code is shown as $y = f(x)$, then its meta-model can be represented as $\hat{y} = g(x)$, with $y = \hat{y} + \varepsilon$, where ε stands for the approximation errors and $\hat{y}$ is the meta-model.

These methods are extremely useful to reduce the computational time. However, it is fundamental to guarantee the goodness of the solution. Modern optimization methods and especially global optimization approaches could lead to macroscopic mistakes if not adequately managed. For this reason, a significant number of design evaluations are required to build meta-models able to simulate the real nature of approximated codes.

Surrogate models are simplified, analytical approximations, based on few supporting points obtained from the simulations of the original evaluation model. Due to their simplicity they allow a low cost prediction of the system behaviour with an arbitrary elevated number of design evaluations during the optimization loop (Barthelemy and Haftka 1993). At the same time, their simplicity could lead to numerical or actual errors, due to the fact that approximated functions could miss the real shape of the domain.

Validation and refinements of approximated models are then necessary before continuing with next optimization steps (Peraudo et al. 2012). In this work, four main techniques are evaluated to find the most suitable one. The list of the algorithms taken into account in this work are the RSM, the Radial Basis Function (RBF), the Kriging and the Chebyshev/Orthogonal Polynomial. An advantage of using orthogonal functions as a basis for fitting is that the inputs can be decoupled in the analysis of variance (Lindman 1974). Chebyshev orthogonal polynomials are a common type of orthogonal polynomials that are particularly useful for equally spaced sample points. They are used when the sampling strategy is an orthogonal array. The *iSight* software used for this analysis implements Taguchi's method (Taguchi 1987) for fitting Chebyshev polynomials from an orthogonal array.

A minimum number of samples have to be produced to obtain a surrogate model. According to Figure 5.1, the analytical model has to be run with the aim of generating the needed points. According to Taguchi's theory, the model generation was obtained thanks to two sensitivity analyses of both noise factors and control factors (Lum and McGuirk 2005; Journel and Huijbregts 1978). The collected data were used to build up the approximated models.

5.2.4 Optimization process

An exploratory technique was used to better investigate the design space. An optimization process is very sensible to the chosen optimization strategy. A gradient-based algorithm usually provides a local optimum, without evaluating any other feasible optima if the design space is not linearly defined. The choice of an evolutionary technique (e.g. a genetic algorithm) is motivated by the desire to investigate the whole design space, with the scope of finding the global optimum (Goldberg 1989; Fonseca and Fleming 1993; Deb 2001), avoiding to get stuck in local solutions.

Several genetic algorithms are available in literature. In this paper the Multi-Island Genetic Algorithm (MIGA) was used. This technique can be implemented even if the optimization problem is not a multi-objective one. Each design point is perceived as an individual with a certain value of fitness, based on the value of the objective function and constraint penalty. An individual with a better value of the objective function and low penalty has a higher fitness value. The main feature of MIGA, distinguishing it from traditional genetic algorithms, is that each population of individuals is

divided into several sub-populations called "islands". All of the traditional genetic operations are performed separately on each sub-population. Some individuals are then selected from each island and migrated to different islands periodically. This operation is called "migration". Two parameters control the migration process: migration interval, which is the number of generations between each migration and migration rate, which is the percentage of individuals migrating from each island at the time of migration (Mukhtar et al. 2010; Fonseca and Fleming 1993).

The deterministic single-objective optimization consisted in maximizing the current density at a given voltage, without imposing any constraint. The optimization performed was a deterministic one, according to the previous generated data. The approximated model was built to speed up the optimization process. The results were carried out at a voltage of 0.2 V, since this area of the polarization curve is characterized by possible flooding phenomena and by a sharp decrease in the generated power, hence making the model more sensible to changes. Therefore, it can be assumed that the validation of the surrogate model in such a condition extends the applicability of the same approach at any other voltage within the cell operating range.

5.3 Results and discussions

5.3.1 Design space evaluation

The design space evaluation was carried on by running 100 simulations and performing a set of successive analyses. After the run completion, the first step of the design space evaluation consisted in determining the level of orthogonality of the input variables.

Two different correlation matrices are presented for both noise and control factors (Table 5.1 and Table 5.2, respectively), obtained for the present case study.

Table 5.1 Noise factors correlation matrix, showing the mutual influence of each variable on the others. 1 indicates a perfect match; 0 indicates a complete non-correlation

	i_{0a}	i_{0c}	c_r	sat_{rate}
i_{0a}	1	-0.127	-0.114	0.0725
i_{0c}	-0.127	1	0.124	-0.029
c_r	-0.114	0.124	1	-0.066
sat_{rate}	0.0725	-0.029	-0.066	1

Table 5.2 Control factors correlation matrix, showing the mutual influence of each variable on the others. 1 indicates a perfect match; 0 indicates a complete non-correlation

	T_a	Rh_a	T_c	Rh_c	*Compr*
T_a	1	-0.082	0.238	0.102	0.0064
Rh_a	-0.082	1	0.026	-0.091	-0.062
T_c	0.238	0.026	1	0.12	0.11
Rh_c	0.102	-0.091	0.12	1	0.0352
Compr	0.0064	-0.062	0.11	0.0352	1

As can be seen, both noise and control factors present a very low correlation. These results are important because, as stated before, this is a useful preliminary step to get a good fitting response of the meta-model, avoiding to get confounding behaviors. If the correlation factor is not close to a zero value, there is some level of confounding of the independent variables and this would affect the ability to estimate the source of variability in the system response and the associated model coefficients (Francis et al. 1999). The ability of the surrogate model to approximate the reality in a

better way is given by the lack of void spaces in the design space. If void spaces are present, the surrogate model would consider regions not covered by data, making the model error excessive.

The second step consisted in the plotting of the scatter plots and the Pareto plot.

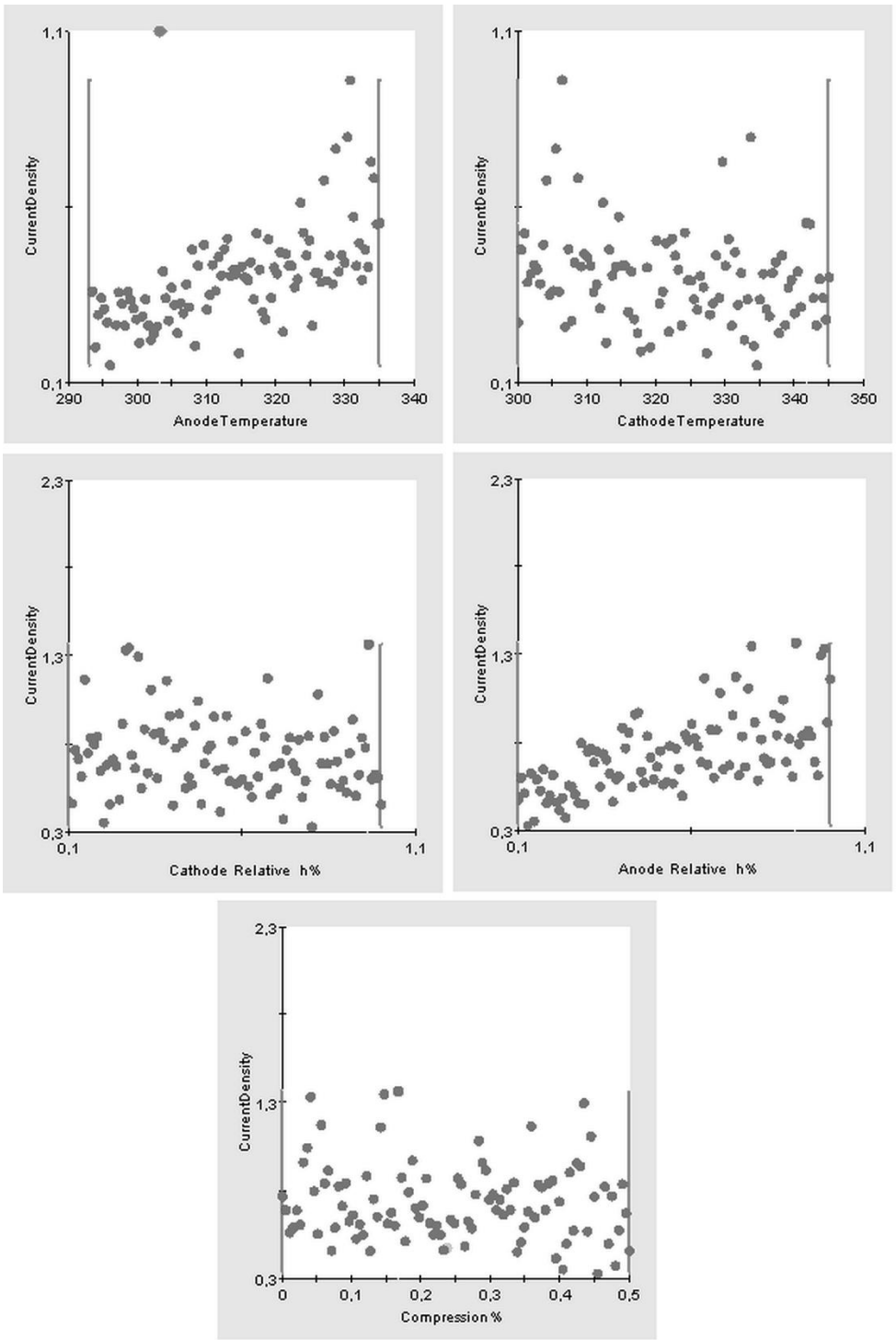

Figure 5.3 Scatter plots obtained fort the sensitivity analysis of the control factors

Figure 5.3 reports the scatter plots of the control factors, indicating the correlation between the current density and all of the control factors separately. The x-axis indicates the variation range

considered for the specific variable. Each point of the scatter plot represents one of the 100 performed simulation. The scatter plots usually define the existing relationship between the performance in a qualitative way (i.e. the current density, and each design variable: the more the simulation points are packed together, the more the variable influences the current density). Furthermore, a global trend could be identified out of these plots, giving information about the dependency of the output on the input shown.

In particular, the most relevant plot is the current density vs. anode relative humidity one, where a direct proportionality between the two variables can be clearly identified. It is important to notice the dispersion of the points while moving towards a higher anode relative humidity, in an anode relative humidity range of 0.8 to 1.0, significantly higher than in other areas of the chart. This could be caused by a low number of simulations done, determining a lower number of data in this region. The result is the lost of the linear trend that characterizes the plot. Regarding the cathode relative humidity, the trend seems to be quite the opposite, but not presenting well-defined boundaries, as it is for the anode one, instead.

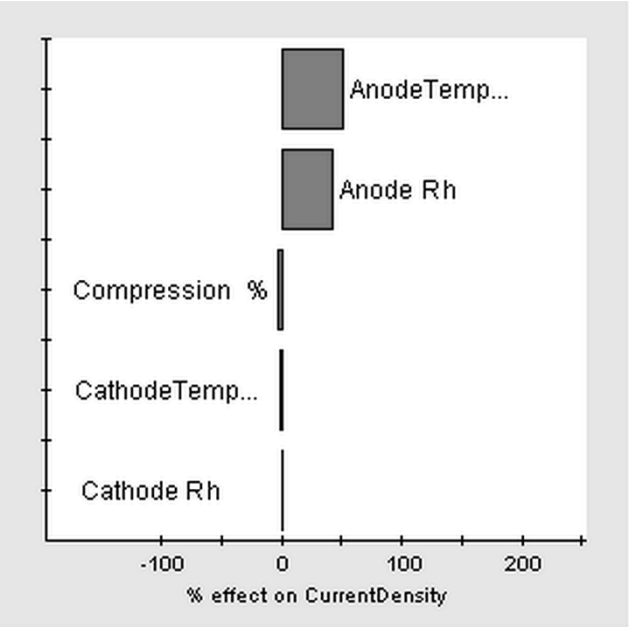

Figure 5.4 Pareto plot of the control factors

The Pareto plot in Figure 5.4 clearly shows the relative weight of each of the selected control factors on the objective variable. This type of chart is extremely important since it gives the user useful information to select the most important variables to be included in future optimization analyses and discard the less relevant ones – i.e. reducing the design space complexity. This approach is recommended whenever the number of variables that influence the system is too high. The anode temperature and the anode relative humidity can be identified as the two main parameters affecting the current density. As already mentioned before, the blue bars indicate a positive increment of the current density when the input grows, whereas red bars represent a reduction of the output when the input increases, in accordance with the trend represented by the previously described scatter plots.

The same procedure is adopted for the noise factors. Figure 5.5 reports their scatter plots, indicating the correlation between the current density and the noise variables. The most representative of the scatter plots presented in Figure 5.5 is the cathode exchange current one, showing a parabolic trend

relating the increment of the variable to the growth of the current density. In particular, the low spread of the points identify a significant dependency of current on the cathode exchange current density, especially in case of values of exchange current density falling within the range from 0 to 2; on the other hand, as it gets closer to 5, the relationship becomes weaker. The other plots do not provide any particular trend.

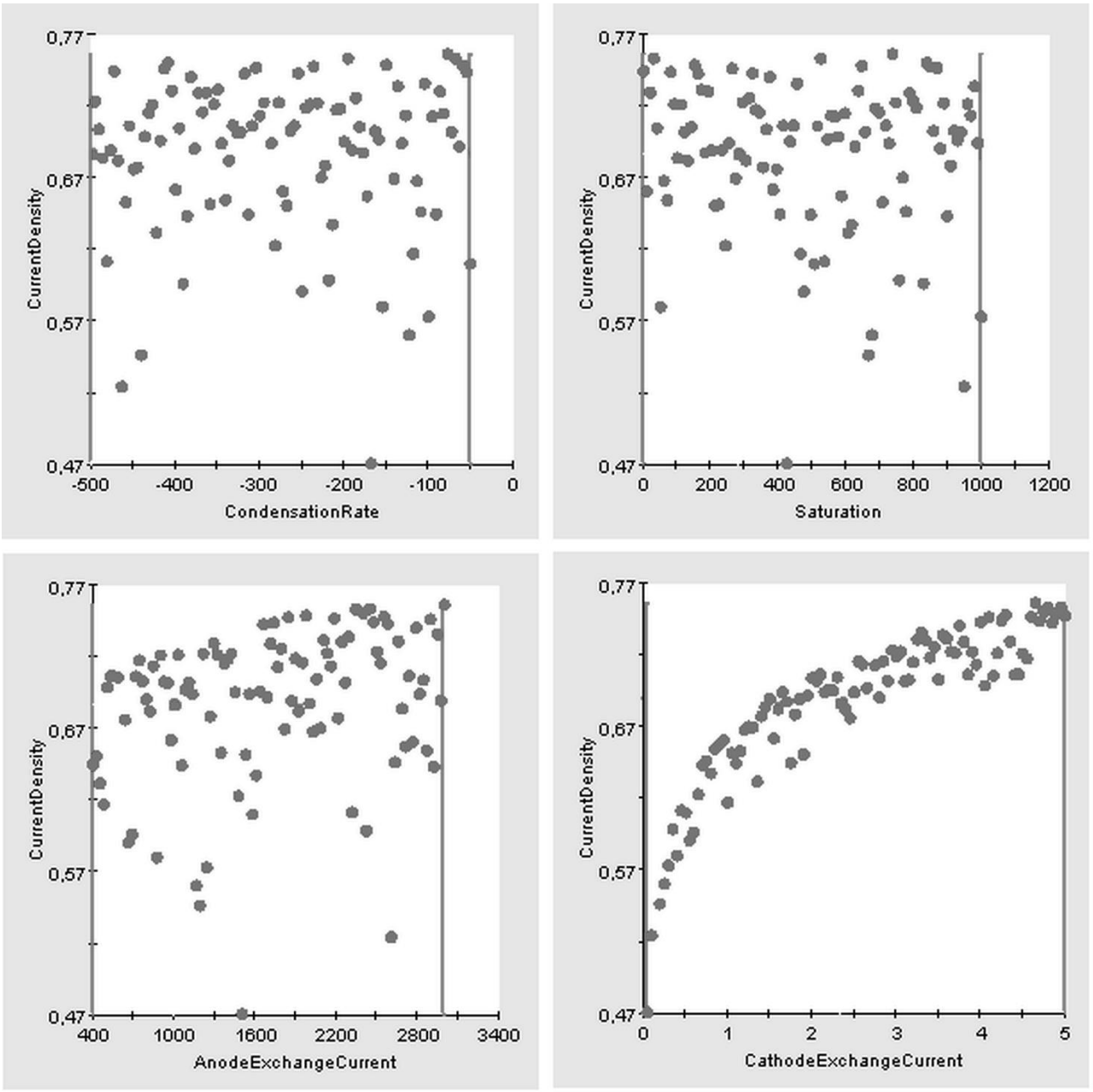

Figure 5.5 Scatter plots obtained fort the sensitivity analysis of the noise factors

As a conclusion, Figure 5.6 shows the Pareto plot of the noise factors, and it is quite clear that the most leading parameter is the cathode exchange current density. Moreover, the anode exchange current has more effects than condensation and saturation, and it cannot be neglected.

As a matter of fact, at the cathode side, the membrane is continuously humidified thanks to the water produced by the electrochemical reaction. On the other hand, the anode usually experiences

difficulty in keeping the right membrane humidification, since the presence of liquid water is strictly connected to its transport through the membrane itself and the hydrogen inlet humidification. Despite the membrane is thin, a good amount of membrane humidity must be guaranteed at its two sides, being humidification at only one side not enough. Therefore, the strong importance of humidity at the anode becomes clear. Being the membrane humidification directly proportional to the electric conductivity of the membrane, a higher value of humidification means a higher electric current. This is the reason why it is extremely important to monitor and correctly set the right value of anodic temperature and humidity.

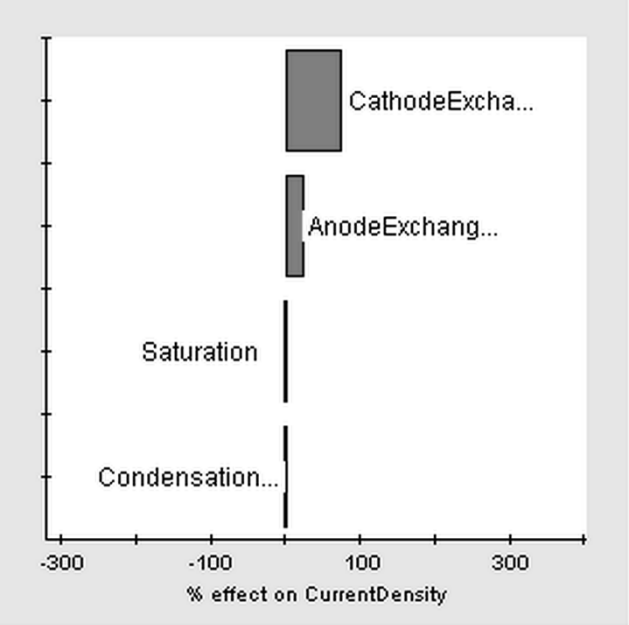

Figure 5.6 Pareto plot of the noise factors

The reason for the importance of the anode temperature could be justified considering the operating point here simulated, equal to 0.2 V in output. At this low voltage value, the current production is high, meaning a high liquid water production at the cathode side. The back-diffusion of water through the membrane, given by the gradient of concentration at the two sides, is enhanced and can counterbalance the electro-osmotic drag. A lower relative humidity at the anode (i.e. a high inlet temperature) helps in removing the excess water, which could imply water flooding. This behavior, on the other hand, is opposed at low or medium current densities, where very high anode relative humidity is always required to prevent the membrane drying.

The cathode exchange current density shows a great influence on the polarization curve, being perfectly in-line with the physical explanation already given.

5.3.2 Surrogate modelling and error estimate

Two tables were obtained, summing up the error analysis. The first presented case study is the approximation of the control factors matrix. The other set of parameters, the noise factors, were set as constant. The noise factors values are presented in Table 5.3.

Four approximation techniques were investigated to evaluate which one is the most performing. A useful tool to understand the quality of the surrogate model is the error analysis (Table 5.4).

Table 5.3 Constant values used for the noise factors when building the surrogate model for the control factors

c_r (1/s)	i_{0a} (A/m^2)	i_{0c} (A/m^2)	sat_{rate} (-)
200	1700	2	400

Table 5.4 Approximation techniques used to build the surrogate models for the control factors

Approximation technique	*Technique options*	*Number of cross-validation points (-)*	*Average error (%)*	*Maximum error (%)*	R^2 (-)
RSM	Quadratic	99	2.727	15.429	0.91647
RBF	-	99	1.816	14.604	0.92013
Orthogonal	Chebyshev 3° order polynomial	99	2.628	15.713	0.91542
Kriging	-	99	6.072	44.231	0.70623

To perform an error analysis (NIST/SEMATECH, 2011), some points are requested for a cross-validation: a number of data points were removed from the sampling data set, one at a time. For each of the removed points, the approximation coefficients were re-calculated, and the exact and approximate output values were compared. The removed point was then put back into the data set and the next point was removed. The choice of points is random, and the total amount of the points was equal to the number of points generated by the DoE, performing in this way a more detailed error analysis. As can be seen from Table 5.4, the Kriging approximation method provides an average and maximum error about three times the error obtained with other methods. Moreover, the RBF technique is the most performing (1.816% of average error) and the orthogonal polynomial and RSM approximations also provides an acceptable error (~ 2.7% of average error).

The R^2 value, also known as the coefficient of determination, is the ratio of the explained variation to the total variation. It is a mathematical measure of the error which estimates with a single number how well the assumed functional form of the response measures the variability of the supplied response data. A perfect fit of the response data corresponds to an R^2 value of 1.0. R^2 is defined as:

$$R^2 = \frac{\sum(\hat{y}_i - \bar{y})^2}{\sum(y_i - \bar{y})^2} \tag{5.2}$$

where y_i is the observed value for the i^{th} row of the DoE, $\hat{y}_i$ is the predicted value for the i^{th} row of the DoE, and $\bar{y}$ is the average of the observed values (NIST/SEMATECH, 2011). As can be seen from Table 5.4, Kriging approximation method provides an R^2 value that is quite far from the unit value if compared to the results provided from the other methods, showing the worst approximation. Figure 5.7 provides a useful plot to give a better idea of the entity of the average error obtained thanks to the RBF.

It is an actual vs. predicted plot showing the actual values of the response (obtained with the CFD analysis) plotted against the predicted equation for the response based on the assumed functional form. An even distribution of the data along the perfect fit line (in black) indicates smoothness of the assumed model and provides an overview of the shape of the model error (NIST/SEMATCH, 2011). As a conclusion, the RBF method was chosen for the next optimization process. Nevertheless, a validation process is needed to verify if the point is a real physical value. These analyses will follow the optimization process and will be presented in the next chapters.

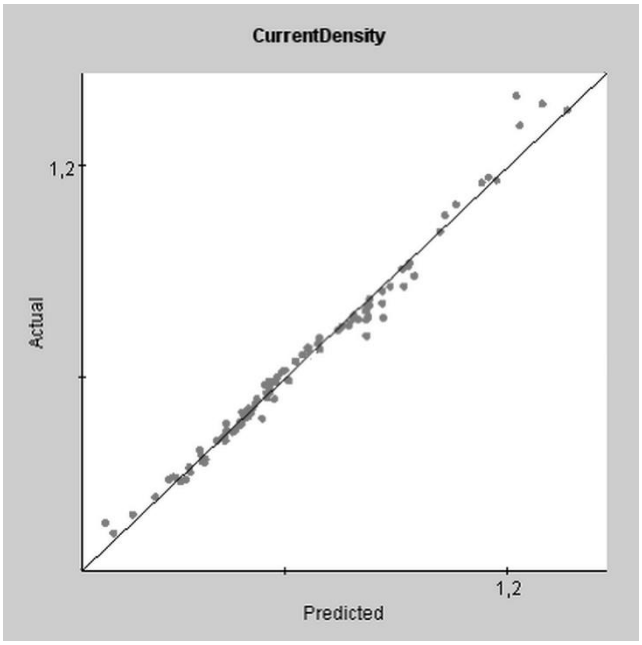

Figure 5.7 Plot of the error given by the RBF approximation

As done before, the same approximation techniques were investigated also for the noise factors, keeping constant the control factors values (Table 5.5). The error analysis is presented in Table 5.6, providing a useful decision tool. As can be seen, the Kriging approximation method provides an average error that is about two times the error obtained with the RSM and orthogonal method, while it is about three times the error given by the RBF technique. Moreover, the Kriging approximation method provides a maximum error that is greater than the errors obtained with the other methods. The other techniques, instead, provide very similar results. The Kriging approximation method provides an R^2 value that is quite far from the unit value if compared to the results provided from the other methods, showing the worst approximation. Even if the orthogonal approach presents some better performance if compared with the RBF methodology, the latter was tested to verify if it could be used to create also this surrogate model.

Table 5.5 Constant values used for the control factors when building the surrogate model for the noise factors

Rh_a (%)	T_a (K)	Rh_c (%)	T_c (K)	Compr (%)
90	300	85	310	15

Table 5.6 Approximation techniques used to build the surrogate models for the noise factors.

Approximation technique	*Technique options*	*Number of cross-validation points (-)*	*Average error (%)*	*Maximum error (%)*	R^2 (-)
RSM	Quadratic	99	3.427	37.830	0.90852
RBF	-	99	2.582	34.576	0.90468
Orthogonal	Chebyshev 3° order polynomial	99	3.299	32.115	0.91932
Kriging	-	99	5.819	52.143	0.67478

Other error analysis tools could be used, e.g. the Model Fit Error (MFE) and the Model Representation Error (MRE) (Peraudo et al. 2012).

5.3.3 Optimization process and validation

At this point, two different optimization processes were performed, depending on which set of parameters was fixed. The results are presented for two different sets, one set managing the noise factors values and a second one using the control factors values. As outlined in the previous chapter, it should be noted that the optimizations were performed on the approximate models, obtained thanks to the RBF technique.

As reported in Table 5.7 and Table 5.8, for the genetic algorithm some population parameters were set: 20 subpopulations were created for each one of the 20 different islands, defining a sufficient number of samples (400). A very important result was obtained: the optimized current density value is about 0.76 A/cm^2 in the case of the noise factors optimization, i.e. keeping the control factors constant.

The baseline starting current density value was 0.72 A/cm^2 at a voltage of 0.2 V. It must be underlined that noise factors are not controllable and modifiable, since their values depends mainly on physics laws.

Table 5.7 Optimization results for the noise factors values

Approximation technique	***Optimization algorithm***	***Optimized noise factors***				
		c_r ***(1/s)***	i_{0a} ***(A/m^2)***	i_{0c} ***(A/m^2)***	sat_{rate}	***Current density (A/m^2)***
RBF	Multi-Island 20 subpopulations, 20 islands	-153.967	2999.762	4.9994	632.082	0.7614

Table 5.8 Optimization results for the control factors values

Approximation technique	***Optimization algorithm***	***Optimized control factors***					
		Rh_a ***(%)***	T_a ***(K)***	Rh_c ***(%)***	T_c ***(K)***	***compr (%)***	***Current density (A/cm^2)***
RBF	Multi-Island 20 subpopulations, 20 islands	0.9991	335	0.9917	300	0.335	1.7266

The second optimization uses the control factors as design variables, while the noise factors are set constant. The results are given in Table 5.8. As can be seen, the same number of population parameters were set. Compared to the previous optimization loop, a different result was obtained: the optimized current density value is about 1.7266 A/cm^2, much higher than the starting value. The control factors can be tuned easily by the user if compared to the noise factors, making them the real key to optimize fuel cell operations.

A validation process is needed to verify if optimal solutions found by the genetic algorithm is physically acceptable (Min et al. 2006) and in accordance with a direct CFD simulation.

Starting from the set of optimized parameters listed in Table 5.7 and Table 5.8, a validation was done recurring to the multidisciplinary CFD cell model, to extract the simulated value of current density – the predicted "real" value, and compare it to the one estimated by the surrogated approach. The results are reported in Table 5.9.

As shown in Table 5.9, the results are extremely accurate for both the approximated optimization processes, confirming the goodness of the surrogate modelling technique and validating it completely.

Table 5.9 Evaluation of the error committed using the surrogate model for the optimization process

	Noise factors case study	***Control factors case study***
Estimated optimal current density (surrogate model, A/cm^2)	0.7614	1.7266
Simulated current density (CFD model A/cm^2)	0.7620	1.7412
Error (%)	0.078	0.839

All of the simulations were obtained with an HP xw6600 Workstation equipped with Intel Xeon architecture, with four dual core units (eight processors) and 8 Gb of RAM. The average time required for obtaining a single operating point of the fuel cell polarization curve using a complete CFD simulation is around 15 minutes, considering the fluid dynamics solution sufficiently converged. The total time required to obtain the sensitivity analysis with 100 points (requiring the execution of 100 different CFD simulations), together with the data management and post-processing operations, was of about 3 days and 23 hours. This can be considered the time spent to obtain the surrogate model. Nevertheless, having such meta-model available, it is possible to obtain a new polarization curve point in the order of few seconds of computational time, instead of using a complete CFD simulation. This allows for a rapid optimization analysis (requiring sometimes hundreds of simulations), requiring about 10 minutes for the whole meta-model-based MDO process.

6. CONCLUSIONS

The present thesis has been developed with the aim of creating a multidisciplinary numerical model of a proton exchange membrane fuel cell encompassing all of the main physical aspects involved in this kind of technology, from a fluid-dynamics to an electrochemical and thermal viewpoint. One of the most important features recommended for this model was its robustness and hence reliability in the predicted numerical results. The scope for creating this model was to create a preliminary virtual test bench of a fuel cell in order to create a valid instrument for future fuel cell power systems design, development and analysis, as well as for optimization purposes.

These requirements and objectives cannot be reached without the implementation of a good simulation framework. From an optimization and sensitivity point of view, the setup of a stable and reliable numerical model becomes mandatory.

The PEM fuel cell and alkaline electrolyser stacks multidisciplinary model developed in this thesis started from the investigation of other lumped parameters models available in literature to find pros and cons of already available models.

The numerical model has been developed starting from other works, simplifying them and expanding their capabilities with the inclusion of all of the physical aspects the fuel cell exhibits. In particular, improved fluid-dynamics, electrochemistry and thermodynamics have been deeply investigated and correctly modelled within the fuel cell. The model has been developed through successive improvements, starting from a preliminary model, and adding complexity. One of the most relevant aspects considered in the models development was the particular attention paid at the transient phenomena. Transient response of fuel cell and electrolysers stack becomes crucial in the design phase of a real system.

Together with the modelling of the fuel cell and electrolyser stacks, all of the other main ancillary elements were modelled to obtain a complete fuel cell and electrolyser systems. The elements modelled were motors, air compressors, membrane humidifiers fed by humidified air and water heat-exchangers (intercoolers), gas storage subsystems and flow mixers. All of these elements were modelled in the same manner of the stacks and then calibrated and validated with the available data. All of these elements were created to allow the user to obtain an arbitrary system layout simply putting together the model blocks in the same way of a standard Simulink block. Attention was paid to the transient aspects also in this case.

The stacks and the main elements were validated, and then put together to simulate the complete behaviour of the entire system. The calibration process and validation was performed. In particular, the PEM fuel cell stack was validated separately from the system. The results of the validation process showed an excellent correspondence between the experimental data available for the stack and the results obtained from the model simulation. Average and maximum errors were

calculated during a simulation of about 3500 seconds at each second. For both of them, their value was below the 1.0 percent, indicating the perfect correspondence between experimental and simulation data. The correspondence was met both in the steady-state and transient response. The electrolyser system was validated with experimental data and other model data available from other authors. Also in this case, the error between experimental and simulation data was excellent. The validation and calibration of the other elements of the system revealed in some cases errors acceptable, usually below the 10 percent. The optimal results given by the validation of the models revealed the high fidelity of the models developed.

The complete systems were then simulated and the results were analysed considering all of the most relevant variables of each block of the systems.

Together with the lumped parameters model, a sensitivity analysis on a PEM fuel cell modelled in CFD was performed. The main scope of this work was to set up an optimization environment dedicated to the optimal design of PEM fuel cells, and to assess its reliability and feasibility when applied to such technologies. This methodology was applied to a relatively simple and small PEM fuel cell model.

The analyses carried out in this work showed the potentialities of the surrogate modelling technique combined with an optimization process. The main aspects considered involved the setup of an automated MDO process based on a surrogate model obtained thanks to a previous sensitivity analysis performed recurring to a Monte Carlo Simulation. This approach was chosen with the aim of estimating the parameters affection on the global cell performance.

The unconstrained deterministic single-objective MDO processes performed, finding the optimal solution in terms of maximum current density the cell can produce at a given voltage, was followed by a validation process of the optimal solution was tested to confirm the effectiveness and quality of the whole process implemented (i.e. keeping the average error to a minimum value). As a conclusion, this work showed the potentialities of the application of such techniques for the optimal design of fuel cells.

The objective of creating a virtual test bench in order to create a valid instrument for future fuel cell power systems design, development and analysis, as well as for optimization purposes can be considered sufficiently achieved.

APPENDIX

A.1 Ideal open circuit voltage function of temperature

The ideal open circuit voltage function of temperature is obtained from the approximation of the Gibbs free energy with temperature, integrating the species (H_2, O_2 and H_2O) specific heat (c_p) polynomial functions.

The change in molar Gibbs free energy (ΔG_f, measured in J mol^{-1}) is expressed through the change in molar enthalpy (Δh_f, in J^{-1}mol^{-1}) and molar entropy (Δs_f, measured in J mol^{-1} K^{-1}) in the form:

$$\Delta G_f = \Delta h_f - T\Delta s_f = h\text{-}_{H_2O} - h_{H_2} - \frac{1}{2}h_{O_2} - T\left(s_{H_2O} - s_{H_2} - \frac{1}{2}s_{O_2}\right) \quad \text{(A.1.1)}$$

Being the change of variables defined as the enthalpy (entropy) of products minus the enthalpy (entropy) of reactants. The variation of enthalpy and entropy with temperature can be defined as:

$$h_T = h_{298.15} + \int_{298.15}^{T} c_p dT \quad \text{(A.1.2)}$$

$$s_T = s_{298.15} + \int_{298.15}^{T} \frac{1}{T} c_p dT \quad \text{(A.1.3)}$$

with $h_{298.15}$ and $s_{298.15}$ are the reference temperature values indicated in Table 1.

The polynomial functions representing $c_p = c_p(T)$, estimated empirically, are the following:

$$c_{p_{steam}}(T) = 143.05 - 58.040T^{0.25} + 8.2751T^{0.5} - 0.036989T \quad \text{(A.1.4)}$$

$$c_{p_{liquid}}(T) = -203.606 + 1.52329T - \frac{3196.413}{1e6}T^2 + \frac{2474.455}{1e9}T^3 + \frac{3.855326e6}{T^2} \quad \text{(A.1.5)}$$

$$c_{p_{H_2}}(T) = 56.505 - 22222.6T^{-0.75} + 116500T^{-1} - 560700T^{-1.5} \quad \text{(A.1.6)}$$

$$c_{p_{O_2}}(T) = 37.432 + 2010.2 \times 10^{-5}T^{1.5} - 178570T^{-1.5} + 2368800T^{-2} \quad \text{(A.1.7)}$$

With c_p defined in J mol^{-1} K^{-1}.

Appendix A

Table A. 1 Values of h and s at reference temperature for hydrogen fuel cells

Species	h_f **(J mol^{-1})**	**S (J mol^{-1} K^{-1})**
H_2O (liquid)	-285838	70.05
H_2O (steam)	-241827	188.83
H_2	0	130.59
O_2	0	205.14

Calculating the equations above in the temperature interval 373.15 K - 1200 K, a linear approximation of the resulting Δg_f can been calculated, with the resulting correlation:

$$\Delta G_f(T) = 52.7T - 245325 \quad \text{(A.1.8)}$$

Calculated with liquid water formation and a R^2 approximation error equal to 0.9994.

A.2 Gas diffusion layer FEM model

```
%GDL FEM discretization.
clear all

nz = 50;
D=zeros(2,nz*2);
flag = 0;
dz = 1e-6;
dt = 1e-8;
K = dt/2/dz^2;

%Tempor:
T = 320;
P = 130000;
x1 = 0.7*ones(nz,1);
x1(1) = 0.9;
x1(nz) = 0.1;
x2 = 0.65*ones(nz,1);
x2(1) = 0.0;
x2(nz)=0.8;

x3 = 1-x2-x1;
%-------------

D12 = 4.281e-6*T^(2.334)/P;          %(O2-H2O)
D13 = 5.338e-4*T^(1.5)/P/exp(83.63/T);  %(O2-N2)
D23 = 4.477e-6*T^2.334/P;            %(H2O-N2)

figure(1)

for tempo = 1 : 100


for p = 1 : nz
```

```
%Matrix D calc
DetB = (D23*x1(p)+D13*x2(p)+D12*x3(p))/(D12*D13*D23);
D(1,p+flag) = 1/DetB*((D23*x1(p)+D12*(x2(p)+x3(p)))/D12/D23);
D(1,p+1+flag) = -1/DetB*((D12-D13)*x1(p)/D12/D13);
D(2,p+flag) = -1/DetB*((D12-D23)*x2(p)/D12/D23);
D(2,p+1+flag) = 1/DetB*((D13*x2(p)+D12*(x1(p)+x3(p)))/D12/D13);
flag = flag + 1;
end

%A matrix build
A=zeros(2*(nz-2),2*(nz-2));
for p = 2 : nz-1

for i = 1 : 2
   for ip = 1 : 2
      for j = 1 : nz-2
         for jp = 1 : nz-2
               Dp = D(i,2*(p-1)+ip)/2+D(i,2*p+ip)/2;
               Dm = D(i,2*(p-1)+ip)/2+D(i,2*(p-2)+ip)/2;
            if (i==ip && j==jp)
                  A(((i-1)*(nz-2)+j),((ip-1)*(nz-2)+jp))=1+K*(Dp+Dm);
            else
            if (i~=ip && j==jp)
                  A(((i-1)*(nz-2)+j),((ip-1)*(nz-2)+jp))=K*(Dp+Dm);
            else
               if (j == (jp-1))
                  A(((i-1)*(nz-2)+j),((ip-1)*(nz-2)+jp))=-K*(Dm);
               else
                  if (j == (jp+1))
                     A(((i-1)*(nz-2)+j),((ip-1)*(nz-2)+jp))=-K*(Dp);
                  end
               end
            end
            end
         end
      end
   end
end
end

% %B matrix build
B=zeros((nz-2)*2,1);
for i = 1 : 2
   if (i == 1)
      x=x1;
   else
      x=x2;
   end

   for j = 1 : nz-2
      B((i-1)*(nz-2)+j)=x(j)+K*((D(i,2*j+1)/2+D(i,2*(j+1)+1)/2)*(x1(j+2)-x1(j+1)) + ...
         (D(i,j*2+1)/2+D(i,(j-1)*2+1)/2)*(x1(j)-x1(j+1))+...
         (D(i,2*j+2)/2+D(i,2*(j+1)+2)/2)*(x2(j+2)-x2(j+1))+...
         (D(i,2*j+2)/2+D(i,2*(j-1)+2)/2)*(x2(j)-x2(j+1)));
   end
end

C=A\B;
```

```
x1(2:nz-1)=C(1:(nz-2));
x2(2:nz-1)=C((nz-1):2*(nz-2));
x3=1-x1-x2;
end
```

REFERENCES

Adzapka, K.P., Agbossou, K., Dubé, Y., Dostie, M., Fournier, M., Poulin, A., 2008. *PEM fuel cells modelling and analysis through current and voltage transient behaviors*. IEEE Trans. Energy Convers. 23(2):581-591.

Ahluwalia, R.K., Wang, X., 2007. *Buildup of nitrogen in direct hydrogen polymer-electrolyte fuel cell stacks*. J: Power Sources. 171: 63-71.

Ahmadi, N., Rezazadeh, S., Mirzaee, I., Pourmahmoud, N., 2012. *Three-dimensional computational fluid dynamic analysis of the conventional PEM fuel cell and investigation of prominent gas diffusion layers effect*. J Mech Sci And Tech 26: 2247-2257.

Ahmed, S.K., Chmielewsi, D.J., 2011. *Closed-loop hydration dynamics in the membrane of a PEM fuel cell*. J. Power Sources. 196: 5555-5563.

ANSYS, 2011. *ANSYS FLUENT fuel cell modules manual*. ANSYS, Inc, USA.

Bagotsky, V.S., 2006. *Fundamentals of electrochemistry*. *2nd edition.* New Jersey, U.S., John Wiley & Sons, Inc. ISBN: 13 9780471700586.

Ballard, 2007. *Mark9 SSL. Product manual and integration guide*.

Bao, C., Ouyang, M., Yi B., 2006. *Modeling and control of air stream and hydrogen flow with recirculation in a PEM fuel cell system - I. control-oriented modeling*. Int. J. Hydrogen Energy. 31: 1879-1896.

Barthelemy, JF. M., Haftka, R.T., 1993. Approximation concepts for optimum structural design – A review. Struct. Optim. 5: 129-144.

Bernstein, A.V., Kuleshov, A.P., 2009. *Construction of orthogonal non-linear manifolds in the problem of dimension reduction.* In: Proceedings of 7th International School – Seminar on Multivariate statistical analysis and econometrics.

Bird, J.P., 2002. *Model of the air system transients in a fuel cell vehicle.* M.Sc. thesis. Mechanical engineering. Virginia Polytechnic Institute and State University. Virginia, U.S.

Box, G.E.P., Draper, N.R., 1969. *Evolutionary operation: A statistical method for process management*. John Wiley & Sons, New York.

Cemmi, A., Pozio, A., 2008. *Processo di elettrolisi dell'acqua per la produzione di idrogeno*. ENEA – Dip. Tecnologie per l'Energia, Fonti Rinnovabili e Risparmio Energetico, Roma, Italy.

Ceraolo, M., Miulli, C., Pozio, A., 2003. *MOdelling static and dynamic behaviour of proton exchange membrane fuel cells on the basis of electro-chemical description*. J. Power Sources. 113: 131-144.

Chen, D., Li, W., Peng, H., 2008. *An experimental study and model validation of a membrane humidifier for PEM fuel cell humidification control*. J. Power Sources. 180:461-467.

Chen, W., Allen, J.K., Schrage, D.P., Mistree, F., 1997. *Statistical experimentation methods for achieving affordable concurrent systems design*. AIAA Meeting Papers on Disc, pp. 921-930.

Chen, Y-S., Peng, H., 2008. *A segmented model for studying water transport in a PEMFC*. J. Power Sources. 185: 1179-1192.

Chu, K., Ryu, J., Sunwoo, M., 2007. *A lumped parameter model of the polymer electrolyte fuel cell*. J. Power Sources. 171: 412-423.

Cressie, N.A.C., 1993. *Statistics for spatial data, revised edition*. John Wiley & Sons, New York.

Dawes, J.E., Hanspal, N.S., Family, O.A., Turan, A., 2009. *Three-dimensional CFD modelling of PEM fuel cells: an investigation into the effects of water flooding*. J. Chem. Engin. Sci. 64: 2781-2794.

Deb, K., 2001. *Multi-objective optimization using evolutionary algorithms*. John Wiley & Sons, New York.

Dutta, S., Shimpalee, S., Van Zee, J.W., 1999. *Effect of humidity on PEM fuel cell performance. Part II - numerical simulation*. Proc. of ASME IMECE, Nashville, TN, HTD 364-1, pp.367-374(1999).

Dutta, S., Shimpalee, S., Van Zee, J.W., 2000. *Three-dimensional numerical simulation of straight channel PEM fuel cells*. J. Applied Electrochem. 30: 135-146.

Dutta, S., Shimpalee, S., Van Zee, J.W., 2001. *Numerical prediction of mass-exchange between cathode and anode channels in PEM fuel cell*. Int. J. Heat and Mass Transf. 44: 2029-2042.

D3.4.3 2009. *Optimisation and robust design capabilities – achievements, needs and orientations*. CRESCENDO FP7-234344 © Copyright CRESCENDO Consortium.

EG&G Technical Servicing Inc., 2004. *Fuel cell handbook. Seventh edition*. West Virginia, U.S., Department of Energy.

Evangelista, J., Phillips, B., Gordon, L., 1975. *Electrolytic hydrogen production. An analysis and review*. Lewis Research Center, Ohio, U.S. Nasa technical memorandum. NASA TM X-71856.

Falcão D.S., Gomes P.J., Oliveira V.B., Pinho C., Pinto A.M.F.R., 2011. *1D and 3D numerical simulations in PEM fuel cells*. Int. J. Hydrogen Energy 36: 12486-12498.

Fonseca C.M., Fleming P. J., 1993. *Genetic algorithms for multiobjective optimization: formulation, discussion and generalization*. In Proceedings of the 5th international conference on genetic algorithms, San Mateo, CA, USA.

Francis, D.P., Coats A.J., Gibson D., 1999. *How high can a correlation coefficient be? Effects of limited reproducibility of common cardiological measures*. Int. J. Cardiol. 69: 185–199.

Garcìa-Valverde, R., Espinosa, N., Urbina, A., 2012. *Simple PEM water electrolyser model and experimental validation*. Int. J. Hydrogen Energy. 37: 1927-1938.

Gilliam, R.J., Graydon, J.W., Kirk, D.W., Thorpe, S.J., 2007. *A review of specific conductivities of potassium hydroxide solutions for various concentrations and temperatures*. Int. J. Hydrogen Energy. 32: 359-364. doi: 10.1016/j.ijhydene.2006.10.062

Goldberg D.E., 1989. *Genetic algorithms in search, optimization and machine learning*. Addison-Wesly publishing company, Alabama.

Grimes, C.A., Varghese, K., O., Ranjan, S., 2008. *Light, Water, Hydrogen. The solar generation of hydrogen by water photoelectrolysis*. New York, U.S., Springer. ISBN: 9780387331980.

Guvelioglu G.H., Stenger H.G., 2005. *Main and interaction effects of PEM fuel cell design parameters*. J. Power Sources 2: 424-433.

Halpert, G., Harvey, F., Surampudi, S., 1999. *Batteries and fuel cells in space*. Electrochem. Soc.

Häussinger, P., Lohmüller, R., Watson, A.M., 2012. *Ullmann's encyclopedia of industrial chemistry*. Vol.18, Hydrogen, 2. Production. Pp. 249-307. Wiley-VCH, Germany.

Haynes, W.M., Lide, D.R., Bruno, T.J., 2012. *CRC handbook of chemistry and physics* (93rd Edition). CRC Press

Henao C., Agbossou K., Hammoudi, M., Dubé, Y., Cardenas, A., 2014. *Simulation tool based on a physics model and an electrical analogy for an alkaline electrolyser*. J. Power Sources. 250: 58-67.

Hou, Y., Yang, Z., Wan, G., 2010. *An improved dynamic voltage model of PEM fuel cell stack*. Int. J. Hydrogen Energy. 35: 11154-11160.

Hu W., Enying, L., Li, G.Y., Zhong, Z.H., 2008. *A meta-model optimization methodology based on multi-level fuzzy clustering space reduction strategy and its applications*. Computers & Ind. Engin. 55:503-532.

Huisseune, H., Willockx, A., De Paepe, M., 2008. *Semi-empirical along-the-channel model for a proton exchange membrane fuel cell*. Int. J. Hydrogen Energy. 33: 6270-6280.

Ivy, J., 2004. *Summary of electrolytic hydrogen production*. NREL – National Renewable Energy Laboratory, Golden, Colorado, U.S. NREL/MP-560-36734

Journel, A., Huijbregts, C., 1978. *Mining Geostatistics*. Academic Press, London.

Kim C., Sun, H., 2012. *Topology optimization of gas flow channel in an automotive fuel cell*. Int. J. Automot. Tech. 13:783-789.

Kim, H-S., Min, K., 2008. *Experimental investigation of dynamic responses of a transparent PEM fuel cell to step changes in cell current density with operating temperature*. J. Mech. Sci. and Tech. 22: 2274-2285.

Koehler, J.R., Owen, A.B., 1996. *Computer experiments. Handbook of Statistics*. Elsevier Science, New York, pp. 261-308.

Larminie, J., Dicks, A., 2003. *Fuel cell systems explained. Second edition*. England, John Wiley & Sons Ltd. ISBN: 047084857X.

Lienhard I.V.J.H., Lienhard V.J.H., 2003. *A heat transfer textbook. Third edition.* Phlogiston Press, Cambridge, Massachussetts, U.S.

Lindman, H.R., 1974. *Analysis of variance in complex experimental designs*. San Francisco: W. H. Freeman & Co. USA.

Lum, K.W., McGuirk, J.J., 2005. *Three-dimensional model of a complete polymer electrolyte membrane fuel-cell model formulation, validation and parametric studies*, J. Power Sources, 143: 103-124.

Luo, N., Miley, G.H., Gimlin, R., Burton, R., 2008. *Hydrogen-peroxide-based fuel cells for space power systems*, J. Propuls. And Power, 24: 583-589.

Maher, A.R., Sadiq Al-Baghdadi, 2009. *A CFD study of hygro-thermal stresses distribution in PEM fuel cell during regular cell operation*. J. Renew. Energy 34: 674-682.

Meng, H., 2007. *A two phase non-isothermal mixed-domain PEM fuel cell model and its application to two-dimensional simulations*. J. Pow. Sources. 168: 218-228.

Menon, V., Janardhanan, V.M., Tischer, S., Deutschmann, O., 2012. *A novel approach to model the transient behaviour of solid-oxide fuel cell stacks*. J. Pow. Sources. 214: 227-238.

Meurer, C., Barthels, H., Brocke, W.A., Emonts, B., Groehn, H.G., 1999. *Phebus – An autonomous supply system with renewable energy: six years of operational experience and advanced concepts*. Solar Energy. 67: 131-138.

Min, C.H., He, Y.L., Liu, X.L., Yin, B.H., Jiang, W., Tao, W.Q., 2006. *Parameter sensitivity examination and discussion of PEM fuel cell simulation model validation. Part II: results of sensitivity analysis and validation of the model*. J. Pow. Sources. 160: 374-385.

Motupally, S., Becker, A.J., Weidner, J.W., 2000. *Diffusion of water in Nafion 115 membranes*. J. Electrochem. Soc. 147: 3171-3177.

Mukhtar B., Javaid Zaidi S., Naim Faqir M., 2010. *Multi-objective function optimization for PEM fuel cell system*. ECS Trans. 26: 77-88.

Nehrir, M.H., Wang, C., 2009. *Modeling and control of fuel cells. Distributed generation applications*. New Jersey, U.S., John Wiley & Sons Ltd. ISBN: 9780470233283.

Ni, M., Leung, M.K.H., Leung, D.Y.C., 2008. *Energy and exergy analysis of hydrogen production by a proton exchange membrane (PEM) electrolyser plant*. J. Energy Convers. And Manag. 49: 2748-2756.

NIST/SEMATECH 2011. *E-handbook of statistical methods*.

Nitta, J., Karvonen, S., Himanen, O., Mikkola, M., 2007. *Modelling the Effects of Inhomogeneous Compression of GDL on Local Transport Phenomena in a PEM Fuel Cell*. Fuel Cells, 0(0):410-421.

Noren, D.A., Hoffman, M.A., 2005. *Clarifying the Butler-Volmer equation and related approximations for calculating activation losses in solid oxide fuel cell models*. J. Pow. Sources, 152: 175-181. doi: 10.1016/j.jpowsour.2005.03.174

Park, S-K, Choe, S-Y, Choi, S-h, 2008. *Dynamic modelling and analysis of a shell-and-tube type gas-to-gas membrane humidifier ™for PEM fuel cell applications*. Int. J. Hydrogen Energy. 33:2273-2282.

Pathapati, P.R., Xue, X., Tang, J., 2004. *A new dynamic model for predicting transient phenomena in a PEM fuel cell system*. Renew. Energy. 30: 1-22.

PermaPure *fuel cell humidifiers*, 2013. Available from: http://www.permapure.com/products/humidifiers/fc-series-humidifiers/?ind=fuelcell&prod=676. Last access: 27/08/2013

Pisani, L., Murgia, G., Valentini, M., D'Aguanno, B., 2002. *A new semi-empirical approach to performance curves of polymer electrolyte fuel cells*. J. Power Sources. 108: 192-203.

Pukrushpan, J.T., Stefanopoulou, A.G., Peng, H., 2004. *Control of fuel cell power systems: principles, modelling, analysis and feedback design*. U.S. Springer-Verlag. ISBN: 1852338164.

Rubinstein, R.Y., Kroese, D.P., 2007. *Simulation and the Monte Carlo method*. 2nd ed. John Wiley & Sons, New York.

Secanell, M., Songprakorp, R., Djilali, N., Suleman, A., 2010. *Optimization of a proton exchange membrane fuel cell membrane electrode assembly*. Struct. Multidisc. Optim. 40: 563-583.

Sharifi Asl, S.M., Rowshanzamir S., Eikani M.H., 2010. *Modelling and simulation of the steady-state and dynamic behaviour of a PEM fuel cell*. Ijnt. J. Energy. 35: 1633-1646.

Siegel, N.P., Ellis, M.W., Nelson, D.J., Von Spakovsky, M.R., 2003. *A two-dimensional computational model of PEMFC with liquid water transport*. J. Power Sources 128: 173-184.

Sivertsen, B.R., Djilali N., 2005. *CFD-based modelling of proton exchange membrane fuel cells*. J. Power Sources 141: 65-78.

Smedsrud, H., 2007. *Dynamic model and control of heat exchanger networks*. 5th year project work. Norwegian University of Science and Technology. Department of Chemical Engineering. 2007.

Springer, T.E., Zawodzinski, T.A., Gottesfled, S., 1991. *Polymer electrolyte fuel cell model*. J. Electrochem. Soc. 138: 2334-2342.

Stigler, S.M., 1989. *Francis Galton's account of the invention of correlation*. Stat. Sci. 4: 73-79.

Su, A., Ferng, Y.M., Shin, J.C., 2010. *CFD investigating the effects of different operating conditions on the performance and the characteristics of a high-temperature PEMFC*. J. Energy, 35: 16-27.

Tabachnick, B., Fidell, G., Linda S., 2007. *Using multivariate statistics*. 5th ed. Pearson International Edition, Boston.

Taguchi, G., 1987. *System of experimental design: engineering methods to optimize quality and minimize cost*. Kraus International Publications, MI, USA.

Tobias, C.W., 1959. *Effect of gas evolution on current distribution and ohmic resistance in electrolysers*. J. Electrochem. Soc. 106: 833-839

Ulleberg, Ø., 2003. *Modeling of advanced alkaline electrolyzers: a system simulation approach*. Int. J. Hydrogen Energy. 28: 21-33.

Urbani, F., Barbera, O., Giacoppo, G., Squadrito, G., Passalacqua, E., 2008. *Effect of operating conditions on a PEFC stack performance.* Int. J. Hydrogen Energy 33: 3137-3141.

Verhaert, I., Vernhelst, S., Janssen, G., Mulder, G., De PAepe, M., 2011. *Water management in an alkaline fuel cell*. Int. J. Hydrogen Energy. 26: 11011-11024.

Vermeiren, P., Adriansens, W., Moreels, J.P., Leysen, R., 1997. *Evaluation of the Zirfon® separator for use in alkaline water electrolysis and Ni-H_2 batteries*. Int. J. Hydrogen Energy. 23: 321-324.

Vigna Suria O., Testa E., Peraudo P., Maggiore P., 2011. *A PEM fuel cell distributed parameters model aiming at studying the production of liquid water within the cell during its normal operation: model description, implementation and validation*. In SAE World Congress 2011, MI, USA.

Vilekar, S.A., Datta, R., 2010. *The effect of hydrogen crossover on open-circuit voltage in polymer electrolyte membrane fuel cells*. J. Power Sources. 195: 2241-2247. doi: 10.1016/j.jpowsour.2009.10.023.

Wang C.Y., 2004. *Fundamental models for fuel cell engineering*. Chem. Rev. 104: 4727-4766.

Wei, Y., Yong, T., Minqiang, P., Zongtao, L., Biao, T., 2010. *Model prediction of effects of operating parameters on proton exchange membrane fuel cell performance*. J. Renew. Energy. 35: 656-666.

Welty, J.R., Wicks, C.E., Wilson, R.E., Rorrer, G.L., 2007. *Fundamentals of momentum, heat and mass transfer*. 5th edition. John Wiley and Sons.

Xue X., Tang, J., Smirnova, A., England, R., Sammes, N., 2004. *System level lumped-parameter dynamic modeling of PEM fuel cell*. J. Power Sources. 130: 188-204.

Yu, X., Zhou, B., Sobiesiak, A., 2005. *Water and thermal management for Ballard PEM fuel cell stack*. J. Power Sources. 147: 184-195.

Zhang, H., Lin, G., Chen, J, 2010. *Evaluation and calculation on the efficiency of a water electrolysis system for hydrogen production*. Int. J. Hydrogen Energy. 35: 10851-10858.

Zhou, L., Zhou, Y., 2001. *Determination of compressibility factor and fugacity coefficient of hydrogen in studies of adsorptive storage*. Int. J. Hydrogen Energy. 26: 597-601.